



---

**Forschungszentrum Karlsruhe**  
in der Helmholtz-Gemeinschaft

---

**Wissenschaftliche Berichte**  
FZKA 7242

**Validation of Target  
Parameters of ENVISAT  
Chemistry Instruments  
with Correlative Balloon  
Observations Obtained by  
MIPAS-B**

**G. Zhang**

Institut für Meteorologie und Klimaforschung

Juli 2006



**Forschungszentrum Karlsruhe**

in der Helmholtz-Gemeinschaft

Wissenschaftliche Berichte

FZKA 7242

**Validation of target parameters of ENVISAT  
chemistry instruments with correlative balloon  
observations obtained by MIPAS-B<sup>\*</sup>**

Guochang Zhang

Institut für Meteorologie und Klimaforschung

\*Von der Fakultät für Physik der Universität Karlsruhe (TH)  
genehmigte Dissertation

Forschungszentrum Karlsruhe GmbH, Karlsruhe

2006

Für diesen Bericht behalten wir uns alle Rechte vor

Forschungszentrum Karlsruhe GmbH  
Postfach 3640, 76021 Karlsruhe

Mitglied der Hermann von Helmholtz-Gemeinschaft  
Deutscher Forschungszentren (HGF)

ISSN 0947-8620

urn:nbn:de:0005-072421

**Validation of target parameters of ENVISAT  
chemistry instruments with correlative balloon  
observations obtained by MIPAS-B**

**Validierung von Zielparametern der  
Chemieinstrumente auf ENVISAT mit MIPAS-  
Ballonmessungen**

Zur Erlangung des akademischen Grades eines  
DOKTORS DER NATURWISSENSCHAFTEN

von der Fakultät für Physik der  
Universität Karlsruhe (TH)

genehmigte

DISSERTATION

von

Master of Phys. Guochang Zhang

aus China

Tag der mündlichen Prüfung:  
Referent:  
Korreferent:

09. Juni 2006  
Prof. Dr. H. Fischer  
Priv. Doz. Dr. habil. C. E. Blom



## Abstract

Mankind is facing the challenges of climate anomaly and air pollution. Pollution control and the understanding of climate anomaly depend on long-term, accurate, and extensive observations of the atmosphere. On 1 March, 2002, the ENVISAT satellite was launched by ESA. It is an advanced polar-orbiting Earth observation satellite with three chemistry instruments for remote sounding of trace gases in the atmosphere. These three instruments are MIPAS, SCIAMACHY, and GOMOS. Since then, they have produced numerous data. For the proper application in scientific research and other fields, these data have to be validated by different approaches. One of them is intercomparison between these data and independent measurements from other instruments.

MIPAS-B is a well-established Fourier transform spectrometer operated onboard balloons. Embedded in the ENVISAT validation programme of the chemical instruments, three balloon flights were carried out with MIPAS-B from Aire sur l'Adour, France, on 24/25 September 2002, from Kiruna, Sweden, on 20/21 March 2003, and again from Kiruna, on 2/3 July 2003. The temperature profiles and the volume mixing ratio (VMR) profiles of H<sub>2</sub>O, O<sub>3</sub>, HNO<sub>3</sub>, CH<sub>4</sub>, N<sub>2</sub>O, and NO<sub>2</sub> were retrieved carefully from the MIPAS-B spectra measured during these flights.

The quality of coincidence in space and time between MIPAS-B and MIPAS-ENVISAT observations for these three flights is excellent (except for the temporal offset in the third flight), providing the opportunities to check the MIPAS data under favourable conditions. To enhance the statistics of the validation, the trajectory comparison approach was applied. In addition, for the validation of NO<sub>2</sub> which is a chemically active gas, the MIPAS-B NO<sub>2</sub> data were photochemically adjusted with the help of the KASIMA chemical model. The validation of MIPAS off-line data V4.61 was carried out between 356 and 3 hPa (8-39 km), but for NO<sub>2</sub> only between 42 and 3 hPa (22-39 km).

The individual comparisons show that the discrepancies of all target parameters exceed the combined total errors at certain levels of altitude. The statistical results validate the accuracy of MIPAS-ENVISAT data for temperature and the six key gas species—H<sub>2</sub>O, O<sub>3</sub>, HNO<sub>3</sub>, CH<sub>4</sub>, N<sub>2</sub>O, and NO<sub>2</sub> in the overlapping altitude region. The exception is H<sub>2</sub>O in the region of 356-195 hPa (8-12 km). Agreements in the middle stratosphere are better than in the lower stratosphere and upper troposphere. In the altitude region of 123-8 hPa (15-33 km) (for NO<sub>2</sub>, the region is 23-8 hPa (26-33 km)), the precision of MIPAS-ENVISAT data for H<sub>2</sub>O, O<sub>3</sub>, CH<sub>4</sub>, NO<sub>2</sub> was validated, which is not the case for HNO<sub>3</sub> and N<sub>2</sub>O. As regards temperature, the precision was validated in principle above the altitude of about 17 hPa, but not below this level.

MIPAS-ENVISAT measurements for H<sub>2</sub>O show a positive bias above the altitude of about 20 hPa, though the bias is still within the combined total errors. Besides, the MIPAS-ENVISAT H<sub>2</sub>O profiles often reveal strong oscillations. Between about 195 hPa and 80 hPa (12-18 km), MIPAS-ENVISAT measured high values for CH<sub>4</sub> and N<sub>2</sub>O. Below the level of about 80 hPa (18 km), CH<sub>4</sub> and N<sub>2</sub>O profiles of MIPAS-ENVISAT show strong oscillations, sometimes leading even to unphysical values. Oscillations occasionally occur in the HNO<sub>3</sub> and NO<sub>2</sub> profiles.

The conclusions drawn for the SCIAMACHY O<sub>3</sub> and NO<sub>2</sub> data as analysed with the scientific processor of the IUP/IFE are based on trajectory comparison results. The SCIAMACHY

accuracy for O<sub>3</sub> was validated in the 9-28 km altitude range. Above 26 km, SCIAMACHY data start to show a positive bias that exceeds the combined total errors above 28 km. The accuracy of NO<sub>2</sub> data was validated between 9-39 km with mean differences smaller than 0.52 ppbv or 6.3%.

Only one O<sub>3</sub> profile and one NO<sub>2</sub> profile of GOMOS off-line data V6.01 were compared with MIPAS-B correlative measurements using a coincident comparison approach. Preliminary results show that GOMOS measurements for O<sub>3</sub> and NO<sub>2</sub> agree with MIPAS-B data with respect to their combined errors in general. The O<sub>3</sub> and NO<sub>2</sub> profiles of GOMOS oscillate with large amplitude especially in the upper altitude region. It is impossible to give any statistical conclusion for GOMOS data from the point of MIPAS-B data so far.



# Validierung von Zielparametern der Chemieinstrumente auf ENVISAT mit MIPAS- Ballonmessungen

## Zusammenfassung

Die größten Herausforderungen, denen der Mensch derzeit gegenübersteht, sind die Klimaänderung und Luftverschmutzung. Um die Schadstoffkonzentration zu überwachen und den Klimawechsel genau zu verstehen bedarf es langfristiger, präziser und umfassender Beobachtungen der Atmosphäre. Am 1. März 2002 startete die ESA den Satelliten ENVISAT. Hierbei handelt es sich um einen hochentwickelten, auf einer polaren Umlaufbahn ausgesetzten Erdbeobachtungssatelliten, der mit drei chemischen Messgeräten für die Fernerkundung von Spurengasen in der Atmosphäre ausgerüstet ist: MIPAS, SCIAMACHY und GOMOS. Mittlerweile haben diese Instrumente eine große Datenmenge produziert. Für die Nutzung in der wissenschaftlichen Forschung und anderen Bereichen müssen diese Daten validiert werden. Dazu werden verschiedene Methoden eingesetzt. Eine davon besteht in einem Vergleich dieser Daten mit unabhängigen Messungen anderer Instrumente.

MIPAS-B ist ein an Bord von Ballons eingesetztes Fourier-Transform-Spektrometer. Im Rahmen des ENVISAT-Validierungsprogramms der chemischen Messgeräte wurden drei Ballonflüge mit MIPAS-B durchgeführt. Diese starteten am 24./25. September 2002 in Aire sur l'Adour, Frankreich, am 20./21. März 2003 in Kiruna, Schweden und am 2./3. Juli 2003 wieder in Kiruna. Auf der Grundlage der während dieser Flüge gemessenen MIPAS-B-Spektren wurden die Temperaturprofile und die Profile für das Volumenmischungsverhältnis von  $\text{H}_2\text{O}$ ,  $\text{O}_3$ ,  $\text{HNO}_3$ ,  $\text{CH}_4$ ,  $\text{N}_2\text{O}$  sowie  $\text{NO}_2$  bestimmt.

Die räumliche und zeitliche Übereinstimmung der MIPAS-B- und MIPAS-ENVISAT-Beobachtungen ist für diese drei Flüge hervorragend (mit Ausnahme des zeitlichen Unterschieds beim 3. Flug). Damit ist eine Überprüfung der MIPAS-Daten sehr gut möglich. Um die statistische Grundlage für die Validierung zu erweitern, wurde außerdem die Methode des Trajektorienvergleichs eingesetzt. Für die Validierung der Werte für  $\text{NO}_2$ , ein chemisch aktives Gas, wurden die MIPAS-B-Daten für  $\text{NO}_2$  mit Hilfe des chemischen Modells KASIMA photochemisch angepasst. Die MIPAS-Offline-Daten V4.61 konnten zwischen 356 und 3 hPa (8 – 39 km) validiert werden, für  $\text{NO}_2$  konnte nur der Bereich zwischen 42 und 3 hPa (22 – 39 km) verglichen werden.

Die Vergleiche zeigen, dass die Abweichungen aller Zielparameter in bestimmten Höhen den kombinierten Gesamtfehler überschreiten. Die statistischen Ergebnisse bestätigen die Genauigkeit der MIPAS-ENVISAT-Daten für die Temperatur und die 6 wichtigsten Gasverbindungen  $\text{H}_2\text{O}$ ,  $\text{O}_3$ ,  $\text{HNO}_3$ ,  $\text{CH}_4$ ,  $\text{N}_2\text{O}$  und  $\text{NO}_2$  im überlappenden Höhenbereich. Eine Ausnahme ist  $\text{H}_2\text{O}$  im Bereich zwischen 356 und 195 hPa (8 – 12 km). Die Werte zeigen in der mittleren Stratosphäre eine bessere Übereinstimmung als in der unteren Stratosphäre und der oberen Troposphäre. Im Höhenbereich von 123 – 8 hPa (15 – 33 km) (für  $\text{NO}_2$  zwischen 23 und 8 hPa (26 – 33 km)) wurde die sog. Präzision der MIPAS-ENVISAT-Daten für  $\text{H}_2\text{O}$ ,  $\text{O}_3$ ,  $\text{CH}_4$  und  $\text{NO}_2$  validiert; für  $\text{HNO}_3$  und  $\text{N}_2\text{O}$  war dies nicht der Fall. Die Präzision der

Temperaturbestimmung konnte generell in Höhen über etwa 17 hPa, nicht aber unterhalb davon validiert werden.

Die MIPAS-ENVISAT-Messungen für H<sub>2</sub>O zeigen eine positive Abweichung in Höhen oberhalb von etwa 20 hPa, die aber immer noch im Rahmen des Gesamtfehlers liegt. Darüber hinaus zeigen die H<sub>2</sub>O-Profile von MIPAS-ENVISAT oft starke Schwankungen. Zwischen etwa 195 hPa und 80 hPa (12 – 18 km) wurden von MIPAS-ENVISAT hohe Werte für CH<sub>4</sub> und N<sub>2</sub>O gemessen. In Höhen unterhalb von etwa 80 hPa (18 km) weisen die CH<sub>4</sub>- und N<sub>2</sub>O-Profile von MIPAS-ENVISAT starke Schwankungen, manchmal sogar physikalisch nicht erklärbare Werte auf. Die HNO<sub>3</sub>- und NO<sub>2</sub>-Profile zeigen dagegen nur gelegentlich Schwankungen.

Die von SCIAMACHY mit Hilfe des Prozessors der IUP/IFE gemessenen O<sub>3</sub>- und NO<sub>2</sub>-Werte wurden einem Trajektorienvergleich unterzogen. Damit ließ sich die Genauigkeit des SCIAMACHY-Messinstruments für O<sub>3</sub> im Höhenbereich von 9 – 28 km validieren. Oberhalb von 26 km zeigen die SCIAMACHY-Daten eine positive Abweichung. Oberhalb von 28 km liegt diese über dem Gesamtfehler. Die Genauigkeit der NO<sub>2</sub>-Daten wurde zwischen 9 und 39 km validiert. Die mittleren Abweichungen betragen unter 0,52 ppbv oder 6,3 %.

Lediglich ein O<sub>3</sub>-Profil und ein NO<sub>2</sub>-Profil der GOMOS-Offline-Daten V6.01 wurden mit Hilfe der Koinzidenzmethode mit den MIPAS-B-Messungen verglichen. Vorläufige Ergebnisse zeigen, dass die GOMOS-Messungen für O<sub>3</sub> und NO<sub>2</sub> hinsichtlich ihrer Gesamtfehler mit den MIPAS-B-Daten übereinstimmen. Die O<sub>3</sub>- und NO<sub>2</sub>-Profile von GOMOS schwanken mit einer größeren Amplitude, insbesondere im oberen Höhenbereich. Statistische Schlussfolgerungen für die GOMOS-Daten im Vergleich zu den MIPAS-B-Daten können jedoch noch nicht gezogen werden.

## Contents

<b>1. Introduction</b> .....	<b>1</b>
<b>2. The atmosphere</b> .....	<b>3</b>
<b>2.1 Thermal structure and composition of the atmosphere</b> .....	<b>3</b>
2.1.1 Temperature.....	3
2.1.2 Composition .....	4
<b>2.2 Fundamentals of atmospheric dynamics and thermodynamics</b> .....	<b>6</b>
2.2.1 The primitive equations.....	6
2.2.2 Hydrostatic approximation .....	7
2.2.3 Geostrophic approximation .....	8
2.2.4 Potential temperature.....	8
2.2.5 Potential vorticity .....	8
<b>2.3 Stratospheric chemistry</b> .....	<b>8</b>
<b>3. Methodology of Validation</b> .....	<b>12</b>
<b>3.1 Objective of validation</b> .....	<b>12</b>
<b>3.2 Factors of influence on validation</b> .....	<b>12</b>
<b>3.3 Validation strategy and approaches</b> .....	<b>13</b>
<b>3.4 Mathematics for validation</b> .....	<b>15</b>
<b>4. Chemistry instruments onboard ENVISAT</b> .....	<b>17</b>
<b>4.1 MIPAS</b> .....	<b>18</b>
4.1.1 Principle and structure .....	18
4.1.2 Characteristics and Operation.....	18
4.1.3 Data products.....	20
<b>4.2 SCIAMACHY</b> .....	<b>20</b>
4.2.1 Principle and structure .....	20
4.2.2 Characteristics and operation.....	20
4.2.3 Data products.....	21
<b>4.3 GOMOS</b> .....	<b>22</b>
4.3.1 Principle and structure .....	22
4.3.2 Characteristics and operation.....	22
4.3.3 Data products.....	22
<b>5. Balloon version of MIPAS</b> .....	<b>24</b>
<b>5.1 Principle of a Fourier Transform Spectrometer</b> .....	<b>24</b>
5.1.1 Interference and Fourier transformation .....	24
5.1.2 Instrumental line shape.....	26
5.1.3 Discrete Fourier transformation.....	28
<b>5.2 Instrument characteristics</b> .....	<b>28</b>
5.2.1 The construction of MIPAS-B.....	29
5.2.2 Performance.....	30
<b>5.3 Operation and data processing</b> .....	<b>30</b>
<b>6. Retrieval algorithms</b> .....	<b>34</b>
<b>6.1 Radiative transfer model</b> .....	<b>34</b>
<b>6.2 Inversion theory</b> .....	<b>36</b>
<b>6.3 KOPRA</b> .....	<b>38</b>
<b>7. Retrieval of atmospheric parameters from MIPAS-B</b> .....	<b>40</b>
<b>7.1 Flights of MIPAS-B</b> .....	<b>40</b>

7.1.1 Flight No. 11.....	40
7.1.2 Flight No. 13.....	41
7.1.3 Flight No .14.....	41
<b>7.2 Parameters configuration and input data for retrieval .....</b>	<b>43</b>
7.2.1 Microwindows.....	43
7.2.2 A priori data and the Tikhonov-Phillips regularization approach.....	46
7.2.3 Vertical retrieval grid.....	47
7.2.4 Spectroscopic molecular database .....	47
7.2.5 Continuum effect .....	47
<b>7.3 Output of retrieval .....</b>	<b>49</b>
<b>7.4 Error estimation.....</b>	<b>49</b>
<b>7.5 Retrieval results for the temperature and each gas .....</b>	<b>49</b>
7.5.1 Temperature.....	49
7.5.2 H <sub>2</sub> O .....	52
7.5.3 O <sub>3</sub> .....	52
7.5.4 HNO <sub>3</sub> .....	55
7.5.5 CH <sub>4</sub> and N <sub>2</sub> O .....	57
7.5.6 NO <sub>2</sub> .....	60
<b>8. Intercomparison of measurements .....</b>	<b>62</b>
<b>8.1 General.....</b>	<b>62</b>
8.1.1 Diagnostics of match quality .....	62
8.1.2 Trajectory model .....	65
<b>8.2 MIPAS.....</b>	<b>67</b>
8.2.1 Temperature.....	67
8.2.2 H <sub>2</sub> O .....	78
8.2.3 O <sub>3</sub> .....	89
8.2.4 HNO <sub>3</sub> .....	97
8.2.5 CH <sub>4</sub> .....	106
8.2.6 N <sub>2</sub> O.....	114
8.2.7 NO <sub>2</sub> .....	122
<b>8.3 SCIAMACHY .....</b>	<b>130</b>
8.3.1 O <sub>3</sub> .....	130
8.3.2 NO <sub>2</sub> .....	133
<b>8.4 GOMOS .....</b>	<b>138</b>
<b>9. Discussion.....</b>	<b>140</b>
9.1 Vertical grid of profile representation. ....	140
9.2 Estimation of the vertical resolution influence.....	141
9.3 Comparison in potential temperature frame.....	143
<b>10. Summary and outlook .....</b>	<b>145</b>
<b>References.....</b>	<b>148</b>
<b>Appendix A: Supplementary data for MIPAS-B retrievals .....</b>	<b>156</b>
<b>Appendix B: Number of match points for trajectory comparisons .....</b>	<b>158</b>
<b>Appendix C: Tangent point geolocations of MIPAS-B and MIPAS-ENVISAT LOS as well as ECMWF temperature fields .....</b>	<b>160</b>
<b>Acronyms .....</b>	<b>163</b>
<b>List of figures and tables .....</b>	<b>164</b>

## Chapter 1

### Introduction

In the past several decades, many observations and simulations had led to remarkable advances in our understanding of the atmosphere. It has become more and more clear that the human activities could cause severe environmental issues. Two notable examples are the stratospheric ozone depletion (*Farman, J. C. et al., 1985*) and the enhanced greenhouse effect. Ozone decline yields an increase of the harmful ultraviolet radiation on the Earth's surface. The greenhouse effect leads to the global warming and a series of adverse environment changes. However, due to the giant complexity of the atmosphere, more reliable observations of the atmosphere are necessary. Among the variety of means of atmospheric measurements, remote sounding from satellite has its own importance because it can provide long term global coverage observations.

In April 1964, The Television and InfraRed Observing Satellite (TIROS) was launched to space. This was the first satellite for the purpose of meteorological research (*Chen, H. S., 1997*). Since then many new remote sensing satellites were developed. In March 2002, the **ENV**iromental **SAT**ellite (ENVISAT) was launched by ESA (**E**uropean **S**pace **A**gency). It is an advanced polar-orbiting Earth observation satellite. The observations of ENVISAT support the Earth science research and allow monitoring of the evolution of environmental and climatic changes. Onboard the ENVISAT, there are three chemistry instruments. They are: MIPAS (**M**ichelson **I**nterferometer for **P**assive **A**tmospheric **S**ounding), SCIAMACHY (**S**Canning **I**maging **A**bsorption **S**pectro**M**eter for **A**tmospheric **C**Hartograph**Y**) and GOMOS (**G**lobal **O**zone **M**onitoring by **O**ccultation of **S**tars). The main mission of these three remote sounding instruments is to measure the trace gases in the atmosphere.

In order to ensure the data from the satellite instruments can be correctly used, validation activities are absolutely necessary. Aircraft- or balloon-borne instruments as well as instruments used on ground can be calibrated in the laboratory both before and after making measurements. However, such thorough calibrated processes cannot be feasibly performed for instruments in space. Therefore, the comparison of measurements from the space instruments with other well established instrument observations is the principal approach of validation for instruments in space. Among the well-established instruments for validation, balloon-borne instruments can provide observations in a larger altitude range and with better vertical resolution as compared to ground based or aircraft-borne instruments. Even though the satellite instruments also have the capability to perform measurements in very large altitude regions, high quality coincident measurements are sparse. Thus, balloon observations are usually to be regarded as a key component in satellite instrument validation activities in spite of the limited number and short period of observations. The balloon version of MIPAS (MIPAS-B) is the precursor of MIPAS onboard the ENVISAT (MIPAS-E). Before MIPAS-B was deployed for the validation campaigns of the chemistry instruments onboard ENVISAT, it had already been successfully flown several times since 1995 from high- and mid- latitude in different seasons in the framework of large international scientific field campaigns.

There are a lot of considerations necessary when balloon-borne instruments are used for validation. The most important one is the quality of coincidence in time and space between the balloon measurements and the satellite measurements. Through careful selection of launching date and weather conditions, three MIPAS-B flights for ENVISAT validation have

## 1. Introduction

been carried out during the years 2002 and 2003. The first one took place at mid-latitude from Aire sur l'Adour, France, during 24/25 September 2002. The second flight was performed in Arctic winter on 20/21 March 2003 in Kiruna, Sweden. And the third flight also was carried out from Kiruna but in Arctic summer on 2/3 July 2003. The quality of match between MIPAS-B observations and MIPAS-E observations in these three flights has been excellent to satisfactory except for the temporal offset in the third flight.

Based on the atmospheric spectra measured by MIPAS-B, the profiles of temperature and Volume Mixing Ratios (VMRs) of many trace gases can be retrieved using KOPRA (The **K**arlsruhe **O**ptimized and **P**recise **R**adiative transfer **A**lgorithm), which is a software package specially designed for the data analysis of the MIPAS instruments. These profiles of MIPAS-B will be compared with the correlative measurements of MIPAS-E, SCIAMACHY and GOMOS. For MIPAS-E validation, MIPAS-B measurements will be compared to the off-line data under the nominal mode of MIPAS-E for the temperature and the VMR of all six key trace gases — H<sub>2</sub>O, O<sub>3</sub>, HNO<sub>3</sub>, CH<sub>4</sub>, N<sub>2</sub>O and NO<sub>2</sub>. These off-line data of MIPAS-E was retrieved by the latest version V4.61 of level 2 products processor until the end of May 2005. Because SCIAMACHY operational data quality is not good enough for validation so far and the species of target parameters for comparison are limited, here only scientific data of O<sub>3</sub> and NO<sub>2</sub> were compared with MIPAS-B correlative measurements. GOMOS measurements in bright and twilight limb condition are not good enough for validation. So, only the off-line O<sub>3</sub> vertical profiles under dark limb condition of GOMOS retrieved by the latest version V6.0a of level 2 products processor were compared with MIPAS-B correlative measurements.

Since the number of MIPAS-B launches is restricted due to logistical and financial constrains, the statistics is very limited by this kind of coincidence validation approach. In order to overcome this shortcoming, trajectory mapping was adopted for the validation of MIPAS-E and SCIAMACHY. However, this modelling technique needs to be applied carefully since it may introduce additive uncertainty to the quality of the validation.

NO<sub>2</sub> is a short-lived trace gas. Its concentration changes rapidly within one hour during sunrise and sunset. The NO<sub>2</sub> profiles of MIPAS-B, MIPAS-E and SCIAMACHY which could have experienced a rapid concentration change between the related measurement times were simulated by KASIMA (**K**arlsruhe **S**imulation **M**odel of the Middle **A**tmosphere), which is a 3-D chemistry transport model (CTM) of the atmosphere developed by Kouker (*Kouker, W., et al. 1999*). The possible influences to the quality of NO<sub>2</sub> validation due to the temporal offset between MIPAS-B and MIPAS-E or SCIAMACHY were evaluated by the model simulation.

## Chapter 2

# The atmosphere

The Earth's atmosphere is the gaseous matter surrounding the Earth. It is the basis of human being and other life. The thermodynamics, chemistry, dynamics and their interaction with the Earth surface determine the atmospheric behaviour.

## 2.1 Thermal structure and composition of the atmosphere

### 2.1.1 Temperature

From the surface of the Earth to the top level, the height of the atmosphere is about 500 km. According to its thermal structure, the atmosphere is divided into several layers along the vertical direction. Each layer is a region where the change of temperature as a function of altitude has a constant sign. The typical picture of the atmospheric thermal structure is provided by the vertical profile of temperature in Figure 2.1. From the surface up to about 10 km, the temperature decreases with altitude at a nearly constant lapse rate. This layer is the troposphere. The troposphere is vertically well-mixed because of the negative temperature gradient. The upper boundary of the troposphere is the tropopause. The location of the tropopause varies with latitude and season. At the equator, its mean altitude is approximately 17 km, while in polar region its altitude is only about 8 km. The stratosphere is marked by a negative lapse rate due to the absorption of solar ultraviolet by ozone. So this layer has weak vertical motion. The stratopause as the upper boundary of the stratosphere lies at an altitude of about 50 km. Above the stratopause, the temperature again decreases with altitude in the mesosphere where the ozone heating diminishes. Convective motion and radiative processes are both important in the mesosphere. The mesopause is at about 85 km. Above the mesopause, the temperature increases steadily in the thermosphere. In this region, free electrons and ions appear due to the ionization of atoms and molecules.

The troposphere and the tropopause are called the lower atmosphere. The region from tropopause up to about 100 km is named middle atmosphere (*Andrew, D. G., et al., 1987*).

The temperature varies with latitude significantly. In the troposphere, temperature decreases with latitude. In the stratosphere, temperature is warmest over the summer pole and decrease steadily to coldest value over the winter pole. In the mesosphere, the horizontal temperature gradient is reversed. The coldest temperatures are over the summer pole, which lies in perpetual daylight, and the temperatures increase steadily to warmest values over the winter pole, which lies in perpetual darkness.

## 2. The atmosphere

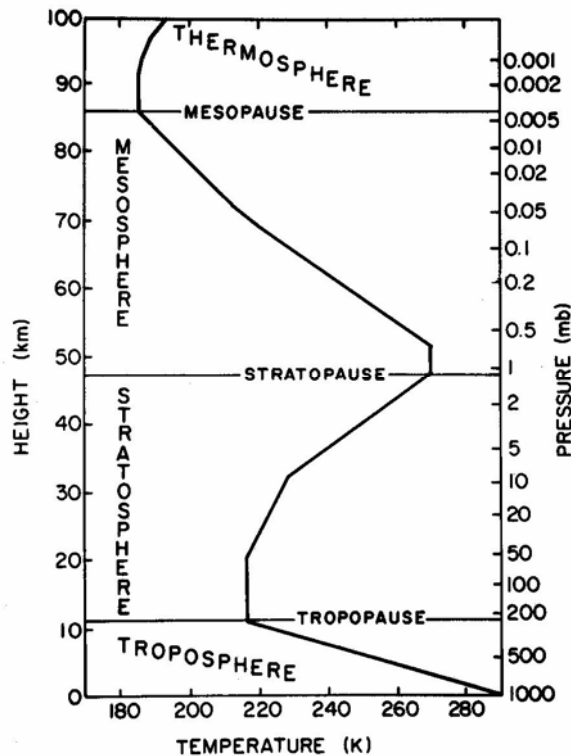


Figure 2.1: Middle latitude temperature profile below 100 km (*US Standard Atmosphere, 1976*).

### 2.1.2 Composition

There are a variety of gases in the atmosphere. In terms of volume,  $N_2$  and  $O_2$  account for 78% and 21% of total volume, respectively. Ar,  $H_2O$ ,  $CO_2$ , and  $O_3$ , along with other minor constituents comprise the residual 1% of the atmosphere. The trace species, like  $H_2O$ ,  $CO_2$  and  $O_3$ , play a key role in the energy balance and the climatology of the Earth even though they are small in abundance. Besides, the aerosols are also one important constituent of the atmosphere. The atmospheric aerosols comprise liquid and solid particles existing in the atmosphere. Aerosols usually serve as the condensation nuclei for water droplet and ice crystals. Hence, they are key factors to cloud formation. Aerosols also play a very important role in the energy balance of the Earth and the atmospheric chemistry. The distribution of constituents varies with respect to altitude, latitude, longitude and time. Here, we only describe the gases relating to the validation of ENVISAT chemical instruments below the stratopause.

#### Carbon dioxide ( $CO_2$ ):

$CO_2$  as a chemically inert major trace gas is well mixed through the stratosphere like the primary constituents  $N_2$  and  $O_2$ . Therefore, its transition is very suitable for temperature retrieval. It has a nearly uniform stratospheric mixing ratio of about 370 ppmv in the year of 2000 (*WMO, 2003*). Involved in chemical and biological processes,  $CO_2$  is produced naturally near the surface. However, the influence of human activities is proven in recent measurements. Over the last two decades, the mean growth rate at the surface is  $\sim 1.5 \text{ ppmv yr}^{-1}$  (*WMO, 2003*). The rapid increase of  $CO_2$  has prompted concerns over the global warming because of the role  $CO_2$  plays in trapping radiative energy in the lower atmosphere.

#### Water vapour ( $H_2O$ ):

Owing to its involvement in radiative processes, for cloud formation and in exchanges of energy with the oceans, water vapour is a key major trace species in the atmosphere.



## 2.1 Thermal structure and composition of the atmosphere

Most of the water vapour originates near the equator at warm ocean surfaces. Through vertical transport (convection) and horizontal transport (advection), the water vapour is being redistributed. Water vapour is mainly confined to the troposphere. With increasing altitude, its concentration exponentially decreases from a maximum of about 4% at the surface to a minimum of about a few ppmv at the tropopause. The reason leading to the minimum is because all air entering from the troposphere into the stratosphere passes through the extremely cold tropical tropopause, where most of the water vapour is frozen out. Above the tropopause, the mixing ratio of water vapour has a gradual increase (ca. 2-7 ppmv in the stratosphere) due to the source provided by oxidation of methane (*Andrew, D. G., et al., 1987*). Water vapour may be removed at the bottom of the stratosphere through condensation and precipitation at middle and high latitudes. Its characteristic lifetime in the lower stratosphere is several years.

### **Ozone (O<sub>3</sub>):**

O<sub>3</sub> is the most importance trace species in the middle atmosphere. By absorption of ultraviolet radiation, O<sub>3</sub> protects the biosphere from the damaging of ultraviolet radiation and maintains the energy balance of the atmosphere.

O<sub>3</sub> is the production of O reaction with O<sub>2</sub>. The efficiency of this reaction is very high in the stratosphere over tropical regions. Therefore, its mixing ratio increases with altitude and reaches the maximum of about 8-10 ppmv at ~37 km (*Andrew, D. G., et al., 1987*). The zonal-mean distribution of O<sub>3</sub> indicates that it is concentrated in the stratosphere. The total vertical column abundance of ozone near the equator is ~250 DU (**D**obson **U**nits, which is equivalent to the depth the ozone column in thousandths of a centimeter if brought to standard temperature and pressure.) while at high latitudes it exceeds 400 DU. However, the ozone depletion can lead to minimum values around 100 DU over Antarctica. The ozone depletion problem discovered two decades ago has become one of the most important subjects of atmospheric research.

The lifetime of ozone in the lower stratosphere is about several weeks. So it can be treated as a tracer of air parcels motion. At the stratopause, the O<sub>3</sub> lifetime is only ~1 hour due to the strong photochemical processes.

### **Nitric acid (HNO<sub>3</sub>):**

The active nitrogen NO<sub>x</sub> (=NO + NO<sub>2</sub>) is a very important catalyst of ozone depletion. Because HNO<sub>3</sub> is a reservoir of NO<sub>x</sub>, HNO<sub>3</sub> plays a crucial role in O<sub>3</sub> destruction, especially in the “ozone hole” formation over Antarctica. HNO<sub>3</sub> is the product of NO<sub>2</sub> reaction with OH. Typically, the mixing ratio of HNO<sub>3</sub> increases with the altitude and reaches the maximum of ~7 ppbv at about 25 km. However, the vertical mixing ratio of HNO<sub>3</sub> significantly depends on the latitude in the middle atmosphere (*WMO, 1986*). Diurnal variation does not occur below 50 km. The seasonal variability of HNO<sub>3</sub> is not large except in the arctic winter. The photolysis and the oxidation reaction with OH are the two primary loss processes. Because HNO<sub>3</sub> is readily incorporated into rain droplets, wet deposition is also a major channel of HNO<sub>3</sub> loss. The lifetime of HNO<sub>3</sub> is ~1 day in the higher stratosphere and ~1 month in the lower stratosphere (*Brasseur, G. P., et al., 1999*).

### **Methane (CH<sub>4</sub>):**

Methane is a carbon containing species in the atmosphere. Because it is the most abundant and the most ubiquitous hydrocarbon in the atmosphere, it plays a great role to the global atmosphere chemistry involved in carbon-containing compounds. As a tracer of atmospheric motion, methane is very useful in chemistry instrument validation. Like CO<sub>2</sub> and H<sub>2</sub>O, CH<sub>4</sub> is

## 2. The atmosphere

also ascribed to be greenhouse efficient. Methane is produced primarily by anaerobic bacteria. Peat bogs, swamp, ponds, rice pads, humid tundra, and fermentation of animal's ruminant etc. produce large amounts of methane. Mankind mining and industrial activities may constitute as much as 20% of CH<sub>4</sub> production. Methane is well mixed in the troposphere, where it has a constant mixing ratio of ~1.7 ppmv (*Salby, M. L., 1996*). In the stratosphere, the mixing ratio of methane decreases with the altitude as a result of oxidation. This is a long lived gas with lifetime of about several months to 10 years in the stratosphere.

### **Nitrous oxide (N<sub>2</sub>O):**

Nitrous oxide is the major source of NO<sub>x</sub> in the stratosphere. Therefore, it is an important agent in controlling the stratospheric ozone balance. Nitrous oxide is also a greenhouse gas. Like Methane, Nitrous oxide is an excellent long-lived tracer. Nitrous oxide is produced by bacterial processes in soil and using nitrogen fertilizers as well as combustion of fossil fuels. Nitrous oxide is a long lived gas. In the troposphere and lower stratosphere, the lifetime of N<sub>2</sub>O is ~120 years (*Seinfeld, J. H., et al., 1998*). Therefore it is well mixed in the troposphere with mixing ratio of ~320 ppbv. In the stratosphere, the mixing ratio of N<sub>2</sub>O decreases with altitude due to dissociation.

### **Nitrogen dioxide (NO<sub>2</sub>):**

Nitrogen dioxide is a chemistry-active species that is closely related to ozone depletion. In the stratosphere, nitrogen dioxide is produced by the reaction of nitric oxide with ozone. At low altitude, it is from the reaction of nitric oxide with peroxy radicals. Under sunlit conditions, Nitrogen dioxide is converted rapidly to nitric oxide by photolysis or by reaction with atomic oxygen. Nitrogen dioxide can be removed from the atmosphere via dry deposition or the conversion to its reservoirs like HNO<sub>3</sub>. In the troposphere, the mixing ratio of NO<sub>2</sub> is between few pptv to 100 pptv. In the stratosphere, the value of mixing ratio increases with altitude and reaches a peak value of about 10 ppbv around 38 km (*Brasseur, G. and S. Solomon., 1986*). Diurnal variations of NO<sub>2</sub> are strong in the stratosphere and mesosphere. Its lifetime is only several minutes to hours in the stratosphere. Hence, the match quality in time is important when comparing the NO<sub>2</sub> measurements of two instruments.

## **2.2 Fundamentals of atmospheric dynamics and thermodynamics**

### **2.2.1 The primitive equations**

The factors that determine the atmospheric behavior are: (a) atmosphere as a compressible fluid, (b) gravity, (c) the Earth's rotation, (d) energy exchange between atmosphere and its environment, particularly through the radiation process, (e) chemistry. Therefore, the theories that appreciate to describe the atmospheric behavior should include the dynamics, thermodynamics, and chemistry.

Applying the Newton's second law of motion to an air parcel of density  $\rho$  moving with velocity  $\vec{V}$  in the presence of a pressure gradient  $\nabla\bar{p}$  and a gravitational field  $\vec{g}$ , the following equation is obtained under the Earth frame (*Houghton, J. T., 1986*):

$$\frac{d\vec{V}}{dt} = (\vec{g} - \bar{\Omega} \times (\bar{\Omega} \times \bar{R})) - \frac{1}{\rho} \nabla\bar{p} - 2\bar{\Omega} \times \vec{V} + \vec{F}, \quad (2.1)$$

where  $\vec{F}$  is the frictional force on the air parcel,  $\bar{\Omega}$  is the angular velocity of the Earth rotation.  $\bar{R}$  is the radius vector.  $\bar{\Omega} \times (\bar{\Omega} \times \bar{R})$  represents the centripetal acceleration. The third term on the right hand side of (2.1) is the Coriolis acceleration.

## 2.2 Fundamentals of atmospheric dynamics and thermodynamics

Another basic equation termed continuity equation is (Andrews, D. G., 2000):

$$\frac{\partial \rho}{\partial t} + \nabla \cdot (\rho \vec{V}) = 0. \quad (2.2)$$

Equation (2.2) is based on the mass conservation. It states that the net flow of mass into unit volume per unit time is equal to the location change of density.

The first law of thermodynamics for the ideal gas is given by:

$$c_p \frac{\partial T}{\partial t} - \frac{1}{\rho} \frac{\partial p}{\partial t} = Q, \quad (2.3)$$

where  $T$  is the temperature,  $c_p$  the specific heat capacity of air at constant pressure, and  $Q$  is the net heating rate per unit mass. (2.3) is commonly called the thermodynamic energy equation in meteorology. In the lower atmosphere, the main physical process contributing to  $Q$  are latent heating and cooling from condensation and evaporation of water vapour, respectively. In the stratosphere and mesosphere,  $Q$  is determined by radiative heating through absorption of ultraviolet radiation of ozone and radiative cooling via emission of infrared radiation of ozone, carbon dioxide and water vapour.

Equation (2.1), (2.2) and (2.3) are the main equations that describe the behaviour of the atmosphere. They are called the primitive equations.

### 2.2.2 Hydrostatic approximation

Analysis of equation (2.1) in general is usually a complicated process. Under some dynamics conditions, this equation can be simplified and it is more helpful to indicate the physical mechanism on the atmospheric behaviour. Considering the synoptical-scale (~1000 km) or larger in horizontal dimension, (2.1) can be replaced approximately by:

$$\frac{\partial p}{\partial z} = -g\rho. \quad (2.4)$$

This is the hydrostatic equation. The state equation of the ideal gas is:

$$p = RT\rho, \quad (2.5)$$

where  $R$  is the gas universal constant of unit mass of air. Eliminating  $\rho$  with (2.5) and integrating (2.4) from the surface to an altitude  $z$  yields:

$$p = p_s \exp\left(-\int_{z_s}^z \frac{dz'}{H(z')}\right), \quad (2.6)$$

where  $p_s$  and  $z_s$  is the pressure and the altitude at the surface, respectively.  $H(z) = R_s T(z) / g$  is called the scale height, where  $R_s$  is the special gas constant.  $H(z)$  represents the characteristic vertical dimension of mass distribution and varies from about 8 km near the surface to about 6 km in very cold regions of the atmosphere (Salby, M. L., 1996).

## 2. The atmosphere

### 2.2.3 Geostrophic approximation

Performing a similar analysis as in 2.2.2, but on the horizontal component of equation (2.1), other terms are negligible if they compare to the pressure gradient and Coriolis acceleration. This leads to the geostrophic approximation (*Andrews, D. G., 2000*):

$$fV_x = -\frac{1}{\rho} \frac{\partial p}{\partial y}, \quad (2.7)$$

$$fV_y = \frac{1}{\rho} \frac{\partial p}{\partial x}, \quad (2.8)$$

where  $f = 2\Omega \sin \phi$  is the Coriolis parameter.  $\phi$  is the latitude. (2.7) and (2.8) indicate that for a synoptic-scale system, the horizontal pressure gradients are balanced by Coriolis forces associated with the horizontal winds.

### 2.2.4 Potential temperature

The air parcels usually experience thermodynamic processes from one state to another without exchange or only little exchange of energy with their surrounding air. This is an adiabatic process. Let  $Q=0$ , using the ideal gas law and integrating (2.3), a new equation yields (*Andrews, D. G., 2000*):

$$\theta = T \left( \frac{p_0}{p} \right)^\kappa, \quad (2.9)$$

where  $\kappa = R/c_p$ . The value of  $p_0$  is usually taken to be 1000 hPa.  $\theta$  is called the potential temperature. This is a conserved parameter along an adiabatic path in state space. Therefore,  $\theta$  can be used as a tracer of air motion, e.g. in calculation of the trajectory of an air parcel. The air parcels in adiabatic state can only move along the isentropic surface. Hence, the state parameters of air parcels can be displayed in the potential temperature coordinate.

### 2.2.5 Potential vorticity

The vorticity is the curl of the velocity vector  $\vec{V}$ . It is a measure of the local rotation of the flow. Under the assumption of inviscid and adiabatic motions, starting from equation (2.1), the potential vorticity (sometimes called Ertel potential vorticity) is (*Salby, M. L., 1996*):

$$PV = \frac{\zeta_\theta + f}{-\frac{1}{g} \left( \frac{\partial p}{\partial \theta} \right)}, \quad (2.10)$$

where  $\zeta_\theta$  is the relative vorticity evaluated on a certain isentropic level with respect to the Earth's surface.  $f = 2\Omega \sin \phi$  is the Coriolis parameter. The potential vorticity of an air parcel is conserved under inviscid adiabatic conditions. So it is a dynamic tracer of horizontal motion. Together with the potential temperature, this tracer will be useful in judging if the same air parcel was observed by different instruments.

## 2.3 Stratospheric chemistry

The atmospheric chemistry together with the radiation and the transport of air masses in the atmosphere determine the distribution of gases and temperature. Therefore, the influences of

### 2.3 Stratospheric chemistry

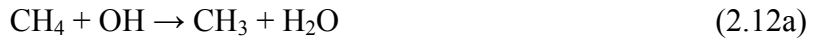
atmospheric chemistry to the validation should not be omitted. Except carbon dioxide, which is chemically quite inert, the major chemical reactions of H<sub>2</sub>O, O<sub>3</sub>, HNO<sub>3</sub>, CH<sub>4</sub>, N<sub>2</sub>O, and NO<sub>2</sub> in the stratosphere will be presented in the following sections.

#### H<sub>2</sub>O and CH<sub>4</sub>

The reaction of water vapour provides the major source of OH radicals in the atmosphere.



The methane reaction with OH provides H<sub>2</sub>O production (*Brasseur, G. P., et al., 1999*):



A chain of reactions initiated by (2.12a) produces CH<sub>2</sub>O. CH<sub>2</sub>O can be oxidized by OH as follows.



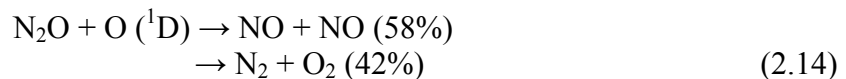
(2.12a) and (2.12b) indicate that the oxidation of one molecule of methane yields about 2 molecules of H<sub>2</sub>O. Therefore, the summation of mixing ratio of H<sub>2</sub>O and the double mixing ratio of CH<sub>4</sub> is nearly a constant (i. e., H<sub>2</sub>O + 2\* CH<sub>4</sub> ≈ 7 ppmv) in the stratosphere.

#### N<sub>2</sub>O

Nitrous oxide is the primary source of active nitrogen to the stratosphere on a global basis. Approximately 90% of N<sub>2</sub>O in the stratosphere is destroyed by photolysis (*Seinfeld, J. H., et al., 1998*).



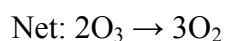
The reaction of N<sub>2</sub>O with O (<sup>1</sup>D) yields two branches, namely



N<sub>2</sub>O and CH<sub>4</sub> have a compact relationship in the stratosphere. This is because both gases have a similar lifetime in this altitude range.

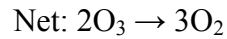
#### NO<sub>2</sub>, HNO<sub>3</sub>, and O<sub>3</sub>

The atmospheric chemistry of NO<sub>2</sub> and HNO<sub>3</sub> is extremely important to the O<sub>3</sub> depletion. Because of rapid interconversion, NO<sub>2</sub> and NO are often grouped together as NO<sub>x</sub> (=NO + NO<sub>2</sub>). NO<sub>x</sub> is referred to as “active nitrogen.” The following reactions describe the conversion between NO<sub>2</sub> and NO as well as the catalytic O<sub>3</sub> depletion by the NO<sub>x</sub> cycle (*Seinfeld, J. H., et al., 1998; Brasseur, G. P., et al., 1999*).

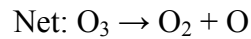
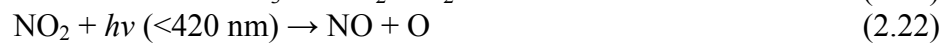


## 2. The atmosphere

The concentration of NO<sub>2</sub> relative to NO is controlled by reaction (2.17) if atomic oxygen is sufficiently abundant. The reaction (2.17) controls the daytime partitioning between NO and NO<sub>2</sub> since the production of atomic oxygen ceases at night. In the lower stratosphere, O<sub>3</sub> is more prevalent. Another NO<sub>x</sub> cycle is:



The third NO<sub>x</sub> cycle is:



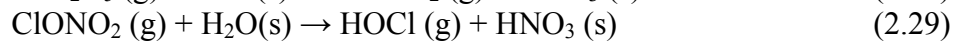
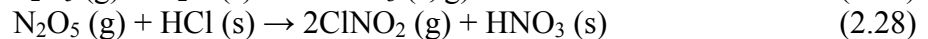
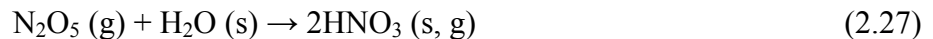
The reactions of (2.15), (2.17), and (2.22) indicate that the mixing ratio of NO<sub>2</sub> depends on the day and night time heavily.

N<sub>2</sub>O<sub>5</sub> and ClONO<sub>2</sub> are the major reservoirs of NO<sub>x</sub>. The relative reactions are:



here M refers to O<sub>2</sub> or N<sub>2</sub>.

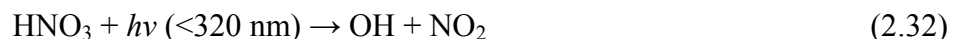
HNO<sub>3</sub> is also an important reservoir of odd-nitrogen. Depending on temperature, the reactions of heterogeneous hydrolysis of N<sub>2</sub>O<sub>5</sub> and ClONO<sub>2</sub> on sulphate aerosols or on particles of polar stratospheric clouds is an important channel of HNO<sub>3</sub> production.



where s represents the solid or liquid state and g represents the gas phase. Another reaction to form HNO<sub>3</sub> is:

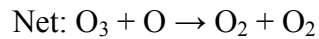


The reactions of HNO<sub>3</sub> destruction are:



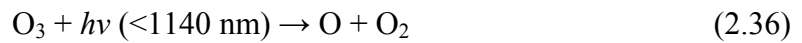
### 2.3 Stratospheric chemistry

O<sub>3</sub> depletion is one of the most important research subjects in the atmosphere. There are many chemistry channels leading to O<sub>3</sub> depletions. Besides NO<sub>x</sub> cycles mentioned previously, HO<sub>x</sub> (H + OH + HO<sub>2</sub>) cycles, ClO<sub>x</sub> (Cl + ClO) and BrO<sub>x</sub> (Br + BrO) cycles have similar catalytic O<sub>3</sub> depletion chemistry mechanism. The general formulation is:

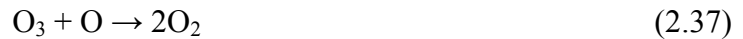


where X represents H, OH, NO, Cl or Br.

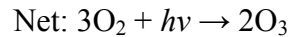
Photodissociation is also an important pathway of O<sub>3</sub> destruction:



O<sub>3</sub> can also react with O to generate O<sub>2</sub>.



The formation of ozone in the stratosphere occurs through the following reactions.



The pathways on ozone depletion and formation mentioned above are only the major ones. There are many books and papers which present more details on the chemistry of ozone and other species (e.g., *Seinfeld, J. H., et al., 1998; Brasseur, G. P. et al., 1999; and Warneck, P., 1988*).

## **Methodology of Validation**

Once an instrument has been built, its characteristics were determined in the laboratory. When this instrument begins to conduct real measurements, the performance of the instrument may be inconsistent with the initial description in the laboratory. Therefore, a validation process is necessary. The validation is implemented through a series of comparisons with other independent measurements. For numerous instruments, their validation is a straightforward way. For example, a ruler for length measurement can be validated via comparison to a standard one. However, the validation for the instruments in space is a very complicated process due to the complexity of the instruments in space and the diversity of impact factors to the validation. Here, we will describe the objective of validation, the factors that can influence the validation results and the approaches of validation associated with the chemical instruments in space.

### **3.1 Objective of validation**

The objective of validation activities is to assess and validate the performance of an instrument. It includes the measurement precision (random error), the measurement accuracy (systematic error plus random error), internal consistency and the instrument stability with respect to time.

### **3.2 Factors of influence on validation**

In order to validate the performance of a new instrument via intercomparison between the new instrument measurements and other independent instruments observations, the key problem is whether the same thing was measured by these different instruments and whether the same thing was compared. For atmospheric chemistry instruments, there are many factors which can hamper them to measure the same air masses and to compare the measurements directly. These factors arise from the atmospheric characteristics and the instruments themselves.

Due to the complexity of the new instrument in space, it is difficult to ensure the new instrument and other independent sensors can measure at the same geolocation and at the same time. Since atmospheric parameters, like temperature, pressure and the VMR of gases vary with geolocation and time, sampling at different locations will give additive uncertainty to validation results. The time difference of sampling also hampers the same air masses to be measured. The reason lies in two aspects. First, the atmosphere is a fluid. The air masses are transported from one location to another continuously. Secondly, some gases are chemically active species. Their concentration will be changed after an interval of time through chemical reactions.

Many factors prevent the same air masses being measured and the measurement being compared easily from different instruments due to their different characteristics. These factors include: 1. The vertical and horizontal resolution of the instruments. For example, the measurements of an instrument, which uses an in-situ observation, are from the sampling to the small air volumes. While the measurement from the remote sounding sensor represents an average value of an observation in a large air volume. In general, the quantitative comparison between these two kinds of instruments can not be carried out directly. 2. Different data representations. (e.g., using altitude, pressure or potential temperature



coordinate, the altitude grid for profiles representation). 3. Usually, the atmospheric parameters are obtained through complicated numerical inversion calculations. An a priori information is often used during the inversion process. Different a priori information for different instruments can also influence the results of the comparison of measurements.

### 3.3 Validation strategy and approaches

The general strategies of validation are:

**(1) To perform a comparison with a variety of other well-established instruments.** These well-established instruments include radiosondes, microwave radiometers, infrared, visible and/or ultraviolet spectrometers, lidars, in-situ sensors, etc. They can perform the measurements on the ground, onboard balloon, aircraft, satellite, rockets or space shuttle in an in-situ or remote sounding way. Different instruments and different kind of measurement have their own advantages and disadvantages. The observation from ground stations has the capability to provide long-term measurement data. However, the data from higher altitudes is limited and the altitude resolution is generally poor. If the measurements are performed onboard balloon, aircraft, rocket or space shuttle, a lot of data covers different locations and times. Unfortunately, the amount of such experiments is restricted due to financial and logistical constraints. To compare the measurements of a new instrument with already validated instruments onboard a satellite is a useful way for validation since many global data are available. The shortcoming is that usually the match quality in space and time is poor.

**(2) The temporal and spatial differences of the measurements between the new instrument and the well-established instruments should be as small as possible.** Otherwise the new instrument will not be well validated due to the additive uncertainty from atmospheric variability.

**(3) To measure the long-lived gases like H<sub>2</sub>O, O<sub>3</sub>, N<sub>2</sub>O and CH<sub>4</sub> etc.** This choice will avoid the atmospheric chemistry to influence the comparison of measurements.

**(4) Significant number of validation campaigns and long period of validation activities.** Due to the complexity of the instruments onboard the satellite, the performance of the instrument assessed around one location at a specific time doesn't automatically mean that in another place and/or at another time this instrument has the same performance. Hence, the experiment for validation should be carried out at different sites with different geophysical conditions and preferably last over the whole lifetime of the instrument.

**(5) The data for validation also need to be validated.** Although a well-established instrument has been calibrated carefully both before and after validation campaign, the possibility of making mistakes during the validation is still there. To compare its measurements with other well-established instruments will be helpful to find out these mistakes and therefore to increase the reliability of the validation result.

The following approaches are usually applied for validation.

#### **(1) Coincident comparisons**

In this process, different instruments make "coincident" observations. The criterion to define a "coincident" observation is made within specified distance and time. For example, for the remote sounding instruments in space the spatial separations are typically hundreds of kilometers while the time between such measurements can range from minutes to days or longer (*Morris, G. A., et al., 2000*). The main disadvantage is that relative rare data for validation can be obtained with this approach.

#### (2) Zonal mean comparisons

An approach for evaluating instrument accuracy involves the comparison of zonal mean. While statistically more satisfying than coincident studies, zonal mean analysis has its own shortcomings. First, longitudinal gradients are lost in the zonal averaging. Second, in some cases the temporal difference between the measurements used to compile the zonal average maps is quite large. Third, the comparisons of zonal mean data are limited to specific latitudes (*Morris, G. A., et al., 2000*).

#### (3) Trajectory Mapping (TM)

Trajectory mapping (*Pierce, R. B., et al., 1994; Morris, G. A., et al., 1995, 2000*) employs a two-dimensional model of atmospheric motions to isentropically advect the measured air masses forward and backward in time from the point at which they were measured. Meteorological analyses provide the winds which determine the magnitude and direction of air parcels motion at each time step. The trajectory technique constructs its synoptic maps by advecting a large number of measurements made at different times to the same instant in time. These maps are known as “trajectory maps.” TM takes advantages of quasi-conserved quantities following air parcel motion, namely the mixing ratio and potential temperature (PT). PT is reasonably well conserved along air parcel trajectories for 5-10 days (*Morris, G. A., et al., 2000*). By sampling the synoptic maps created from one instrument at the time and location of the observations of the second instrument, the measurements on the same air mass by both instruments can be compared for long-lived species. Just as the “coincident comparison,” TM technique also needs match criteria in terms of time and space. The use of coincidence criteria reflects a compromise between the need to retain a large set of comparison pairs and the attempt to minimize spatial and temporal variations. A 1000 km/8 hour coincidence window is used by Cunnold, et al., (*Cunnold, D. M., et al., 1991*). A 12 hour of temporal separation, 5° latitude and 8° longitude has also been used (*Lu, C. -H., et al., 2000*) as coincidence criteria. More stringent coincidence criteria of (+/-) 1 hour, 10° longitude, 1° latitude and 20 K potential temperature were used to determine which HALOE air mass trajectories were included in the comparison with ER-2 flight path data (*Pierce, R. B., et al., 1997*).

Like the TM, the Coordinate Mapping (CM) technique employs also quasi-conservative quantities along the air parcel motion. It not only considers the mixing ratio and potential temperature but also the Potential Vorticity (PV) (*McIntyre, M. E., 1980; Schoeberl, M. R., et al., 1993; Lait, L. R., et al., 1990; Randel, W. J., et al., 1995; Atkinson, R. J., et al., 1997*). The technique involves a transformation of trace gas data from 3-D physical space (latitude-longitude-pressure) into 2-D potential vorticity-potential temperature coordinates, a flow-following “dynamical” reference frame. The 2-D character of this reference frame makes it analogous to a zonal mean analysis. As a contrast, the TM technique is analogous to the coincident analysis.

Trajectory Hunting Technique (THT) is a mutation of TM technique. It tries to find air parcels sampled at least twice by the same or different platforms over the course of a few days (*Danilin, M. Y., et al., 2000, 2002*). It needs less computational efforts and the results are not sensitive to a choice of a particular time like TM.

Although TM and the similar techniques can increase the statistic significance of validation, these approaches have their own drawbacks. (a) These techniques should not be directly used for species with short photochemical lifetime or experiencing rapid microphysics (like condensation or evaporation of H<sub>2</sub>O and HNO<sub>3</sub> from polar stratospheric clouds). At least a

### 3.4 Mathematics for validation

photochemical or microphysical model would be required in these cases. (b) The results are linked to a particular meteorological situation and data set choice and may not be considered as general result. (c) Trajectory calculations and possible extra model analysis for match air parcels introduce their own uncertainties.

#### (4) Gases correlation analysis technique.

Under certain conditions, the VMR relationship of two specific gases is approximately stable with respect to the geolocation and the time, for example, the N<sub>2</sub>O-CH<sub>4</sub> correlation, N<sub>2</sub>O-NO<sub>y</sub> correlation and N<sub>2</sub>O-CFCs correlations (*Chang, A. Y., et al., 1996*). Well above the tropopause and below about 40 km at mid-latitudes, the total hydrogen budget (H<sub>2</sub>O + 2CH<sub>4</sub>) should maintain a fairly constant field (*Abbas, M. M., et al., 1996*). They usually serve as good check of the internal consistency of the instrument.

In addition, the evaluation of sunrise/sunset differences in both diurnally varying (e.g. NO, NO<sub>2</sub>, N<sub>2</sub>O<sub>5</sub>) and non-varying (e.g. N<sub>2</sub>O, CH<sub>4</sub>, CFC12) constituents as well as the examination of characteristic profile shapes, relative latitudinal and long-term changes in observations of stable gases during successive orbits (in particular at their crossing locations) are also the typical approaches of internal consistency testing (*ESA, 2000*)

#### (5) Model simulation

Model calculations can help to estimate the mismatch influence to validation. While the model results might be different from reality in an absolute sense, they should be good in a relative sense for correcting the discrepancy caused by the temporal and spatial mismatch (*Wetzel, G., et al., 2004*).

### 3.4 Mathematics for validation

Assuming a variable  $x$  was measured  $n$  times. The arithmetic mean of  $x$  is given as:

$$\bar{x} = \frac{1}{n} \sum_{i=1}^n x_i. \quad (3.1)$$

its corresponding standard deviation (variance) is:

$$\sigma^2 = \frac{1}{(n-1)} \sum_{i=1}^n (x_i - \bar{x})^2. \quad (3.2)$$

$\sigma$  describes the dispersion extent around the mean value, i.e. giving the precision of an instrument measurement. If different  $x_i$  ( $i=1, 2, \dots, n$ ) have different errors  $\delta x_i$ , the weighted mean and the corresponding standard deviation is:

$$\bar{x} = \frac{\sum_{i=1}^n w_i x_i}{\sum_{i=1}^n w_i}, \quad (3.3)$$

and

### 3. Methodology of Validation

$$\sigma^2 = \frac{\sum_{i=1}^n w_i^2 \sigma_i^2}{\left(\sum_{i=1}^n w_i\right)^2}, \quad (3.4)$$

where

$$w_i = \frac{1}{\delta x_i^2}. \quad (3.5)$$

Besides the precision, the accuracy of a measurement is another index to describe the performance of an instrument. It is defined as the difference between a result (or mean) and the true value  $\mu$  (*IUPAC, 1978*).

## Chemistry instruments onboard ENVISAT

ENVISAT (**ENV**iromental **SAT**ellite) was launched by ESA on March 1, 2002. It is an advanced polar-orbiting Earth observation satellite. The measurements of ENVISAT support the Earth science research and allow monitoring of the evolution of environmental and climatic changes. The dimension of ENVISAT is 26m×10m×5m when flying at 800 km altitude with 98.55° inclination. The total weight is about 8000 kg. One orbit period is approximately 100 minutes. Therefore ENVISAT can finish about 14 orbits per day. The same orbit can be repeated with a period of 35 days. The designed mission period is 5 years (ESA, 2000, ESA, 2002).

There are ten key instruments onboard ENVISAT. These instruments have the capability to provide the observations of atmosphere, ocean, land, and ice. Three of the ten instruments are responsible for atmospheric remote sensing. They are: MIPAS (**M**ichelson **I**nterferometer for **P**assive **A**tmospheric **S**ounding), SCIAMACHY (**S**canning **I**maging **A**bsorption **S**pectro**M**eter for **A**tmospheric **C**hartography), and GOMOS (**G**lobal **O**zone **M**onitoring by **O**ccultation of **S**tars).

Figure 4.1 depicts the scheme of ENVISAT which shows the site of MIPAS, SCIAMACHY, and GOMOS on the satellite. These three atmosphere remote sensing instruments will be described in this chapter briefly.

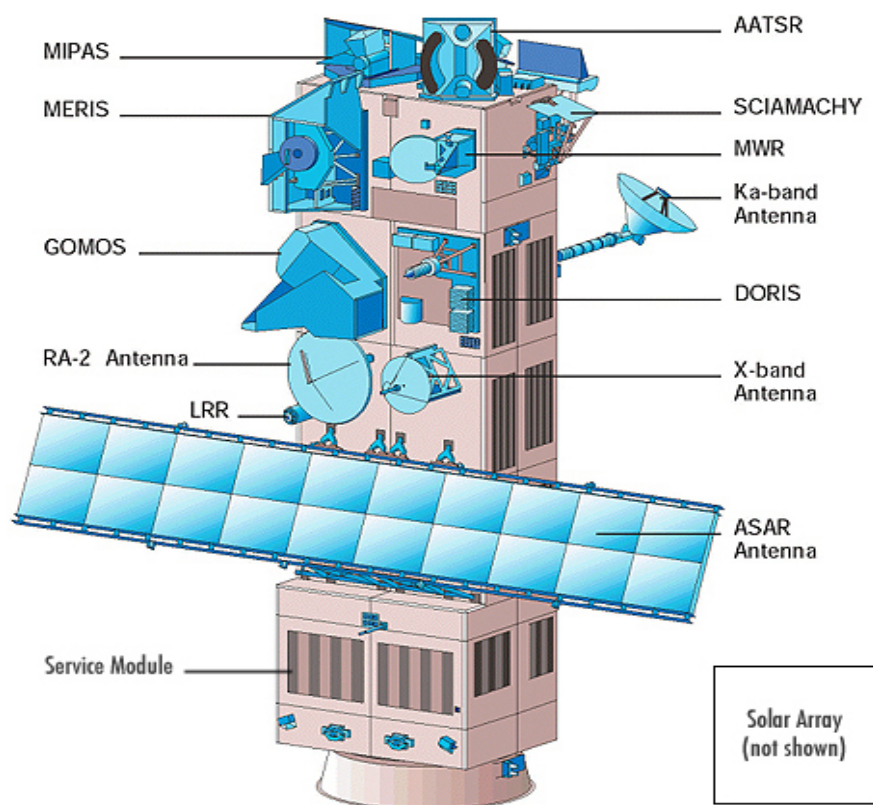


**Figure 4.1:** The scheme of ENVISAT with the three remote sensing instruments, MIPAS, SCIAMACHY and GOMOS (ESA, 2000).

## 4.1 MIPAS

### 4.1.1 Principle and structure

MIPAS is a limb scanning Fourier transform spectrometer. It comprises an optical and electronic module. Total weight is about 320 kg. Figure 4.2 outlines its main structure and working principle.

Incoming atmospheric light arriving at the input ports is collected by the input optics (mainly steering mirrors and a telescope) and directed on to a two-beam interferometer (based on a Michelson interferometer) which can make observations of broadband spectra at very high spectral resolution. The second input port is closed by a cold black body and is intended to suppress stray light.

Within the interferometer the incoming light is divided by a beam splitter into two beams of similar intensity. These are directed on to two moving retro-reflectors which direct them on to a beam combiner. Here the beams are superimposed and interfere; the resulting intensity at the output ports varies as a function of optical path difference. This interference modulated signal, as a function of optical path difference, constitutes an interferogram which is the Fourier transform of the spectrum of the incoming radiation. The original spectrum can be reconstructed from the recorded interferogram by an inverse Fourier transform.

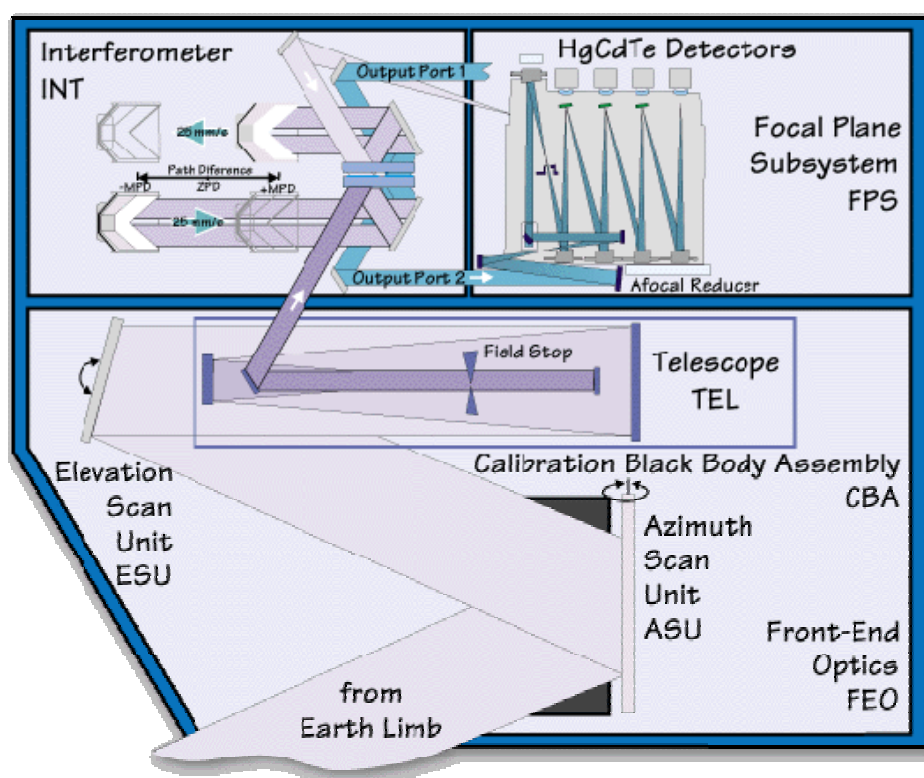


Figure 4.2: The working principle of MIPAS (ESA, 2000).

### 4.1.2 Characteristics and Operation

MIPAS is a very sensitive infrared Fourier transform spectrometer. The spectral coverage is set from 14.6 microns to 4.1 microns ( $685\text{ cm}^{-1}$  to  $2410\text{ cm}^{-1}$ ) and is divided into five bands: band A ( $685\text{--}970\text{ cm}^{-1}$ ), band AB ( $1020\text{--}1170\text{ cm}^{-1}$ ), band B ( $1215\text{--}1500\text{ cm}^{-1}$ ), band C ( $1570\text{--}1750\text{ cm}^{-1}$ ) and band D ( $1820\text{--}2410\text{ cm}^{-1}$ ). This range covers almost the complete thermal

## 4.1 MIPAS

infrared region. The NESR (Noise Equivalent Spectral Radiance), which characterises the instrument noise in terms of incident radiance, is about  $50 \text{ nW/cm}^2 \text{ sr cm}^{-1}$  at the long wavelength side, decreasing to  $4 \text{ nW/cm}^2 \text{ sr cm}^{-1}$  at the short wavelength side. The spectral resolution (unapodized) is  $0.035 \text{ cm}^{-1}$  with the relative spectral accuracy of  $0.0025 \text{ cm}^{-1}$ . This high resolution and sensitive spectrometer has the capability of sounding temperature and pressure as well as tens of species of gases in the middle atmosphere simultaneously during day and night, for example,  $\text{O}_3$ ,  $\text{H}_2\text{O}$ ,  $\text{N}_2\text{O}$ ,  $\text{CH}_4$ ,  $\text{HNO}_3$ , CFC11, CFC12,  $\text{NO}$ ,  $\text{NO}_2$ ,  $\text{N}_2\text{O}_5$ , and  $\text{ClONO}_2$ . In addition, MIPAS can also observe tropospheric cirrus clouds, polar stratospheric clouds and aerosol particle distribution. Figure 4.3 illustrate its coverage capability in space.

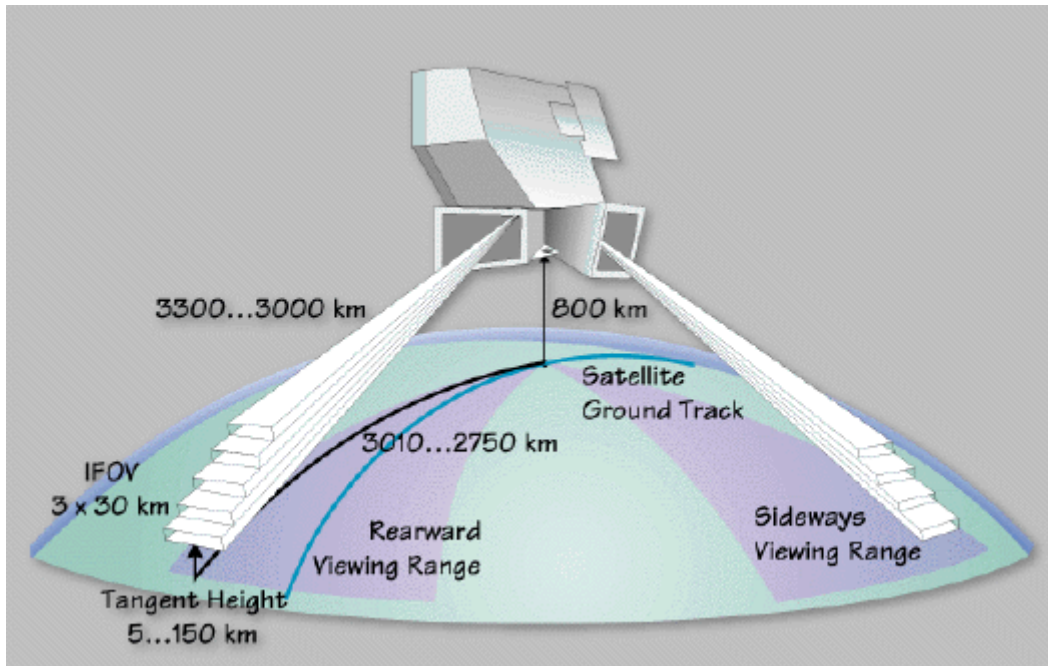


**Figure 4.3:** MIPAS measurement geometry (ESA, 2000).

The instrument is capable of performing measurements in two pointing regimes: rearwards within a  $35^\circ$  wide range in the anti-flight direction, and sideways within a  $30^\circ$  wide area in the anti-sun direction. The rearward viewing range is used for most measurements, as it provides a good Earth coverage, including the polar regions. The sideways range is important for observation of special events, like volcano eruptions, trace-gas concentrations across major air traffic routes, or concentration gradients perpendicular the dusk/dawn lines. In nominal observation mode, the rearward pointing range is used. The altitude range to the nominal mode is from 6 km to 68 km with a vertical resolution of 3 km and a horizontal resolution of approximately  $30 \text{ km} \times 500 \text{ km}$ .

MIPAS is a rapid limb scanning spectrometer. A complete high resolution spectrum is measured within 4.45 s (plus 0.6 s for the speed reversal of the slides). MIPAS obtains a series of spectra from different limb heights within about 75 s to allow the retrieval of species concentration profiles. To the nominal mode, one basic elevation scan sequence typically comprises 17 high-resolution spectra (ESA, 2002).

MIPAS observation time is 10:00 local time at the descending equatorial overpath and 22:30 local time at the ascending equatorial overpath. Typically, 75 limb sequences can be acquired in each orbit.

### 4.1.3 Data products

MIPAS provides many data products corresponding to different data processing stages. Level 0 products include MIPAS raw data, time and general quality information. The calibrated limb radiance data, geolocation data, product quality information, processing parameters, noise assessment data and offset calibration data comprise the level 1 products.

Level 2 (L2) products contain geophysical parameters, product quality information, residual spectra, fitted continuum data, processing parameters and other auxiliary data. The primary data inside are vertical profiles of pressure, temperature, volume mixing ratios of, H<sub>2</sub>O, O<sub>3</sub>, HNO<sub>3</sub>, CH<sub>4</sub>, N<sub>2</sub>O, and NO<sub>2</sub>. These data are also named operational data. In order to distinguish them from the science data retrieved by IMK-AME (A research group named Algorithm development and MIPAS-ENVISAT at the Institut für Meteorologie und Klimaforschung). Further, the operational L2 products are divided into Near-Real-Time (NRT) data (about three hours after the raw data reaching to the surface) and off-line data.

Since middle infrared emission spectra are strongly sensitive to temperature, and in general limb observations are strongly affected by the observation geometry, the pressure and temperature profile retrieval has to be finished simultaneously before the retrieval of volume mixing ratios for gaseous species starts. The validation of the primary operational data measured under nominal mode of MIPAS by using the correlative MIPAS-B (balloon version of MIPAS) observations is the major content of this study.

## 4.2 SCIAMACHY

### 4.2.1 Principle and structure

SCIAMACHY is an imaging spectrometer covering the spectral region from the ultraviolet to the near infrared radiation. The primary mission objective of this instrument is to perform global measurements of trace gases in the troposphere and in the stratosphere. It contains optical modules, detector modules and Scanners/Sun follower modules.

In the optical module, the light from the atmosphere is fed by the scanner unit (consisting of an azimuth and an elevation scanner) into the telescope, which directs it onto the entrance slit of the spectrometer. The spectrometer contains a predisperser which separates the light into three spectral bands followed by a series of dichromatic mirrors which further divide the light into a total of eight channels. A grating is located in each channel to diffract the light into a high-resolution spectrum which is then focused onto eight detectors. The predisperser also serves as a Brewster window to separate polarised light, a part of which is sensed by the Polarisation Measurement Device (PMD). The output of the PMD is later used to correct for the polarisation effects. Light reflected off the slit is directed to the sun follower, which controls the scan mirrors in the Sun and Moon occultation mode. Each spectrometer channel is equipped with a detector module. The detector module consists of the detectors and their Detector Module Electronics (DME). The DME controls the associated detector, reads out the integrated charge, amplifies the analogue signal and then digitises this signal. The digital signal of each channel is transferred to the science data processing unit (*ESA, SCIAMACHY*).

### 4.2.2 Characteristics and operation

SCIAMACHY can observe the transmitted, backscattered, and reflected radiation from the atmosphere in the wavelength range between 240 nm and 2400 nm. It has a relatively high spectral resolution of 0.2 nm to 0.5 nm, and in selected regions between 2.0 nm and 2.4 nm. The high resolution and the wide wavelength range make it possible to detect many different



## 4.2 SCIAMACHY

trace gases despite low concentrations, for example, O<sub>3</sub>, NO<sub>2</sub>, H<sub>2</sub>O, N<sub>2</sub>O, CO, CH<sub>4</sub>, OClO, H<sub>2</sub>CO and SO<sub>2</sub>. In addition, SCIAMACHY has the capability to sound clouds and aerosols.

SCIAMACHY has three different viewing geometries: nadir, limb, and sun/moon occultation which yield total column values as well as distribution profiles in the stratosphere and (in some cases) the troposphere for trace gases and aerosols. In nadir mode, the typical spatial resolution is 30 km×30 km to 30 km×240 km. While in limb and sun/moon mode, the altitude range of observation is from 0 to 100 km with a vertical resolution of 3 km. The horizontal resolution ranges from 240 to 960 km depending on the scan range, scan speed, tangent height and optical properties of the atmosphere. SCIAMACHY is designed to obtain global coverage within 3 days at the equator and more rapidly at higher latitudes.

In order to fulfill the scientific and technical requirements, SCIAMACHY is designed to operate under many different measurement modes. These measurement modes are the combination of nadir, limb and sun/moon occultation viewing geometries. To the dayside mode, solar occultation is performed when possible. Moon occultation is performed in the southern hemisphere every second orbit whenever possible. For the rest of the dayside, limb measurements are alternating with nadir ones. For the eclipse/nighttime mode, long integration times are necessary. Besides, calibration measurements can be performed on an orbital, daily, weekly, or a monthly basis.

### 4.2.3 Data products

Based on the data processing time sequence, the data products comprise level 1B and level 2 products.

Level 1B products are geolocated engineering calibrated data. They store individual spectra corresponding to the different scientific modes (nadir, limb, sun/moon occultation) spectrally and radiometrically calibrated as well as a solar reference spectrum. In order to support SCIAMACHY calibration/monitoring activities, the level 1B also includes individual measurements corresponding to special monitoring states. The raw measurements are also kept within the product.

The SCIAMACHY L2 data are categorized into operational products and scientific products. According to the potential use of the data and the complexity of algorithms, the operational product generation has been split between near-real-time processing and off-line processing. Level 2 NRT products are based on nadir measurements only. Limb and sun/moon occultation will be processed by off-line processors.

The SCAMACHY L2 products nominally include:

- A: Vertical column amounts of O<sub>3</sub>, NO<sub>2</sub>, H<sub>2</sub>O, N<sub>2</sub>O, CO, CH<sub>4</sub>, OClO, H<sub>2</sub>CO, and SO<sub>2</sub>.
- B: Cloud fractional cover and top height.
- C: Aerosol absorption indicator.
- D: Stratospheric profiles of O<sub>3</sub>, NO<sub>2</sub>, BrO, H<sub>2</sub>O, N<sub>2</sub>O, CO, CH<sub>4</sub>, pressure and temperature.
- E: Stratospheric profiles of Aerosol.

Since the quality of the operational data are not good enough for validation so far, here only the profiles of O<sub>3</sub> and NO<sub>2</sub> from the scientific products which were retrieved by Institut für Umweltphysik (IUP), University Bremen will be compared with the MIPAS-B correlative measurements.

## 4.3 GOMOS

### 4.3.1 Principle and structure

GOMOS is an atmospheric measurement instrument by occultation of stars. This is the first time that the star occultation measurement principle is used for ozone profiling from space. The primary GOMOS mission objectives are the measurement of profiles of ozone,  $\text{NO}_2$ ,  $\text{NO}_3$ ,  $\text{OClO}$ , temperature, and water vapour day and night in global coverage. As shown in Figure 4.4, the instrument line of sight can be successively oriented towards stars and maintained whilst the star is setting behind the Earth's atmosphere observed on the horizon. During the star occultation, the ultraviolet, visible and near-infrared spectra of the star are continuously recorded (*ESA, GOMOS*).

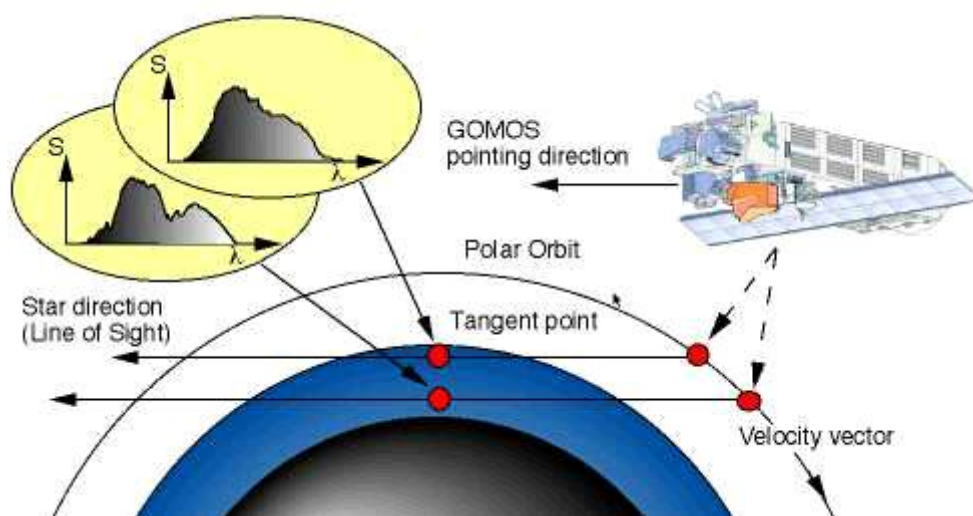


**Figure 4.4:** GOMOS measurement principle (*ESA, GOMOS*).

### 4.3.2 Characteristics and operation

GOMOS is a spectrometer covering the wavelength range from 250 nm to 950 nm with spectral resolution 1.2 nm in UV/VIS and 0.2 nm in NIR. Due to the requirement of operating on very faint stars (down to magnitude 4 to 5), a large telescope (30 cm  $\times$  20 cm aperture) was used to collect sufficient signal in order to fulfil the very high sensitivity requirement to the instrument. Detectors with high quantum efficiency and very low noise were developed to achieve the required signal to noise ratios.

The main mode of operation of GOMOS is the occultation mode. During this mode the instrument is, as a result of a macro command, autonomously acquiring and tracking stars as they set through the atmosphere. The uniformity mode, the spatial spread mode and the linearity mode are called monitoring modes, which enable in orbit monitoring and recalibration of important instrument performance parameters used in the ground processing. GOMOS measurements shall be performed in dark limb conditions (night side), or bright limb conditions (day side), or twilight limb conditions.

GOMOS has the capability to observe the atmosphere from 15 km to 100 km with high vertical resolution of 1.7 km. Typically, over 600 profiles are measured every day.

### 4.3.3 Data products

The GOMOS products are grouped according to processing levels. Level 0 comprise the raw spectrometer data, photometer data, recording time and other auxiliary data. Level 1a are the

### 4.3 GOMOS

Level 0 data after they have been sorted and filtered by low-level quality checks. Level 1b are GOMOS geolocated and calibrated background spectra (limb) data and transmission spectra.

The main data products of level 2 are vertical profiles of O<sub>3</sub>, NO<sub>2</sub>, NO<sub>3</sub>, O<sub>2</sub>, H<sub>2</sub>O, air, aerosol, temperature and turbulence.

At present, GOMOS measurements in bright and twilight limb conditions are not good enough for validation. Here only O<sub>3</sub> vertical profiles of GOMOS obtained under the dark limb conditions are going to be compared with the MIPAS-B measurements carried out during flight No. 11.

## Balloon version of MIPAS

Several FTIR spectrometers, known as MIPAS (**M**ichelson **I**nterferometer for **P**assive **A**tmospheric **S**ounding) have been developed for operation on aircraft and stratospheric balloon gondolas and proposed for operation on a satellite, respectively, by the Institut für Meteorologie und Klimaforschung (*Fischer, H., 1992, 1993; Fischer, H., and Oelhaf, H. 1996; Blom, C. E., et al., 1994, 1995, 1999*). The balloon-borne MIPAS (MIPAS-B) can be regarded as the precursor of MIPAS onboard ENVISAT (MIPAS-E).

The MIPAS-B as a limb sounding spectrometer in the mid infrared offers the simultaneous coverage of tens of constituents, for example, CO<sub>2</sub>, O<sub>3</sub>, H<sub>2</sub>O, CH<sub>4</sub>, and the NO<sub>y</sub> components (i.e. NO, NO<sub>2</sub>, HNO<sub>3</sub>, HO<sub>2</sub>NO<sub>2</sub>, N<sub>2</sub>O<sub>5</sub>, and ClONO<sub>2</sub>) along with its source gas N<sub>2</sub>O with a comparably high degree of freedom in terms of measurement scenario and launch window. MIPAS-B measurements are useful for the validation and improvement of instruments onboard satellite and of chemical-dynamical models of the atmosphere that are required for a reliable prediction of future ozone changes and the anthropogenic impact on the Earth's climate. Many articles have been published on the developments and scientific results of MIPAS-B (e.g. *Fischer, H, 1992, 1993; Oelhaf, H., et al., 1994, 1998, 2003; Wetzell, G., 1995, 1997, 2002; Höpfner, M., et al, 2002; Stowasser, M., et al., 1999, 2002; Friedl-Vallon, F. et al., 2004*).

Some restrictions in the application of infrared spectroscopy in general apply also to MIPAS-B are: Firstly, some of the light molecules with permanent dipole moment cannot be measured in the mid infrared but in the far infrared and in the microwave region using their rotational features. Secondly, the small scale variations of gas concentration in the vertical cannot be resolved due to the limitation of the vertical resolution of 1.5-3 km (*Fischer, H., 1992*). Thirdly, in the presence of optically thick clouds, MIPAS-B cannot measure trace gas profiles at low tangent altitudes. Finally, weather condition and launch limitation burden the logistic and financial constraints and hence, the numbers and duration of the balloon flights are limited.

Because the measurements of MIPAS-B are being used to validate the MIPAS-E operational data as well as the SCIAMACHY and GOMOS data, it is necessary to describe this instrument in more detail in terms of working principle, instrument characteristics, and operation processes.

### 5.1 Principle of a Fourier Transform Spectrometer

#### 5.1.1 Interference and Fourier transformation

The core component of MIPAS-B is the Michelson interferometer. Figure 5.1 illustrates the general principle of an interferometer.

## 5.1 Principle of a Fourier Transform Spectrometer

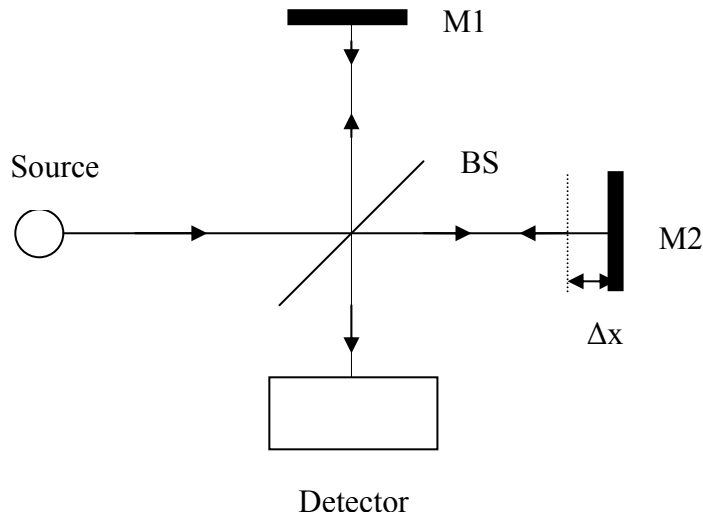


**Figure 5.1:** The principle of the Michelson interferometer.

Light from the source is divided into two light beams by BS (beamsplitter, a partially reflecting/transmitting optical unit). One beam reaches M1 (a total reflector), another one reaches M2 (a moveable total reflector). Then both beams are reflected back and interfere at the beamsplitter. The detector records an intensity that depends on the path difference of these two beams.

Assume that the source emits monochromatic light. Then the light is a cosine function of the path  $x'$  and time  $t$ .

$$a(x', t) = A \cos(2\pi\nu x' - \omega t), \quad (5.1)$$

where  $a$  represents the intensity of the electric field.  $\nu = 1/\lambda$  is the wavenumber,  $\omega = 2\pi f$ , and  $f$  is the frequency of the light wave.  $A$  represents the amplitude. The superposition of two beams with same  $\omega$  and  $A$  will be,

$$\begin{aligned} s &= a_1 + a_2 \\ &= A \cos(2\pi\nu x_1 - \omega t) + A \cos(2\pi\nu x_2 - \omega t) \\ &= 2A \cos(\pi\nu x) \cos(2\pi\nu(x_2 + x_1/2) - \omega t), \end{aligned} \quad (5.2)$$

here,  $x = x_1 - x_2$  is the path difference of the two beams. The light intensity of the interferogram is,

$$\begin{aligned} I_\nu(x) &= (2A \cos(\pi\nu x))^2 \\ &= S_0(\nu) [1 + \cos(2\pi\nu x)], \end{aligned} \quad (5.3)$$

where  $S_0(\nu) = 2A^2$  represents the amplitude of the interferogram. Equation (5.3) includes a constant component  $S_0(\nu)$  and a modulated component  $S_0(\nu) \cos(2\pi\nu x)$ . The constant component  $S_0(\nu)$  is usually filtered out in the measurements.  $I_\nu(x)$  will alternate between

## 5. Balloon version of MIPAS

$2 S_0(\nu)$  and 0 as  $x$  changes. These two extreme conditions are termed constructive interference and destructive interference, respectively.

In case of a polychromatic radiation source, just like from the gases in the atmosphere, the intensity of the interferogram is the integral of monochromatic contributions. Considering the initial phase  $\Phi(\nu)$  which depends on the frequency of light, the integral is (in absence of the constant component):

$$\begin{aligned} I(x) &= \int_0^{\infty} S_0(\nu) \cos(2\pi\nu x + \Phi(\nu)) d\nu \\ &= \int_0^{\infty} \frac{S_0(\nu)}{2} e^{i\Phi(\nu)} e^{i2\pi\nu x} d\nu + \int_0^{\infty} \frac{S_0(\nu)}{2} e^{-i\Phi(\nu)} e^{-i2\pi\nu x} d\nu. \end{aligned} \quad (5.4)$$

This is the signal that is recorded by the detector. With  $S(\nu) = \frac{S_0(\nu)}{2} e^{i\Phi(\nu)}$  and  $S(-\nu) = \frac{S_0(\nu)}{2} e^{-i\Phi(\nu)}$ , equation (5.4) becomes,

$$I(x) = \int_{-\infty}^{\infty} S(\nu) e^{i2\pi\nu x} d\nu. \quad (5.5)$$

However, the task of a spectrometer is to obtain the spectrum of a radiation source. (5.5) is nothing but the Fourier transformation of the spectrum. The inverse Fourier transformation allows deriving the  $S(\nu)$ :

$$S(\nu) = \int_{-\infty}^{\infty} I(x) e^{-i2\pi\nu x} dx \quad (5.6)$$

Equations (5.5) and (5.6) form the basis of principle of MIPAS. Nevertheless, the actual process of spectrum acquisition is more complicated. Firstly, the radiances with different wavenumbers may have different phases due to the dispersion of the beamsplitter and frequency-dependent devices. (for the details, see *Trieschmann, O.*, (1999), (2000) and *Friedl-Vallon, F., et al.*, (2004)). Secondly, the path difference  $x$  is not from  $-\infty$  to  $\infty$  but finite. Thirdly, the actual interferogram is sampled only at discrete points and not continuously as assumed in equations (5.5) and (5.6).

### 5.1.2 Instrumental line shape

The real interferometer doesn't have an infinite path difference, i.e. the  $x$  in previous equations are not in the range of  $[-\infty, \infty]$ . Instead, it belongs to  $[-L, L]$ . Assuming a boxcar function  $BX(x)$ , which is zero when  $|x| > L$  and unity when  $|x| \leq L$ , multiplying the infinite interferogram  $I_{inf}(x)$  by  $BX(x)$  then yields a finite interferogram  $I_{fin}(x)$ :

$$I_{fin}(x) = BX(x) I_{inf}(x). \quad (5.7)$$

Hence, according to the equation (5.6), the spectrum  $S_{fin}(\nu)$  measured with a spatially limited interferometer is,

## 5.1 Principle of a Fourier Transform Spectrometer

$$S_{fin}(\nu) = \int_{-\infty}^{\infty} I_{inf}(x) e^{-i(2\pi\nu x)} BX(x) dx. \quad (5.8)$$

According to the convolution theorem, the Fourier transformation of a product of two functions is the convolution of their individual Fourier transformations. Hence, equation (5.8) becomes,

$$\begin{aligned} S_{fin}(\nu) &= S_{inf}(\nu) \otimes bx(\nu) \\ &= \int_{-\infty}^{\infty} S_{inf}(\nu') bx(\nu - \nu') d\nu'. \end{aligned} \quad (5.9)$$

$S_{inf}(\nu)$  can be derived by using equation (5.6).  $bx(\nu)$  is the Fourier transformation of  $BX(x)$ , which is given below:

$$\begin{aligned} bx(\nu) &= \int_{-\infty}^{\infty} BX(x) e^{-i(2\pi\nu x)} dx \\ &= \frac{2L \sin(2\pi\nu L)}{2\pi\nu L}. \end{aligned} \quad (5.10)$$

So the analytical form of  $bx(\nu)$  is a sinc function.

Equation (5.9) states that the sharp line of a spectrum which enters the interferogram is broadened by the interferometer according to the function  $bx(\nu)$ . For this reason,  $bx(\nu)$  is termed Instrumental Line Shape (ILS) function.

Based on the Rayleigh criterion, the spectral resolution is defined as the distance between the maximum of the sinc function and its first minimum, then:

$$\Delta\nu_{rayleigh} = \frac{0.71}{2L}. \quad (5.11)$$

Another criterion to define the spectral resolution is the Full Width at Half Maximum (FWHM):

$$\Delta\nu_{FWHM} = \frac{0.61}{2L}. \quad (5.12)$$

Equation (5.11) and (5.12) both indicate that the spectral resolution of a Fourier transformation spectrometer is proportional to the maximum optical path difference.

The side lobes of the sinc function are not consistent with the actually measured information but rather represent an artefact due to the abrupt truncation of the interferogram at  $x=L$ . Hence, sometimes other cutoff functions whose Fourier transform show fewer side lobes than the sinc function are favorable. The side effect of apodization is the reduction of spectral resolution. The spectra measured with MIPAS-B are apodized with the "Norton-Beer strong" function (Norton, R. H. and Beer, R. 1976, 1977). With this apodization, the spectral resolution is reduced by a factor of 1.6.

## 5. Balloon version of MIPAS

In addition to the limitation of finite path difference, the finite Field Of View (FOV) of the spectrometer causes a self-apodization effect. Due to this effect, a sharp line is detected by the spectrometer as a spectral rectangle. The width is approximately (*Schneider, M., 2002*):

$$\Delta \nu_{self} = \frac{1}{2} \nu_0 \alpha_{max}^2. \quad (5.13)$$

Where  $\nu_0$  is the wavenumber of the detected line and  $\alpha_{max}$  the maximum off-axis angle due to the finite field of view. Therefore, the finite aperture causes an additional broadening of the ILS. Since the width of the spectral rectangle is proportional to  $\nu_0$ , the ILS becomes dependent on the wavenumber.

### 5.1.3 Discrete Fourier transformation

The actual sampling of the interferogram is carried out at discrete points, therefore, the discrete Fourier transformation has to be used instead of the continuous form. Assuming that the interval of sampling is  $\Delta x$ , the maximum path difference is  $\pm L$ , then we shall acquire  $N=1+2L/\Delta x$  (assuming  $N$  is an even) samples from  $x=-L$  to  $L$ . Thus, equation (5.5) becomes:

$$I(n\Delta x) = \frac{1}{\sqrt{N}} \sum_{m=-\frac{N}{2}}^{\frac{N}{2}-1} S(m\Delta \nu) e^{i2\pi \frac{nm}{N}}, \quad (5.14)$$

equation (5.6) is replaced by:

$$S(m\Delta \nu) = \frac{1}{\sqrt{N}} \sum_{n=-\frac{N}{2}}^{\frac{N}{2}-1} I(n\Delta x) e^{-i2\pi \frac{nm}{N}}, \quad (5.15)$$

where the continuous variables  $x$  and  $\nu$  have been replaced by  $n\Delta x$ , and  $m\Delta \nu$ , respectively. The relation between  $\Delta \nu$  and  $\Delta x$  is as follows:

$$\Delta \nu = \frac{1}{N\Delta x}. \quad (5.16)$$

## 5.2 Instrument characteristics

From 1986 to 1989 the first cryogenically cooled MIPAS-B was built to enable observations of the vertical distribution of chemical constituents independent of external light sources from high-altitude (*Friedl-Vallon, F., et al., 1999*). It flew four times successfully between 1989 and 1992. This instrument experienced a crash landing in March 1992 at the end of the **European Arctic Stratospheric Ozone Experiment (EASOE)** campaign. A new advanced instrument version of MIPAS-B was designed and built in 1993-1994 (*Fischer, H. and Oelhaf, H., 1996; Friedl-Vallon, F., et al., 2004*). This instrument has been upgraded in various aspects compared to its predecessor, particularly regarding the pointing system and the spectral coverage. From 1995 to 2005, in total 15 flights have been carried out successfully for numbers of science research missions. The description below relates to this instrument. A more detailed description of the instrument and its performance can be found in *Friedl-Vallon, F., et al., (2004)*.



### 5.2.1 The construction of MIPAS-B

The MIPAS-B instrument consists of five primary modules: (1) the gondola, (2) the Line-Of-Sight (LOS) stabilization and reference system, (3) the cryogenic spectrometer, (4) the on-board electronics, and (5) the ground control equipment. A part of module of (2) and module (3) is displayed in Figure 5.2.

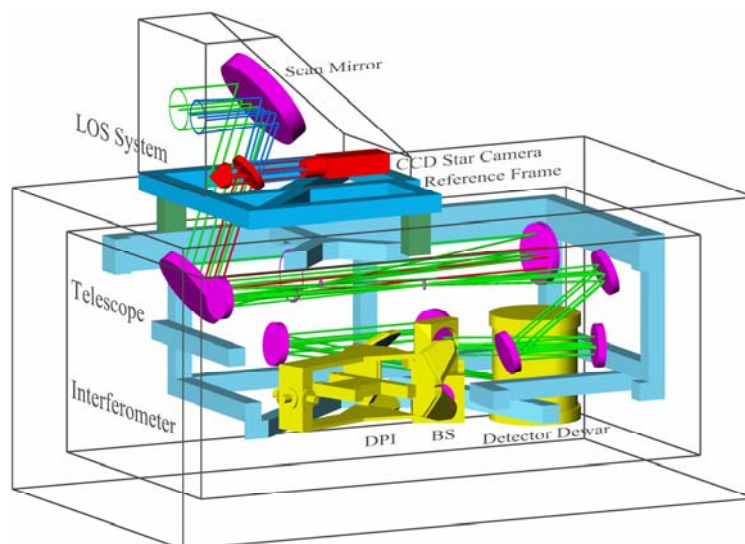


**Figure 5.2:** Mechanical and optical setup of MIPAS-B.

The gondola is a frame construction, developed by the Geneva Observatory, combining high stability and safety with relatively low weight and easy servicing. It has dimensions of approximately  $2.06 \times 1.85 \times 1.87 \text{ m}^3$ .

The LOS system is based on a miniaturized inertial navigation system with embedded GPS (**G**lobal **P**ositioning **S**ystem) that provides the attitude and heading reference of the instrument frame needed for the control loop to maintain the LOS within  $0.22 \text{ mrad}$  ( $3\sigma$ ) at the same elevation angle. The elevation angle of the scan mirror can be from  $20^\circ$  (space measurements for background calibration) to  $-6^\circ$  where the Earth's surface is already in the field of view. Additionally, it allows looking into an internal blackbody for calibration. A CCD star camera takes images of stars in the direction of the LOS that are used as absolute reference. The a posteriori overall knowledge of the elevation angle is better than  $0.3 \text{ mrad}$  ( $3\sigma$ ). For a flight altitude of  $39 \text{ km}$  and a tangent point altitude of  $10 \text{ km}$ , this corresponds to about  $180 \text{ m}$  ( $3\sigma$ ) (Seefeldner, M. and Keim, C., 1995; Maucher, G., 1995).

The spectrometer consists of a three-mirror off-axis telescope, a double-pendulum interferometer, and a four channel liquid-He cooled infrared detector system. The whole spectrometer operates at a temperature of approximately  $215$  to  $220 \text{ K}$ . The heart of the instrument is the double pendulum interferometer (Burkert, P. et al., 1983), a modification of the classical Michelson set-up. It provides two-sided interferograms with a maximal optical path difference of  $\pm 15 \text{ cm}$  resulting in an unapodized spectral resolution of  $0.035 \text{ cm}^{-1}$ . The four-channel detector system with Si:As BIB detectors, operating at a stable temperature between approximately  $5$  and  $7 \text{ K}$ , allows the simultaneous coverage of the most important absorption bands of relevant molecules between  $4.1$  and  $13.3 \mu\text{m}$  (Channel 1:  $750 - 1000 \text{ cm}^{-1}$ , Channel 2:  $1070 - 1557 \text{ cm}^{-1}$ , Channel 3:  $1557 - 1774 \text{ cm}^{-1}$ , Channel 4:  $1774 - 2460 \text{ cm}^{-1}$ ).

## 5. Balloon version of MIPAS

The analogue data is sampled on-board with the full clock rate of about 47 kHz. After conversion with a 16 bit AD-converter, the data of each channel is numerically filtered, mixed with the information of the other channels and the housekeeping data, and send to ground via telemetry at a data rate of 500 kbit/s. An uplink connection of 9600 bit/s ensures full commandability of the instrument during flight. On ground, the raw data is split up again and stored immediately in a data base. At the same time, housekeeping data and interferograms can be viewed and processed to allow on-line evaluation of measured data and of instrumental health.

The total weight of MIPAS-B is around 560 kg, using large balloons ranging in size from 100.000 m<sup>3</sup> to 400.000 m<sup>3</sup>. The float altitudes lie between 29 km and 39 km.

### 5.2.2 Performance

The performance of the spectrometer can be characterized mainly by the attained spectral resolution and sensitivity. The spectral resolution is given by the FWHM of the ILS (see equation (5.12)). The ILS (**I**nstrument **L**ine **S**hape) of MIPAS-B has been characterized by evaluation of flight spectra using the deconvolution approach (*Lengel, A., 2004*). The value for the FWHM differs by 0.5 % in the long wavelength region up to 1.5 % in the short wavelength region from the value that theoretically could be achieved assuming uniform illumination of the entire FOV. The unapodized spectral resolution is 0.035 cm<sup>-1</sup> (corresponding to an apodized spectral resolution of better than 0.07 cm<sup>-1</sup>).

The sensitivity is characterized by the **Noise Equivalent Spectral Radiance** (NESR). The NESR is a function of many parameters: detector performance, integration time, spectral resolution, optical throughput, modulation and transmission of the spectrometer. The achieved NESR during the flight No. 14 in Kiruna, Sweden, 03 July 2004 is shown in Figure 5.3.

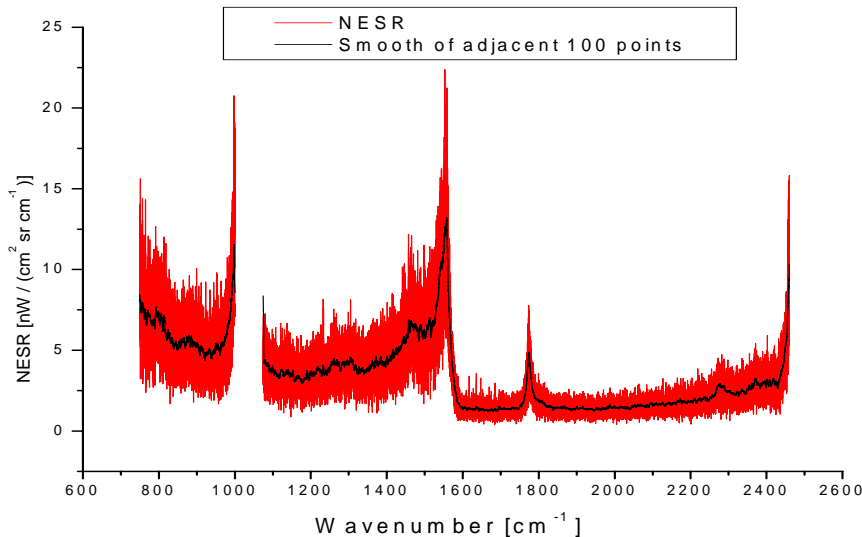


**Figure 5.3:** NESR of Seq. 2 at a tangent point altitude of 26 km during flight No. 14 in Kiruna, Sweden. This NESR is for a single spectrum for all channels.

### 5.3 Operation and data processing

During a balloon flight, the MIPAS-B instrument is carried to an observation altitude ( $Z_{\text{obs}}$ ) between 29 and 39 km (Figure 5.4). The scan mirror in the LOS system is oriented to different elevation angles  $\Phi$  while the azimuth remains fixed. Thus, the radiation of the

### 5.3 Operation and data processing

atmosphere from different altitudes  $Z_{\min}$  (0-39 km) can be measured. Deep space measurements with an elevation angle of  $+20^\circ$  ( $\Phi_{\text{space}}$ ), are performed to determine the instrument background. The altitude resolution relating to the MIPAS-B field of view is less than 3 km.

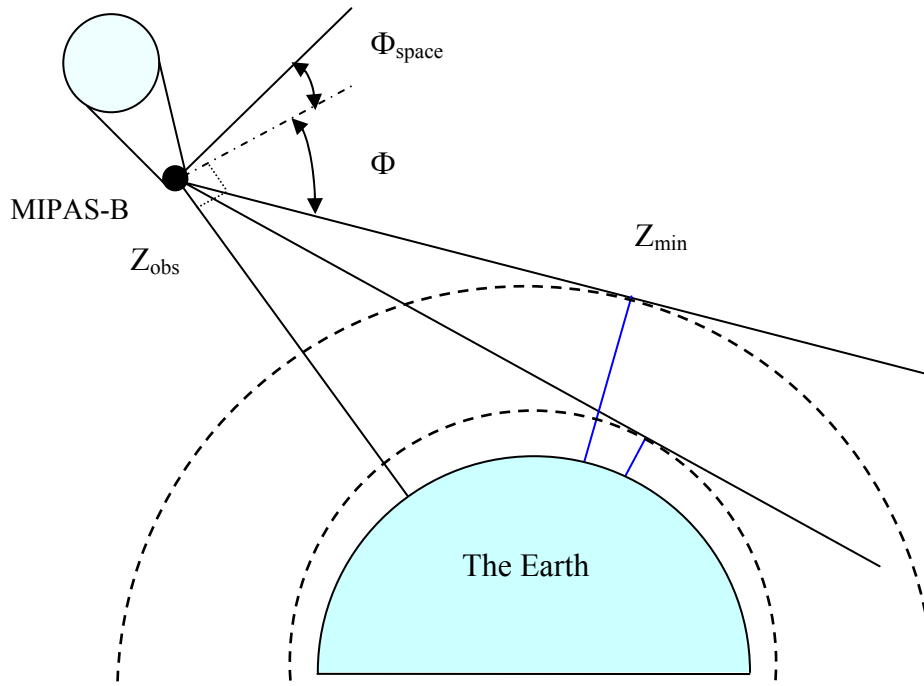


**Figure 5.4:** The scheme of MIPAS-B measurement geometry.  $Z_{\text{obs}}$  is the height of MIPAS-B.  $Z_{\min}$  represents the altitude of the tangent point of the line of sight.  $\Phi$  and  $\Phi_{\text{space}}$  indicate the elevation angle of the scan mirror.

From the raw data of observation to the vertical profiles of the temperature and the volume mixing ratios of various gases, many intermediate data processing steps are needed (see Figure 5.5).

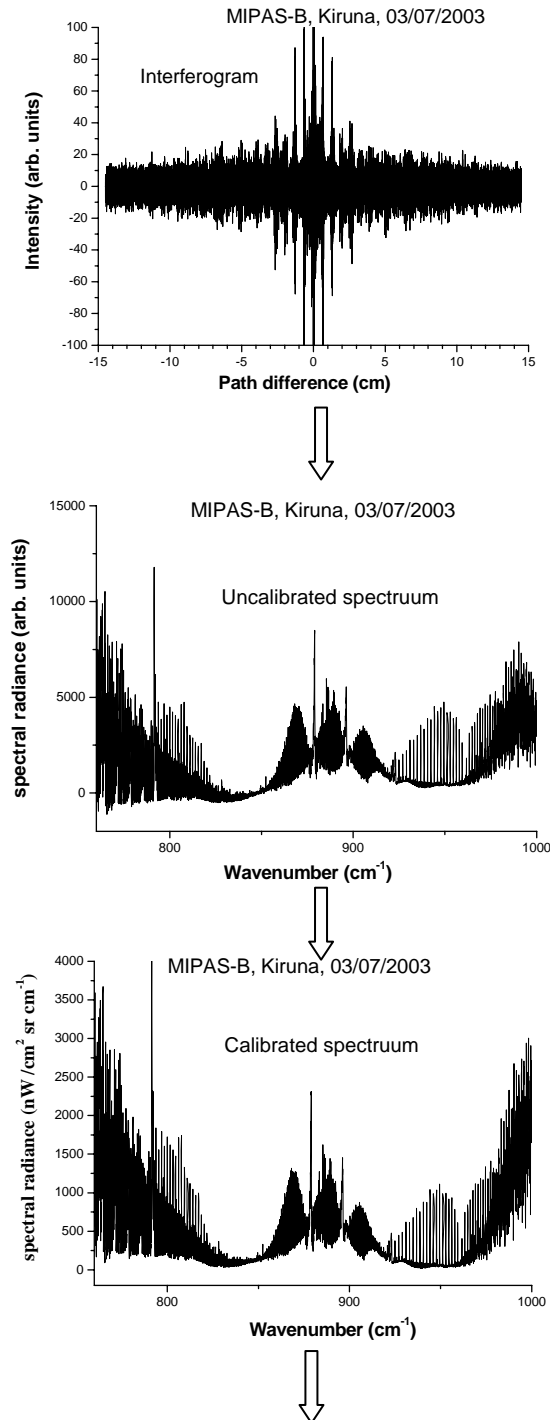
Interferograms recorded by the interferometer are the raw product of MIPAS-B. The recording time of one interferogram is typically 10 seconds. To detect some less abundant species, some interferograms have to be averaged in order to increase the signal-to-noise ratio. For the purpose of characterization and quality control of the instrument as well as data processing, house-keeping data are stored and managed together with the interferograms. The processing steps towards vertical profiles of chemical constituents require auxiliary data (e.g., parameters of the tracking geometry) which must be stored and interrelated with the spectral data.

The measured interferograms are corrected for the detector non-linearity (Kleinert, A., 2006). Then, the phase of the interferogram has to be corrected. The phase is mainly introduced by the discrete sampling, the beamsplitter coating, the electric amplifiers, and the different radiation ports of the instrument, as there are radiation components emitted by the atmosphere, emission of the optical components of the instrument and emission of the beamsplitter. Due to the weak atmospheric signal in case of emission measurements, the phase correction and therefore the phase characterization is the most crucial problem within the first part of the

## 5. Balloon version of MIPAS

processing chain. The classical method of phase determination is combined with a novel approach using a correlation method (Trieschmann, O., et al., 1999; Kleinert, A., 2003).

The corrected interferograms are then transformed into uncalibrated spectra by Fourier transformation.



### 5.3 Operation and data processing

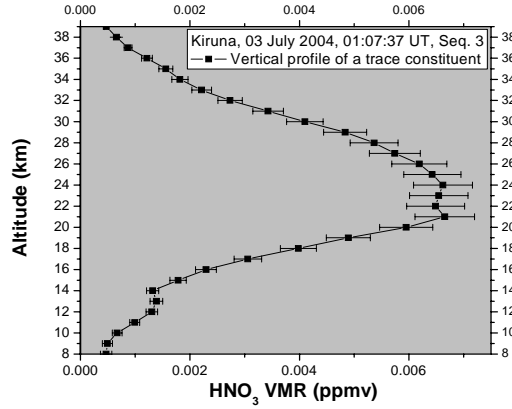


**Figure 5.5:** Typical data processing procedure of MIPAS-B.

Calibration of the spectra (in units of radiance) is based on “deep-space” spectra ( $+20^\circ$  elevation angle) and blackbody spectra both recorded during flight. The equation applied is

$$L_{atm} = (S_{atm} - S_{ds}) \cdot \frac{B(T)}{S_{bb} - S_{ds}}, \quad (5.17)$$

$L_{atm}$  and  $S_{atm}$  indicate the calibrated and uncalibrated atmospheric spectra, respectively.  $S_{ds}$  is the deep space spectrum.  $B(T)$  is the Plank function of the blackbody at temperature  $T$ , and  $S_{bb}$  represents the measured blackbody spectrum.

Calibrated radiance spectra are analyzed with a nonlinear least square fitting procedure, as provided by the software package named KOPRA (Stiller *et al.*, 2000; Höpfner, *M.*, *et al.*, 2002). The details on KOPRA and the inversion theory will be presented in the next chapter.

## Retrieval algorithms

The spectrometer, like MIPAS-B, measures the radiation of the atmosphere. However, the atmospheric state, i.e. the temperature, pressure and the concentration of gases, is the required quantity. The relationship between the measured radiation and the atmospheric state is modelled by the radiative transfer equation. The state parameters can be obtained by solving the equation. Unfortunately, the radiative transfer equation is not linear. Complicated inversion algorithms have been created in order to find the best solution of this equation. In this chapter, the radiative transfer model and the inversion concepts are introduced, followed by a description of the soft package called KOPRA, which is the code used for the retrieval of the profiles of temperature and VMR of gases.

### 6.1 Radiative transfer model

The radiance measured at frequency  $\nu$  at the observer location  $l_{obs}$  as a function of the atmospheric parameters is expressed by the radiative transfer equation (*Stiller, G. P., et al, 2000*):

$$S_{\theta}(\nu, l_{obs}) = S_{\theta}(\nu, l_0)\tau(\nu, l_{obs}, l_0) + \int_{l_{obs}}^{l_0} J(\nu, l)\sigma_{a,total}^{Vol}(\nu, l)\tau(\nu, l_{obs}, l)dl, \quad (6.1)$$

where  $S_{\theta}$ : Spectral radiance for the viewing angle  $\theta$ .  $\sigma_{a,total}^{Vol}$ : absorption coefficient including gases and aerosols per volume.  $\tau(\nu, l_1, l_2)$ : Transmission between  $l_1$  and  $l_2$  for wavenumber  $\nu$ .  $J$ : Source function.  $dl$ : Path element.  $l_{obs}$ : Position of the observer.  $l_0$ : Position of the background radiative source.  $l$ : Path coordinate.

The integration is performed along the line of sight of the instrument with the consideration of the atmospheric refraction. The atmosphere is divided into thin layers and each layer is characterized by constant representative state parameters. The mass-weighted state parameters for species  $g$  in layer  $j$  are:

$$p_{average,g,j} = \frac{1}{m_{g,j}} \int p(l)\rho_g(l)dl, \quad (6.2)$$

$$T_{average,g,j} = \frac{1}{m_{g,j}} \int T(l)\rho_g(l)dl, \quad (6.3)$$

where the particle density  $\rho_g$  of species  $g$  is calculated as:

$$\rho_g(l) = C_{V,g} \frac{N_{avo}}{R} \frac{p(l)}{T_{kin}(l)}, \quad (6.4)$$

here,  $N_{avo}$  is the Avogadro constant,  $R$  the universal gas constant,  $C_{V,g}$  the volume mixing ratio of species  $g$ ,  $T_{kin}(l)$  kinetic temperature at the position  $l$ , and  $p$  is pressure.

## 6.1 Radiative transfer model

In case of Local Thermodynamic Equilibrium (LTE), the source function in equation (6.1) is equal to the Planck function  $B$  of the emitting medium at the kinetic temperature  $T_{kin}$ :

$$J(\nu, l) = B(\nu, T_{kin}(l)). \quad (6.5)$$

The Planck function is:

$$B(\nu, T_{kin}(l)) = \frac{2hc^2\nu^3}{\exp\left(\frac{hc\nu}{k_B T_{kin}(l)}\right) - 1}. \quad (6.6)$$

The spectral atmospheric transmission  $\tau(\nu, l_1, l_2)$  between two points  $l_1$  and  $l_2$  on the line of sight is as follows:

$$\tau(\nu, l_1, l_2) = \exp\left\{-\sum_{g=1}^G \int_{l_2}^{l_1} \sigma_{a,g}(\nu, l) \frac{\partial m_g(l)}{\partial l} dl + \int_{l_2}^{l_1} \sigma_{e,aerosol}^{Vol}(\nu, l) dl\right\}, \quad (6.7)$$

where  $\sigma_{e,aerosol}^{Vol}$ : Aerosol extinction coefficient.  $\sigma_{a,gas}^{Vol}$ : Volume absorption coefficient for gases.  $\sigma_{a,g}$ : Absorption coefficient of the species  $g$ .  $m_g$ : Slant path column amount of species  $g$ .  $G$ : Number of gases taken into account.

The previous section only deals with radiative processes in the atmosphere which is independent of the observing instruments. Considering the field of view of an instrument, equation (6.1) becomes:

$$S_{\theta_0}^{FOV}(\nu, l_{obs}) = \int_{-\theta_{max}}^{\theta_{max}} S_{\theta}(\nu, l_{obs}) W(\theta - \theta_0) d\theta, \quad (6.8)$$

where  $W(\theta - \theta_0)$ : Weighting function related to FOV.  $S_{\theta_0}^{FOV}$ : FOV-convolved spectral radiance for viewing angle  $\theta_0$ .  $\theta_{max}$ : Maximum angle covered by FOV.  $\theta$ : Viewing angle between  $-\theta_{max}$  and  $+\theta_{max}$ .

Recalling equation (5.9), the equation (6.8) will be replaced by the following one if the instrumental line shape was considered:

$$S_{\theta_0}^{ILS}(\nu, l_{obs}) = \frac{\int_{-\infty}^{\infty} S_{\theta_0}^{FOV}(\nu', l_{obs}) ILS(\nu - \nu') d\nu'}{\int_{-\infty}^{\infty} ILS(\nu - \nu') d\nu}, \quad (6.9)$$

where  $S_{\theta_0}^{ILS}$ : Spectral radiance for viewing angle  $\theta_0$ , recorded by an instrument with known FOV and ILS.  $\int_{-\infty}^{\infty} ILS(\nu - \nu') d\nu'$ : Normalization

As for the details about the absorption and extinction coefficients, the calculation of the line intensities, the profile function of the spectral lines, the line mixing effects and the impact of time-dependence of collisions on the line shape as well as the FOV and ILS functions, see e.g. Stiller, G. P., et al., (2000); Kleinert, A., (2003); Friedl-Vallon, F., et al., (2004).

Equation (6.9) describes the radiative forward transfer not only considering the physics of the atmosphere but also the characteristics of the observing system. Through the inversion of this equation, the profiles of MIPAS-B on the concentration of gases and also the temperature can be calculated.

## 6.2 Inversion theory

Let  $Y, X$  represent the measurement data and the state parameters of the atmosphere, respectively.  $P$  represents the parameters that affect the measurements but do not belong to the atmospheric state parameters.  $\varepsilon$  is the error of the measurement. Then the radiative transfer equation can be represented by:

$$Y = f(P, X) + \varepsilon. \quad (6.10)$$

$f(P, X)$  is a function to tie the  $Y$  and  $X$  which is usually based on a very complicated atmospheric model. Giving the model parameters  $X, P$  to calculate  $Y$  is usually called a forward problem. Vice versa, to calculate the parameter  $X$  from the measured data is called an inverse problem. Inversion problems were studied also by numbers of mathematicians, physicists and researchers in atmosphere (Zhdanov, M. S., 2002; Rodgers, C. D., 1976, 1990, 2000, 2003). The retrieval of the VMR profiles of the constituents is a typical inversion calculation. The inverse problem is a well-posed problem, if (1) the solution ( $P, X$ ) of the function exists, (2) the solution is unique, (3) the solution depends continuously on the left-hand side of the equation of (6.10). If at least one of the conditions listed above fails, the inverse problem is an ill-posed problem. Solving the radiative transfer equation is an ill-posed problem, because the unknown profile is a continuous function of height but there is given only a finite number of measurements.

A linear transformation of equation (6.10) can be obtained by operating a Taylor expansion around an assumed profile  $X_0$ .  $X_0$  is near enough the true profile to drop in a linear behavior of the function  $Y$ . The Taylor expansion is truncated to the first term. Then:

$$Y = Y_0 + \left. \frac{\partial Y}{\partial X} \right|_{X=X_0} (X - X_0) + \varepsilon. \quad (6.11)$$

Actually, only a finite number  $n$  of observations and a finite number  $m$  of values to represent the vector  $X$  available to be dealt with. The discrete expression of (6.11) is:

$$Y = Y_0 + K(X - X_0) + \varepsilon, \quad (6.12)$$

where  $K = \left[ \frac{\partial Y}{\partial X} \right]_{X=X_0}$  is a  $n \times m$  Jacobian matrix.

Assuming a Gaussian distribution for the measurement errors, the least-squares fit approach is used for determining the state parameters  $X$  that produce the best simulation of the



## 6.2 Inversion theory

measurement  $Y$ . The  $\chi^2$  function, defined as the square summation of the differences between observations and simulations, weighted by the measurement noise, is:

$$\chi^2 = [Y - (Y_0 + K(X - X_0))]^T V_Y^{-1} [Y - (Y_0 + K(X - X_0))] \quad (6.13)$$

where  $V_Y^{-1}$  is the inverse matrix of a variance-covariance matrix (VCM) associated to the measurement errors. The  $X$  that minimizes the  $\chi^2$  is the solution of (6.12). If the hypothesis of linearity for equation (6.12) is not satisfied, the Gauss-Newton iteration method can be used for seeking its best solution (*Ridolfi, M., et al., 2000*). Then the following equation is derived:

$$X_{i+1} = X_i + (K_i^T V_Y^{-1} K_i)^{-1} K_i^T V_Y^{-1} [Y - f(P, X_i)] \quad (6.14)$$

where  $i$  indicates the iteration index,  $X_i$  the result of the previous iteration,  $K_i$  the Jacobian relative to the  $X_i$  and  $Y - f(P, X_i)$  the residual.

The solution from the equation (6.14) is not stable in some cases. This is intrinsic to the retrieval problem. The solution is represented in a base of functions different from the base of the observations identified by the Jacobian. If the base of the solution contains some components that are nearly orthogonal to the base of the measurements, these components are sensitive to small variations of noise with a consequent instability of solution. The Tikhonov-Phillips regularization technique (*Tikhonov, A. N. and V. Y. Arsenin, 1977*) is a valid method to resolve this problem. After using this regularization technique, equation (6.13) becomes:

$$\chi^2 = [Y - (Y_0 + K(X - X_0))]^T V_Y^{-1} [Y - (Y_0 + K(X - X_0))] + \gamma (X - X_0)^T L^T L (X - X_0), \quad (6.15)$$

where  $\gamma$  is the regularization parameter and  $L$  is an appropriate operator that determines the type of constraint. The solution minimizing the function (6.15) is:

$$X_{i+1} = X_i + (K_i^T V_Y^{-1} K_i + \gamma L^T L)^{-1} \{K_i^T V_Y^{-1} [Y - f(P, X_i)] - \gamma L^T L (X_i - X_0)\}. \quad (6.16)$$

The Levenberg (*Levenberg, K., 1944*) and Marquardt (*Marquardt, D. W., 1963*) solution is a particular case ( $L=I$  a unit operator) of the above equation.

The value of  $X_0$ , the a priori estimation, is usually set equal to zero. However, when some reliable a priori information on the retrieval parameters is available from sources external to the instrument measurements, the retrieval process can be improved by including this information. The retrieval process becomes more stable and fast. However, the a priori information may lead to systematic errors of the retrievals.

The gain matrix, which describes the sensitivity of the retrieval to changes in the measurement, is given by (*Steck, T. and T. von Clarmann, 2001*):

$$G_Y = (K^T V_Y^{-1} K + \gamma L^T L)^{-1} K^T V_Y^{-1}. \quad (6.17)$$

The averaging kernel matrix  $A$  contains the information of how the observing system modifies the true state of the atmosphere. It is defined as:

## 6. Retrieval algorithms

$$A = \frac{\partial \hat{X}}{\partial X_t} = G_Y K, \quad (6.18)$$

where  $\hat{X}$  is the estimated profiles in the linear case and  $X_t$  is the true profile. The rows of matrix  $A$  indicates where the information at each retrieved profile level of altitude originates from, while the columns as a delta-function response show how the retrieval responds to a perturbation of the true profile at one level of altitude. In an ideal inverse method  $A$  would be the identity matrix. In reality, the rows of  $A$  are functions peaking at the appropriate level and with a half-width which is a measure of the vertical resolution of the observing system, thus providing a simple characterization of the relationship between the retrieval and the true state (Ceccherini, S., et al., 2002).

The number of degrees of freedom  $F$  is a useful index to characterize the number of independent pieces of information for retrieval.  $F$  is defined as the trace of the averaging kernel matrix  $A$ :

$$F = \text{tr}(A). \quad (6.19)$$

For the retrieval errors, three components are considered (Steck, T., 2002):

1. Retrieval noise error:

$$V_{ran} = G_Y V_Y G_Y^T. \quad (6.20)$$

2. Smoothing error:

$$V_s = (A - I) V_E (A - I)^T. \quad (6.21)$$

where  $I$  is the identity matrix and  $V_E$  is the covariance of an ensemble of true states about the mean state. Often a true covariance matrix  $V_E$  is not known, and therefore the estimation of the smoothing error is inaccurate. In this study, the smoothing errors were not calculated.

3. Systematic or forward parameter error:

$$V_F = G_Y K_B V_B K_B^T G_Y^T. \quad (6.22)$$

where  $V_B$  is the error covariance matrix of the forward model parameters  $B$  (e.g. the temperature, spectroscopic data).  $K_B$  is the corresponding Jacobian matrix. The total error is the summation of last three errors.

$$V_{total} = V_{ran} + V_s + V_F. \quad (6.23)$$

### 6.3 KOPRA

KOPRA is a software package specially designed for the data analysis of the instrument MIPAS. Based on the measured atmospheric spectra and instrumental parameters such as NESR, ILS, FOV, the profiles about the temperature, pressure, and VMRs of numbers of gases can be retrieved. The following items introduce the main features of KOPRA.

### 1. Global fit analysis of the limb scanning sequence

A global fit approach (*Carlotti, M., 1988*) is adopted for the retrieval of each vertical profile. This approach fits the spectral data relating to a complete limb-scanning sequence simultaneously. Compared with the onion-peeling method, (*McKee, T. B., et al., 1969; Goldman, A., and R. S. Saunders, 1979*) the global fit provides a more sophisticated determination of the correlations between atmospheric parameters at the different altitudes. It permits the full exploitation of the hydrostatic equilibrium condition and is more compatible with the modelling of the finite field of view of the instrument. Unlike the case of the onion peeling method, global fit permits the retrieval at a fixed pressure-altitude level which can be different from the level of the limb scanning sequence.

### 2. Microwindows

The redundancy of information measured by MIPAS makes it possible to select a set of narrow spectral intervals containing the best information on the target parameters, whereas the intervals containing little or no information are ignored. This set of narrow intervals of wavenumber is called microwindows (*Echle, G., et al., 1999, 2000; Ridolfi, M., 2000*). Use of microwindows allows for the size of analyzed spectral elements to be limited and avoids the analysis of spectral regions that are characterized by uncertain spectroscopic data, interference by non-target species, non-local thermodynamic equilibrium and line mixing effects etc. More generally, priority can be given to the analysis of spectral elements with most information on the target species being less affected by systematic errors, e.g. temperature uncertainties causing errors to the VMR retrieval. The selection of microwindows is based on the long standing experience with MIPAS-B. For methods to determine the microwindows objectively, see von Clarmann, T. et al., (1998b), (1998c); Dudhia, A., et al., (2002).

### 3. Occupation matrix

A method to combine microwindows in the frequency-altitude space is the occupation matrix technique. In this technique, microwindows are selected also altitude depended. This altitude-dependent microwinds matrix can be either created by an algorithm (*von Clarmann, T, et al., 1998a*) or assembled.

### 4. Sequential retrieval of the parameters

The unknowns to be retrieved are pressure, temperature, VMR profiles of gases, atmospheric continuum. The latter includes all the emission sources that are frequency independent within a microwindow and zero-level correction accounts for an additive microwindows-dependent offset. The retrieval sequences of these unknowns are as follows. Firstly, temperature and pressure are retrieved simultaneously. However, for MIPAS-B, the pressure is not retrieved because MIPAS-B has an accurate LOS system. The tangent altitudes are calculated with high accuracy based on GPS-measured balloon altitude and the LOS elevation angle. Hence, with high accuracy, pressure is the known parameter when considering the hydrostatic equilibrium condition. Secondly, the target species VMR profiles are retrieved individually or simultaneously, depending on the selection of microwindows.

## Retrieval of atmospheric parameters from MIPAS-B

The retrieval quality of MIPAS-B measurements is crucial to the validation conclusions. Here, the retrieval process and the results are presented. These include the introduction of MIPAS-B flights; the parameter configuration of KOPRA; the typical retrieved profiles for each target parameter and the associated fitted spectra, averaging kernel and errors estimation.

### 7.1 Flights of MIPAS-B

During the years of 2002 and 2003 three MIPAS-B flights for ENVISAT validation have been carried out. The first one took place from Aire sur l'Adour, (France 44°N, 0°E), during 24/25 September 2002. The second flight was performed on 20/21 March 2003 from Esrange, Kiruna, (Sweden 68°N, 21.°E) and the third flight was carried out also from Kiruna on 2/3 July 2003. According to the flight history of MIPAS-B, these three flights are Flight No. 11, Flight No. 13 and Flight No. 14, respectively. These elaborated designed field campaigns covered the mid latitude in autumn as well as the high latitude region in later winter and summer of the northern hemisphere. Figure 7.1, Figure 7.2, and Figure 7.3 show the time and geolocations of MIPAS-B measurements along with the time and geolocations of the MIPAS-E (MIPAS onboard ENVISAT), GOMOS (only in Figure 7.1) and SCIAMACHY (only in Figure 7.3) measurements. For MIPAS-B, a measured sequence which comprises a set of consecutive scans at different altitudes is named Seq. XXX. While for MIPAS-E, the sequence is named Rec. XXX. In the Figures, the time and geolocation represent the mean time and mean geolocation of each sequence. The MIPAS-B limb sequences are displayed in black lines. MIPAS-E limb sequences are shown in red bars or white bars. In Figure 7.1, the region sounded by GOMOS is marked by a blue ellipse. The regions which are surrounded by the green line in Figure 7.3 are the areas that were observed by SCIAMACHY. The colour coded background is the potential vorticity field (Figure 7.1 and Figure 7.2) or the temperature field (Figure 7.3) at a selected level of altitude.

#### 7.1.1 Flight No. 11

The launch time of Flight No. 11 was at 18:43 UT on 24 September 2002. Float was reached at a maximum ceiling altitude of 39.2 km at 21:47 UT just 20 minutes before the ENVISAT overpass. Due to a surprisingly northern component of the wind direction at this altitude which would have brought the gondola over the Pyrenean Mountains the valve had to be opened for some time to bring the balloon down by about 1.6 km where the wind blew from west. The cut was at 23:50 UT. During the nominal measurement program (during ascent within the stratosphere and at ceiling) all systems worked nominal. Four sequences, Seq. S, Seq. N3, Seq. W, and Seq. E, were collected during the about 2 hours of ceiling (or slow descent). Seq. S and Seq. N3 can be used for comparison to the Rec. 15 (and/or Rec. 14) and Rec. 16 of MIPAS-E, respectively. Seq. W and Seq. E are helpful to check the horizontal gradient of temperature and the VMRs of gases and for trajectory comparison. The closest GOMOS star occultation of the same orbit was very close in time and location. SCIAMACHY does not perform observations at night time. The colour coded potential vorticity at 675 K (about 27 km altitude) indicates the edge of the developing polar vortex at about 45° latitude.

## 7.1 Flights of MIPAS-B

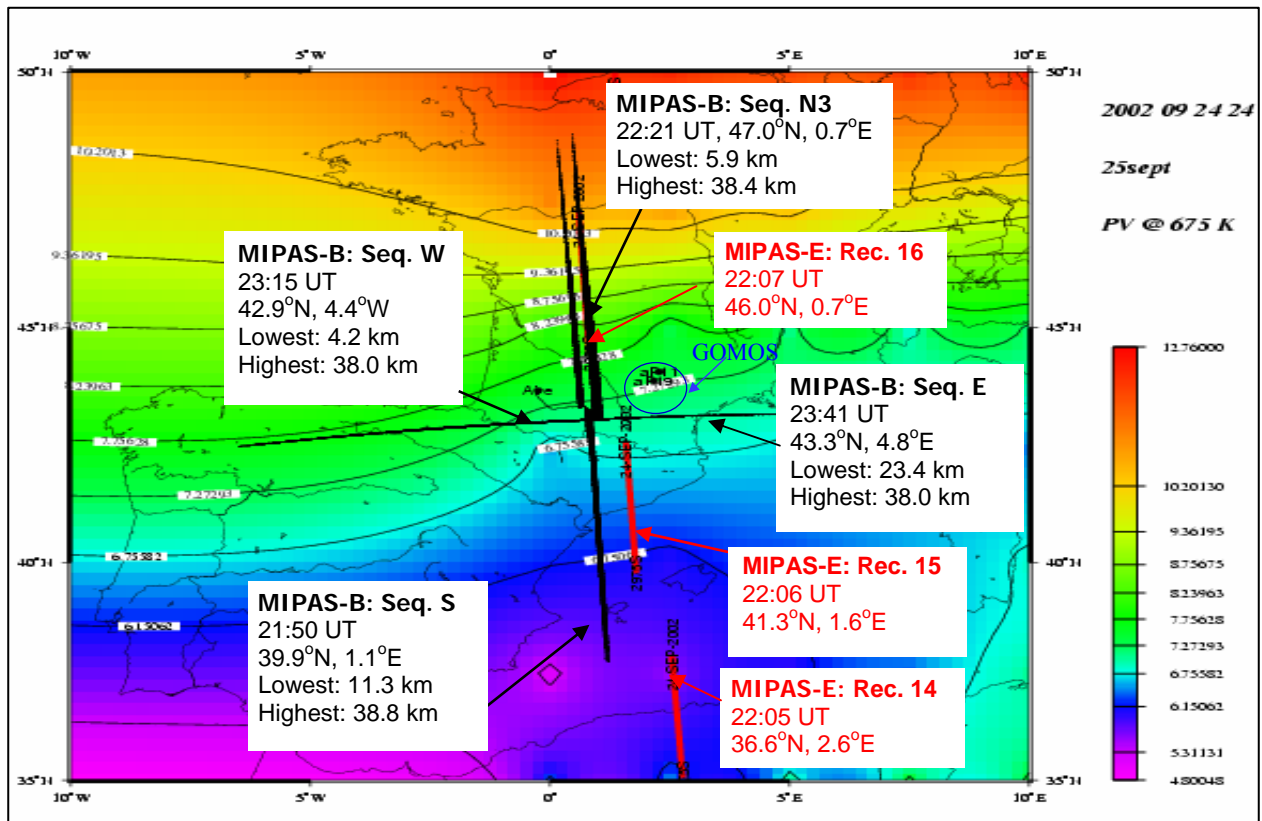


**Figure 7.1:** MIPAS-B lines-of-sight (black) for Flight No. 11 and MIPAS-E limb sequences (red) as well as the closest GOMOS star occultation of the same orbit (blue ellipse). The background is the colour-coded potential vorticity field at 675 K (~26.5 km).

### 7.1.2 Flight No. 13

From 18:22 UT (March 20) to 9:38 UT (March 21), the flight duration of Flight No. 13 was more than 15 hours. The long duration of this flight was possible since the balloon was released right into the centre of the polar vortex where the wind speeds are very low. Several limb sequences were measured matching the evening and morning overpasses of MIPAS-E, respectively. The Seq. N3a and the Seq. D15c which are the best sequences for MIPAS-E validation with respect to the match quality were retrieved for this study. Besides, numerous limb sequences (not shown here) that were collected in this flight will be used for other scientific studies.

### 7.1.3 Flight No. 14

The Flight No. 14 of MIPAS-B was carried out under the midnight sunshine. The launch time was 22:26 UT of July 2, 2003 and the landing time was 02:06 UT of July 3. Two limb sequences for validation were measured during this flight, named Seq. 2 and Seq. 3, respectively, according to the time order of measurements. The Seq. 2 measurement started from 0:13:33 UT and ended at 0:48:34 UT of July 3, resulting in a mean time of 0:27:39 UT on July 3. In this period, the MIPAS-B flight level changed from 32 to 39 km while the tangent point heights of the measurement were from 8 to 39 km. The mean latitude and longitude of the tangent points of the LOS (Line Of Sight) were (70.3°N, 27.6°E). The Seq. 3 measurements began from 0:51:38 UT and were finished at 01:20:50 UT of July 3. Its mean measurement time was 01:13:13 UT. The flight height was about 39 km during the Seq. 3 measurement period and the tangent altitudes account from 8 to 39 km. The mean geolocation of the measurements was (69.3°N, 11.0°E). All functions of the MIPAS-B instrument worked nominal during this flight.

7. Retrieval of atmospheric parameters from MIPAS-B

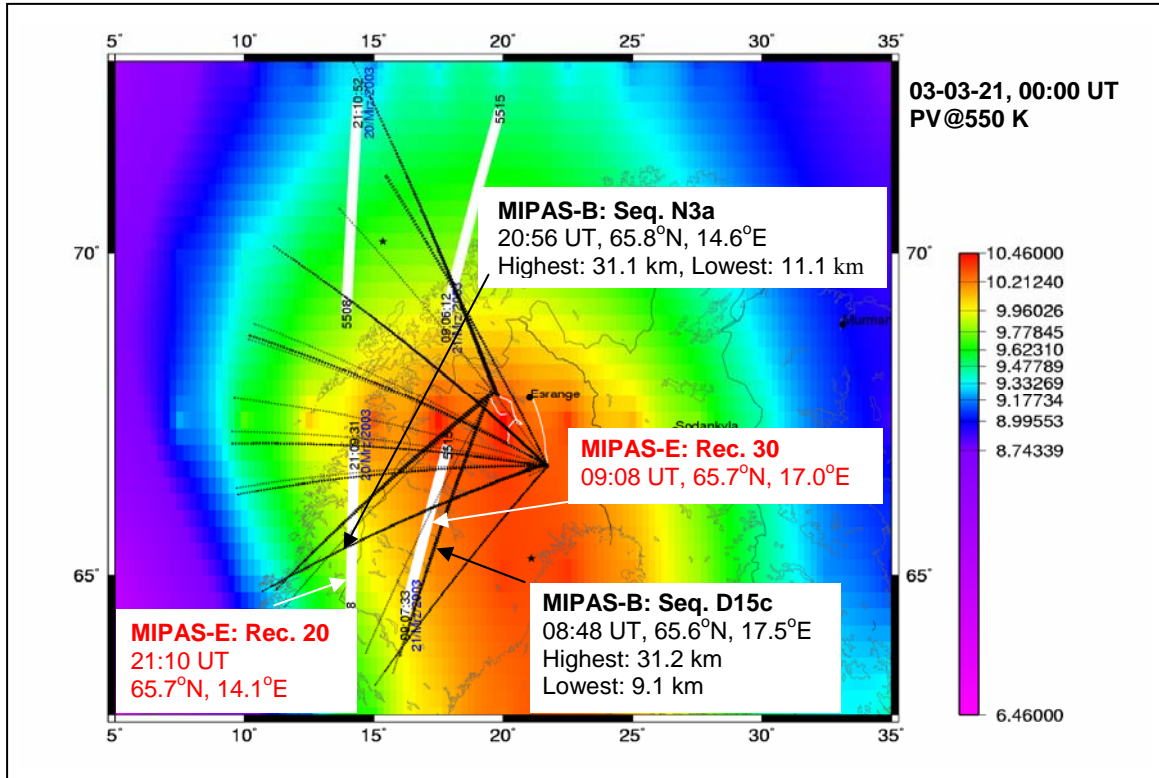


**Figure 7.2:** MIPAS-B lines-of-sight (black) for Flight No. 13 and MIPAS-E limb sequences (white). The background is the colour-coded potential vorticity field at 550 K (~22.8 km)

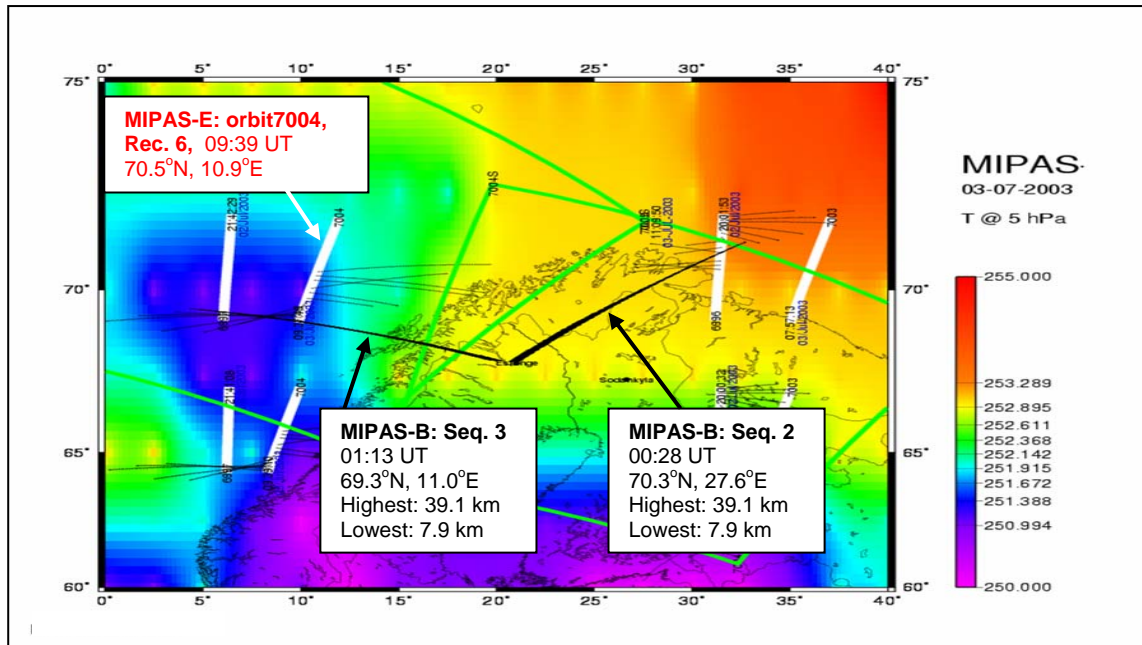


**Figure 7.3:** MIPAS-B lines-of-sight (black) for Flight No. 14 and MIPAS-E limb sequences (white). The background is the colour-coded temperature field at 5 hPa (~37.2 km). End points of the black dotted lines which are far from the MIPAS-E overpasses indicate the location of air masses sounded by MIPAS-E at the time of the MIPAS-B observation. The regions which are surrounded by the green lines are the areas that were observed by SCIAMACHY.

## **7.2 Parameters configuration and input data for retrieval**

### **7.2.1 Microwindows**

The MIPAS-B proven microwindows for retrieval of the temperature and the VMRs of gases are given in Table 7.1. These microwindows are located in the channel 1, channel 2, and channel 3 of the MIPAS-B detector system, respectively.

Figures 7.4 to Figure 7.6 show the sequence of recorded spectra (calibrated) of Seq. S during the 11th flight of MIPAS-B corresponding to channel 1, channel 2 and channel 3, respectively. The dominant gases in channel 1 are CO<sub>2</sub>, O<sub>3</sub> and HNO<sub>3</sub>. While the signatures of H<sub>2</sub>O, CH<sub>4</sub>, N<sub>2</sub>O, O<sub>3</sub>, HNO<sub>3</sub> and CO<sub>2</sub> are most significant in channel 2. In channel 3, H<sub>2</sub>O and NO<sub>2</sub> present strong signatures.

7. Retrieval of atmospheric parameters from MIPAS-B

**Table 7.1: The microwindows used for the retrieval from the MIPAS-B spectra.**

Target parameters	MIPAS-B_Channel1 (cm <sup>-1</sup> )	MIPAS-B_Channel2 (cm <sup>-1</sup> )	MIPAS-B_Channel3 (cm <sup>-1</sup> )
Temperature	(801.40, 801.71), (810.76, 811.14), (812.28, 812.66), (941.29, 946.99), (948.51, 951.51), (951.99, 956.69).		
H <sub>2</sub> O	(807.99, 808.62), (824.51, 825.30).	(1210.19, 1212.60), (1218.09, 1219.09), (1243.48, 1244.52).	(1589.51, 1591.89), (1595.48, 1596.79), (1602.18, 1603.12).
O <sub>3</sub>	(763.48, 764.58), (765.03, 765.89), (766.62, 767.28), (768.11, 768.80), (776.02, 777.15), (779.09, 779.85), (780.61, 781.89), (782.16, 783.51), (786.90, 788.10), (788.45, 789.59), (794.08, 795.18), (795.98, 796.50), (800.43, 801.47), (801.64, 802.65), (803.92, 804.34), (808.41, 808.97), (822.06, 823.09), (823.47, 824.41), (964.88, 965.95), (968.09, 968.96).	(1140.10, 1143.49), (1143.90, 1149.74), (1150.40, 1155.99), (1156.79, 1159.41), (1161.62, 1162.21), (1163.31, 1163.80), (1166.60, 1168.12), (1170.40, 1171.19), (1175.09, 1175.51), (1178.48, 1179.00), (1181.10, 1181.41), (1182.80, 1183.31), (1193.33, 1193.85), (1195.20, 1195.58).	
HNO <sub>3</sub>	(863.85, 868.75), (868.79, 874.01).		
CH <sub>4</sub> and N <sub>2</sub> O		(1161.93, 1164.94), (1180.41, 1184.00), (1216.09, 1219.99), (1220.48, 1223.52), (1228.49, 1229.80), (1256.88, 1267.11).	
NO <sub>2</sub>			(1585.02, 1589.51), (1591.89, 1593.72), (1596.48, 1601.11), (1601.49, 1602.53), (1604.01, 1606.60), (1607.61, 1609.19), (1610.29, 1614.99).



## 7.2 Parameters configuration and input data for retrieval

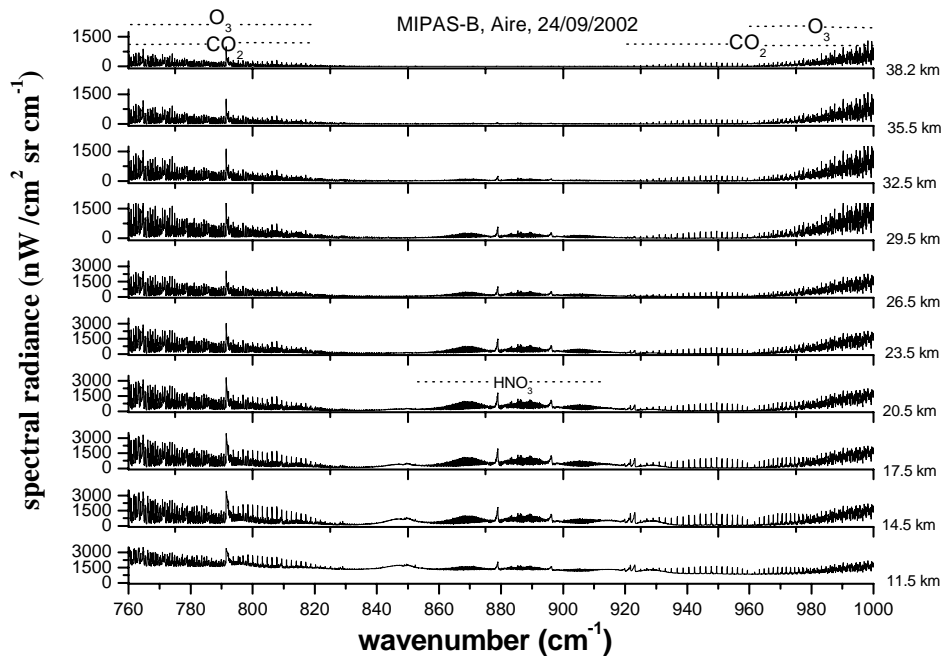


Figure 7.4: Channel 1 spectra subset at different altitudes recorded in Seq. S of MIPAS-B Flight No. 11.

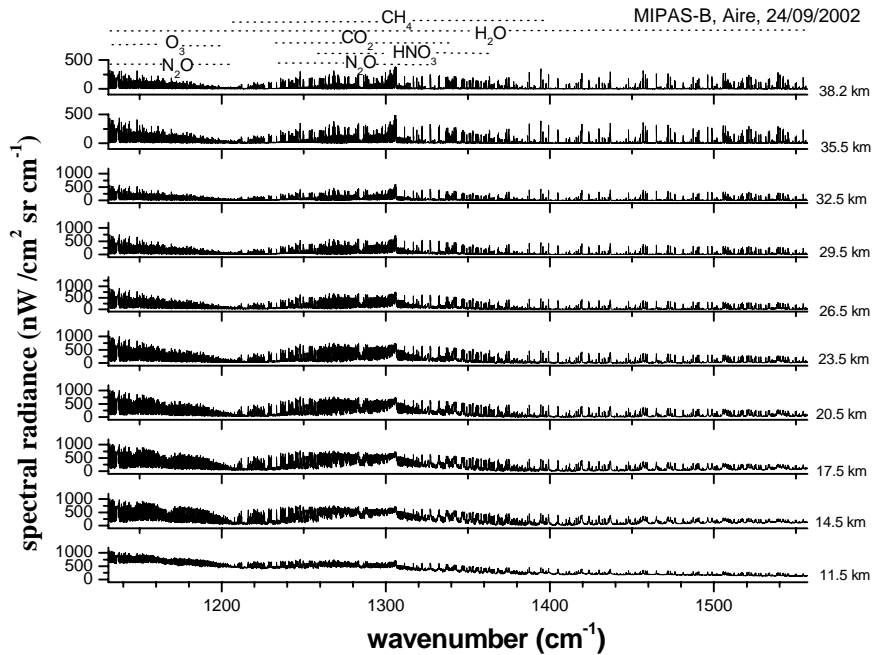
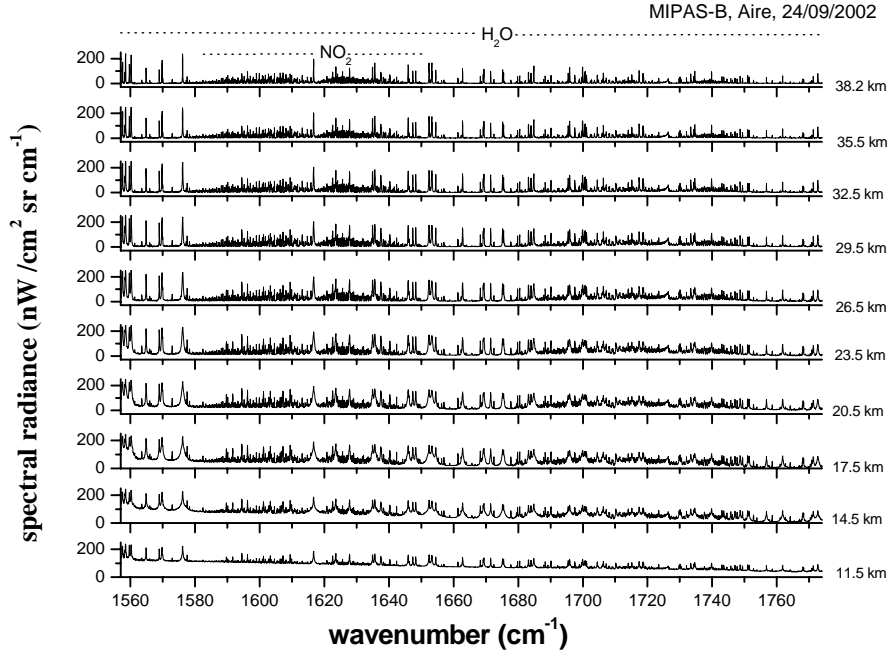


Figure 7.5: Channel 2 spectra subset at different altitudes recorded in Seq. S of MIPAS-B Flight No. 11

## 7. Retrieval of atmospheric parameters from MIPAS-B



**Figure 7.6:** Channel 3 spectra subset at different altitudes recorded in Seq. S of MIPAS-B Flight No. 11

### 7.2.2 A priori data and the Tikhonov-Phillips regularization approach

The a priori profile is the initial profile for the iteration calculation. The a priori profile doesn't change during the iteration process. From surface to 0.1 hPa, the data on the a priori profile for the temperature are from the ECMWF (European Center of Medium range Weather Forecast) and/or the radiosonde measurements near the MIPAS-B flight region shortly before or after the balloon was launched. Above this level of altitude as well as for trace species, the standard profiles corresponding to different climatologies (mid latitude summer for Flight No. 11, Arctic winter for Flight No.13 and Arctic summer for Flight No. 14) were employed.

The Tikhonov-Phillips regularization technique was adopted for all retrieved profiles. The  $L$  (see equation (6.16), the  $\gamma L^T L$  in the last term) for smoothing constrains is the first derivative operator.

$$L = \begin{bmatrix} -1 & 1 & 0 & \dots & 0 \\ 0 & -1 & 1 & \ddots & \vdots \\ \vdots & \ddots & \ddots & \ddots & 0 \\ 0 & \dots & 0 & -1 & 1 \end{bmatrix}. \quad (7.1)$$

This type of operator constrains the retrieved profiles to the shape of an a priori profile but not to the absolute values.

The value of  $\gamma$  determines the strength of the constraint. One way to determine the optimal value of  $\gamma$  is the L-curve method which is a trade-off between the residual spectra and the side condition (Hansen, P.C., 1992). However, due to the very low noise in the MIPAS-B spectra often systematic errors dominate the total errors and thus the typical shape of the L curve seldom appeared in our retrieval. Other methods (Li, J., et al., 1999; Steck, T., 2002) to select

## 7.2 Parameters configuration and input data for retrieval

the optimal value of  $\gamma$  are also not practical in our case. Therefore, the value of  $\gamma$  was determined empirically seeking for a compromise between the smoothness of the retrieved profile and the standard variance of the residual spectra.

The regularization matrix  $R$  for the state vector consists of block matrices along its diagonal. It is,

$$R = \begin{bmatrix} \gamma_1 L^T L & 0 & \dots & 0 \\ 0 & \gamma_2 L^T L & \ddots & \vdots \\ \vdots & \ddots & \ddots & 0 \\ 0 & \dots & 0 & \gamma_{cont} L^T L \end{bmatrix}, \quad (7.2)$$

where  $\gamma_1, \gamma_2, \dots$ , represent the regularization parameters for the retrieved state parameters (e.g., temperature, VMRs of gases include the VMRs of the main interfering gases), respectively. The  $\gamma_{cont}$  applies for the continuum profile. All other minor interfering gases are considered in the forward calculation but not adjusted and regularized during the retrieval.

### 7.2.3 Vertical retrieval grid

KOPRA permits to perform the retrieval at a fixed retrieval grid. From the point of KOPRA itself, an arbitrary vertical grid is possible. However, the vertical resolution and the accuracy with which the retrieved profiles are determined are generally anticorrelated (*Carlotti M., and B. Carli, 1994*) and are strongly dependent on the grid where the retrieval points are presented. Normally, it requires that the vertical grid should be at least as fine as the vertical resolution of scan. Here, the retrieval vertical grid with a step of 1 km is adopted, since MIPAS-B vertical resolution is less than 3 km and the measurement grid was typically 1.5 km.

### 7.2.4 Spectroscopic molecular database

The retrieval of the target parameters profiles was based on the HITRAN 2004 database. The spectroscopic molecular database HITRAN (HIGH-resolution TRANsmision database) is an international standard compilation of absorption parameters that enable the calculation of atmospheric spectral simulations from the microwave to the visible. The parameters for the different species generally include molecular and isotope numbers, line positions, transition intensities, air-broadened and self-broadened halfwidth's, lower state energies, temperature dependencies of line widths, quanta indices and others.

### 7.2.5 Continuum effect

Continuum radiation from aerosols, thin clouds, far line wings etc., should be considered during the retrieval, especially at the lower altitudes where these effects are increasing. The initial continuum is always set to zero. The grid is the same as the retrieval grid for the target parameters. One continuum profile is retrieved for each microwindow. Before starting the retrieval of the target parameters, the range of the altitude in which the continuum effects exist should be determined. This problem is solved by analysis of the calculated continuum profile (i.e., the absorption coefficients profiles). Figure 7.7 shows an example of a calculated continuum profile. According to the profiles of the absorption coefficients, the continuum effects influence the retrieval up to about 14 km in this case.

## 7. Retrieval of atmospheric parameters from MIPAS-B

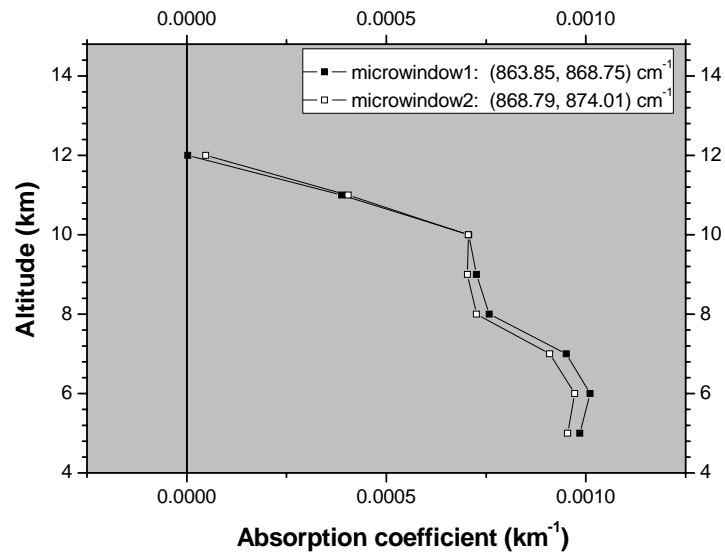


**Figure 7.7:** The profiles of the absorption coefficients in the microwindows for  $\text{HNO}_3$  retrieval of Seq. 3, Flight No. 14.

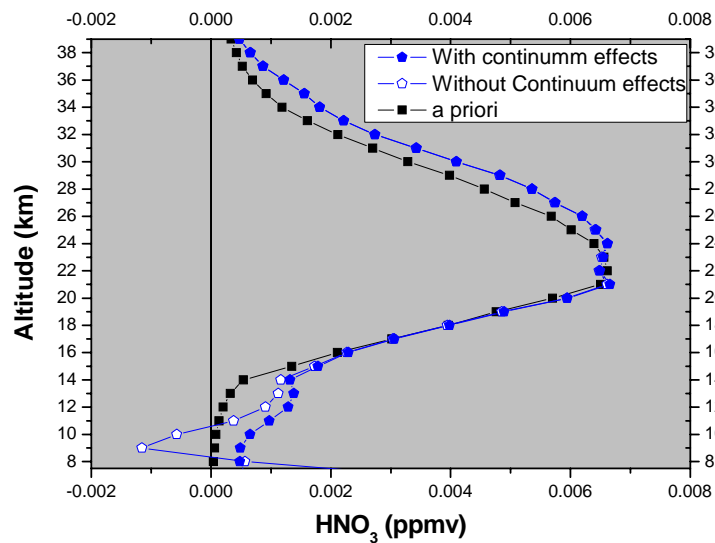


**Figure 7.8:** An example of the continuum effect on the retrieval. The blue curve with solid symbol is the retrieved  $\text{HNO}_3$  profile of Seq. 3, Flight No. 14. The curve with open symbols is also a retrieved  $\text{HNO}_3$  profile for the same sequence but without the continuum consideration. Other settings of retrieval for both cases were the same.

Figure 7.8 illustrates a typical continuum effects influence to the retrieved profiles. Obviously, the influence only appears at the lower altitudes.

### 7.3 Output of retrieval

The output of the retrieval contains: **1.** The profile of the target parameters i.e., the profile of temperature and/or the VMRs of H<sub>2</sub>O, O<sub>3</sub>, HNO<sub>3</sub>, CH<sub>4</sub>, N<sub>2</sub>O, and NO<sub>2</sub>. This is the main objective of the retrieval. **2.** The continuum profile as mentioned in section 7.2.5. **3.** In order to compensate for the radiance calibration uncertainty or unknown atmospheric effects, an altitude dependent absolute radiance offset is retrieved per microwindow. **4.** A first-order spectral calibration is performed by the knowledge of the distance of the interferogram sampling. This calibration is not very exact. Therefore, an altitude independent frequency offset was retrieved together with the retrieval of the target parameters. The frequency shift retrieval doesn't need regularization either. **5.** The auxiliary data output. These data consist of the calculated spectra, the residual spectra (the calculated spectra minus the measured spectra), the numbers of the degrees of freedom, and the averaging kernel matrix. This auxiliary data are very useful to diagnose the retrieval quality.

Some data (i.e. the numbers of the degrees of freedom, the altitude range of the profiles, the latitude range of the continuum effects, the use of the occupation matrix, vertical resolution) about the retrieval for all the target parameters of each sequence are listed in the appendix A. The use of the occupation matrix will be discussed in the next section.

### 7.4 Error estimation

The retrieved temperature errors consist of the random errors from the noise of measured spectra  $\sigma_N$ , LOS error  $\sigma_L$  which is caused by the uncertainty of the elevation angle knowledge, spectroscopic data error of CO<sub>2</sub>  $\sigma_{CO_2}$  (which also takes into account the uncertainty of the VMR of CO<sub>2</sub>) and the spectrum calibration error  $\sigma_{cal}$ . The VMR profiles errors comprise the noise error as well as cross-correlation effects of the fitted species error  $\sigma_{inter}$  (in case of  $\sigma_{inter}$  is significant), LOS error, temperature error  $\sigma_T$  and spectroscopic data error  $\sigma_S$ . The smoothing error is neglected since the retrieval is regarded as an estimation of a state smoothed by the averaging kernel rather than an estimation of the true state. The total 1- $\sigma$  error  $\sigma_{total}$  for temperature is:

$$\sigma_{total} = \sqrt{\sigma_N^2 + \sigma_L^2 + \sigma_{CO_2}^2 + \sigma_{cal}^2}. \quad (7.3)$$

For the VMRs of gases,

$$\sigma_{total} = \sqrt{\sigma_N^2 + \sigma_{inter}^2 + \sigma_L^2 + \sigma_T^2 + \sigma_S^2}. \quad (7.4)$$

## 7.5 Retrieval results for the temperature and each gas

### 7.5.1 Temperature

Because the CO<sub>2</sub> concentration is well known below the mesopause and the variation of CO<sub>2</sub> mixing ratios is very little with altitude throughout large regions of the atmosphere, it is suitable to infer the temperature profile from the CO<sub>2</sub> emission bands. The six microwindows used for the temperature retrieval are (801.40, 801.71), (810.76, 811.14), (812.28, 812.66), (941.29, 946.99), (948.51, 951.51), and (951.99, 956.69) (cm<sup>-1</sup>). These microwindows belong to the CO<sub>2</sub> transition of  $\nu_3$  R12,  $\nu_3$  R24,  $\nu_3$  R26,  $\nu_4$  P18,  $\nu_4$  P12 and P14, as well as  $\nu_4$  P6, respectively (Stiller, G. P., et al., 1995). Due to the interference of H<sub>2</sub>O radiance, the H<sub>2</sub>O concentration is also retrieved along with the temperature retrieval. The profiles of other gases were kept unchanged during the fitting process.

## 7. Retrieval of atmospheric parameters from MIPAS-B

Figure 7.9 illustrates the temperature retrieval results for Seq. N3a of Flight No. 13. Panel A gives the measured spectra and the fitted spectra in the fourth microwindow at the tangent altitude of 20 km and their difference (residual spectra). The measured spectrum at this altitude is one of 16 limb scans used to retrieve the temperature profile shown in panel B. A high quality retrieval should ensure the residual radiances to lie within the range of NESR approximately. The MIPAS-B NESR in (941.29, 946.99) ( $\text{cm}^{-1}$ ) at the tangent altitude of 20 km is about 4 ( $\text{nW}/\text{cm}^2 \text{ sr cm}^{-1}$ ). Most of the residual radiances shown in panel A are less than this value of NESR. Panel C shows the averaging kernels. The large values of responses indicate that the retrieved profile is mainly from the MIPAS-B measured spectra. The vertical resolution, which is the **F**ull **W**idth at **H**alf **M**aximum (FWHM) of the column of the averaging kernel, is given in panel D. At most levels of altitude, the vertical resolution of the retrieved profiles are between 2-3 km and only slightly larger than the 2 km which is the typical vertical resolution delivered by the FOV of MIPAS-B. At the top and the bottom of the profile, the vertical resolution degraded indicating the weak sensitivity of the instrument to the signal changes. The error estimation is shown in panel E. The best retrieved profile, the retrieved profiles when perturbing the retrieval with the spectrum calibration errors, LOS errors, and CO<sub>2</sub> spectroscopic data errors, respectively, are presented on the left side. The errors are exhibited on the right side. Among all the error sources, the CO<sub>2</sub> spectroscopic data error is the dominant one. The second one is the spectrum calibration error. The LOS induced errors increase towards the tropopause. The noise errors are small in the whole altitude range.

## 7.5 Retrieval results for the temperature and each gas

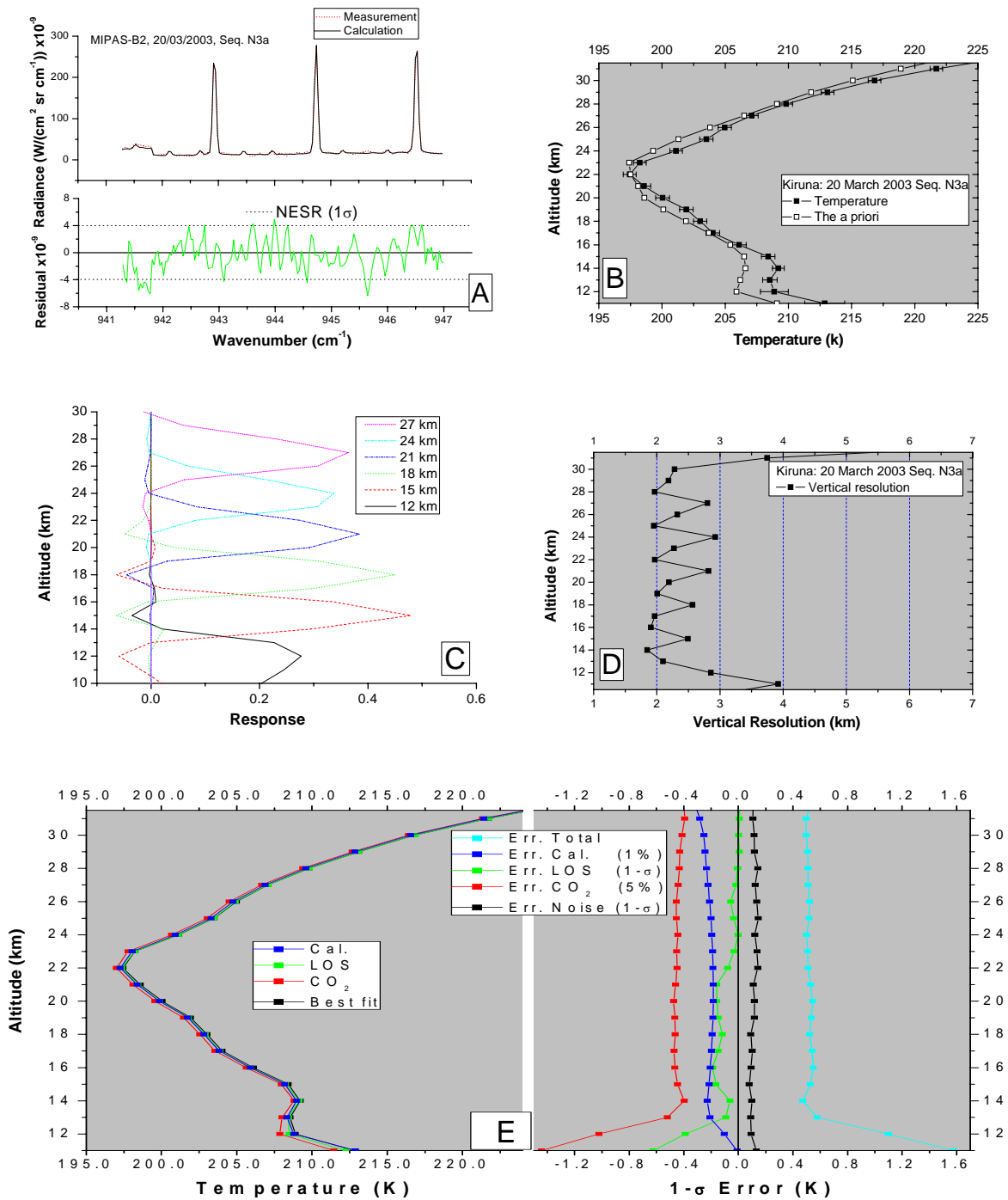


**Figure 7.9:** Typical retrieval of the temperature. A: The upper panel shows the measured spectrum (black line) and the calculated spectrum (red line) for tangent altitude of 20 km. The lower panel shows the differences between these two spectra. B: The retrieved temperature profile and the a priori profile for the retrieval. C: The averaging kernels for some selected levels of altitude. D: The vertical resolutions of MIPAS-B measurements. E: The left panel illustrates the retrieved temperature profiles when considering the spectrum calibration errors, LOS errors, and CO<sub>2</sub> spectroscopic data errors including VMR profile uncertainties, respectively, along with the best fit profile shown in panel B. The right panel exhibits the errors.

The situation of the temperature retrieval for other sequences is similar to what has been described above. For Seq. N3, Seq. W of Flight No. 11 and Seq. D15c of Flight No.13, the measured spectra at lower altitudes were not used for the temperature retrievals because these spectra were contaminated by continuum emission. The altitude boundary of the retrieved

VMRs profiles of gases are determined by the boundary of the retrieved temperature profiles in the same sequence. The altitude ranges of the profiles which were actually deployed for the validation were presented in appendix A.

### 7.5.2 H<sub>2</sub>O

The definition of microwindows for the H<sub>2</sub>O retrieval is as follows: (807.99, 808.62), (824.51, 825.30), (1210.19, 1212.60), (1218.09, 1219.09), (1243.48, 1244.52), (1589.51, 1591.89), (1595.48, 1596.79), (1602.18, 1603.12) (cm<sup>-1</sup>). The lines of H<sub>2</sub>O in these microwindows belong to the  $\nu_2$  band of H<sub>2</sub>O. The strongest lines of H<sub>2</sub>O in the mid infrared are located in the spectral region 1400-1800 cm<sup>-1</sup> whose centre is at 1595 cm<sup>-1</sup>. The weak lines of the H<sub>2</sub>O  $\nu_2$  band appear in the microwindows of (807.99, 808.62) cm<sup>-1</sup> and (824.51, 825.30) cm<sup>-1</sup>. These two microwindows are suitable for the H<sub>2</sub>O retrieval within the upper troposphere. O<sub>3</sub>, CH<sub>4</sub>, N<sub>2</sub>O and NO<sub>2</sub> are the main interfering gases for H<sub>2</sub>O retrieval. Therefore, their VMRs were also included as additional parameters in the H<sub>2</sub>O VMR fit while other VMRs of gases were kept constant.

Figure 7.10 shows the H<sub>2</sub>O retrieval results for Seq. N3a of Flight No. 13. The measured spectra and the fitted spectra as well as the residual spectra in panel A indicate that the fit quality is good at this altitude. The retrieved H<sub>2</sub>O VMR profile and its error bars were presented in panel B. The averaging kernel in panel C shows the large values of responses. Panel D shows that the vertical resolution mainly lies within 2-3 km except at the highest altitude of 31 km and below 12 km. Panel E indicates that the temperature error which is calculated based on 1- $\sigma$  uncertainty dominated the error sources. The spectroscopic data is the second one. Like the temperature retrieval, the LOS induced errors became significant only at lower altitudes and the noise errors are small in the whole altitude range. The situation of the H<sub>2</sub>O retrieval for other sequences is similar to what has been described here.

### 7.5.3 O<sub>3</sub>

The total 34 microwindows for the O<sub>3</sub> retrieval are listed in Table 7.1. These microwindows contain the  $\nu_1$  band of O<sub>3</sub> in the region of 1100-1196 cm<sup>-1</sup>,  $\nu_2$  band covering the spectral interval of 763-825 cm<sup>-1</sup>, and  $\nu_3$  band lines in 964-969 cm<sup>-1</sup> (Flaud, J. -M., *et al.*, 1990). There are weak interferences by H<sub>2</sub>O and CO<sub>2</sub> in the region of O<sub>3</sub>  $\nu_3$  band around 1030-1070 cm<sup>-1</sup>. Weak contributions by CFC-12, N<sub>2</sub>O, H<sub>2</sub>O and CH<sub>4</sub> in the O<sub>3</sub>  $\nu_1$  band are expected in the lower stratosphere but no significant interferences in the middle and upper stratosphere (Echle, G., *et al.*, 1992). The optimized definition of O<sub>3</sub> microwindows reduces these interferences significantly. So the O<sub>3</sub> VMR profile was retrieved by a one-parameter fit. All other VMR profiles of species were kept unchanged during the fit process.

An example of results is shown in Figure 7.11. The residual spectra are near the measurement noise level and the averaging kernel shows a good vertical resolution and therefore the retrieval of O<sub>3</sub> VMR profile is reasonable. The spectroscopic data errors are the major component of the total errors.



### 7.5 Retrieval results for the temperature and each gas

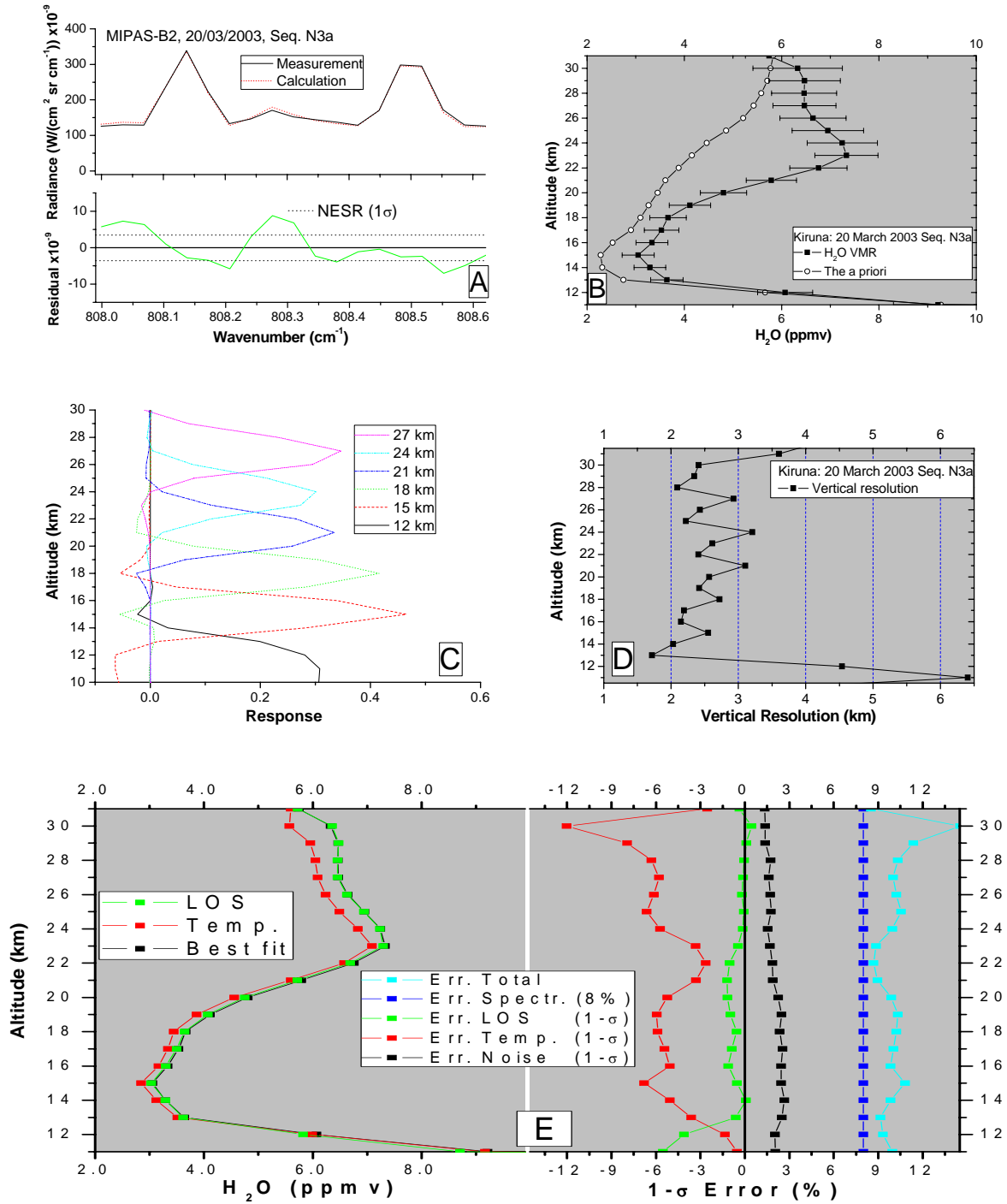


**Figure 7.10:** Typical retrieval of the H<sub>2</sub>O VMR. A: The upper panel shows the measured spectrum (black line) and the calculated spectrum (red line) for tangent altitude of 20 km. The lower panel shows the differences between these two spectra. B: The retrieved H<sub>2</sub>O profile and the a priori profile for the retrieval. C: The averaging kernels for some selected levels of altitude. D: The vertical resolutions of MIPAS-B measurements. E: The left panel illustrates the retrieved H<sub>2</sub>O VMR profiles when considering the temperature errors, and LOS errors, respectively, along with the best fit profile shown in panel B. The right panel exhibits the errors.

## 7. Retrieval of atmospheric parameters from MIPAS-B

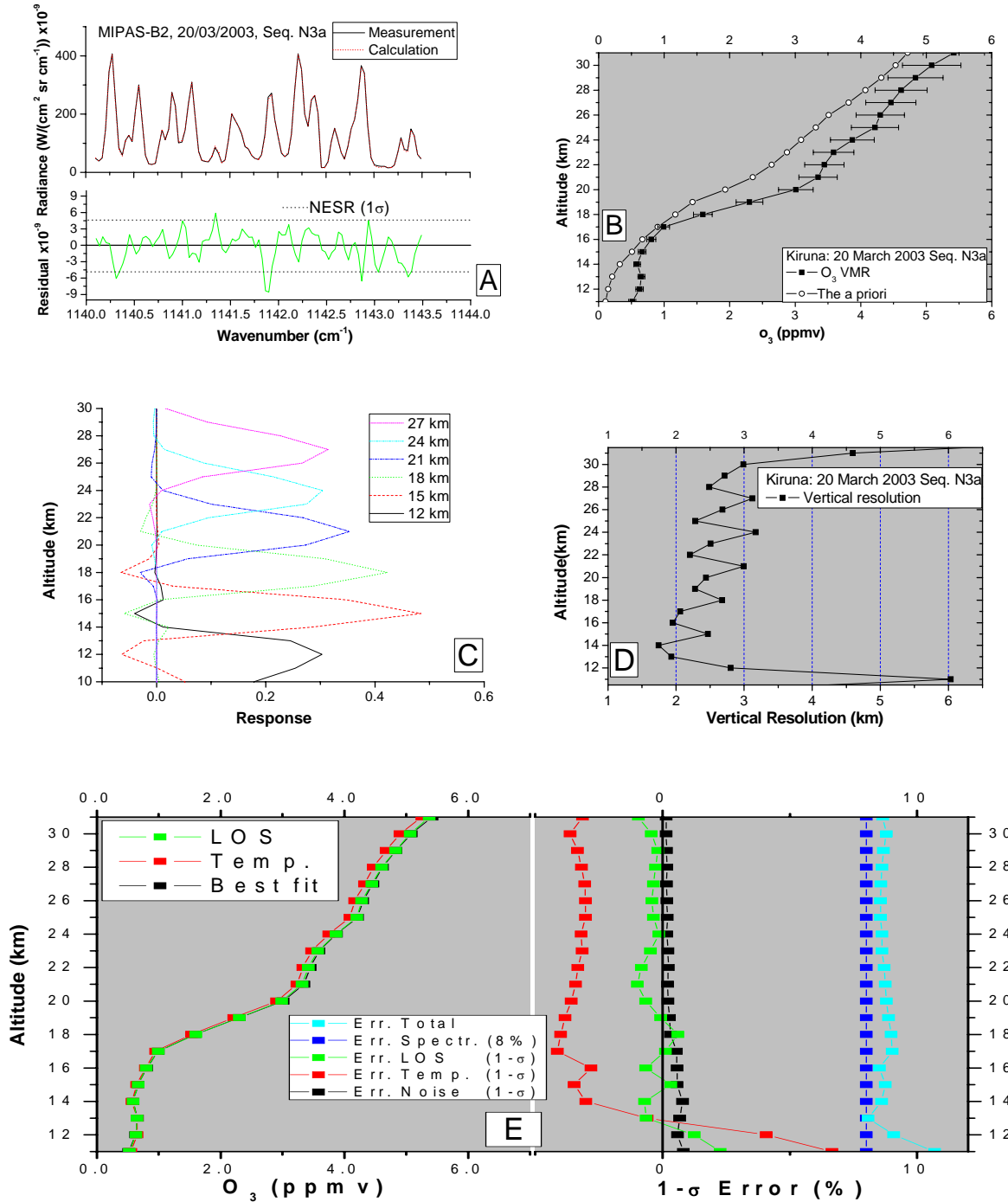


**Figure 7.11:** Typical retrieval of the  $O_3$  VMR. A: The upper panel shows the measured spectrum (black line) and the calculated spectrum (red line) for tangent altitude of 20 km. The lower panel shows the differences between these two spectra. B: The retrieved  $O_3$  profile and the a priori profile for the retrieval. C: The averaging kernels for some selected levels of altitude. D: The vertical resolutions of MIPAS-B measurements. E: The left panel illustrates the retrieved  $O_3$  VMR profiles when considering the temperature errors, and LOS errors, respectively, along with the best fit profile shown in panel B. The right panel exhibits the errors.

#### 7.5.4 HNO<sub>3</sub>

Two relatively broad microwindows, (863.85, 868.75) (cm<sup>-1</sup>) and (868.79, 874.01) (cm<sup>-1</sup>), were employed for the HNO<sub>3</sub> retrieval. These two microwindows lie in the HNO<sub>3</sub> P branch of  $\nu_5$  band located at 868.10 cm<sup>-1</sup>. In these spectral regions, nearly all HNO<sub>3</sub> lines are free from interferences in the lower and middle stratosphere. Above the heights of 40 km, H<sub>2</sub>O, O<sub>3</sub> and CO<sub>2</sub> lines disturb the HNO<sub>3</sub> features. In the troposphere weak interferences are mainly due to OCS and single H<sub>2</sub>O lines. Since MIPAS-B float altitude is less than 40 km, only H<sub>2</sub>O is considered as the interfering gas and was retrieved along with HNO<sub>3</sub> retrieval.

The retrieval quality is satisfactory. The total uncertainty is dominated by spectroscopic errors (Figure 7.12).

Figure 7.13 shows a fit for the HNO<sub>3</sub> VMR retrieval of Seq. 2, Flight No. 14, in the first proven microwindow 863.85-868.75 cm<sup>-1</sup>. Three peaks show up in the residual spectra in the range of 867.82-867.85 cm<sup>-1</sup> from 11 to 20 km. The corresponding levels of altitude are 11 km, 12.5 km and 14 km, respectively. The radiances of these peaks are far beyond the corresponding NESR. In order to avoid the influence of the unknown signature in the measured spectra to the retrieval, the measured spectra in 867.82-867.85 cm<sup>-1</sup> corresponding to 11, 12.5 and 14 km were removed from the proven microwindows by defining a new microwindow 863.85-867.82 cm<sup>-1</sup>. This approach was also adopted in the HNO<sub>3</sub> retrievals for Seq. 3 of Flight No.14.

## 7. Retrieval of atmospheric parameters from MIPAS-B

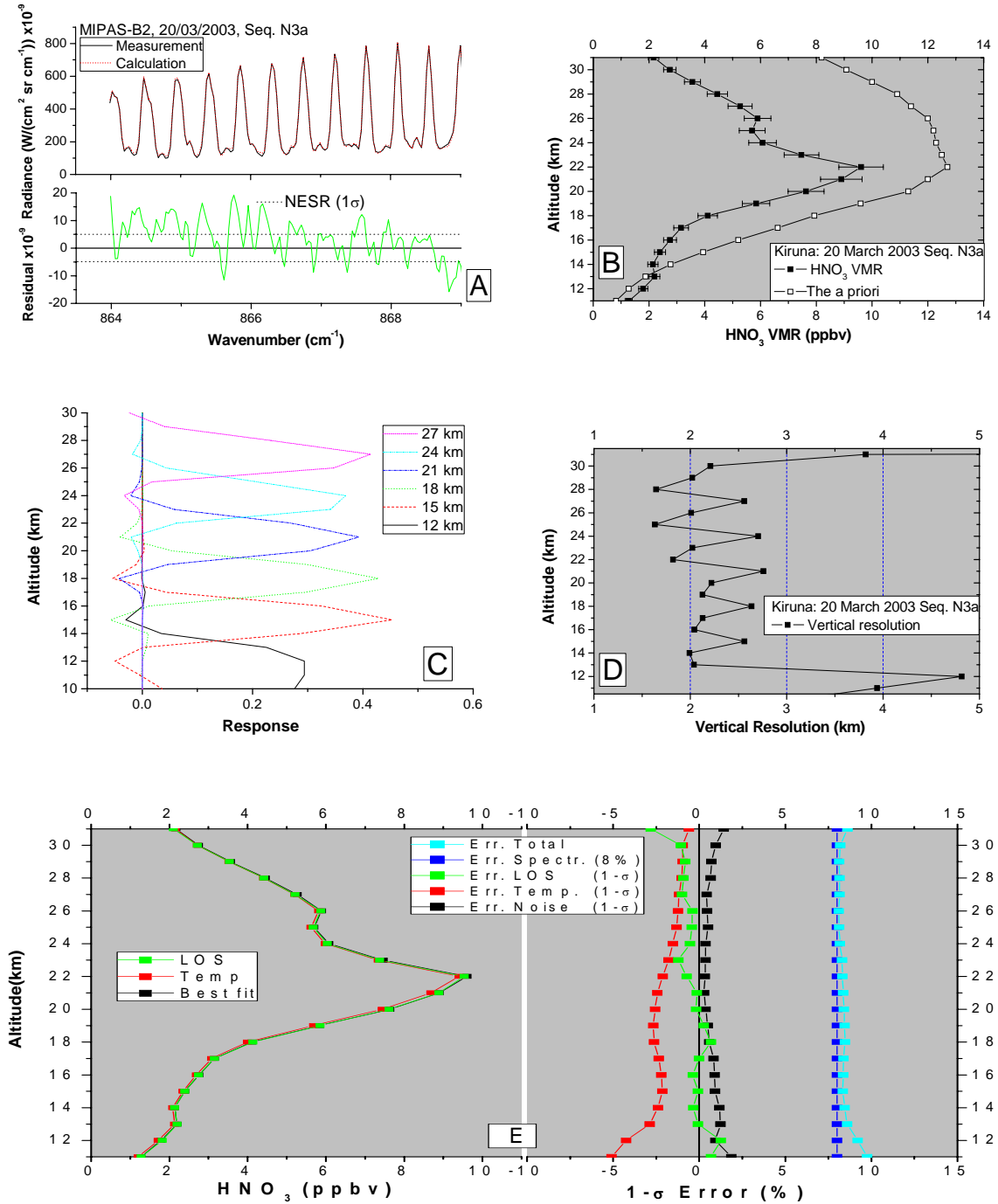


**Figure 7.12:** Typical retrieval of the HNO<sub>3</sub> VMR. A: The upper panel shows the measured spectrum (black line) and the calculated spectrum (red line) for tangent altitude of 20 km. The lower panel shows the differences between these two spectra. B: The retrieved HNO<sub>3</sub> profile and the a priori profile for the retrieval. C: The averaging kernels for some selected levels of altitude. D: The vertical resolutions of MIPAS-B measurements. E: The left panel illustrates the retrieved HNO<sub>3</sub> VMR profiles when considering the temperature errors, and LOS errors, respectively, along with the best fit profile shown in panel B. The right panel exhibits the errors.

## 7.5 Retrieval results for the temperature and each gas

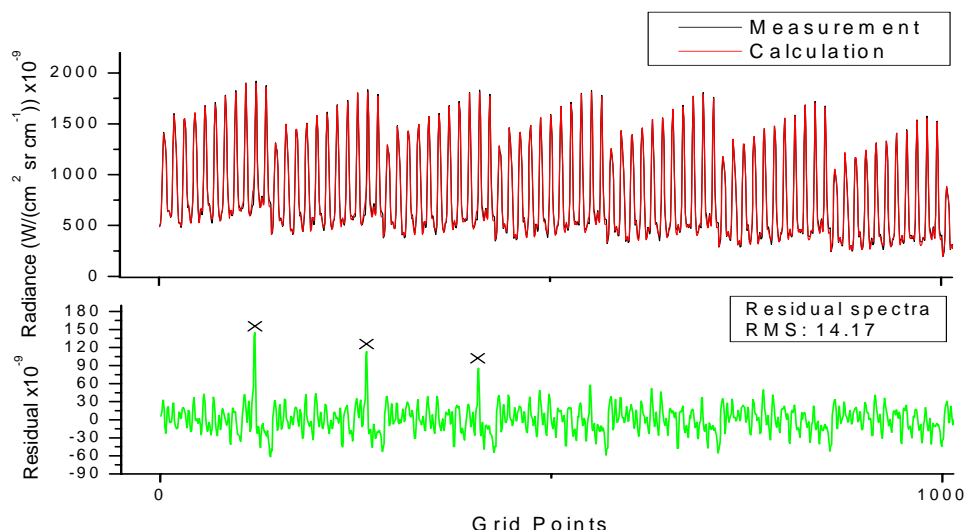


**Figure 7.13:** Part of the spectral fit of HNO<sub>3</sub> proven microwindow (863.85-868.75) (cm<sup>-1</sup>) in the height range of 11-20 km. Three peaks appear (see marks) in the residual spectra at the altitude of 11 km, 12.5 km, and 14 km, respectively.

### 7.5.5 CH<sub>4</sub> and N<sub>2</sub>O

The six microwindows used for CH<sub>4</sub> and N<sub>2</sub>O retrieval are: (1161.93, 1164.94), (1180.41, 1184.00), (1216.09, 1219.99), (1220.48, 1223.52), (1228.49, 1229.80), and (1256.88, 1267.11) (cm<sup>-1</sup>). All lie within the ν<sub>4</sub> band from 1220 cm<sup>-1</sup> to 1350 cm<sup>-1</sup>. CH<sub>4</sub> shows strong features. The spectra in the interval of 1100-1170 cm<sup>-1</sup> contain the P branch of the N<sub>2</sub>O 2ν<sub>2</sub> band. The 2ν<sub>2</sub> band R branch of N<sub>2</sub>O exhibits the strongest features around 1180 cm<sup>-1</sup>. Because CH<sub>4</sub> and N<sub>2</sub>O are interfering gases for each other in the spectral interval defined by the six microwindows, and since these two gases have also a compact relationship, their mixing ratio profiles are retrieved simultaneously in general. The other main interfering gases which were included in the retrieval include H<sub>2</sub>O, O<sub>3</sub>, and N<sub>2</sub>O<sub>5</sub>.

The retrieval results for Seq. N3a of Flight No. 13 are presented in Figure 7.14 and Figure 7.15.

The total errors for both CH<sub>4</sub> and N<sub>2</sub>O are dominated by the temperature error and the spectroscopic data error.

When retrieving the CH<sub>4</sub> and N<sub>2</sub>O VMR profiles for Seq. 3 of Flight No. 14, unreasonable large VMR values for CH<sub>4</sub> at lower altitudes showed up. Figure 7.16 shows the retrieved CH<sub>4</sub> VMR profiles based on individual microwindows. The CH<sub>4</sub> VMR value below the tropopause is about 1.76 ppmv in the year of 2003 (*WMO, 2003*). The microwindows (1216.09, 1219.99), (1220.48, 1223.52) and (1228.49, 1229.80) (cm<sup>-1</sup>) should be responsible for the high bias in the range of 8-12 km. Therefore, an occupation matrix was used in order to avoid using these three microwindows below the 12 km level of altitude.

## 7. Retrieval of atmospheric parameters from MIPAS-B

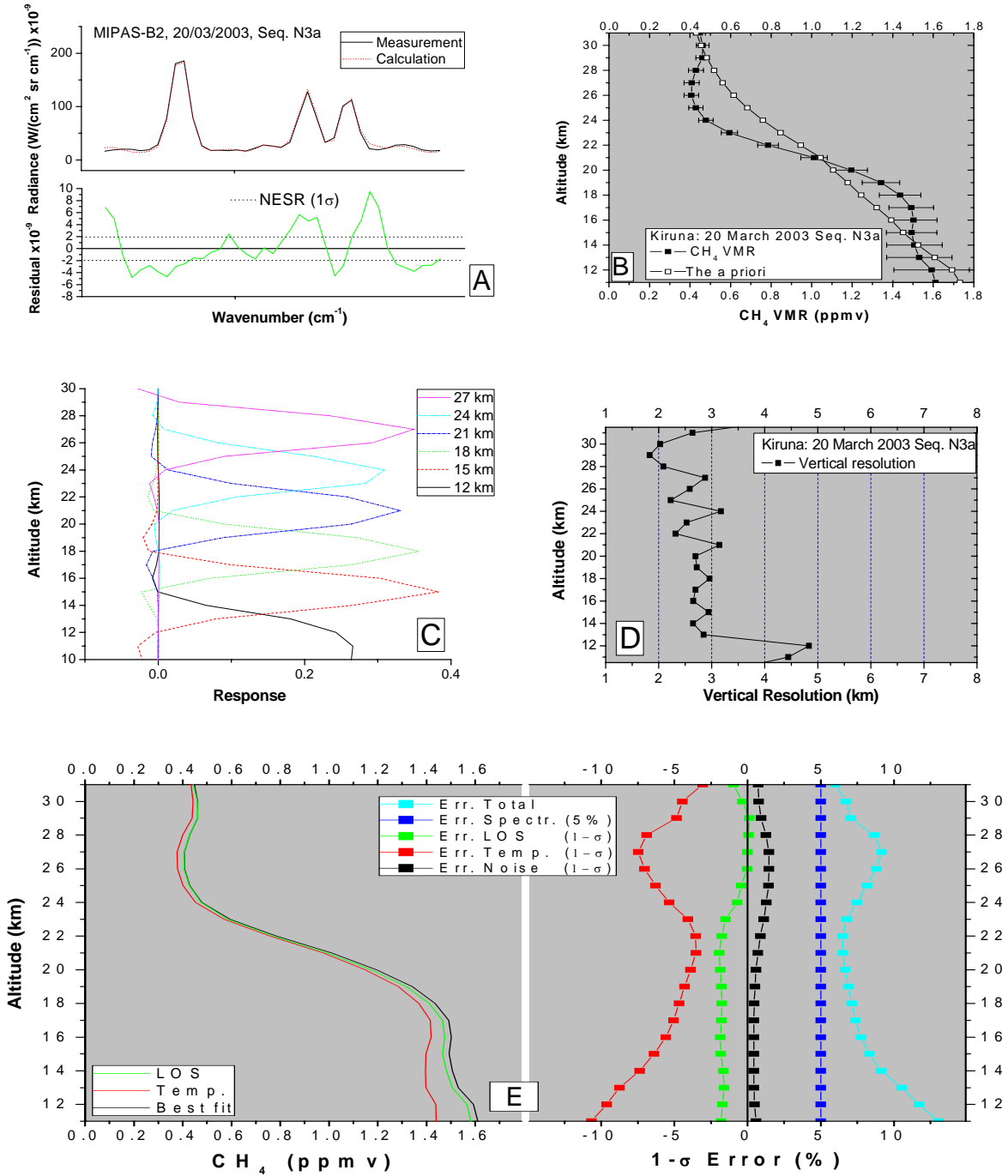


**Figure 7.14:** Typical retrieval of the CH<sub>4</sub> VMR. A: The upper panel shows the measured spectrum (black line) and the calculated spectrum (red line) for tangent altitude of 20 km. The lower panel shows the differences between these two spectra B: The retrieved CH<sub>4</sub> profile and the a priori profile for the retrieval C: The averaging kernels for some selected levels of altitude D: The vertical resolutions of MIPAS-B measurements E: The left panel illustrates the retrieved CH<sub>4</sub> VMR profiles when considering the temperature errors, and LOS errors, respectively, along with the best fit profile shown in panel B. The right panel exhibits the errors.

## 7.5 Retrieval results for the temperature and each gas

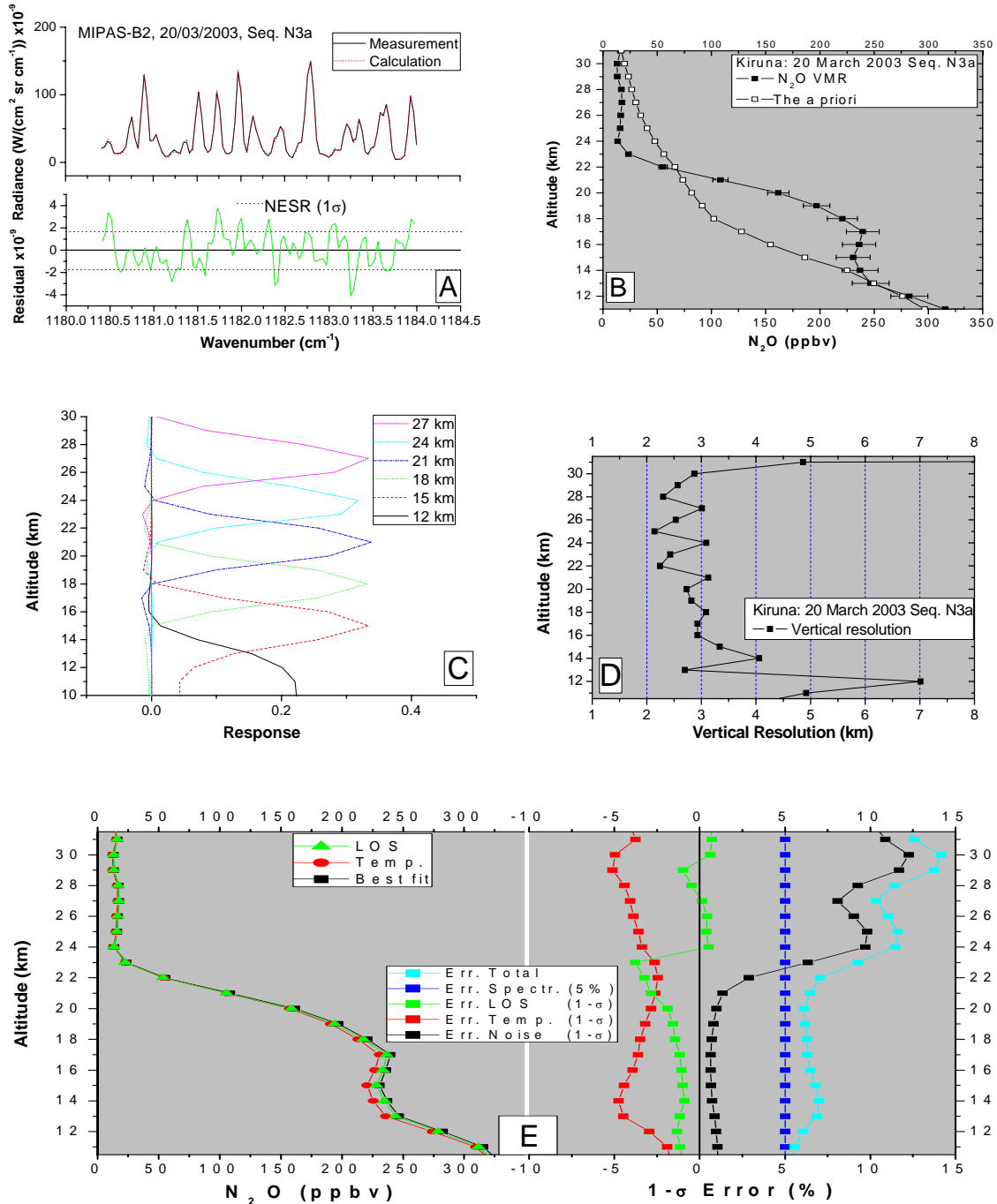


**Figure 7.15:** Typical retrieval of the N<sub>2</sub>O VMR. A: The upper panel shows the measured spectrum (solid line) and the calculated spectrum (dotted line) for tangent altitude of 20 km. The lower panel shows the differences between these two spectra. B: The retrieved N<sub>2</sub>O profile and the a priori profile for the retrieval. C: The averaging kernels for some selected levels of altitude. D: The vertical resolutions of MIPAS-B measurements. E: The left panel illustrates the retrieved N<sub>2</sub>O VMR profiles when considering the temperature errors, and LOS errors, respectively, along with the best fit profile shown in panel B. The right panel exhibits the errors.

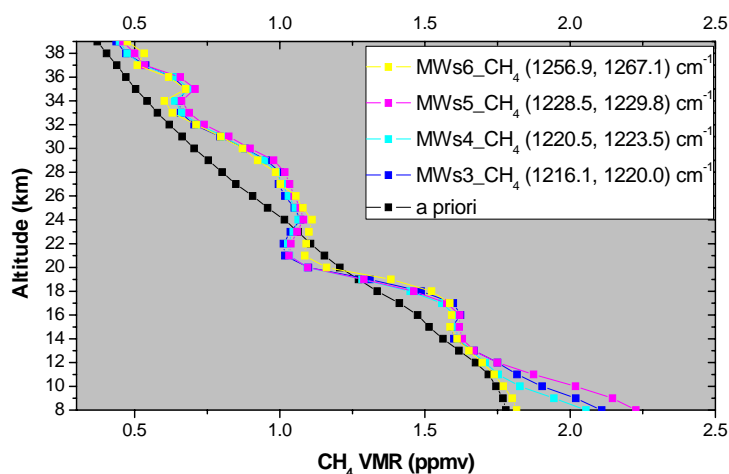


**Figure 7.16:** CH<sub>4</sub> VMR profiles based on individual microwindows. CH<sub>4</sub> VMR values based on Microwindows No. 3, No. 4 and No. 5, respectively are abnormally high at low altitude levels.

### 7.5.6 NO<sub>2</sub>

For the NO<sub>2</sub> retrieval, the microwindows are: (1585.02, 1589.51), (1591.89, 1593.72), (1596.48, 1601.11), (1601.49, 1602.53), (1604.01, 1606.60), (1607.61, 1609.19), and (1610.29, 1614.99) (cm<sup>-1</sup>). This region of spectral frequency between 1585 -1615 cm<sup>-1</sup> belongs to the NO<sub>2</sub> P branch of the  $\nu_3$  band whose centre is located at 1615 cm<sup>-1</sup>. The interferences are mainly from the H<sub>2</sub>O and CH<sub>4</sub> (Echle, G., et al., 1992). However, the microwindows defined here reduce their influence to the NO<sub>2</sub> retrieval. So, only one-parameter fit was performed. Other gases concentration remained unchanged during the retrieval process.

The retrieval results for Seq. N3a of Flight No. 13 are plotted in Figure 7.17. The residual spectra, the averaging kernel and the vertical resolution indicate that the retrieved profile quality was ensured. The temperature and the spectroscopic data uncertainty are the dominant error sources. At lower altitudes, the noise errors, temperature errors, LOS errors as well as the H<sub>2</sub>O errors are extremely large. The reason is that the concentration of NO<sub>2</sub> at lower altitudes is very small and the averaging kernels are ill conditioned. The retrieved profile at these altitudes even gave small negative values. These negative values were not used during the validation process.

In some cases, the continuum effects lead to a deteriorating of fit quality at lower altitudes. The occupation matrix then has to be adopted. The information for which retrieval an occupation matrix has been used is given in Appendix A.

The MIPAS-B retrieved data for validation were listed on the tables which were contained in the Appendix A after all unreasonable data have been filtered out.



### 7.5 Retrieval results for the temperature and each gas

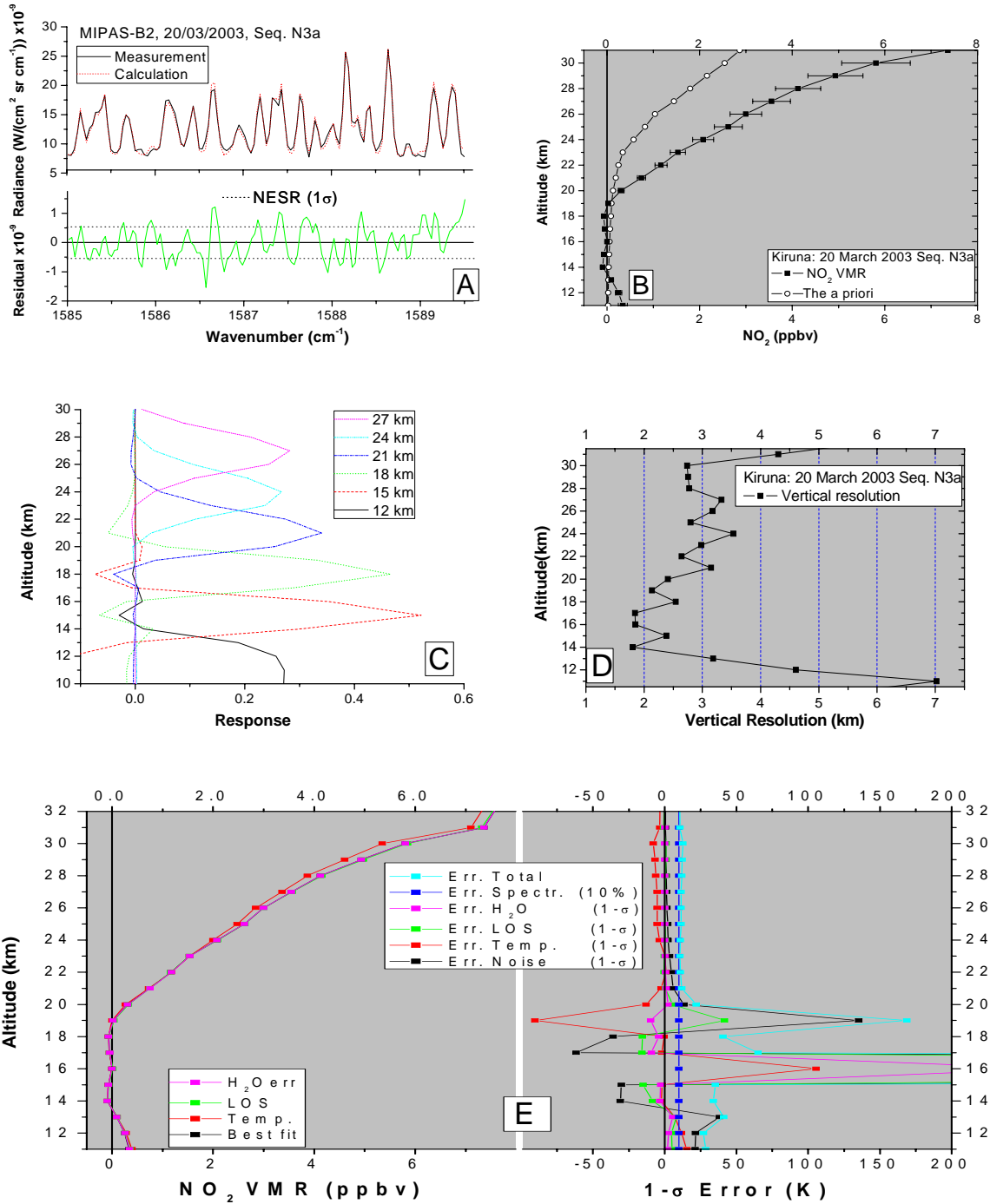


**Figure 7.17:** Typical retrieval of the NO<sub>2</sub> VMR. A: The upper panel shows the measured spectrum (black line) and the calculated spectrum (red line) for tangent altitude of 20 km. The lower panel shows the differences between these two spectra. B: The retrieved NO<sub>2</sub> profile and the a priori for the retrieval. C: The averaging kernels for some selected levels of altitude. D: The vertical resolutions of MIPAS-B measurements. E: The left panel illustrates the retrieved NO<sub>2</sub> VMR profiles when considering the temperature errors, LOS errors, and H<sub>2</sub>O errors, respectively, along with the best fit profile shown in panel B. The right panel exhibits the errors.

## Intercomparison of measurements

Based on the MIPAS-B measurements which have been described in Chapter 7, the validations for MIPAS-E, SCIAMACHY and GOMOS were performed, respectively. To avoid the influence of the errors in the MIPAS-E altitude registration, the validation for MIPAS-E is carried out in pressure coordinates. For SCIAMACHY and GOMOS validation, the altitude coordinate system was adopted.

### 8.1 General

#### 8.1.1 Diagnostics of match quality

For the coincident comparison, the spatial and temporal offsets between different instruments measurements are crucial for validation. Figure 7.1, 7.2 and 7.3 show the scan locations at one specific altitude level for MIPAS-B and MIPAS-E. Table 8.1 gives the mean time and tangent location of MIPAS-B and MIPAS-E observations. However, they are not enough for understanding the match quality since the match quality depends on the altitude levels. Further detailed analysis for the time and space offset is given in this section.

**Table 8.1: Mean time and geolocation of the coincident observations.**

MIPAS-B	Flight No. 11		Flight No. 13		Flight No. 14
Location	Aire sur l'Adour (France)		Kiruna (Sweden)		Kiruna (Sweden)
Date	24 SEP. 2002	24 SEP. 2002	20 MAR. 2003	21 MAR. 2003	03 JUL. 2003
Sequence name	Seq. S	Seq. N3	Seq. N3a	Seq. D15c	Seq. 3
Mean time	21:50 UT	22:21 UT	20:56 UT	08:48 UT	01:13 UT
Mean latitude	39.9°N	47.0°N	65.8°N	65.6°N	69.3°N
Mean longitude	1.1°E	0.7°E	14.6°E	17.5°E	11.0°E
Altitude range	11.3-38.8 km	5.9 - 38.4 km	11.1-31.1 km	9.1-31.2 km	7.9-39.1 km
MIPAS-E (V4.61)	Orbit 2975	Orbit 2975	Orbit 5508	Orbit 5515	Orbit 7004
Sequence name	Rec. 15 & Rec.14	Rec.16	Rec.20	Rec.30	Rec.06
Mean time	22:06 & 22:05 UT	22:07 UT	21:10 UT	09:08 UT	09:39 UT
Mean latitude	41.3°N & 36.6°N	46.0°N,	65.7°N	65.7°N	70.5°N
Mean longitude	1.6°E & 2.6°E	0.7°E	14.1°E	17.0°E	10.9°E

#### 1. Flight No. 11

Figure 8.1.1-1 consists of two panels. The tangent point distances between MIPAS-B and MIPAS-E line-of-sight (LOS) are plotted in Panel A. The curves show that the offset of most of the tangent locations between Seq. N3 and Rec. 16 are within 150 km. This is a very good co-location observation. The distances of the tangents points between Seq. S and MIPAS-E Rec. 14 as well as Seq. S and Rec. 15 indicate that below about 24 km the MIPAS-B measurements of Seq. S should compare better with the measurements of Rec. 14 while above

this level with Rec. 15. The potential vorticity is a good indicator for match quality of observations when the polar vortex exists, because the temperature and the VMRs of gases are distributed homogeneously within the same potential vorticity plane. The colour coded potential vorticity in Figure 7.1 shows that there is a developing polar vortex with the edge at about 45°N latitude. The potential vorticity differences of tangent locations between MIPAS-B and MIPAS-E were plotted in Panel B. It can be expected that the small differences of potential vorticity between the tangent locations of Seq. N3 and Seq. 16 (the curve with down solid triangle) imply that the spatial offset would have little influences to the comparison result. The other two curves in Panel B represent the potential vorticity differences of tangent locations between Seq. S and Rec. 14 (open up triangle) as well as Seq. S and Rec. 15 (solid up triangle), respectively. These two curves show that below about 24 km the Seq. S compares with Rec. 14 while above this level a comparison with Rec. 15 can reduce the geolocation mismatch influence to the validation results. So finally, the pair measurements to be compared with are: Seq. N3 to Rec. 16, below 24 km, Seq. S to Rec. 14; and above 24 km, Seq. S to Rec. 15.

The mean time differences between Seq. N3 and Rec. 16, Seq. S and Rec.15 (or Rec. 14) are 15 minutes and 17 minutes, respectively. The MIPAS-B scan time for one sequence is about 10 minutes and for MIPAS-E less than 1 minute. So the maximum time difference between MIPAS-B and MIPAS-E measurements is within half an hour. The influences of chemistry changes of gases and the air mass movements driven by the wind field within half an hour to the validation is expected to be small. For the NO<sub>2</sub> species, its VMR during the sunset and sunrise period can change significantly even within tens of minutes. However, this case did not happen during Flight No. 11.

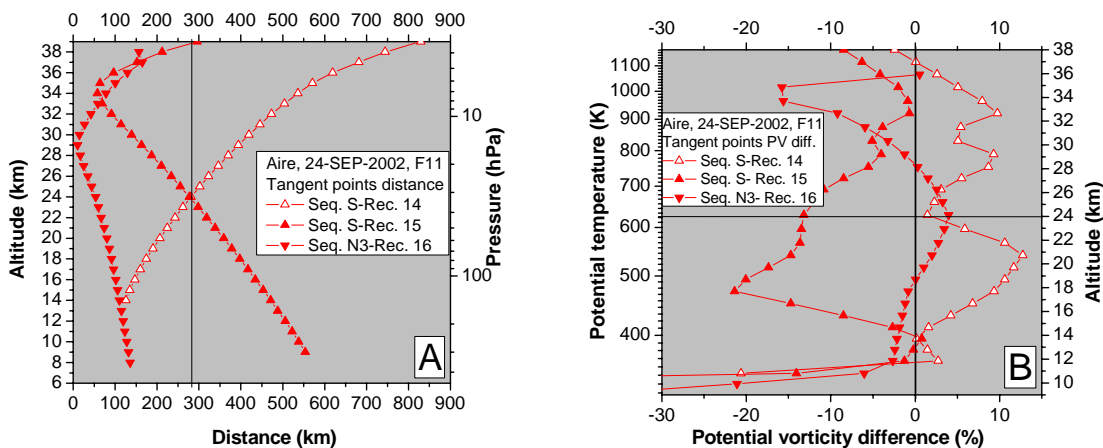


**Figure 8.1.1-1:** (A) The tangent point distances between MIPAS-B Seq. S and MIPAS-E Rec. 14 ( $\Delta$ ), Seq. S and Rec. 15 ( $\blacktriangle$ ) as well as Seq. N3 and Rec. 16 ( $\blacktriangledown$ ). (B) The potential vorticity differences between MIPAS-B and MIPAS-E LOS tangent points. The symbols in each curve have the same meanings as in (A).

## 2. Flight No. 13

The two panels in Figure 8.1.1-2 depict the match quality in space. The maximum distance offset is 330 km (see Panel A). The color code potential vorticity field in Figure 7.2 indicates that not all MIPAS-B measurements and the MIPAS-E orbit 5508 Rec. 20, orbit 5515 Rec. 30 are performed inside the winter polar vortex. Panel B shows that the PV difference of tangent locations between MIPAS-B and MIPAS-E starts to increase with altitude from about 22 km. Therefore, it can be expected that above the 22 km level the mismatch of measurement will deteriorate the comparison result between Seq. N3a and Rec. 20. In order to reduce the spatial

## 8. Intercomparison of measurements

offset influences to the comparison, the part of the comparison results between MIPAS-E Rec. 20 and MIPAS-B Seq. N3a whose corresponding tangent points PV differences are larger than 15% were not taken into account in the final conclusions.

The tangent point distances between Seq. D15c and Rec. 30 were plotted in Panel A (the curve with solid circle symbols). All the distances are less than 200 km. From 20 to 29 km, the tangent locations distances are within 30 km. So this is a perfect co-location measurement except in the range of 29-31 km. This conclusion was also supported by the PV difference curve which plotted is in Panel B (the curve with solid circle symbols).

The mean time differences between Seq. N3a and Rec. 20, Seq. D15c and Rec.30 are only 14 minutes and 20 minutes, respectively. According to the causes mentioned before, the influences of time offsets to the validation need not to be considered in these cases.

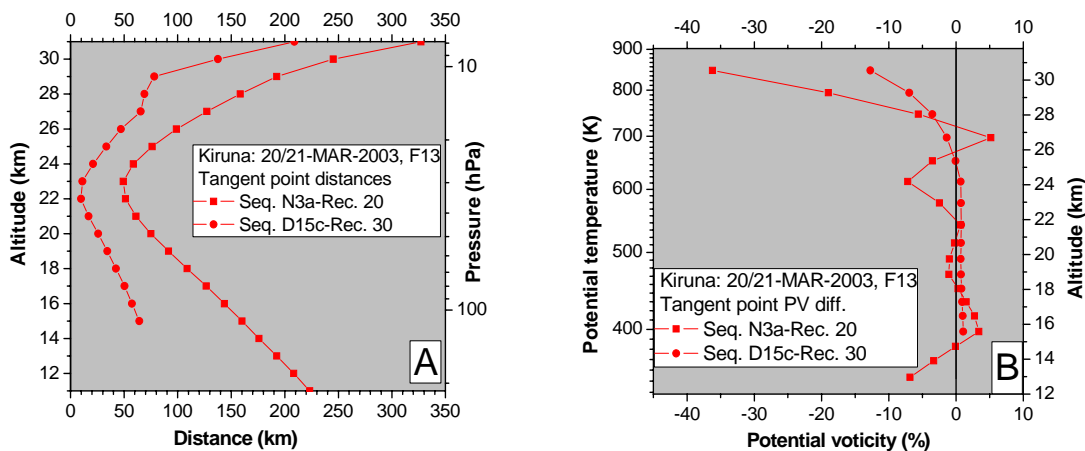


**Figure 8.1.1-2:** (A) The tangent point distances between MIPAS-B Seq. N3a and MIPAS-E Rec. 20 (■), Seq. D15c and Rec. 30 (●). (B) The potential vorticity differences between MIPAS-B LOS tangent points and MIPAS-E LOS tangent points.

### 3. Flight No. 14

The curve in Figure 8.1.1-3 depicts the tangent geolocations distances between Seq. 3 and Rec. 06. It shows that above about 32 km altitude, the offsets increase rapidly with increasing altitude. Between 8 and 32 km, the tangent locations distances are less than 230 km. The PV gradients are small during this summer time flight and can be neglected.

The high match quality for Flight No. 14 was prevented mainly from the large time offset of about 8.5 hours. However, through the analysis of the wind field (see Figure 7.3), the actual match quality is better than it looks in Figure 8.1.1-3. However, the large time offset makes it impossible to compare MIPAS-B and MIPAS-E measurements directly for the  $\text{NO}_2$  species.

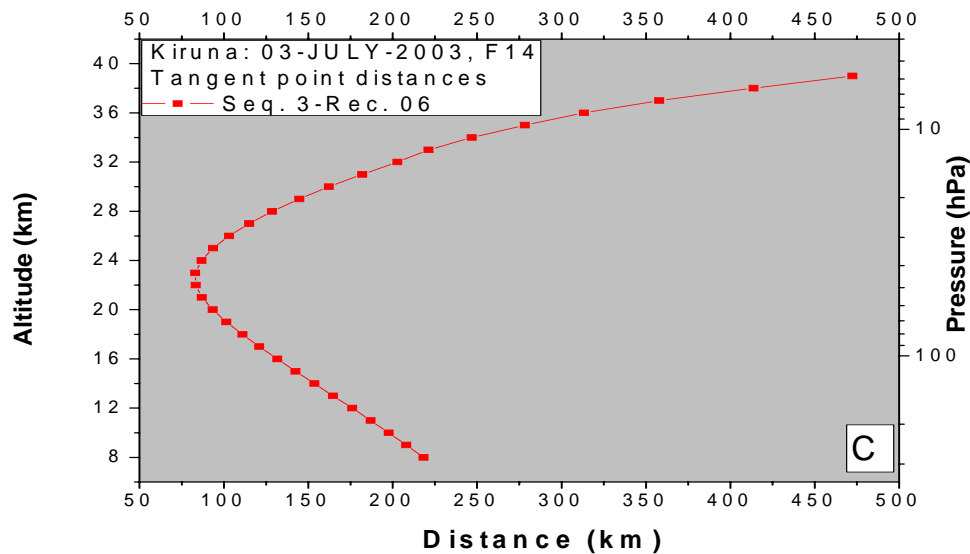


Figure 8.1.1-3: The tangent point distances between Seq. 3 and Rec. 06.

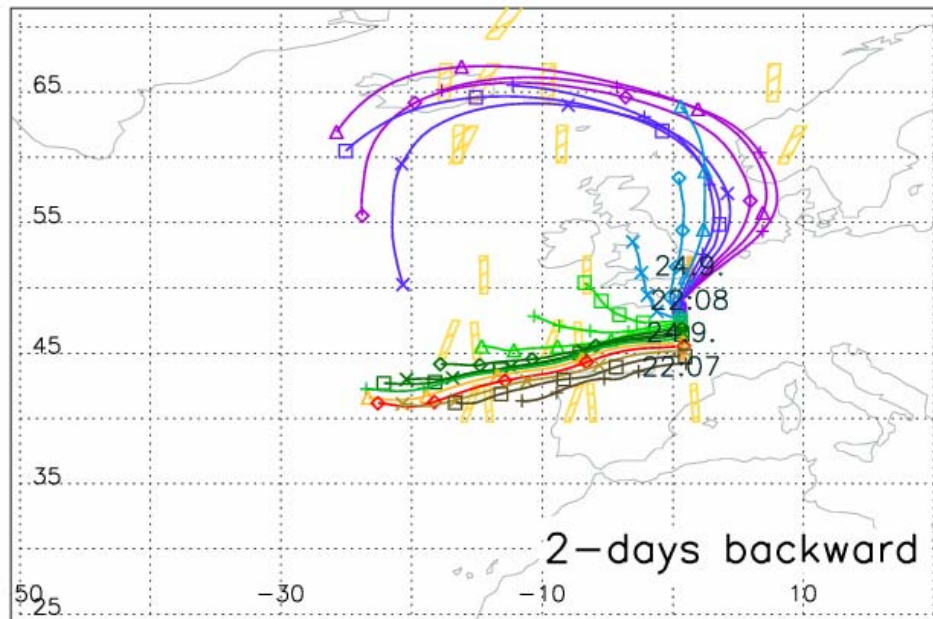
### 8.1.2 Trajectory model

In order to increase the opportunity of using MIPAS-B data and enhance the statistics of the validation, the trajectory model (*Reimer, E., et al., 1997*) approach was adopted. The trajectory model is using the operational ECMWF data every 6 hours on a  $2.5^{\circ} \times 2.5^{\circ}$  latitude/longitude grid, analyses as well as forecasts or a combination of both. Forward and backward air mass trajectories are calculated on isentropic levels from the surface up to 1600 K with interpolation between the levels. The internal time step is 10 minutes and the diabatic, climatological heating rates considered as based on Newtonian cooling. The altitude of the start point can be given as potential temperature, pressure, height above surface or height above sea level. The air mass trajectories can be calculated utmost to eight days limited by ECMWF forecast. Here, only two days forward and backward trajectories are calculated for restricting the uncertainties that are introduced by the model itself (*Grunow, K., 2005*).



The starting points of the air mass trajectories for the validation depend on latitude, longitude and the time of the air masses scanned by MIPAS-B. As an example, Figure 8.1.2-1 exhibits the two days backward air mass trajectories whose start points are (44.2-48.9 °N, 0.5-1.0 °E, 2002-SEP-24 22:10-22:40 UT). These points had been scanned by MIPAS-B Seq. N3 during Flight No.11. The match criteria used here is 1 hour and 500 km. The approach to find the match locations is like the trajectory hunting technique (THT) which was mentioned in Chapter 3. That is, firstly, a ‘target’ profile of MIPAS-E was found if the temporal-spatial distance between the center of the profile and a point A of the trajectory of the air mass measured by MIPAS-B is not larger than (1 hour, 500 km). Secondly, a ‘match point’ which has the same altitude level as the point A was located in the ‘target’ profile.

## 8. Intercomparison of measurements






















MIPAS-B northern scan, flight on 24.09.02  
 2-days backward trajectories  
 file: MN020924.C2B, matches with MIPAS: 1 h, 500 km  
 Orbit: 2946, 2947, 2953, 2954, 2961, 2968, 2975



MIPAS: area of tangent points, match with

	less than 50 percent of air mass trajectories		more than 50 percent of air mass trajectories
---	---	---	---

trajectories: start time and altitude

	24.09.02 22:10 UT	5.9 km		24.09.02 22:20 UT	23.4 km
	24.09.02 22:10 UT	8.3 km		24.09.02 22:20 UT	24.9 km
	24.09.02 22:10 UT	9.8 km		24.09.02 22:20 UT	26.4 km
	24.09.02 22:10 UT	11.3 km		24.09.02 22:20 UT	27.9 km
	24.09.02 22:20 UT	12.8 km		24.09.02 22:30 UT	29.4 km
	24.09.02 22:20 UT	14.3 km		24.09.02 22:30 UT	30.8 km
	24.09.02 22:20 UT	15.8 km		24.09.02 22:30 UT	32.4 km
	24.09.02 22:20 UT	17.3 km		24.09.02 22:30 UT	33.9 km
	24.09.02 22:20 UT	18.9 km		24.09.02 22:40 UT	35.4 km
	24.09.02 22:20 UT	20.3 km		24.09.02 22:40 UT	37.0 km
	24.09.02 22:20 UT	21.8 km			

planned MIPAS geolocations from ESA overpass tables  
 trajectories calculated on 20041028, matches on 20041110, FU Berlin

**Figure 8.1.2-1:** 2-days backward trajectories of air masses that had been scanned by MIPAS-B Seq. N3 during Flight 11. The lines with different color represent the air masses start from Aire sur l'Adour (France 44°N, 0°E) at different levels of altitude. The bars with yellow color represent the tangent locations of MIPAS-E sequences (Grunow, K. 2005).



## 8.2 MIPAS

### 8.2.1 Temperature

#### 1 Coincident comparison for temperature

##### 1.1 Flight No. 11

The temperature comparisons between MIPAS-E and MIPAS-B for Flight No.11 are presented in Panel A and B of Figure 8.2.1-1. For conciseness, we always use black curves to represent MIPAS-B profiles and red curves to represent MIPAS-E profiles. In order to calculate the absolute differences of MIPAS-B minus MIPAS-E measurements, MIPAS-E profiles were interpolated onto MIPAS-B pressure levels in a logarithmic way. Two kinds of combined errors of MIPAS-B and MIPAS-E measurements were plotted in Figure 8.2.1-1. The open circles represent the combined precision errors of MIPAS-B precision errors (without the spectroscopic errors) and MIPAS-E noise errors. The spectroscopic errors were excluded because spectroscopic data contribution to the errors of MIPAS-B and MIPAS-E is similar. These combined errors address the precision boundary of the comparisons. The solid circles represent the combined errors of the total errors of the two instruments including the spectroscopic data errors. This kind of combined error characterizes the accuracy boundary of the comparisons. The equation for the combined errors calculation is

$$\sigma_c = \sqrt{\sigma_B^2 + \sigma_E^2}, \quad (8.1)$$

where  $B$  and  $E$  denote MIPAS-B and MIPAS-E, respectively.

The MIPAS-E temperature profiles of Rec. 14 and Rec. 15 as well as the MIPAS-B temperature profile of Seq. S are plotted in Panel A. The profile of Rec. 15 is more close to the MIPAS-B profile than the profile of Rec. 14 above the altitude of about 30 hPa (24 km) in general. Below this level, MIPAS-B profile matches the profile of Rec.14 perfectly but bias Rec.15 gradually. This is because of the spatial mismatch of the measurements that have been analyzed previously.

In addition to the MIPAS-B versus MIPAS-E comparison, data from ECMWF are displayed. ECMWF (European Center of Medium range Weather Forecast) provides data four times a day at 00, 06, 12 and 24 UT. The horizontal resolution is  $1.125^\circ \times 1.125^\circ$  at 28 pressure levels in the range of 0.1-1013.25 hPa. Two ECMWF profiles are shown in Panel A. The two ECMWF profiles were obtained by interpolating ECMWF data onto MIPAS-E (pink) and MIPAS-B (blue) tangent locations and their measurements time, respectively. Obviously ECMWF measurements are consistent with MIPAS-B and MIPAS-E measurements at the lower levels of altitude but systematically colder at higher levels. This could be explained by a bias in the ECMWF analyses (*Simmons, A., et al., 2005*). Above 30 km, the ECMWF model biases become larger due to missing radiosonde data assimilated into the model. The ECMWF data stood out as the coldest of all data sets between 30 and 45 km in a SPARC (Stratospheric Processes And their Role in Climate) comparison of climatologies (*Randel, W., et al., 2002*).

## 8. Intercomparison of measurements

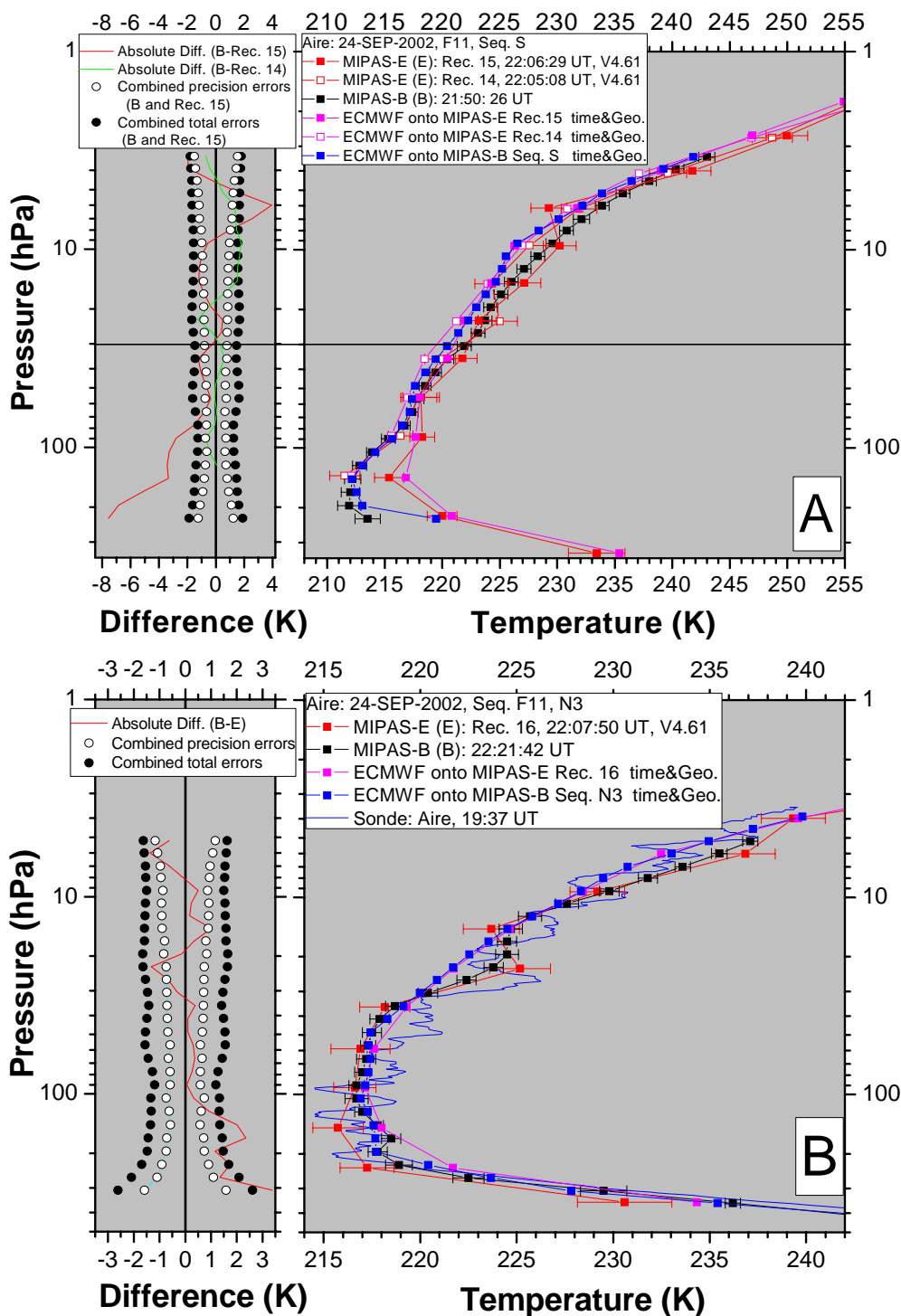


**Figure 8.2.1-1:** Temperature comparisons for Flight No. 11. MIPAS-B profiles, black curves with black square symbols, the error bars represent the total errors; MIPAS-E profiles, red curves with red square symbols, the error bars represent the total errors; ECMWF profiles interpolated onto MIPAS-B tangent locations and measurements time, blue curves with blue square symbols; ECMWF profiles interpolated onto MIPAS-E tangent locations and measurements time, pink curves with pink square symbols; radiosonde profile, solid blue line; the absolute differences of MIPAS-B minus MIPAS-E, solid red line or solid green line; combined precision errors (the combination of MIPAS-E noise error and MIPAS-B errors which includes the noise, LOS, spectrum calibration and CO<sub>2</sub> data errors), open circles; the combined total errors, solid circles. (A) Comparisons between Seq. S and Rec. 14, Seq. S and Rec. 15. Both kind of combined errors are calculated from the Seq. S and Rec. 15 data. When using Rec. 14 data, the combined errors are almost the same. The straight line in Panel A denotes that below this level of altitude Seq. S should compare with Rec. 14 and above to Rec. 15. (B) Comparison between Seq. N3 and Rec. 16.



The MIPAS-E temperature profile of Rec. 16 almost covers the MIPAS-B profile of Seq. N3 perfectly except in the range of 227.9-122.6 hPa (11-15 km) (Panel B of Figure 8.2.1-1). The radiosonde profile (solid blue line), which was measured about 4.5 hours ahead of MIPAS-B Seq. N3 measurements, and the ECMWF profile both are consistent with MIPAS-B profile and are higher than MIPAS-E measurements in the range of 227.9-122.6 hPa. So it seems that MIPAS-E measurements tend to be low in this altitude range. The ECMWF temperature field (see panel A and B in Appendix C) shows that in 11-15 km the temperature gradients are significant. Therefore the influences of the spatial offset to the comparison between MIPAS-B and MIPAS-E are not negligible in this region.

### 1.2 Flight No. 13

Two pair comparisons, Seq. N3a to Rec. 20 and Seq. 15c to Rec. 30, are available for Flight No. 13 (Figure 8.2.1-2). In Panel A, the radiosonde profile is close to Seq. N3a except at the lower altitudes. The agreements among MIPAS-B, MIPAS-E and ECMWF profiles are good except in the range of 34-14 hPa (22-27 km). The ECMWF temperature field (see panel D in Appendix C) indicates that the temperature changed rapidly along the longitude direction. Even though the distances between MIPAS-B and MIPAS-E scan sites are not very large in this range of altitude, the large temperature gradients still can evoke different measurement results to different instruments. The PV differences shown in Panel B of Figure 8.1.1-2 are significant since the edge of the winter polar vortex was located in the observation region. This also implies that the comparison between MIPAS-B and MIPAS-E observations may be impacted by the spatial mismatch. From the measurement geometry depicted in Figure 7.2, the reason leading to the discrepancy is as follows. The scan sequence of MIPAS-E is from high altitude to low altitude. In Figure 7.2, the flight direction of ENVISAT is from the south to north during the period for Rec. 20 recording. Therefore, the temperatures in 22-27 km measured by MIPAS-E lie in the edge of the polar vortex. While the temperatures measured by MIPAS-B in this height region are inside the polar vortex (near the thick end of the black line of Seq. N3a). At the lower altitudes, both instruments measured the temperature in the region near the edge of the polar vortex. So it can be inferred that the discrepancy between MIPAS-B and MIPAS-E profiles are mainly due to the different air masses sounded by the two instruments. To deduce the actual differences of the two measurements, a correction to the original MIPAS-B profile was performed. The corrected MIPAS-B value is:

$$x(z)_c = \frac{x(z)_B}{r(z)}, \quad (8.2)$$

where

$$r(z) = \frac{x(z)_{ecmwfB}}{x(z)_{ecmwfE}}, \quad (8.3)$$

$x(z)_B$  denotes MIPAS-B measured temperature at altitude  $z$ .  $x(z)_{ecmwfB}$  and  $x(z)_{ecmwfE}$  denote the ECMWF values interpolated onto MIPAS-B and MIPAS-E tangent locations and measurement time, respectively. The differences (solid green line) between the corrected MIPAS-B profile and the MIPAS-E profile show that the discrepancy is reduced by 1 K on average (Figure 8.2.1-2 Panel A). However, the bias is still very large. Around 21 hPa, the maximum reaches about 4 K. It seems that the influences of the spatial offset were not completely eliminated due to the relatively large temporal and spatial resolution of ECMWF assimilated data. Another possible reason which led to the large bias is that the horizontal gradient of temperature in the MIPAS-E retrieval was not adopted.

## 8. Intercomparison of measurements

As already shown during the previous description in section 8.2.1, the match quality between Seq. D15c and Rec. 30 was excellent. It can be expected that the difference profile of MIPAS-B minus MIPAS-E almost really reflects the performances of the two instruments for this situation. Above the altitude of 29 hPa (23 km), MIPAS-B and MIPAS-E agree well with respect to their total combined errors (Figure 8.2.1-2 Panel B). Between 29-48 hPa (20-23 km), the small structure appearing in the MIPAS-B profile was not represented in the MIPAS-E profile partly because of the relative low vertical resolution of MIPAS-E and the coarse vertical grid of representation. Below the altitude of 60 hPa (19 km), MIPAS-E data are significantly higher than MIPAS-B measurements. The difference between the radiosonde and the ECMWF profiles at the lower altitudes imply that the meteorological situation is complicated in this region. One possible reason that led to the discrepancy in the low altitude region is the aerosol continuum effects to the MIPAS-B and MIPAS-E retrievals. During the retrieval of MIPAS-B profile, the measured spectra below the altitude of 131 hPa (14 km) have been excluded due to the strong continuum in the spectra. The profile (not shown here) of MIPAS-E retrieved by version 4.57 processor was reaching down to 183 hPa (12 km). When comparing it with the MIPAS-B profile, a very large bias was exhibited in the region of 183 to 15 hPa (12-27 km). When using the V4.61 processor, the lowest boundary of the retrieved profile is only at 120 hPa (15 km) and the discrepancies between MIPAS-B and MIPAS-E have decreased significantly.

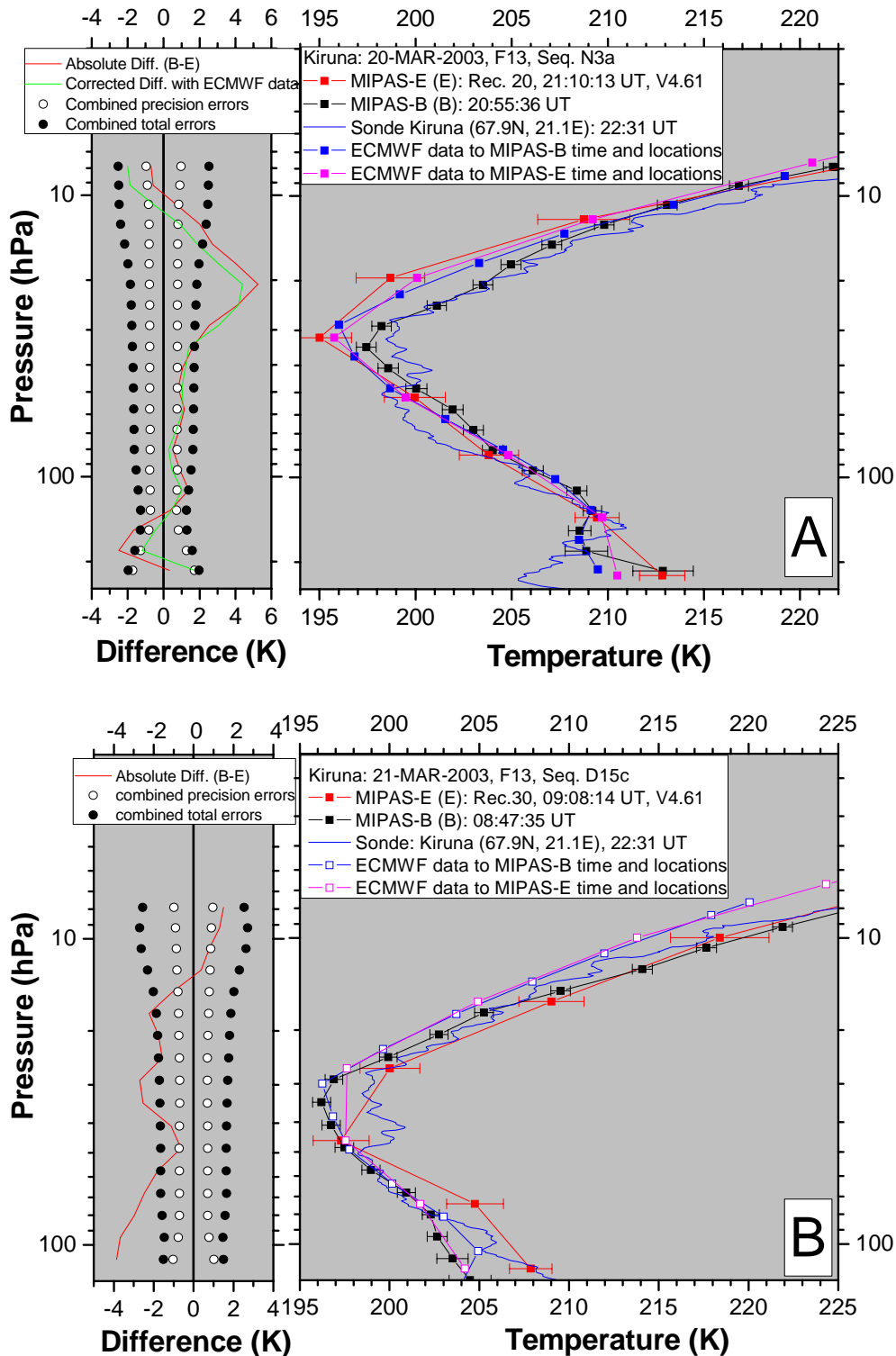


**Figure 8.2.1-2:** Temperature comparisons for Flight No. 13. (A) Comparisons between Seq. N3a and Rec. 20. (B) Comparison between Seq. D15c and Rec. 30. The notation is the same as in Figure 8.2.1-1.

### 1.3 Flight No. 14

MIPAS-B measured two sequences, Seq. 2 and Seq. 3, during Flight No. 14. Unfortunately, the record of MIPAS-E which is suitable to compare with Seq. 2 of MIPAS-B is not yet available. Although the time offset is very large in this co-location measurement the consistency between MIPAS-B and MIPAS-E profiles is excellent (Figure 8.2.1-3). It is not surprising if we look at the differences of the ECMWF temperature field between the MIPAS-

## 8. Intercomparison of measurements

B and MIPAS-E measurement time which were presented in Panel G and H in Appendix C. The ECMWF model shows that the temperature is varying less than 1 K within the sounded region. ECMWF temperature fields also show that the temperature horizontal gradient is also small (not presented here). The radiosonde agrees with MIPAS-B quite well and both profiles present a small structure between 236-147 hPa (11-14 km). This structure did not appear in MIPAS-E profile due to its coarse vertical grid. In the range of 268-44 hPa (10-22 km), ECMWF data are systematically higher than MIPAS-B, MIPAS-E and the radiosonde measurements. The reason needs to be investigated further.

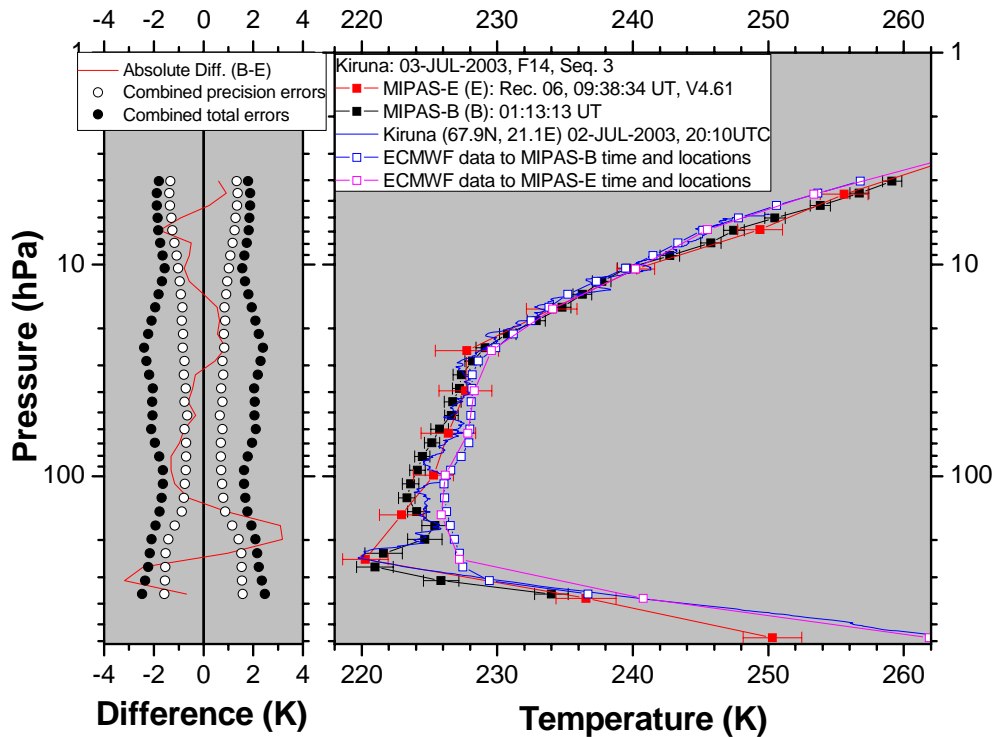


**Figure 8.2.1-3:** Temperature comparison between Seq. 3 and Rec. 06 for Flight No.14. The notation is the same as in Figure 8.2.1-1.

## 2 Trajectory comparison for temperature

### 2.1 Flight No. 11

Scatter plots from comparisons of MIPAS-E against MIPAS-B as obtained from trajectory methods are plotted in Figure 8.2.1-4. The 2 days forward and backward trajectories of the air masses that had been measured by Seq. S, Seq. N3, Seq. W and Seq. E were calculated separately. The coincident points were found out according to the match criteria of 500 km, 1 hour. Depending on the path of the trajectories of the air masses, the switch-off and calibration periods of MIPAS-E and other factors, the number of coincidence points is very different for different MIPAS-B sequences and different levels of altitude. For example, in Panel C and D, only three match points were available at a particular level of altitude for one MIPAS-B measurement, in Panel A and B, eight and twelve match points can be found, respectively, corresponding to one MIPAS-B measurement point.

These scatter plots show that the MIPAS-E temperatures are in good agreement with MIPAS-B temperatures in general. And most of the directly coincident match points are the best in consistency among all match points (including trajectory calculations) due to their better match quality. However, sometimes MIPAS-E measured temperature significantly differs

from MIPAS-B observations. This was mainly caused by the spatial offset in cases where the horizontal gradient of the temperature was large. Obviously, 500 km as a match criterion in space is not strict enough in some cases. For example, Panel C shows that at the low altitude, the measurements of MIPAS-E Rec. 15 are higher than MIPAS-B measurements. We have described in the Panel C of Figure 8.1.1-1 that the tangent locations distances between Rec.15 and Seq. S is about 500 km at low altitudes. And a large temperature gradient existed in this region.

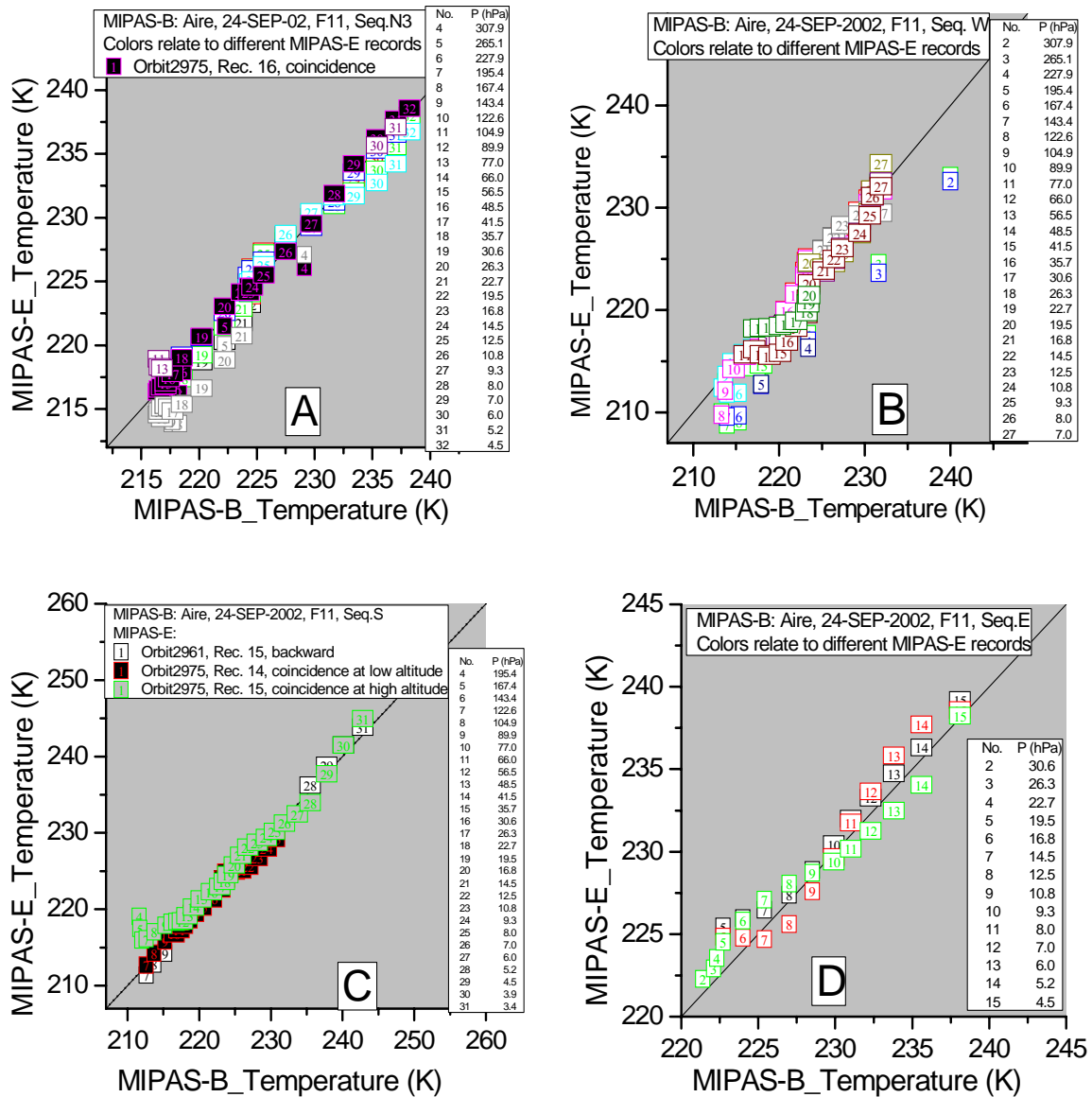


**Figure 8.2.1-4:** Scatter plots of MIPAS-E temperature against MIPAS-B temperature for match points found in two days forward and backward trajectories for Flight No. 11. (A) For MIPAS-B Seq. N3. (B) For MIPAS-B Seq. W. (C) For MIPAS-B Seq. S. (D) For MIPAS-B Seq. E. The numbers in the square symbols represent the match points pressure as listed in the legends. The solid squares denote direct coincident comparisons. The solid straight lines are diagonals of squares. For clarity, the error bars were not shown here.

The mean temperature profiles of MIPAS-E and the correlative MIPAS-B profiles were plotted in Figure 8.2.1-5. The process to calculate the mean profiles of MIPAS-E is as follows. Firstly, interpolating the MIPAS-E measurements of the match points onto the MIPAS-B pressure levels by adopting logarithmic approach, secondly, taking into account the noise errors of MIPAS-E, the weighted averaged value at a specific level of pressure was calculated by averaging all the MIPAS-E measurements of the match points according to the equations

## 8. Intercomparison of measurements

of (3.3) and (3.5), finally, performing the calculation for all related levels of pressure. The errors of the MIPAS-E profiles are the mean of the total errors of the averaged match points.

The difference profiles of MIPAS-B minus MIPAS-E in Figure 8.2.1-5 indicate that the two instruments measurements are consistent with respect to their combined total errors except at low altitudes. Panel C of Figure 8.2.1-5 presents very similar results as Figure 8.2.1-1 Panel A, because two coincident sequences, Rec. 14 and Rec. 15, dominated the mean profile. The sense of the statistics for this mean profile is insignificant since only three match points are available at one level of altitude. And this is also true for Panel D. Panel A of Figure 8.2.1-5 demonstrates a good consistency between MIPAS-E and MIPAS-B. Panel B reveals a cold bias of MIPAS-E measured temperatures below the altitude of 122.6 hPa (15 km). Since the match points found in the trajectories for Seq. S and Seq. E are not as many as for Seq. N3 and Seq. W, the trajectory comparisons for them are not very typical. For conciseness, the corresponding figures to Panel C and D in Figure 8.2.1-4 and Figure 8.2.1-5 for H<sub>2</sub>O, O<sub>3</sub>, HNO<sub>3</sub>, CH<sub>4</sub>, and N<sub>2</sub>O comparisons will not be presented.

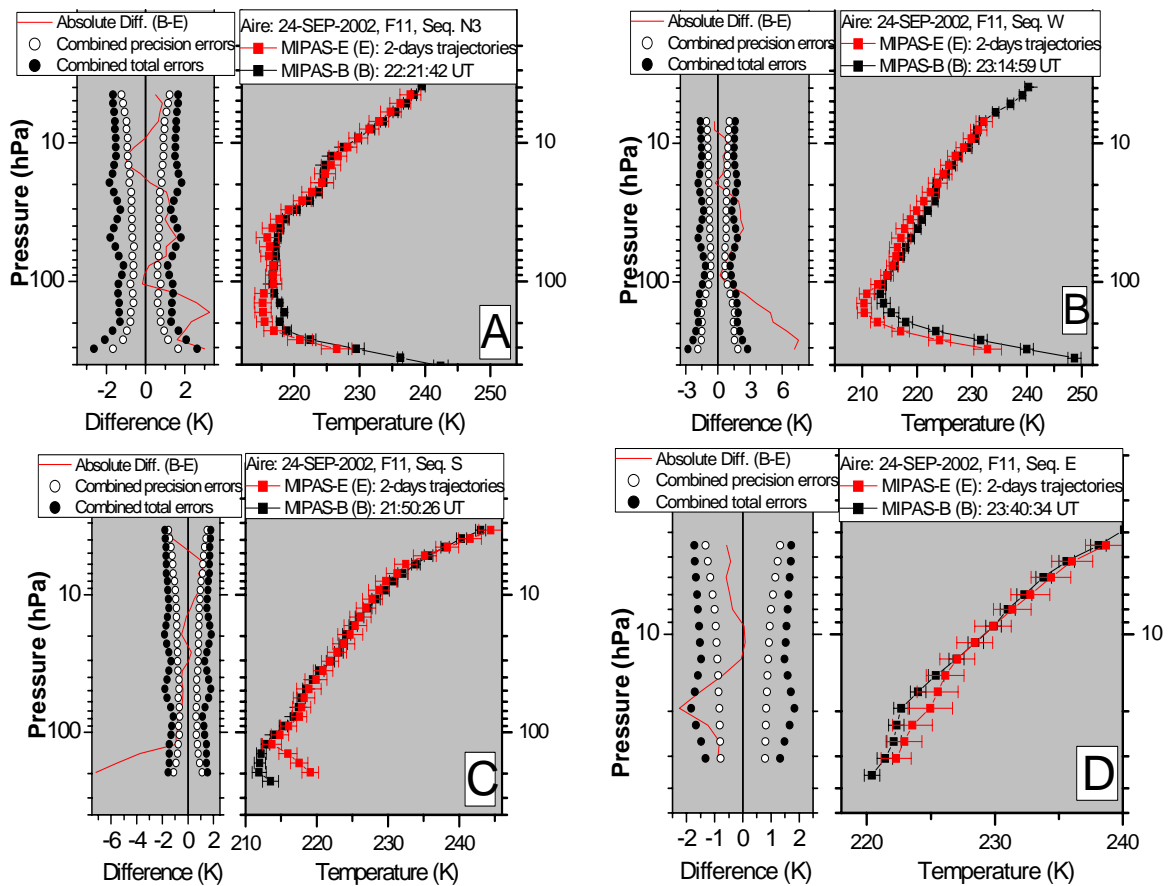


**Figure 8.2.1-5:** MIPAS-B temperature profiles comparison with MIPAS-E mean temperature profiles which were calculated by averaging all the match points at the same level of altitude considering the weights of the MIPAS-E noise errors. The notations are the same as in Figure 8.2.1-1. (A) For MIPAS-B Seq. N3. (B) For MIPAS-B Seq. W. (C) For MIPAS-B Seq. S. (D) For MIPAS-B Seq. E

### 2.2 Flight No. 13

Two scatter plots corresponding to Seq. N3a and Seq. D15c are plotted in Figure 8.2.1-6. Among the match points, the coincident points show an excellent agreement. Other match points show large discrepancy between MIPAS-E and MIPAS-B temperatures. Keeping in mind that all these match points were measured in the region where the winter polar vortex existed. So the comparison results are very sensitive to the match quality.

## 8.2 MIPAS

The comparisons of mean profiles of MIPAS-E with MIPAS-B are illustrated in Figure 8.2.1-7. Panel A shows that the agreement between MIPAS-E and MIPAS-B profiles is slightly better than the coincident comparisons especially in the range of 34-14 hPa. This result shows the statistics advantage of the trajectory method, because the influences of the mismatch to the comparisons were partly averaged out. Panel B shows a similar result as the Panel B of Figure 8.2.1-2 and implies that MIPAS-E measurements show a warm bias compared to MIPAS-B data at low altitudes.

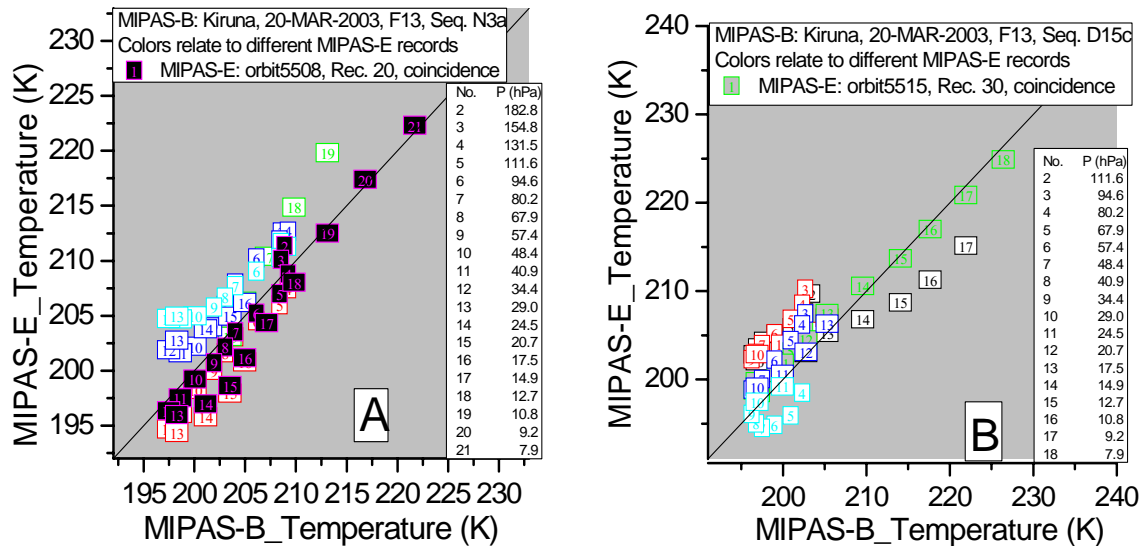


Figure 8.2.1-6: Same as Figure 8.2.1-4 but for flight No. 13. (A) For Seq. N3a. (B) For Seq. D15c.

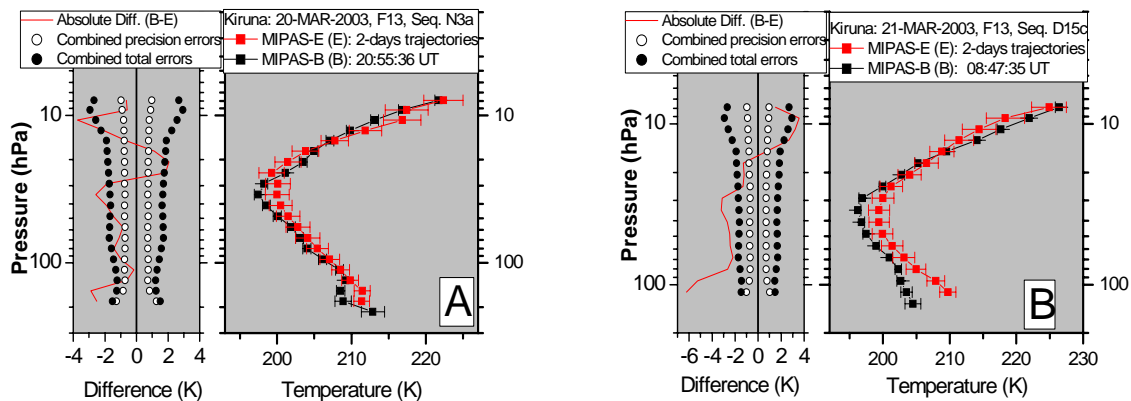


Figure 8.2.1-7: Same as Figure 8.2.1-5 but for Flight No. 13. (A) For Seq. N3a. (B). For Seq. D15c.

### 2.3 Flight No. 14

More match points were found for Seq. 2 and Seq. 3 of MIPAS-B during Flight No. 14 (Figure 8.2.1-8). As a consequence, the statistics of intercomparison is improved. The scatter plots show that most of the match points indicating MIPAS-E measurements agree with MIPAS-B results well except at low altitudes. These results are consistent to the characteristics of the meteorology in polar summer, i.e., the temperature and the VMRs of gases distribution are relative homogenous and stable compared to the polar winter.

The mean profiles of MIPAS-E are in very good agreement with the MIPAS-B profiles (Figure 8.2.1-9). The profiles of differences lie within the total combined total errors almost



## 8. Intercomparison of measurements

in the whole range of altitudes. Panel B of Figure 8.2.1-9 shows a similar result with the coincident comparison. This is an indirect evidence to show that the large time offset did not significantly influence the coincident comparison.

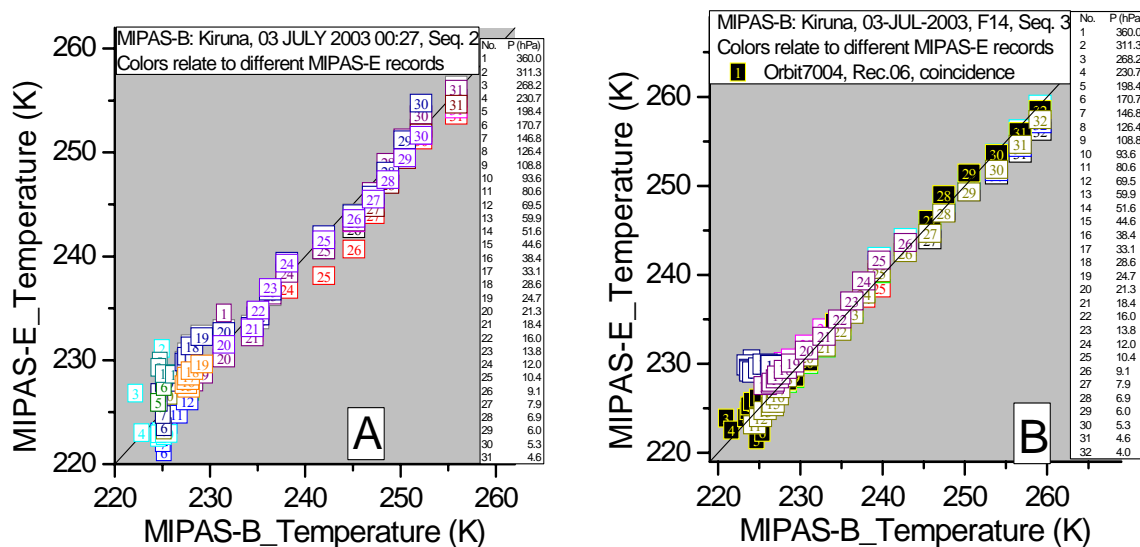


Figure 8.2.1-8: Same as Figure 8.2.1-4 but for Flight No. 14 (A) For Seq. 2. (B) For Seq. 3.

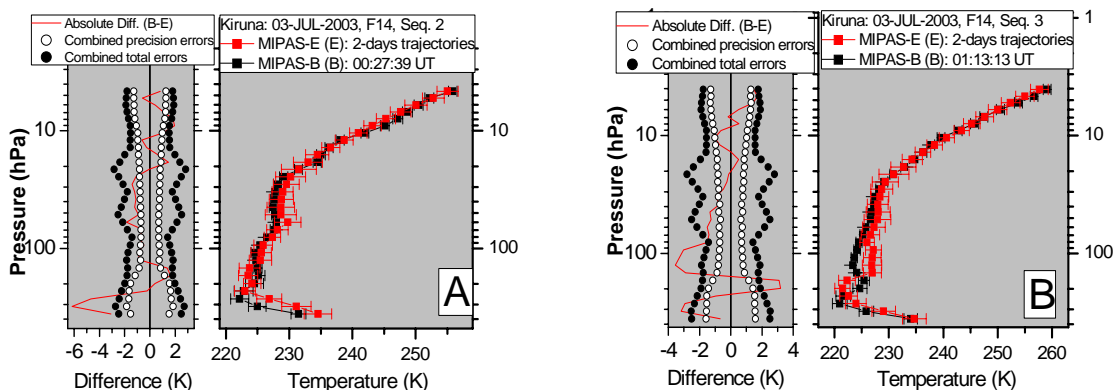


Figure 8.2.1-9: Same as Figure 8.2.1-5 but Flight No. 14 (A) For Seq. 2. (B) For Seq. 3.

The tables in the appendix B list the number of the match points at each level of pressure for all sequences of MIPAS-B. The number of match points is almost the same for the temperature, and the VMRs of  $H_2O$ ,  $O_3$ ,  $HNO_3$ ,  $CH_4$ ,  $N_2O$ . The tables show that the significance of the statistics is not very strong in trajectory comparisons especially at low levels of altitude. However, the synthetical results of all the trajectory comparisons will improve the statistical significance as shown in the next section.

### 3 Summary of temperature comparison

A summary of the temperature comparison between MIPAS-E and MIPAS-B is shown in Figure 8.2.1-10. In principle, there are no systematic biases between the two instruments measurements for coincident comparison and trajectory comparison. The majority of the comparisons were made between about 143 and 4 hPa where the statistics is more reliable. Below the altitude of about 143 hPa, the difference profiles in the graph present a great deal of scatter.



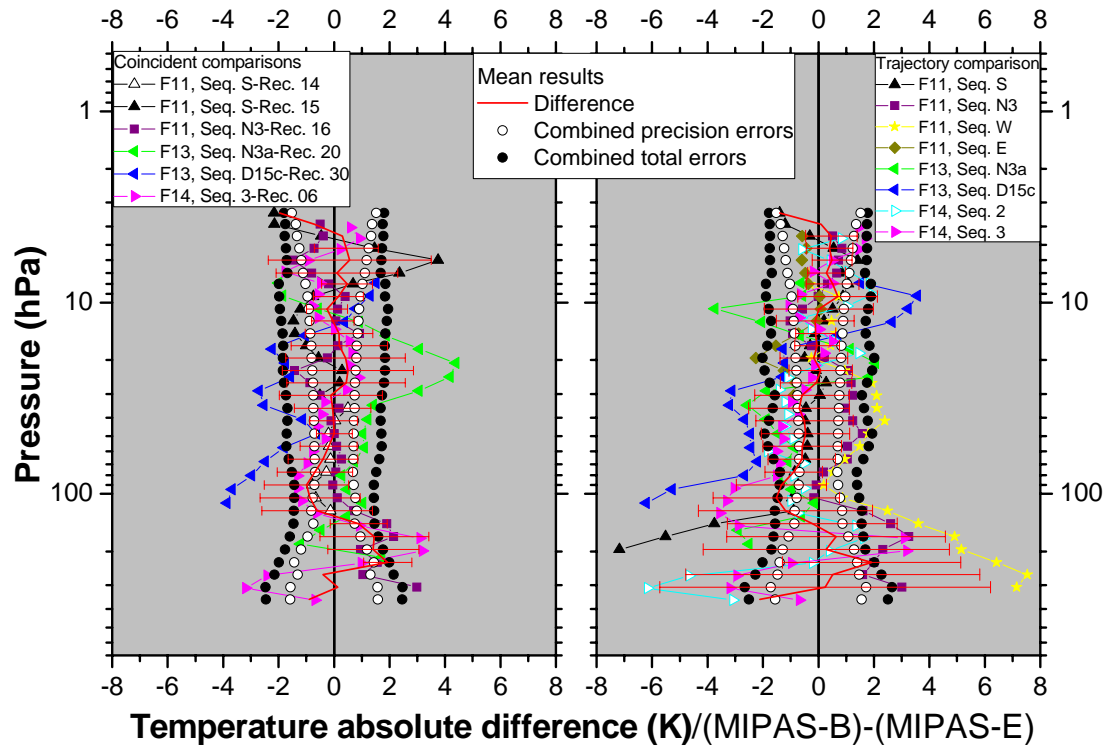


**Figure 8.2.1-10:** Summary comparison of temperature between MIPAS-E and MIPAS-B. There are no standard deviation bars for the top and bottom sections of the mean difference profile since only one or two comparisons are available in these altitude regions. Left: coincident comparison. Right: trajectory comparison.

The average of all the differences of comparison at each level of altitude was calculated for coincidence and trajectories case, respectively, by using equation (3.1). Based on this average, the mean difference over a certain altitude range was calculated considering the weighting of the amount of comparisons at each altitude level. The mean combined total errors and the mean combined precision errors were also averaged over a certain altitude region. According to the systematic behavior of the differences between MIPAS-E and MIPAS-B measurements, the comparisons were separated into four altitude regions: 356-143 hPa (8-14 km), 143-31 hPa, (14-24 km), 31-5 hPa (24-37 km), and 5-3 hPa (37-39 km). The results are listed in table 8.2.

The data in the table shows that between 356-143 hPa, MIPAS-E measurements are lower than MIPAS-B data. In 143-31 hPa, MIPAS-E temperature is higher than MIPAS-B data. In the region of 31-5 hPa, MIPAS-E shows a low bias. In the top region of 5-3 hPa, MIPAS-E gives higher measurements. The coincident comparison is very consistent to the trajectory comparison over the whole altitude range. Above the altitude of 143 hPa, the consistency between MIPAS-E and MIPAS-B measurements in coincident comparison is a little bit better than that of the trajectory comparison. Below the level of 143 hPa, better agreement was demonstrated in the trajectory comparison. This may be due to the effects of statistics. Both coincident comparisons and trajectory comparisons show that the differences of MIPAS-E and MIPAS-B temperature are smaller than their mean combined total errors over the whole altitude range. In this sense, MIPAS-E temperature can be regarded as successfully validated.

The standard deviation of the mean difference was calculated only for the altitude region of 123-8 hPa (15-32 km) where extensive comparisons are available (4-5 comparisons for the coincidence approach and 7-8 comparisons for the trajectory approach). In both comparison approaches, the standard deviations are larger than the combined precision errors in general. This implies that the spread of MIPAS-E measurements for temperature is too large.

## 8. Intercomparison of measurements

**Table 8.2: Mean differences of MIPAS-B minus MIPAS-E temperature as well as the associated mean combined errors and the mean standard deviations.**

Accuracy							
Pressure (hPa)	Height (km)	Absolute difference (K)		Relative difference (%)		Mean combined total errors (K)	
		Coincidence	Trajectory	Coincidence	Trajectory	Coincidence	Trajectory
356-143	8-14	0.92±0.93	0.33±0.95	0.42±0.18	0.13±0.42	1.89±0.37	1.94±0.43
143-31	14-24	-0.39±0.37	-0.72±0.43	-0.19±0.18	-0.35±0.20	1.60±0.12	1.62±0.18
31-5	24-37	0.25±0.25	0.16±0.30	0.12±0.11	0.06±0.13	1.83±0.10	1.81±0.18
5-3	37-39	-1.13±0.42	-0.40±1.00	-0.47±0.34	-0.18±0.40	1.77±0.03	1.77±0.01
Precision							
Pressure (hPa)	Height (km)	Standard deviation (K)		Mean combined precision errors (K)			
		Coincidence	Trajectory	Coincidence	Trajectory		
123-17	15-28	1.52±0.52	2.48±1.49	0.82±0.20	0.93±0.31		
17-8	28-33	1.39±0.75	1.04±0.42	1.00±0.16	1.03±0.16		

### 8.2.2 H<sub>2</sub>O

#### 1 Coincident comparison for H<sub>2</sub>O

##### 1.1 Flight No. 11

The intercomparisons of H<sub>2</sub>O VMR between MIPAS-E and MIPAS-B for flight No. 11 are shown in Figure 8.2.2-1. According to the match quality, below the level of 30 hPa (24 km) MIPAS-B Seq. S is the coincident measurement of Rec. 14 and above it is Rec. 15. Panel A presents the comparisons of Rec. 14 to Seq. S and Rec. 15 to Seq. S. In general, both MIPAS-E profiles agree well with MIPAS-B in most of the height region. This may be due to the low H<sub>2</sub>O VMR horizontal gradients. Below the level of 143 hPa, MIPAS-E H<sub>2</sub>O measurements are lower than MIPAS-B data and beyond the combined total errors. Upwards from the level of 26.3 hPa (25 km) MIPAS-E data become to be higher than MIPAS-B measurements. The two profiles of MIPAS-E show oscillations and the intensity of oscillation increases with increasing altitude. Panel B presents the comparison of Rec. 16 to Seq. N3 with the radiosonde profile measured over the launch pad of MIPAS-B several hours earlier before the Seq. N3 observation. At the lower altitude, the measurements made from radiosonde agree with MIPAS-B and MIPAS-E measurements approximately. At upper height region, obviously the radiosonde H<sub>2</sub>O VMR values depart from the normal distribution of H<sub>2</sub>O. Above the altitude of 143 hPa, MIPAS-E data agree well with MIPAS-B measurements but from the level of 22.7 hPa (26 km) they show a high bias. And below the altitude of 143 hPa, MIPAS-E measured much dryer air masses compared to MIPAS-B. Again the oscillation appears in MIPAS-E profile especially in the upper part. Because of the excellent match quality, the absolute difference profile in Panel B definitely characterizes the difference between MIPAS-E and MIPAS-B in this co-location measurement.

## 8.2 MIPAS

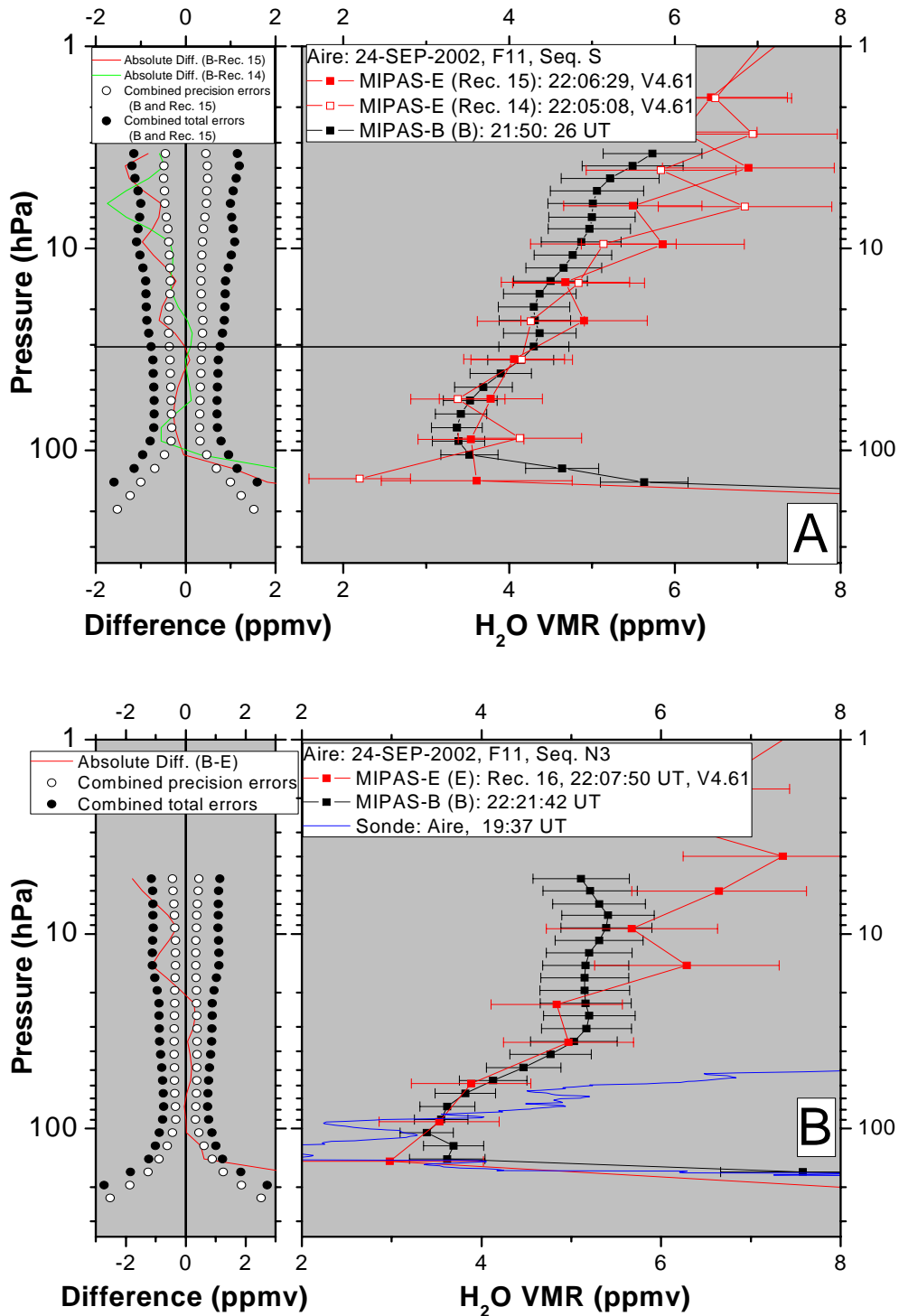


**Figure 8.2.2-1:** H<sub>2</sub>O VMR comparisons for Flight No. 11. MIPAS-B profiles, black curves with black square symbols, the error bars represent the total errors; MIPAS-E profiles, red curves with red square symbols, the error bars represent the total errors; radiosonde profile, solid blue line; the absolute differences of MIPAS-B minus MIPAS-E, solid red line or solid green line; combined precision errors (the combination of MIPAS-E noise errors and MIPAS-B errors including the noise, LOS, and temperature errors), open circles; the combined total errors, solid circles. (A) Comparisons between Seq. S and Rec. 14, Seq. S and Rec. 15. Both kind of combined errors are calculated from the Seq. S and Rec. 15 data. If using Rec. 14 data, the combined errors are almost the same. The straight line denotes that below this level of altitude Seq. S should compare with Rec. 14 and above to Rec. 15. (B) Comparison between Seq. N3 and Rec. 16.

## 1.2 Flight No. 13

The validation campaign of Flight No. 13 was performed in the later polar winter in Kiruna (Sweden). A strong polar vortex existed during the period of the campaign. Panel A presents the comparison of Rec. 15 to Rec. N3a. The agreement is good with respect to the combined total errors (and even the combined precision errors) in the whole height region. This is beyond the expectation because the upper part (above the altitude of about 29 hPa or 23 km) of MIPAS-E profile was measured inside the polar vortex while the MIPAS-B profile was

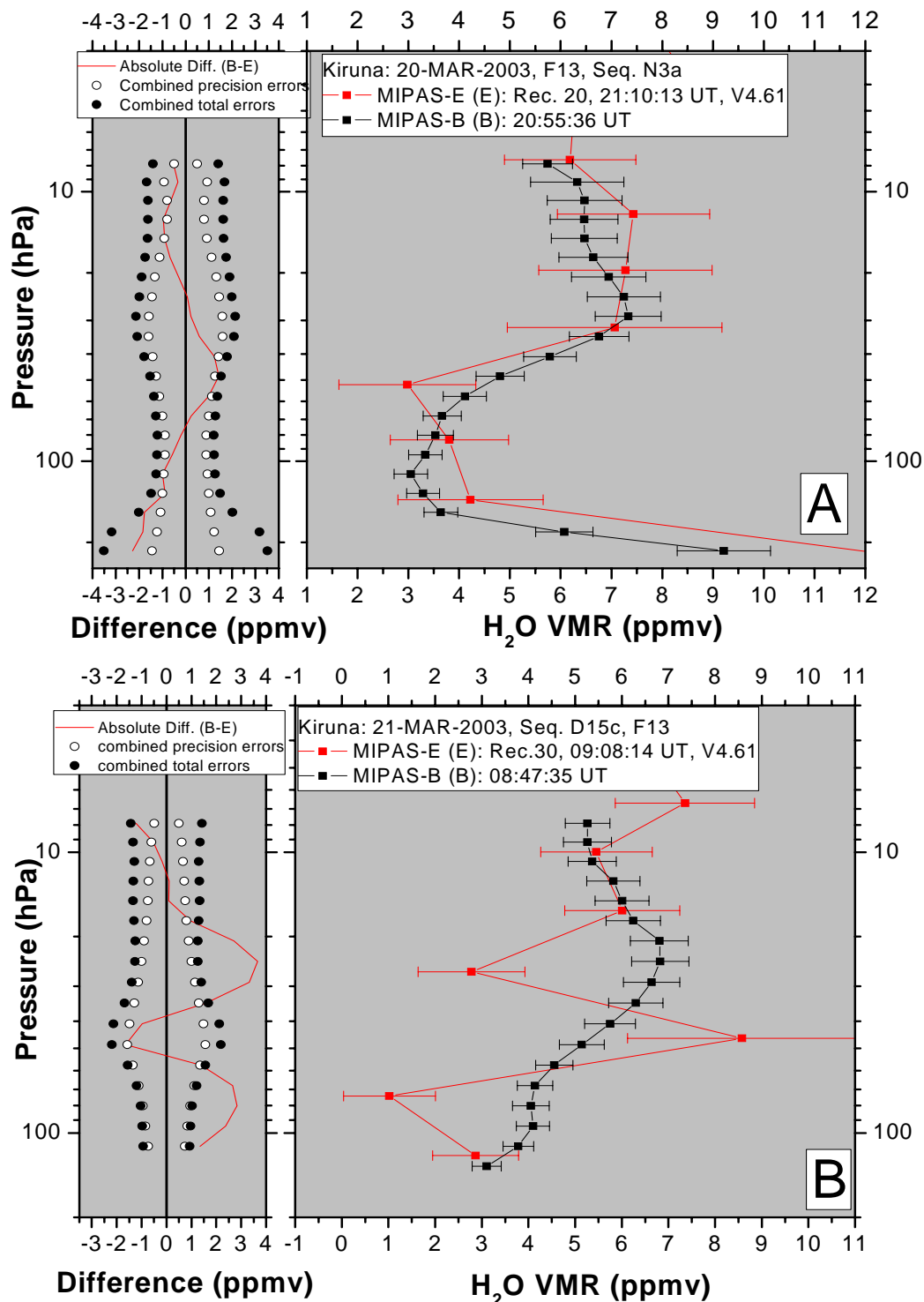
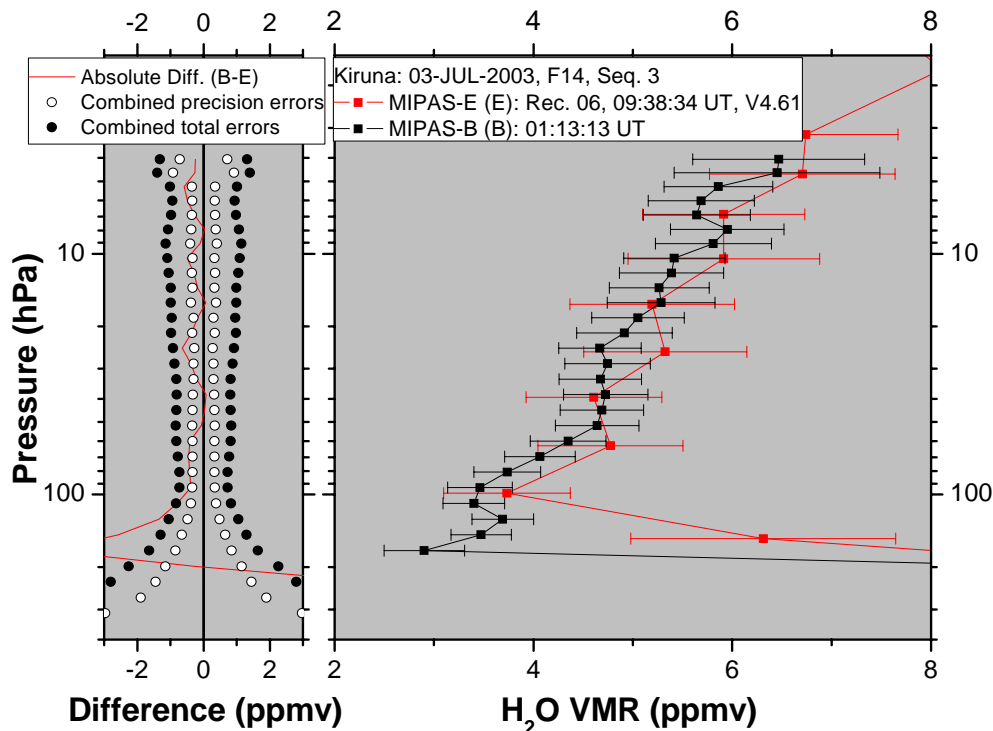


Figure 8.2.2-2: H<sub>2</sub>O VMR comparisons for Flight No. 13. (A) Comparisons between Seq. N3a and Rec. 20. (B) Comparison between Seq. D15c and Rec. 30. The notation is the same as in Figure 8.2.2-1.

observed near the edge of the vortex. Above the level of 21 hPa (25 km), MIPAS-E data is a little bit higher than MIPAS-B data. Below the level of 80 hPa (17 km), MIPAS-E measurements are higher than MIPAS-B. This feature differs from the comparison in Flight No. 11. In Panel B, MIPAS-E profile oscillates significantly. This made the comparison to be difficult. In general, the MIPAS-E profile oscillates around the MIPAS-B profile. In this sense, MIPAS-E measurement is in agreement with the measurement made from MIPAS-B. On the other hand, The H<sub>2</sub>O data points of MIPAS-E are unreasonably high and low and the oscillations are well beyond the expected errors.

### 1.3 Flight No. 14

Only one pair of comparison, Rec. 06 to Seq. 3, is available for Flight No. 14 (Figure 8. 2.2-3). MIPAS-E measurements agree with MIPAS-B observations well though they show a little bit higher values above the altitude of 126 hPa (15 km). Between 198-126 hPa (12-15 km), MIPAS-E gave higher data than MIPAS-B. Below the level of 198 hPa (not shown), MIPAS-E gave a deep low bias. A temporal offset of as large as 8.5 hours should not contribute any differences since the life time of H<sub>2</sub>O is large and the horizontal gradients in the summer polar stratosphere are small.



**Figure 8.2.2-3:** H<sub>2</sub>O VMR comparisons for Flight No. 14 between Seq. 3 and Rec. 06. The notation is the same as in Figure 8.2.2-1.

## 2 Trajectory comparison for H<sub>2</sub>O

### 2.1 Flight No. 11

The scatter plots of MIPAS-E H<sub>2</sub>O VMR against MIPAS-B data found in two days backward and forward trajectories for Flight No. 11 are plotted in Figure 8.2.2-4. Panel A shows that above the altitude of 26.3 hPa, MIPAS-E measurements are larger than the MIPAS-B Seq. N3 data. Below the altitude of 167 hPa (13 km), MIPAS-E data are lower than the measurements

## 8. Intercomparison of measurements

made from MIPAS-B. Between, they agree quite well. The scatter plot in Panel B shows that in the region of 105-17 hPa (16-28 km), a good consistency was obtained. Below the level of 105 hPa, MIPAS-E measurements are lower than MIPAS-B measurements. And above the level of 17 hPa, MIPAS-E data become larger. Figure 8.2.2-5 presents the comparisons between MIPAS-E mean profile and the correlative MIPAS-B measurements. All the results show that above the altitude of about 105 hPa (16 km), the two measurements are nearly in agreement with respect to the combined errors but the departure increases significantly with altitude above the level of about 26 hPa. At lower altitudes, the discrepancy is extremely large. The fine features of the comparisons are similar to the analysis for the scatter plots. An outstanding feature in the panels of Figure 8.2.2-5 is that the oscillation disappeared in the mean profiles of MIPAS-E.

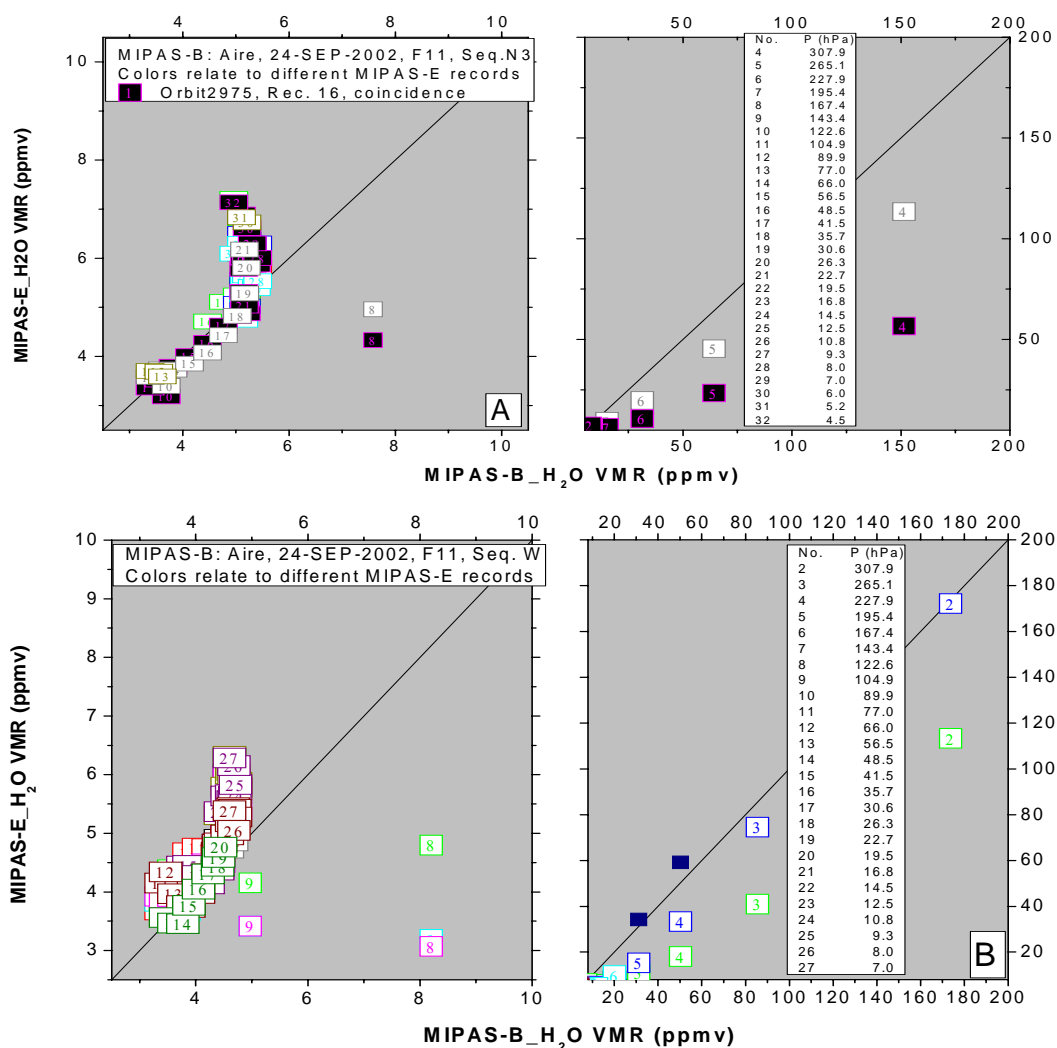


**Figure 8.2.2-4:** Scatter plots of MIPAS-E H<sub>2</sub>O VMR against MIPAS-B H<sub>2</sub>O VMR for match points found in two days forward and backward trajectories for Flight No. 11. (A) For Seq. N3. (B) For Seq. W. The numbers in the square symbols represent the pressure of the match points as listed in the legends. The solid squares denote the match points that have been found during the coincident comparisons. The solid straight lines are diagonals of squares. For clarity, the error bars were not shown here.

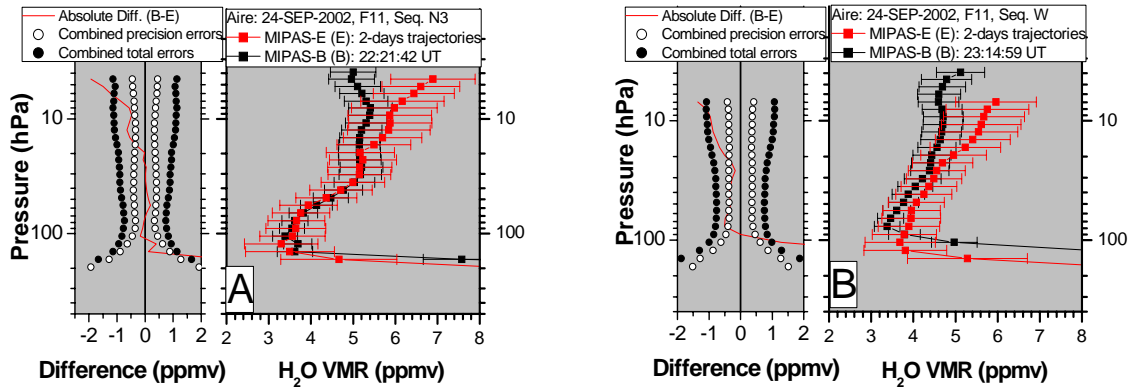


**Figure 8.2.2-5:** MIPAS-B H<sub>2</sub>O VMR profiles comparison with MIPAS-E mean H<sub>2</sub>O VMR profiles which were calculated by averaging all the match points at the same level of altitude considering the weights of the MIPAS-E noise errors. The notation is the same as in Figure 8.2.2-1. (A) For Seq. N3. (B) For Seq. W.

### 2.2 Flight No. 13

The points in the scatter plots of Figure 8.2.2-6 spread in a broad region. Two reasons should be taken into account: Firstly, the strong oscillation of the MIPAS-E profiles; Secondly, inhomogeneities of H<sub>2</sub>O across the polar vortex edge. Despite the scatter of the individual comparison point, the mean profiles of MIPAS-E agree well with the correlative MIPAS-B profiles (Figure 8.2.2-7). Their differences are within the combined total errors in the whole height region. Panel B indicates that MIPAS-E measurements tend to be significantly higher than MIPAS-B observations above the altitude of 15 hPa (27 km).

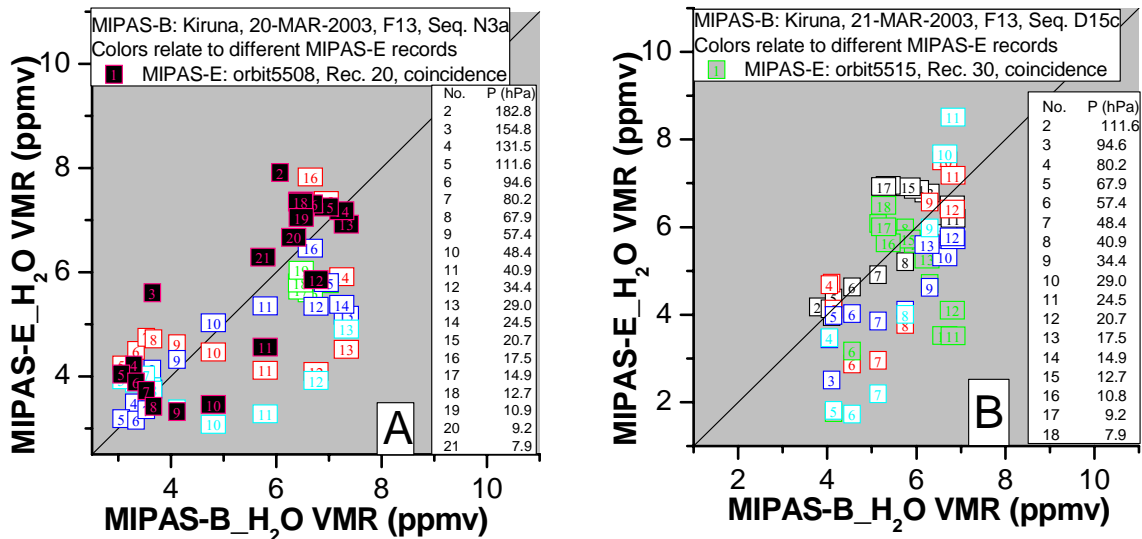


**Figure 8.2.2-6:** Same as Figure 8.2.2-4 but for Flight No. 13. (A) For Seq. N3a. (B) For Seq. D15c.



## 8. Intercomparison of measurements

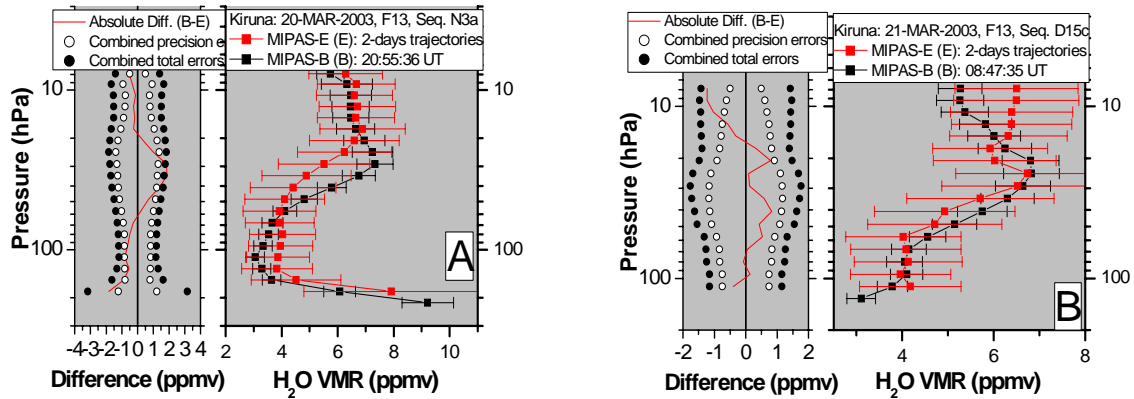


**Figure 8.2.2-7:** Same as Figure 8.2.2-5 but for Flight No. 13. (A) For Seq. N3a. (B) For Seq. D15c.

### 2.3 Flight No. 14

The scatter plots for Flight No. 14 are shown in Figure 8.2.2-8. This time the distribution of the points is more compact and along the diagonal straight line. They indicate the good consistency between MIPAS-E and MIPAS-B measurements except below the level of 147 hPa (14 km) in this geophysical condition. The comparisons between the mean profiles of MIPAS-E and the correlative MIPAS-B profiles show similar results as the scatter plots (Figure 8.2.2-9). Again MIPAS-E data are a little bit higher than MIPAS-B data above the level of 38 hPa (23 km) and lower for the pressure levels in the upper troposphere and lower stratosphere.

The oscillation of the MIPAS-B profiles appears not only in the Flight No. 11, 13 but also in the Flight No. 14 data. Figure 8.2.2-10 presents all MIPAS-E profiles related with the trajectory comparison for Seq. 2. It shows clearly that most of the profiles have the oscillation features while the amplitude is different.



## 8.2 MIPAS

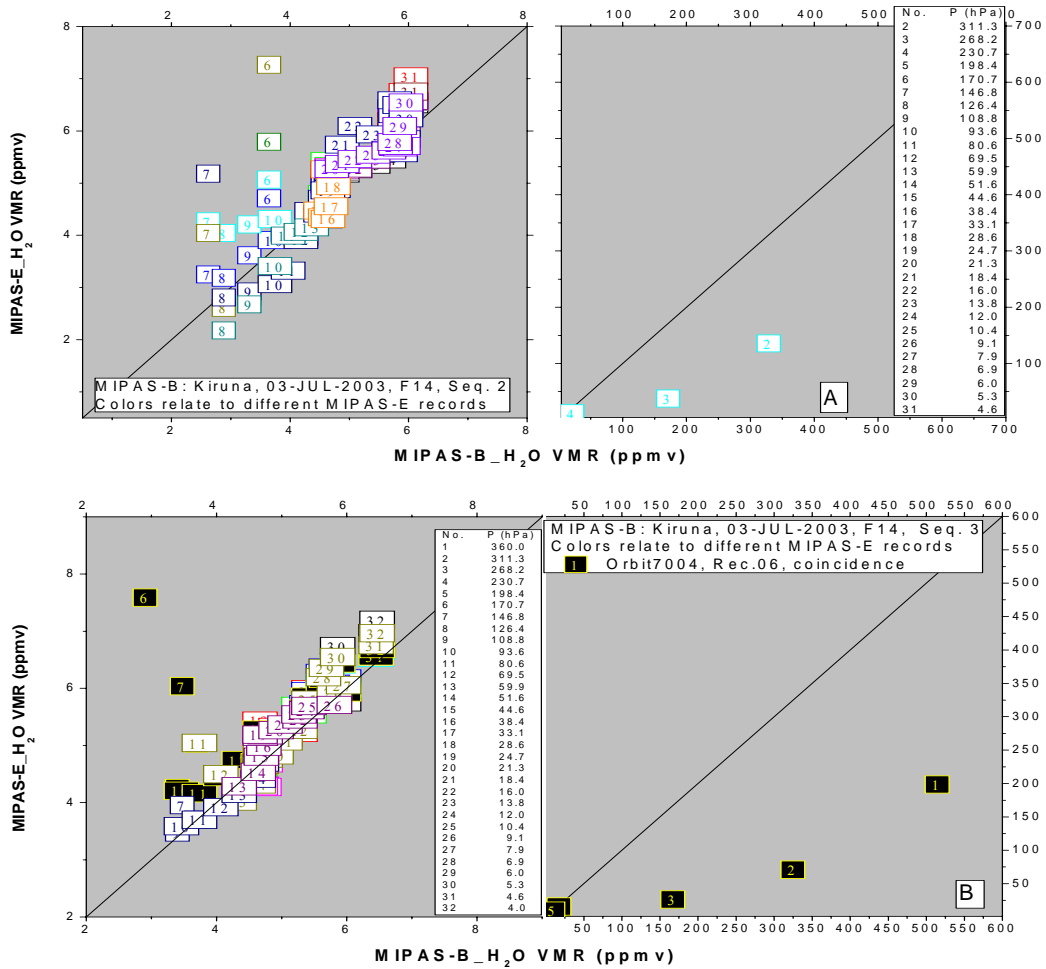


Figure 8.2.2-8: Same as Figure 8.2.2-4 but for Flight No. 14. (A) For Seq. 2. (B) For Seq. 3.

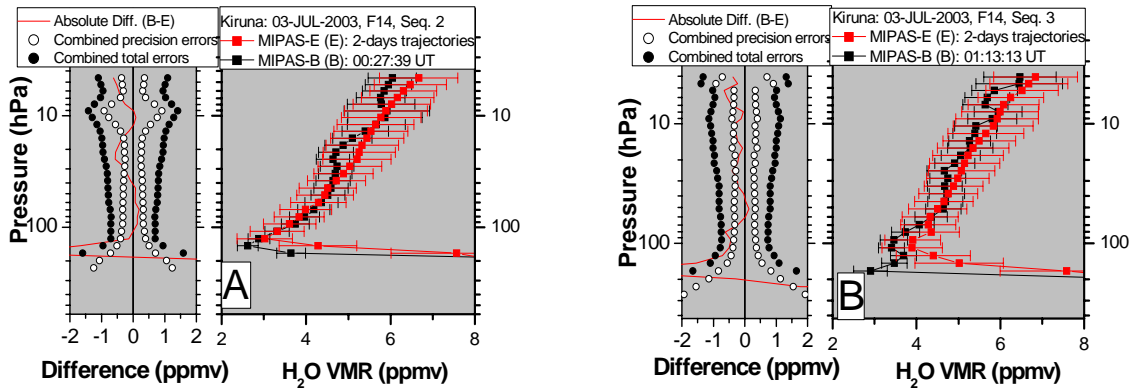
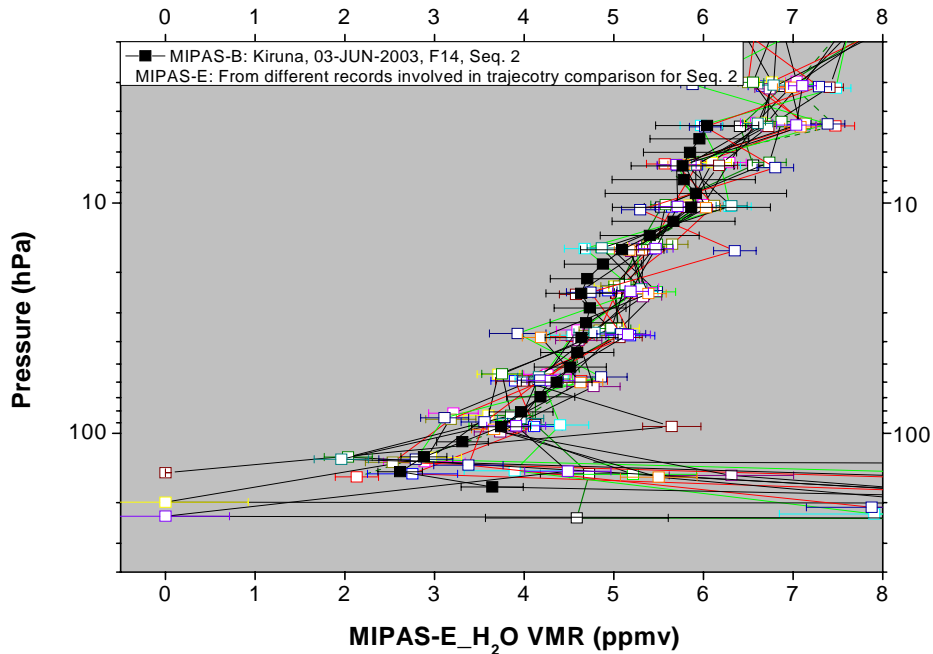


Figure 8.2.2-9: Same as Figure 8.2.2-5 but for Flight No. 14. (A) For Seq. 2. (B) For Seq. 3.

## 8. Intercomparison of measurements



**Figure 8.2.2-10:** H<sub>2</sub>O VMR profile of MIPAS-B Seq. 2 and the MIPAS-E H<sub>2</sub>O VMR profiles associated with the H<sub>2</sub>O VMR trajectory comparison for Seq. 2. Some of the MIPAS-E profiles show strong oscillations.

### 3 Comparison of total hydrogen H<sub>2</sub>O+2\*CH<sub>4</sub>

The total hydrogen, H<sub>2</sub>O+2\*CH<sub>4</sub>, keeps approximate constant in the stratosphere (see related section in Chapter 2). Therefore, it is a suitable parameter for H<sub>2</sub>O and CH<sub>4</sub> measurement comparison and the inner consistency check. Figure 8.2.2-11 presents all H<sub>2</sub>O +2\*CH<sub>4</sub> VMR profiles available for comparison between MIPAS-E and MIPAS-B and their differences. Both coincident comparison (Panel A) and trajectory comparison (Panel B) show similar comparison results. MIPAS-E data are systematically larger than MIPAS-B data above the level of 195 hPa (12 km) but within their combined total errors (not shown here). Below this level, MIPAS-E data show an extremely low bias. Both MIPAS-E and MIPAS-B measurements are consistent with the observations made from Engel, A., et al., (1996) in general but lower than the data from Oelhaf, H., et al., (2002). Since the CH<sub>4</sub> VMR measured by MIPAS-E is higher than MIPAS-B data in 195-15 hPa (12-29 km) and slightly lower in 15-3 hPa (29-39 km) (details will be mentioned later) the high bias of total hydrogen observed from MIPAS-E is mainly due to its overestimate on H<sub>2</sub>O VMR.

## 8.2 MIPAS

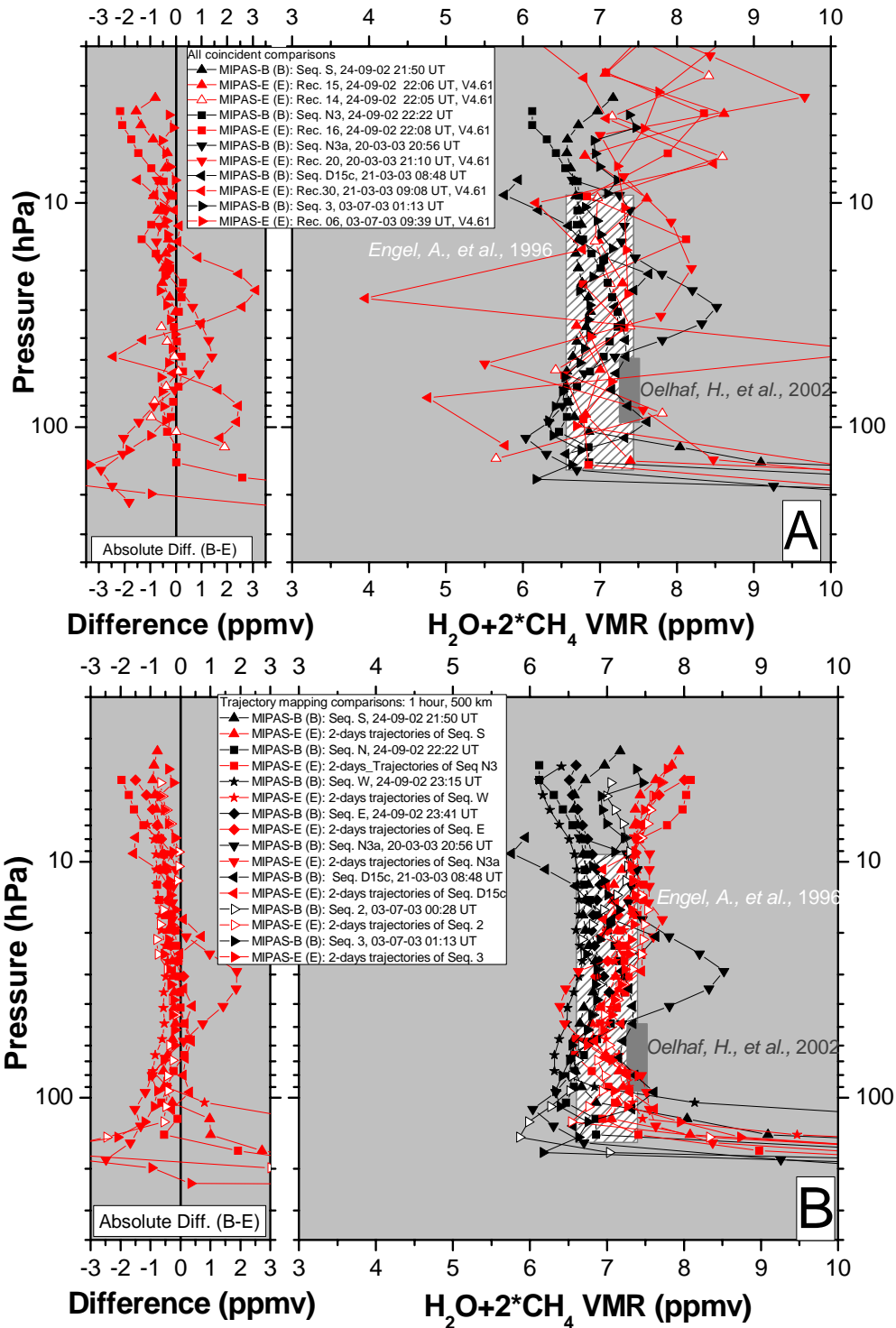


**Figure 8.2.2-11:** Comparison of all  $\text{H}_2\text{O}+2*\text{CH}_4$  VMR profiles of MIPAS-E with MIPAS-B profiles, along with the measurements carried out previously by Engel et al. and Oelhaf, H., et al.. For clarity, the error bars of MIPAS-E and the combined errors were not shown here. (A) Coincident comparison. (B) Trajectory comparison.

### 4 Summary of $\text{H}_2\text{O}$ comparison

The summary of the  $\text{H}_2\text{O}$  VMR comparison between MIPAS-E and MIPAS-B is shown in Figure 8.2.2-12. The high biases of MIPAS-E measurements in most of the altitude region are shown clearly in the difference profiles plot in the subpanel. Taking into account the average method of all the differences of comparison as discussed in the section for temperature comparison, quantitative comparison for  $\text{H}_2\text{O}$  VMR can be divided into four altitude regions:

## 8. Intercomparison of measurements

356-195 hPa (8-12 km), 195-123 hPa (12-15 km), 123-20 hPa (15-27 km) and 20-3 hPa (27-39 km) (Table 8.3). In the region of 356-195 hPa, MIPAS-E measurements are lower than MIPAS-B data. These discrepancies are far beyond the mean combined total errors. In this sense, the measurements of the two instruments are not in agreement in the region of 8-12 km. In 195-123 hPa, MIPAS-E measurements are higher than MIPAS-B measurements by 0.98 ppmv (38.76%) for coincident comparison. However, MIPAS-E shows negative bias in absolute value of 1.13 ppmv but positive bias in relative value of 14.37% for trajectory comparison. This reflects the sensitivity of H<sub>2</sub>O concentration to the altitude around the tropopause. From 123 hPa to 20 hPa, MIPAS-E data are smaller than MIPAS-B data (but show positive value in percent of 0.53% for trajectory comparison). From 20 hPa to 3 hPa, MIPAS-E observations are larger than MIPAS-B data. The discrepancies in the region of 195-3 hPa are still within the mean combined total errors but anyhow must be interpreted as a low bias of MIPAS-E which is increasing with altitude.

For coincident comparison, the standard deviation is 0.91 ppmv. While the mean combined precision error in this height region is 0.62 ppmv. For trajectory comparison, the two values are 0.48 ppmv and 0.62 ppmv, correspondingly. This implies that the H<sub>2</sub>O profiles oscillation of MIPAS-E degrade its precision considerably.

The oscillation of MIPAS-E H<sub>2</sub>O VMR profiles appeared frequently in all three validation scenarios. The cause that leads to the oscillation may be partly residing in the use of coarse vertical grid for retrieval and not using the regularization technique. As H<sub>2</sub>O retrievals are particularly sensitive to temperature errors, sometimes oscillation in temperatures could be another reason for the strong H<sub>2</sub>O oscillation. The oscillation of MIPAS-E retrieved profiles also appeared for other gases, e.g., HNO<sub>3</sub>, CH<sub>4</sub> and N<sub>2</sub>O. However, for these species the phenomena had been depressed after using the new version V4.61 processor. Unfortunately, it seemed that the improvement for H<sub>2</sub>O VMR retrieval is very limited.

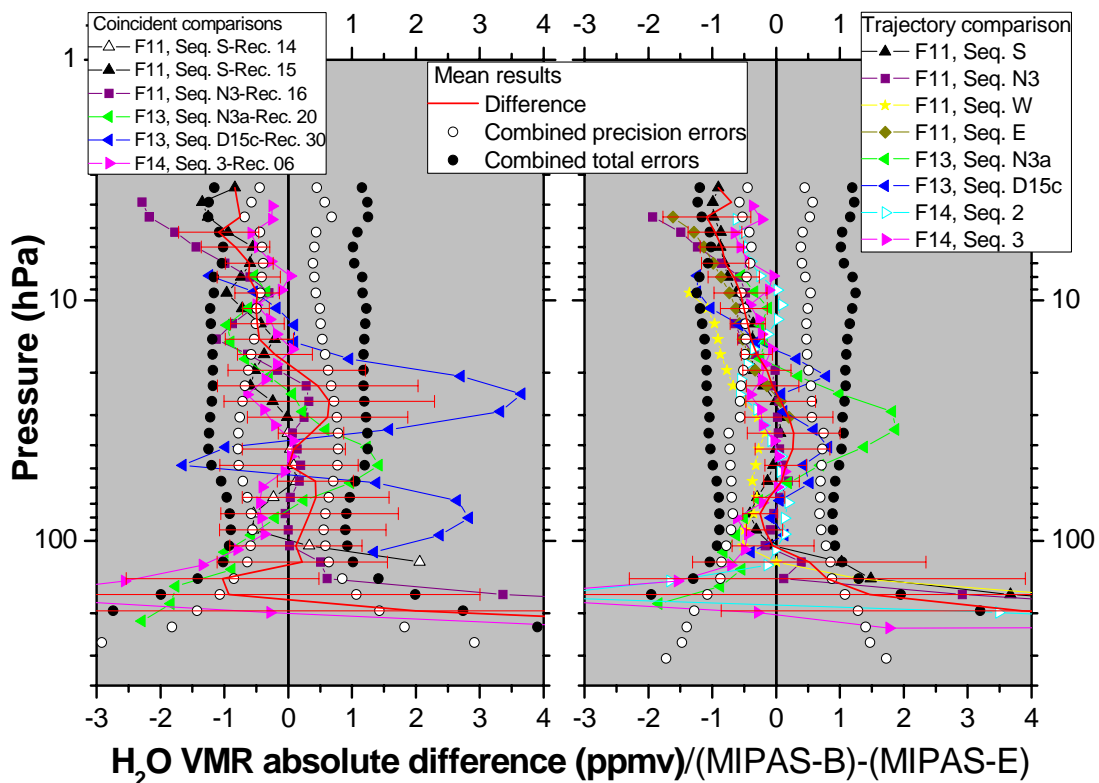


**Figure 8.2.2-12:** Summary comparison of H<sub>2</sub>O VMR between MIPAS-E and MIPAS-B. There are no standard deviation bars for the top and bottom sections of the mean difference profile since only one or two comparisons are available in these altitude regions. Left: coincident comparison. Right: trajectory comparison.

## 8.2 MIPAS

**Table 8.3: Mean differences of MIPAS-B minus MIPAS-E H<sub>2</sub>O as well as the associated mean combined errors and the mean standard deviations.**

Accuracy							
Pressure (hPa)	Height (km)	Absolute difference (ppmv)		Relative difference (%)		Mean combined total errors (ppmv)	
		Coincidence	Trajectory	Coincidence	Trajectory	Coincidence	Trajectory
356-195	8-12	77.58±108.33	61.79±85.10	39.34±32.63	35.15±19.44	12.27±13.98	11.64±12.12
195-123	12-15	-0.98±0.07	1.13±0.47	-38.76±13.09	-14.37±13.59	1.70±0.41	1.62±0.47
123-20	15-27	0.31±0.20	0.06±0.22	5.30±3.52	-0.53±3.84	1.09±0.14	1.00±0.08
20-3	27-39	-0.58±0.23	-0.62±0.24	-10.81±4.36	-12.00±4.48	1.30±0.16	1.14±0.07
Precision							
Pressure (hPa)	Height (km)	Standard deviation (ppmv)		Mean combined precision errors (ppmv)			
		Coincidence	Trajectory	Coincidence	Trajectory		
123-8	15-33	0.91±0.44	0.48±0.36	0.62±0.12	0.62±0.12		

### 8.2.3 O<sub>3</sub>

#### 1 Coincident comparison for O<sub>3</sub>

##### 1.1 Flight No. 11

The intercomparisons of O<sub>3</sub> VMR between MIPAS-E and MIPAS-B for flight No. 11 are shown in Figure 8.2.3-1. According to the match situation, below the level of 30 hPa (24 km) MIPAS-B tangent geolocations are more close to the observation sites of Rec. 14 and above to Rec. 15. Panel A exhibits the comparisons of Rec. 14 to Seq. S and Rec. 15 to Seq. S. In general, both MIPAS-E profiles agree well with MIPAS-B in most of the height region. However, the spatial mismatch influence is clear. At high altitudes, the MIPAS-B profile is more consistent with the profile from Rec. 15 than that of Rec. 14. However, in the lower height region, Rec. 14 of MIPAS-E agrees with the MIPAS-B profile perfectly. Although the differences of consistency between the two comparisons are small in terms of absolute volume mixing ratio, this reflects the capability of MIPAS-E measurement in accuracy in some cases. Panel B presents the comparison of Rec. 16 to Seq. N3 with the ozonesonde profile measured over the launch pad of MIPAS-B several hours earlier before the Seq. N3 observation. Again a perfect agreement between MIPAS-B and MIPAS-E was obtained following a perfect co-location observation. As a reference, the profile made from ozonesonde agrees with MIPAS-B and MIPAS-E profiles well except above the altitude of about 10 hPa where ozonesonde data are not very reliable any more.

## 8. Intercomparison of measurements

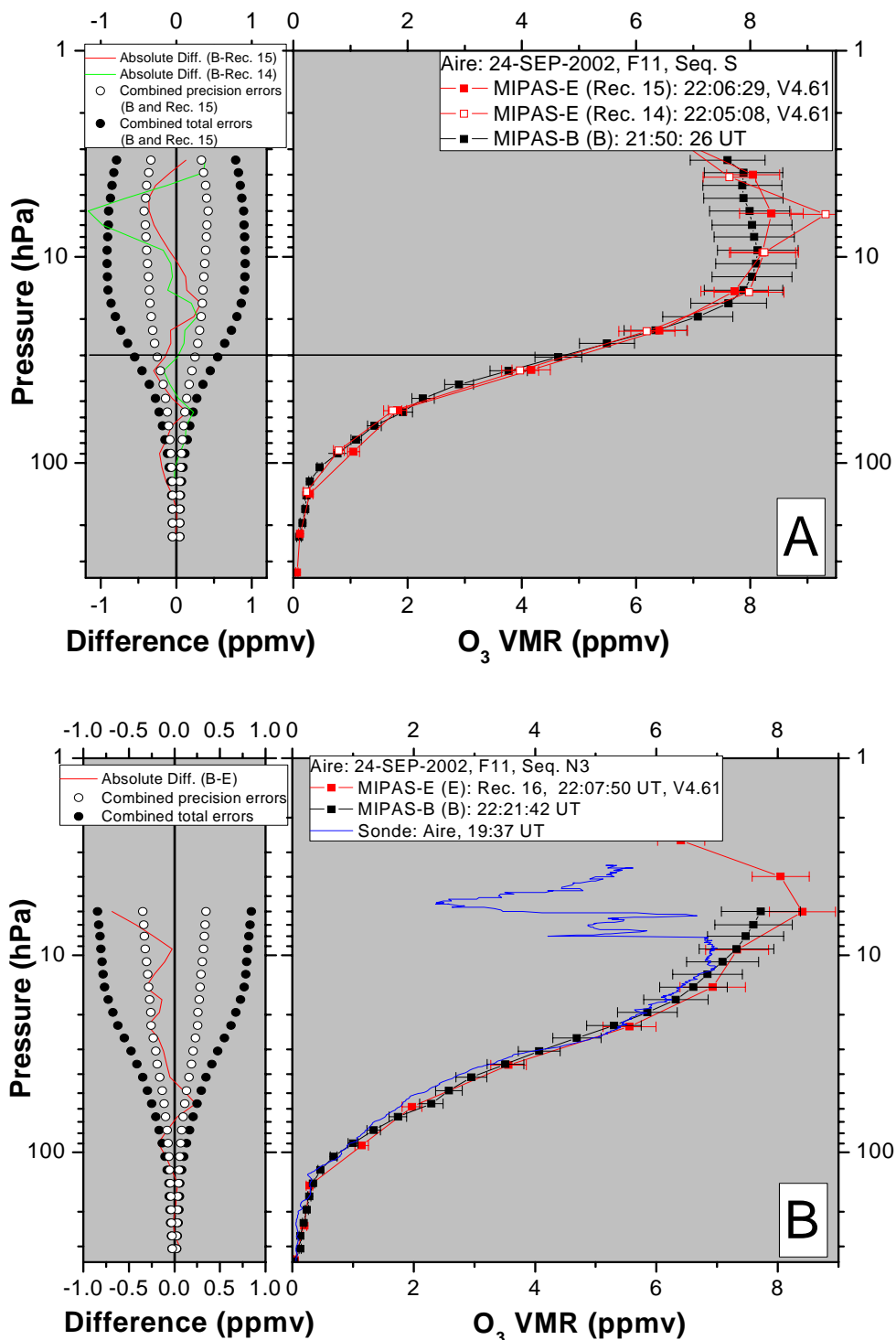


**Figure 8.2.3-1:** O<sub>3</sub> VMR comparisons for Flight No. 11. MIPAS-B profiles, black curves with black square symbols, the error bars represent the total errors; MIPAS-E profiles, red curves with red square symbols, the error bars represent the total errors; radiosonde profile, solid blue line; the absolute differences of MIPAS-B minus MIPAS-E, solid red line or solid green line; combined precision errors (the combination of MIPAS-E noise errors and MIPAS-B errors including the noise, LOS, and temperature errors), open circles; the combined total errors, solid circles. (A) Comparisons between Seq. S and Rec. 14, Seq. S and Rec. 15. Both kind of combined errors are calculated from the Seq. S and Rec. 15 data. If using Rec. 14 data, the combined errors are almost the same. The straight line denotes that below this level of altitude Seq. S should compare with Rec. 14 and above to Rec. 15. (B) Comparison between Seq. N3 and Rec. 16.

### 1.2 Flight No. 13

Two comparisons are shown in Figure 8.2.3-2 for flight No. 13. Panel A presents the comparison of Rec. 20 to Rec. N3a. The agreements are perfect in the upper part of the profiles although MIPAS-B scanned locations inside the polar vortex while MIPAS-E sounded the locations near the edge. Below the altitude of 48 hPa (20 km) a slightly larger discrepancy exists with respect to the combined total errors. The comparison of Rec. 30 with Seq. D15c plotted in Panel B indicates that MIPAS-E measurements are in agreement with the measurements from MIPAS-B quite well below the level of about 15 hPa (27 km). Above, MIPAS-E values are significantly higher than MIPAS-B measurements. Since this pair of measurements was carried out under excellent match quality, the large discrepancy may indicate a problem of the MIPAS-E data. The ozonesonde profile made from Kiruna compares with both MIPAS-B and MIPAS-E profiles. It shows that the ozonesonde data are more consistent with the MIPAS-B Seq. D15c profile though the time offset between ozonesonde and Seq. D15c is larger than that between ozonesonde and Seq. N3a. This is probably due to the fact that locations (67.9°N, 21.1°E) of the ozonesonde are more close to the tangent location of Seq. D15c than the location of Seq. N3a (see Appendix C, figure C-F).

## 8. Intercomparison of measurements

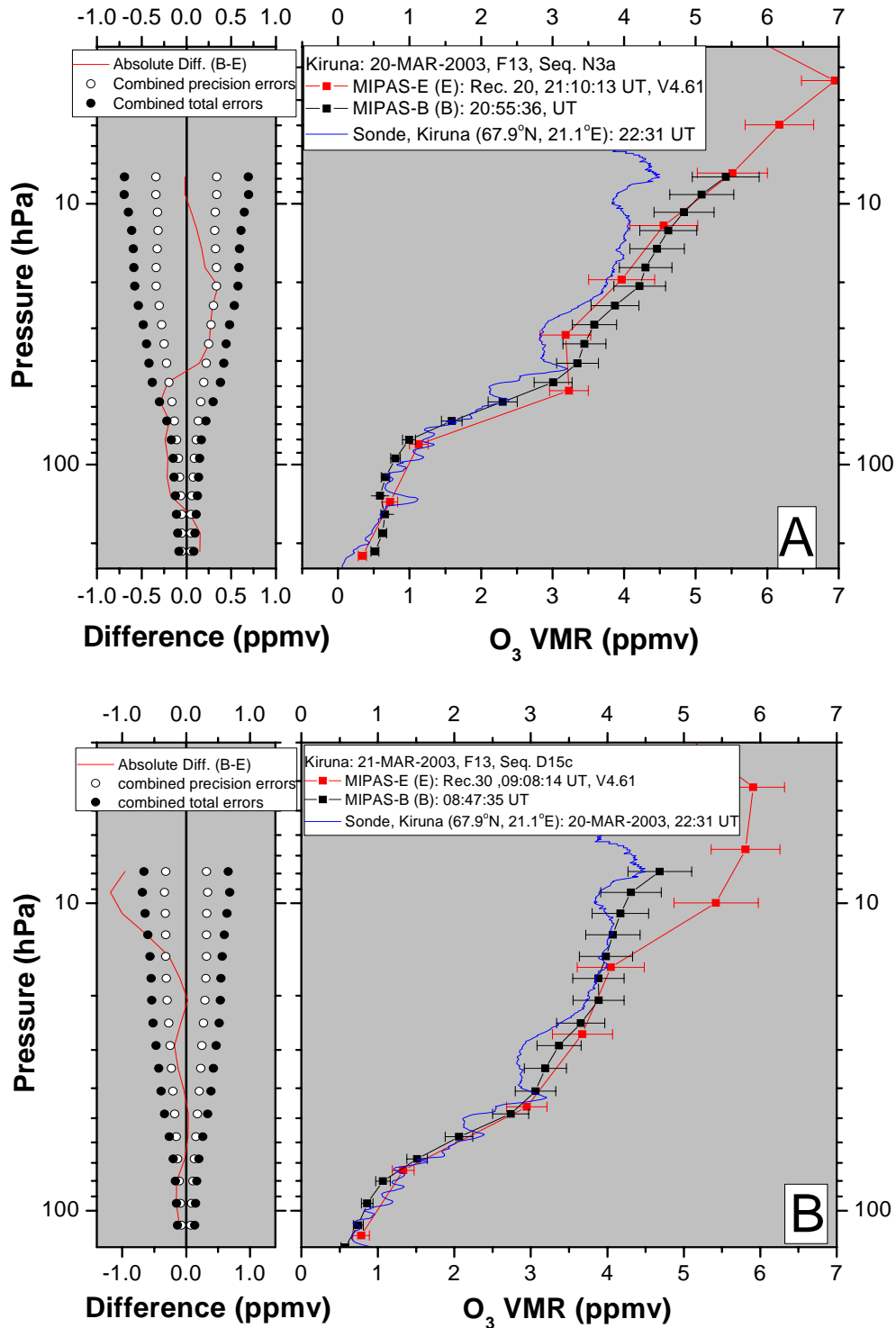


**Figure 8.2.3-2:** O<sub>3</sub> VMR comparisons for Flight No. 13. (A) Comparisons between Seq. N3a and Rec. 20. (B) Comparison between Seq. D15c and Rec. 30. The notation is the same as in Figure 8.2.3-1.

### 1.3 Flight No. 14

The only one available coincident comparison, Rec. 06 to Seq. 3, is plotted in Figure 8.2.3-3. Obviously, MIPAS-E measurements agree well with the MIPAS-B profile in the whole overlapping altitude region. The ozonesonde profile made about 5 hours ahead of the MIPAS-B measurement also shows a perfect agreement with the MIPAS-B profile and a good agreement with the MIPAS-E profile.



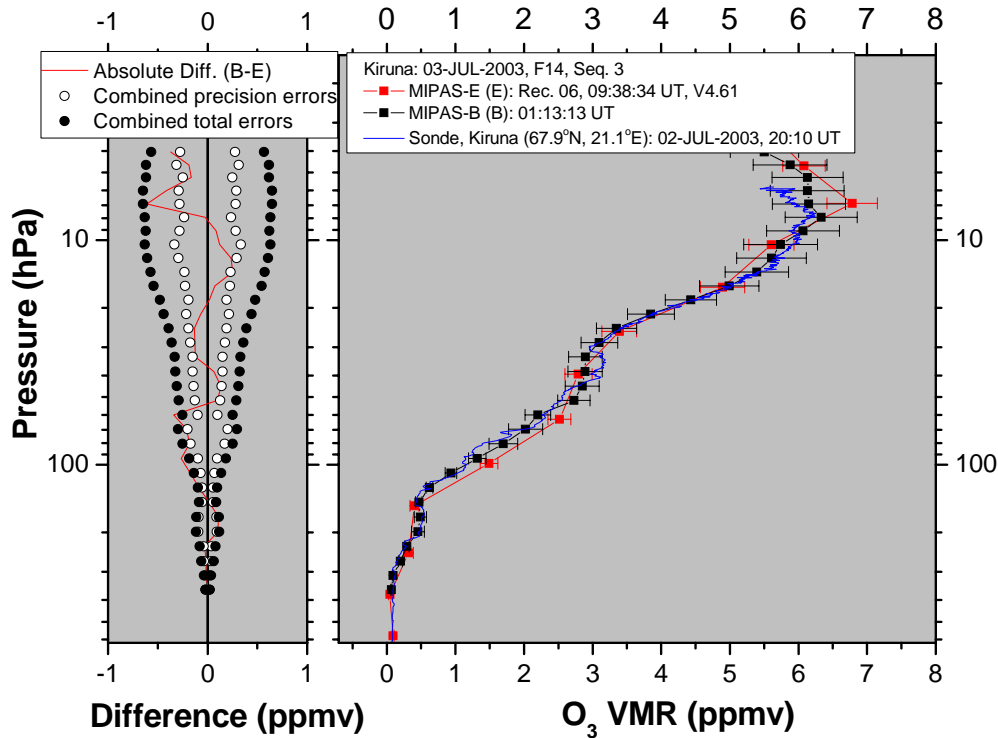


**Figure 8.2.3-3:** O<sub>3</sub> VMR comparisons for Flight No. 14 between Seq. 3 and Rec. 06. The notation is the same as in Figure 8.2.3-1.

## 2 Trajectory comparison for O<sub>3</sub>

### 2.1 Flight No. 11

The trajectory comparisons for Flight No.11 are presented in Figure 8.2.3-4 and 8.2.3-5. The scatter plots indicate that the data points are located fairly well along the diagonal line for all comparisons. And the coincident data points show the best consistency (Panel A of Figure 8.2.3-4). Near the top height region, MIPAS-E data show a slightly high bias (Panel A). Unlike the H<sub>2</sub>O VMR profile, all the scatter plots show that the O<sub>3</sub> VMR profiles of MIPAS-E have no oscillations. The comparisons between the mean profiles of MIPAS-E and MIPAS-B show that the two instruments measurements agree quite well. All the differences are within the combined total errors in the whole height region of comparison. Again, in Panel A of Figure 8.2.3-5, MIPAS-E profile exhibits a slightly higher discrepancy at high altitudes.

### 2.2 Flight No. 13

The scatter plots in Figure 8.2.3-6 confirm the good agreement between MIPAS-E and MIPAS-B measurements for O<sub>3</sub> VMR in general. The degree of scatter is slightly larger if comparing with the scatter plots for Flight No. 11. The profile comparisons presented in Figure 8.2.3-7 give similar results as the coincident comparisons. However, below the level of 29 hPa (23 km) the consistency between Seq. N3a profile and the correlative mean profile of MIPAS-E degraded comparing with the coincident comparison case. This may be due to the influences of polar vortex and the poor statistics. The high bias of MIPAS-E in the upper part (Panel B of Figure 8.2.3-7) is not a new feature, because the mean values in this region are mainly from the Rec. 30 which have been used for coincident comparison (Figure 8.2.3-2).

## 8. Intercomparison of measurements

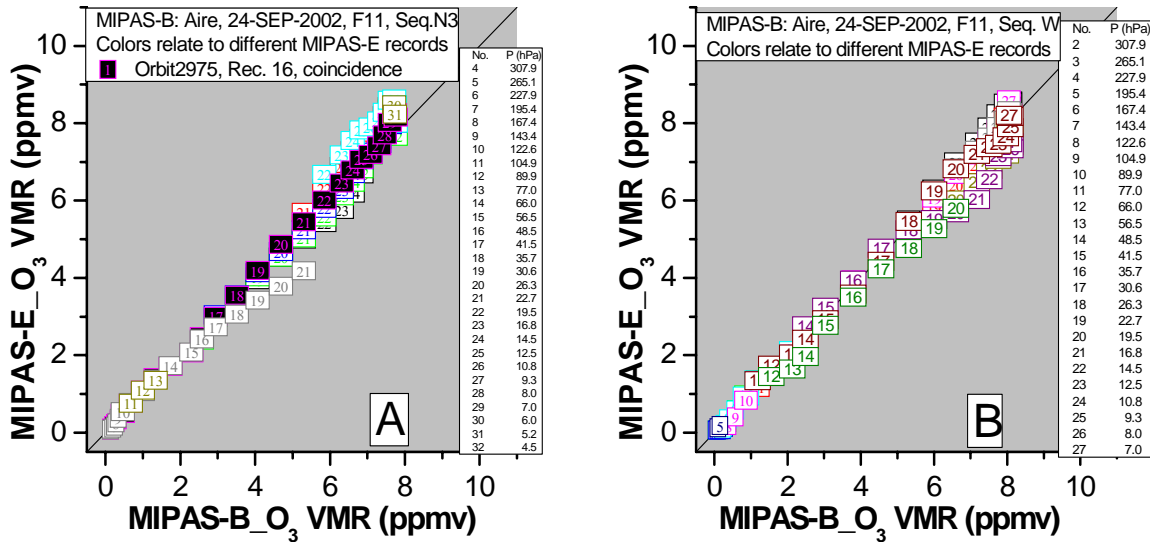


**Figure 8.2.3-4:** Scatter plots of MIPAS-E O<sub>3</sub> VMR against MIPAS-B O<sub>3</sub> VMR for match points found in two days forward and backward trajectories for Flight No. 11. (B) For Seq. N3. (C) For Seq. W. The numbers in the square symbols represent the pressure of the match points as listed in the legends. The solid squares denote the match points that have been found during the coincident comparisons. The solid straight lines are diagonals of squares. For clarity, the error bars were not shown here.

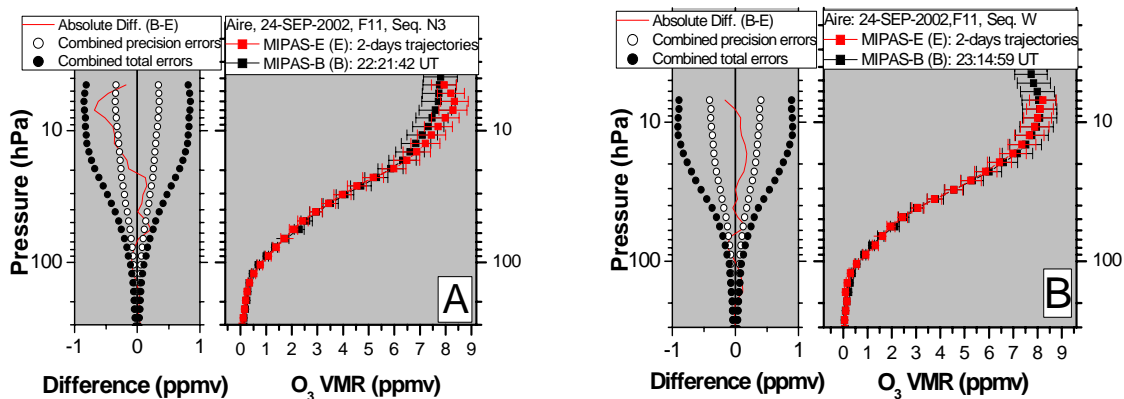


**Figure 8.2.3-5:** MIPAS-B O<sub>3</sub> VMR profiles comparison with MIPAS-E mean O<sub>3</sub> VMR profiles which were calculated by averaging all the match points at the same level of altitude considering the weights of the MIPAS-E noise errors. The notation is the same as in Figure 8.2.2-1. (A) For Seq. N3. (B) For Seq. W.

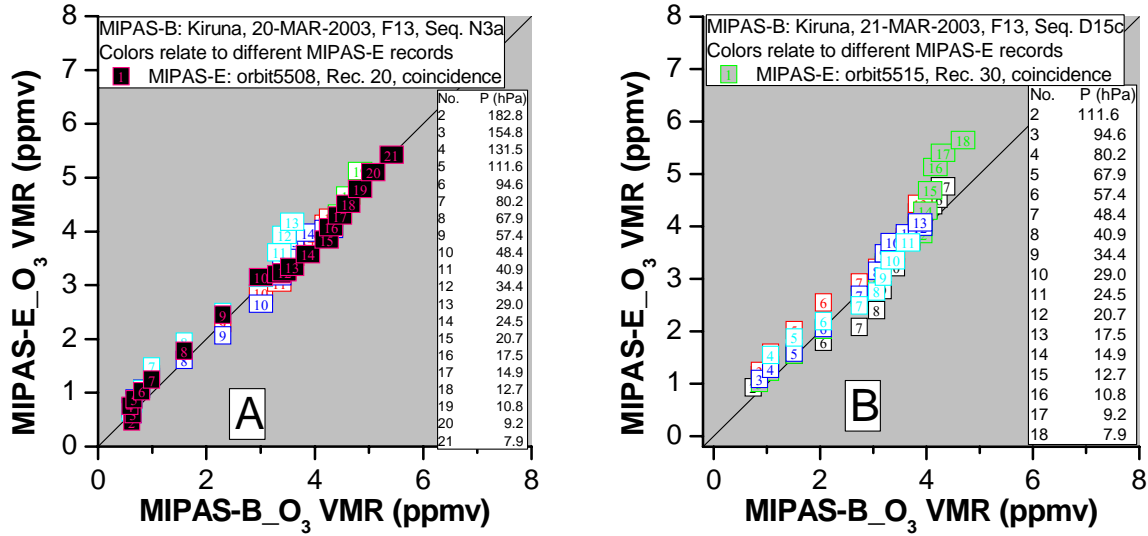


Figure 8.2.3-6: Same as Figure 8.2.3-4 but for Flight No. 13. (A) For Seq. N3a. (B) For Seq. D15c.

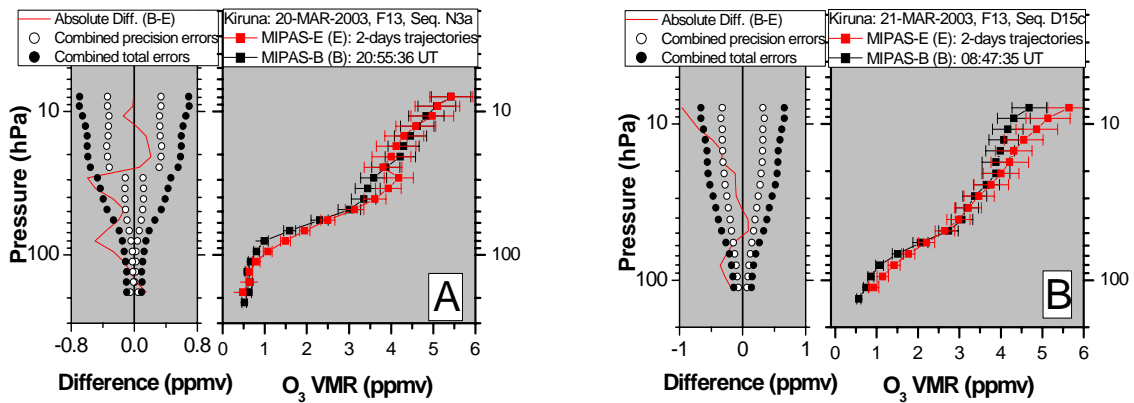


Figure 8.2.3-7: Same as Figure 8.2.3-5 but for Flight No. 13. (A) For Seq. N3a. (B) For Seq. D15c.

### 2.3 Flight No. 14

For Flight No. 14, the comparisons are plotted in Figures 8.2.3-8 and 8.2.3-9. Since more match points were found in the 2 days trajectories, the statistics are more significant than that for Flight No. 11 and 13. The compact points along the diagonal line in the scatter plots indicate the quite good consistency between MIPAS-E and MIPAS-B measurements. The profile comparisons show that the two instruments data agree well with respect to the combined total errors except at lower altitudes. MIPAS-E data tend to be a little bit higher than MIPAS-B values in the upper part.

## 8. Intercomparison of measurements

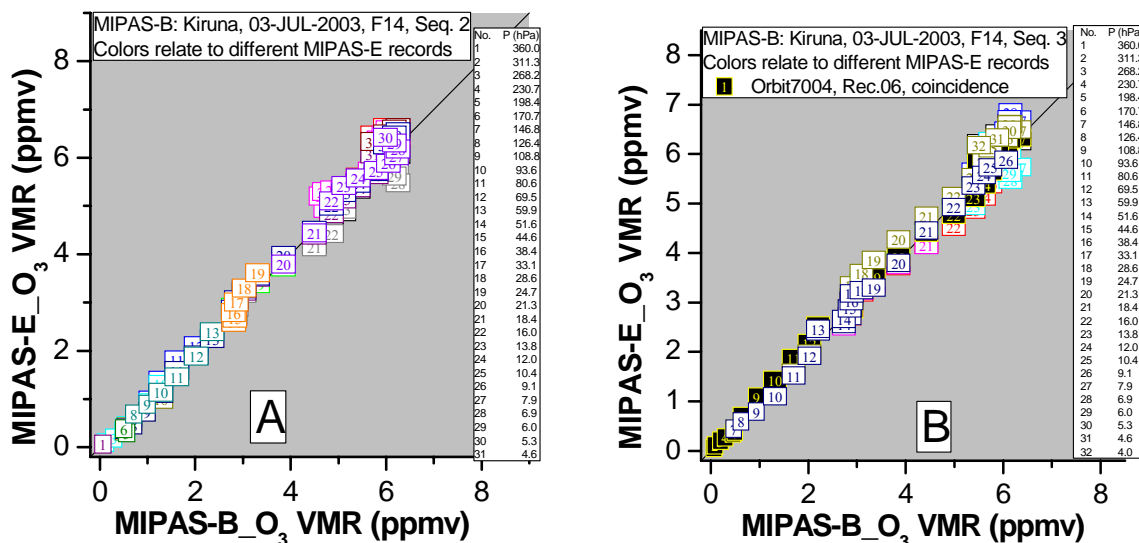


Figure 8.2.3-8: Same as Figure 8.2.3-4 but for Flight No. 14. (A) For Seq. 2. (B) For Seq. 3.

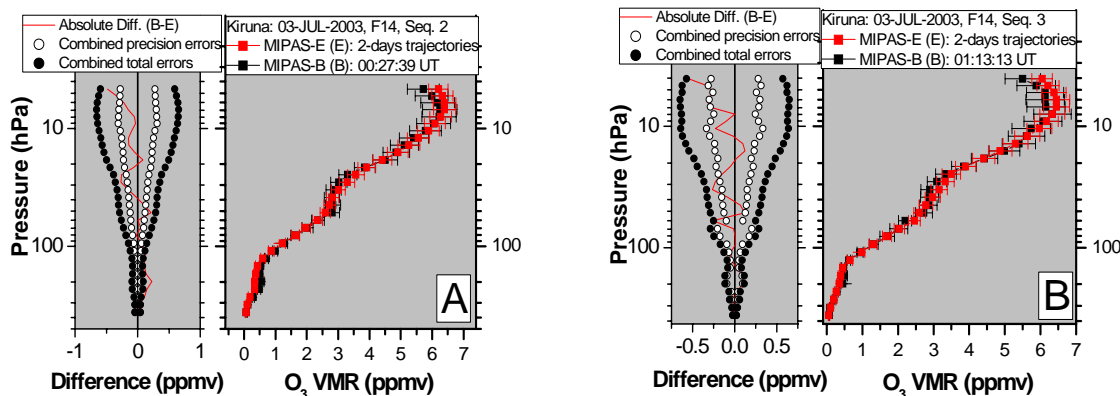


Figure 8.2.3-9: Same as Figure 8.2.3-5 but for Flight No. 14. (A) For Seq. 2. (B) For Seq. 3.

### 3 Summary of O<sub>3</sub> comparison

All difference profiles of MIPAS-B minus MIPAS-B for O<sub>3</sub> are plotted in Figure 8.2.3-10. As a whole impression, the agreements are quite well especially in the middle stratosphere. Below the level of about 143 hPa (14 km), MIPAS-E measured lower values than MIPAS-B. In the upper altitude region, the MIPAS-E values tend to be higher than MIPAS-B values. The largest difference of 1.2 ppmv was found at 9 hPa (30 km) during the coincident comparison.

The quantitative analysis of the summary comparison was done in two height regions (Table 8.4): below the level of 143 hPa (14 km) and above. MIPAS-E data show a low bias below the level of 143 hPa. Above this level, MIPAS-E measurements are larger than MIPAS-B data. Both differences are smaller than the mean combined total errors. In summary, MIPAS-E and MIPAS-B measurements are very consistent in the whole overlapping altitude region in the sense of statistics. However, there is a trend that MIPAS-E data tend to become larger than MIPAS-B data with increasing altitude.

The standard deviation and the corresponding mean combined precision errors of O<sub>3</sub> for coincident and trajectory comparisons show that MIPAS-E data for O<sub>3</sub> are compact.

In addition, unfavorable oscillation features seldom appeared in the O<sub>3</sub> VMR profiles made from MIPAS-E. From the point of MIPAS-B data, MIPAS-E is very successful in the O<sub>3</sub> measurements in the stratosphere.

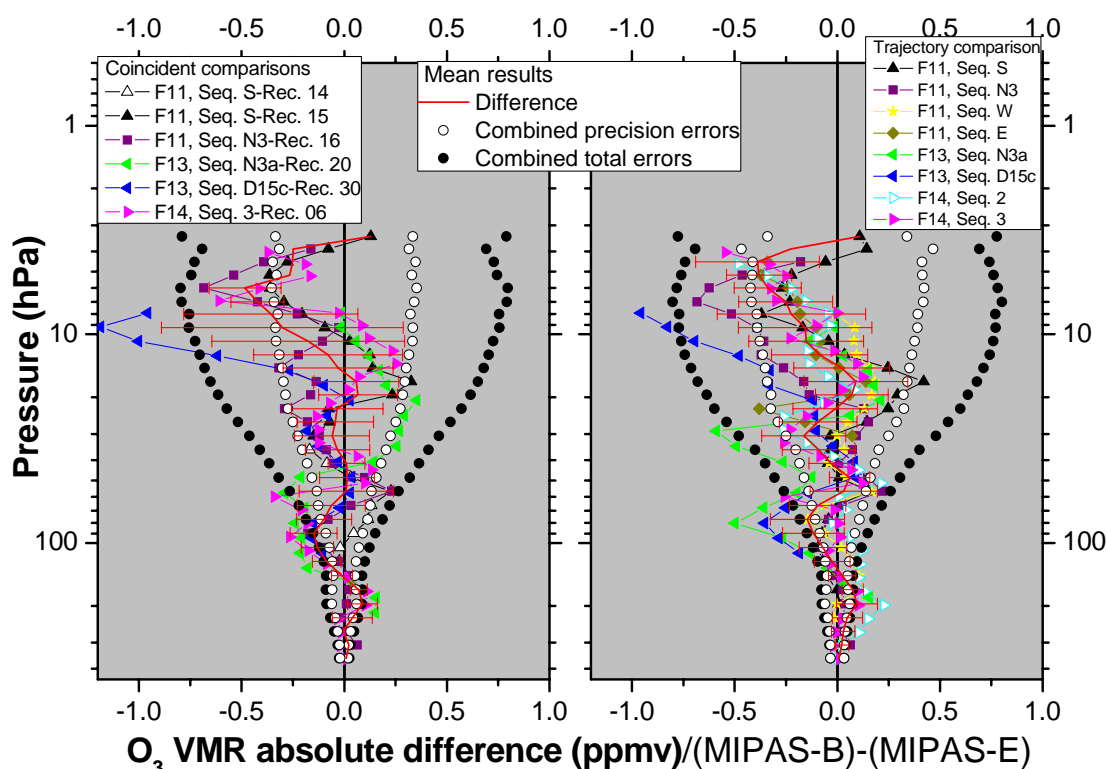


**Figure 8.2.3-10:** Summary comparison of O<sub>3</sub> VMR between MIPAS-E and MIPAS-B. There are no standard deviation bars for the top and bottom sections of the mean difference profile since only one or two comparisons are available in these altitude regions. Left: coincident comparison. Right: trajectory comparison.

**Table 8.4:** Mean differences of MIPAS-B minus MIPAS-E O<sub>3</sub> as well as the associated mean combined errors and the mean standard deviations.

Accuracy							
Pressure (hPa)	Height (km)	Absolute difference (ppmv)		Relative difference (%)		Mean combined total errors (ppmv)	
		Coincidence	Trajectory	Coincidence	Trajectory	Coincidence	Trajectory
356-143	8-14	0.05±0.03	0.05±0.03	11.02±7.03	14.49±5.70	0.07±0.02	0.06±0.02
143-3	14-39	-0.10±0.14	-0.09±0.13	-3.95±5.30	-3.30±4.41	0.48±0.24	0.52±0.25
Precision							
Pressure (hPa)	Height (km)	Standard deviation (ppmv)		Mean combined precision errors (ppmv)			
		Coincidence	Trajectory	Coincidence	Trajectory		
123-8	15-33	0.22±0.14	0.19±0.07	0.21±0.10	0.24±0.12		

## 8.2.4 HNO<sub>3</sub>

### 1 Coincident comparison for HNO<sub>3</sub>

#### 1.1 Flight No. 11

The HNO<sub>3</sub> coincident comparisons for Flight No. 11 are shown in two panels of Figure 8.2.4-1. The comparisons between MIPAS-B Seq. S and MIPAS-E Rec. 14 and 15 illustrate the

## 8. Intercomparison of measurements

spatial offset effects clearly (Panel A). Below the level of about 31 hPa (24 km), Seq. S is the nearest observation of Rec. 14. The agreements between them are much better than the agreements between Seq. S and Rec. 15. Unfortunately, the oscillation of Rec. 14 profile around the 31 hPa level is an exception among the good agreements. Above the level of 31 hPa, Seq. S is the nearest observation of Rec. 15 instead of Rec. 14. Although the agreements between Seq. S and Rec. 15 are similar to Seq. S and Rec. 14 and both consistencies are well in general, the agreement between Seq. S and Seq. Rec. 15 is a little bit better than the agreement between Seq. S and Rec. 14 at the higher altitude. Also, Rec. 15 profile has the oscillation features. In one word, the comparison between Seq. S and Rec. 14 and/or Rec. 15 exhibits a high degree of agreement between the two instruments observations. However, the oscillation of MIPAS-E profile hampers the further increase of the consistency. The comparison between Seq. N3 and Rec. 15 shows that the two measurements agree quite well. Almost all the measurement differences are within the combined total errors. Reminding the excellent match quality for this pair of profiles, it can be concluded that MIPAS-B and MIPAS-E measurements for HNO<sub>3</sub> have the capability to reach a very high degree of agreement at mid latitudes.

### 1.2 Flight No. 13

For Flight No. 13, two coincident comparisons are available (Figure 8.2.4-2). The comparison of Seq. N3a with Rec. 20 (Panel A) indicates that the two instruments measurements agree in general. However, in small altitude regions, the discrepancies are obviously beyond the combined total errors. This is understandable if taking into account the potential vorticity of the tangent location shown in Panel B of Figure 8.1.1-2. The altitude regions where the large discrepancies exist are roughly consistent with the region where the PV differences of the tangent points are also significant. Another feature in Panel A is that the peak position of the MIPAS-E profile is about 2 km lower than that of MIPAS-B. We also suspect that it was caused by the polar vortex though the evidence is not clear. The altitude distance between the tangent points of these two instruments may influence the result. Obviously, contribution of the spatial offset to the Rec. 20 to Seq. N3a comparison exists. Unfortunately, further quantitative analysis is impossible at present. The comparison between Rec. 30 and Seq. D15c (Panel B) shows that MIPAS-E profile agrees well with MIPAS-B if smoothing the oscillation effects made from MIPAS-E profile. The peak positions of the two profiles are close though the peak position of MIPAS-E is still a little bit lower compared to MIPAS-B due to the use of different vertical resolutions. The good agreement between Rec. 30 and Seq. D15c indirectly confirm that the discrepancies in Rec. 20 to Seq. N3a are partly caused by the spatial mismatch.

## 8.2 MIPAS

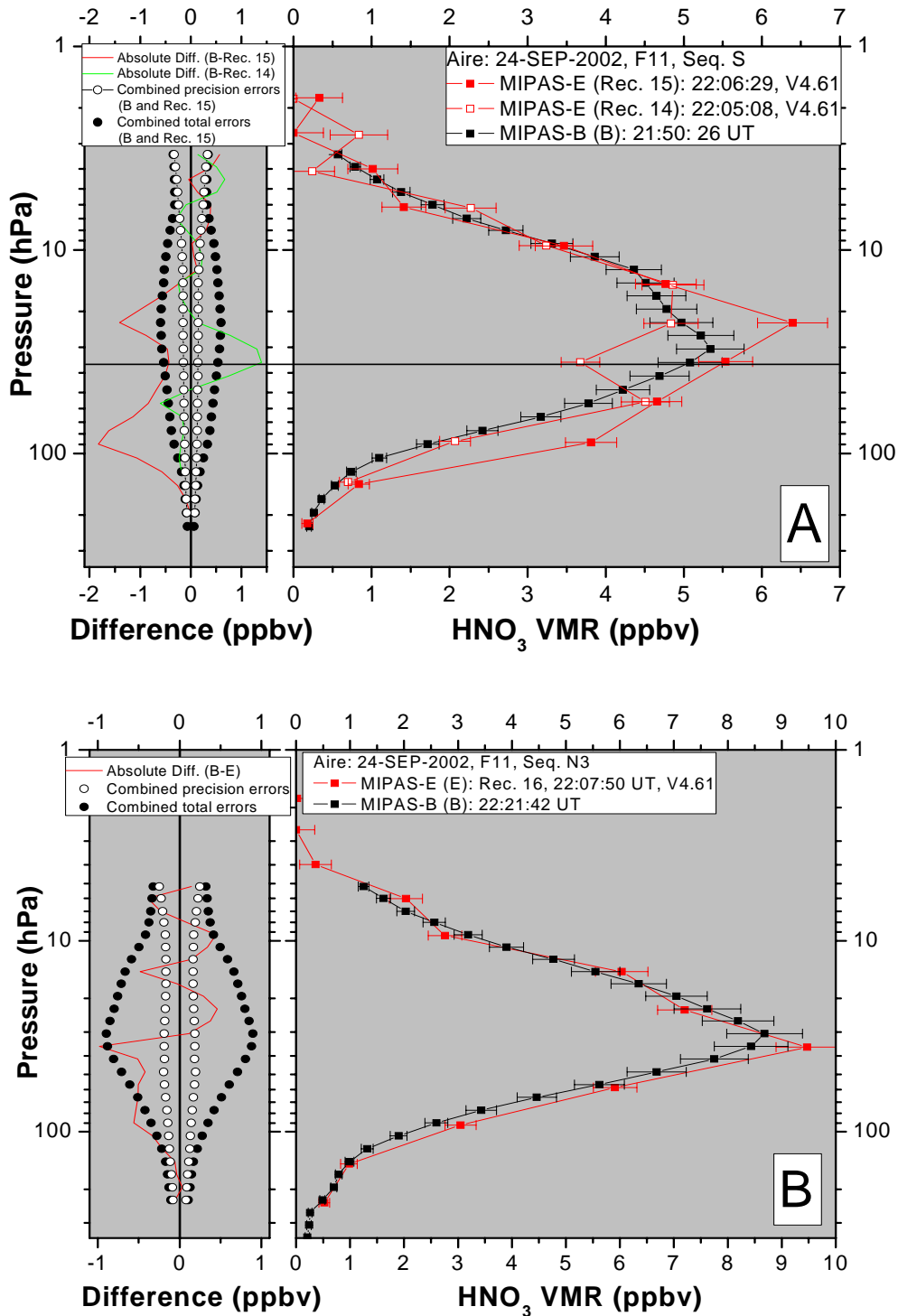


**Figure 8.2.4-1:** HNO<sub>3</sub> VMR comparisons for Flight No. 11. MIPAS-B profiles, black curves with black square symbols, the error bars represent the total errors; MIPAS-E profiles, red curves with red square symbols, the error bars represent the total errors; the absolute differences of MIPAS-B minus MIPAS-E, solid red line or solid green line; combined precision errors (the combination of MIPAS-E noise errors and MIPAS-B errors including the noise, LOS, and temperature errors), open circles; the combined total errors, solid circles. (A) Comparisons between Seq. S and Rec. 14, Seq. S and Rec. 15. Both kind of combined errors are calculated from the Seq. S and Rec. 15 data. If using Rec. 14 data, the combined errors are almost the same. The straight line denotes that below this level of altitude Seq. S should compare with Rec. 14 and above to Rec. 15. (B) Comparison between Seq. N3 and Rec. 16.

## 8. Intercomparison of measurements

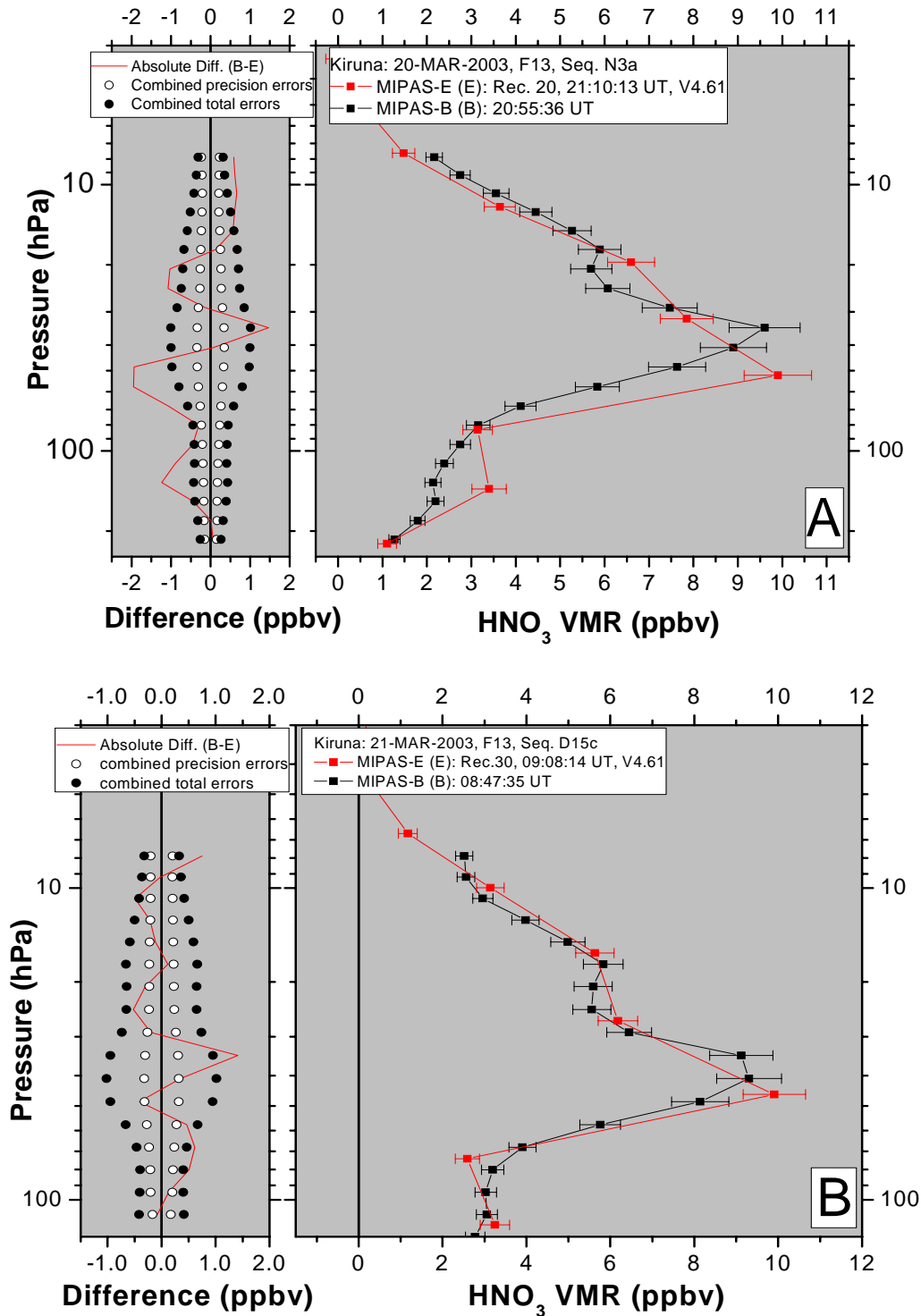


**Figure 8.2.4-2:** HNO<sub>3</sub> VMR comparisons for Flight No. 13. (A) Comparisons between Seq. N3a and Rec. 20. (B) Comparison between Seq. D15c and Rec. 30. The notation is the same as in Figure 8.2.4-1.

### 1.3 Flight No. 14

The only coincident comparison for Flight No. 14 is shown in Figure 8.2.4-3. The discrepancies which are beyond the combined total errors lie in the height region of 147-60 hPa (14-20 km) and the region near the top and lower altitude. The discrepancy at high altitudes may be partly caused by the large spatial offset. As a whole, the consistency is good



especially concerning the structure of the profiles: the peak position and the turning point at about 152 hPa both were characterized consistently by MIPAS-B and MIPAS-E profiles.

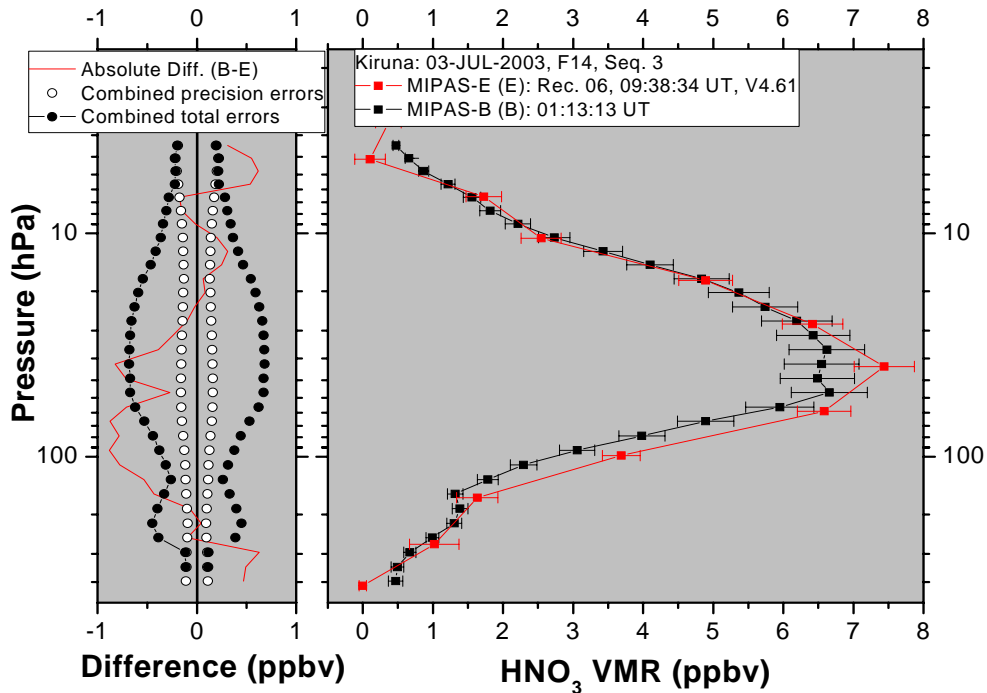


**Figure 8.2.4-3:** HNO<sub>3</sub> VMR comparisons for Flight No. 14 between Seq. 3 and Rec. 06. The notation is the same as in Figure 8.2.4-1.

## 2 Trajectory comparison for HNO<sub>3</sub>

### 2.1 Flight No. 11

Four pairs of comparisons are available in Flight No. 11. Two of them are plotted in Figure 8.2.4-4 and 8.2.4-5. The scatter plots in Figure 8.2.4-4 disclose the details of the comparison between MIPAS-E and MIPAS-B. These scatter plots show that the two instruments measurements agree with each other in general. The scatter plots also imply that only part of the MIPAS-E profiles have oscillation features. The profile comparison in Figure 8.2.4-5 shows that the MIPAS-E measurements agree well with the MIPAS-B data in most altitude regions. The discrepancies mainly appeared at the higher altitudes and/or lower altitudes (Figure 8.2.4-5).

## 8. Intercomparison of measurements

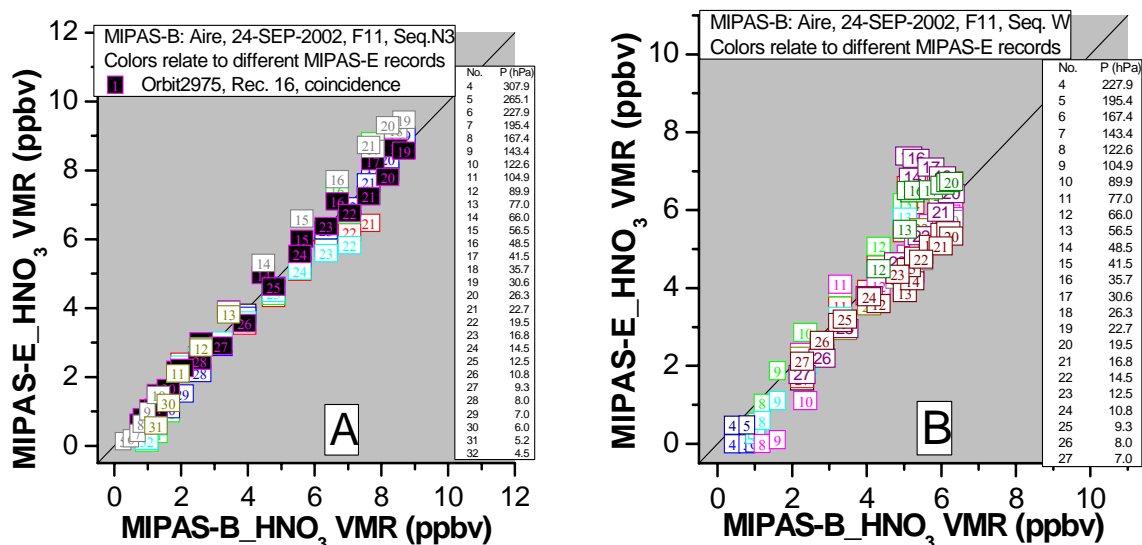


**Figure 8.2.4-4:** Scatter plots of MIPAS-E  $\text{HNO}_3$  VMR against MIPAS-B  $\text{HNO}_3$  VMR for match points found in two days forward and backward trajectories for Flight No. 11. (A) For Seq. N3. (B) For Seq. W. The numbers in the square symbols represent the pressure of the match points as listed in the legends. The solid squares denote the match points that have been found during the coincident comparisons. The solid straight lines are diagonals of squares. For clarity, the error bars were not shown here.

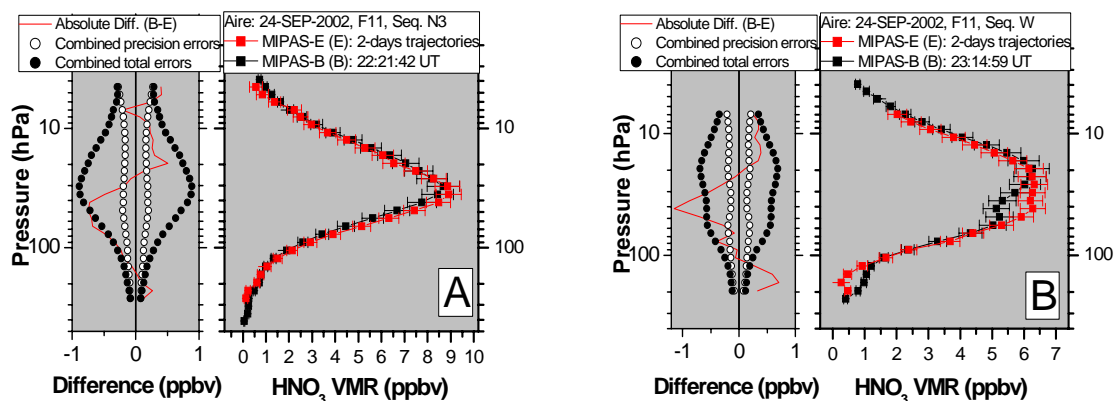


**Figure 8.2.4-5:** MIPAS-B  $\text{HNO}_3$  VMR profiles comparison with MIPAS-E mean  $\text{HNO}_3$  VMR profiles which were calculated by averaging all the match points at the same level of altitude considering the weights of the MIPAS-E noise errors. The notation is the same as for Figure 8.2.2-1. (A) For Seq. N3. (B) For Seq. W.

### 2.2 Flight No. 13

The feature of the two scatter plots appearing in Figure 8.2.4-6 is very similar to the scatter plot for  $\text{H}_2\text{O}$  (Figure 8.2.2-6), i.e., the points spread in a broad region. The reasons are also similar, i.e., the oscillation of the  $\text{HNO}_3$  VMR profiles of MIPAS-E and the polar vortex influence. Since the amplitude of the oscillation and the oscillating part of the profiles is not as large as for the  $\text{H}_2\text{O}$  VMR profiles, the degree of scatter shown here is lower than in the case of  $\text{H}_2\text{O}$ . Despite the spread of the points, the distribution of the points is around the diagonal straight line. The comparisons of the mean profiles of MIPAS-E with MIPAS-B retrievals show that the two instruments have got consistent results in general though the discrepancies at lower altitudes are still more or less beyond the combined total errors. Comparing with the corresponding coincident cases, the consistency in trajectory comparison for Seq. N3a was improved since the statistics reduces the spatial offset contribution to the comparison result. On the contrary, the agreement degraded in the trajectory comparison for Seq. D15c because the match quality for the coincident measurements was much better than

the criteria (500 km, 1 h) set for the trajectory method. The uncertainty becomes apparent here since the statistics significance is not good enough.

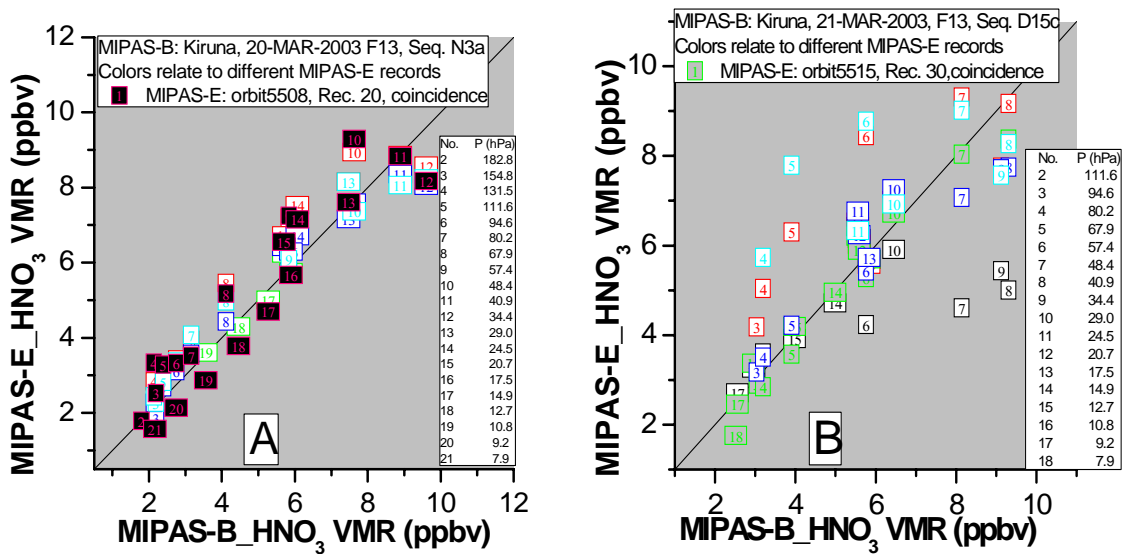


Figure 8.2.4-6: Same as Figure 8.2.4-4 but for Flight No. 13. (A) For Seq. N3a. (B) For Seq. D15c.

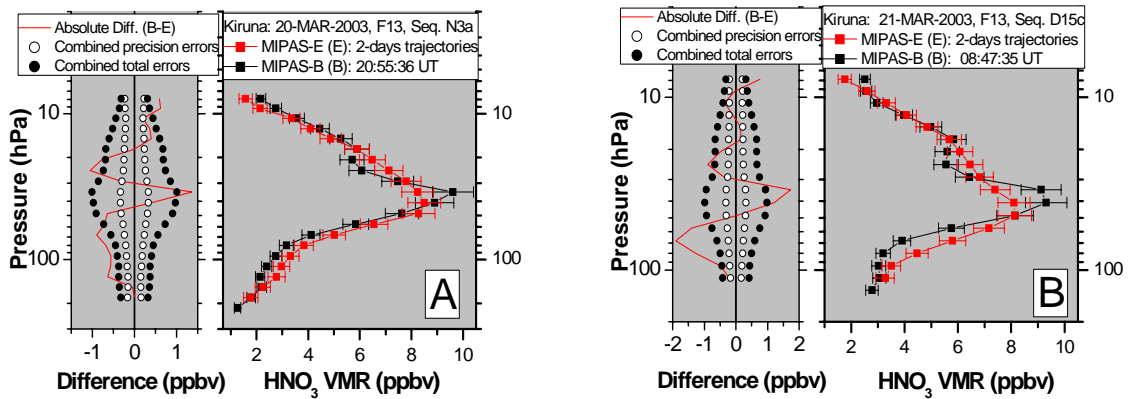


Figure 8.2.4-7: Same as Figure 8.2.4-5 but for Flight No. 13. (A) For Seq. N3a. (B) For Seq. D15c.

### 2.3 Flight No. 14

Figure 8.2.4-8 and Figure 8.2.4-9 present the trajectory comparisons for Flight No. 14. The compact points in the scatter plots distributes along the straight line of expectation indicate that MIPAS-E HNO<sub>3</sub> measurements agree with MIPAS-B data quite well. The exception appeared at the higher and/or lower altitudes. These judgments can be seen more clearly in the profiles comparison (Figure 8.2.4-9).

## 8. Intercomparison of measurements

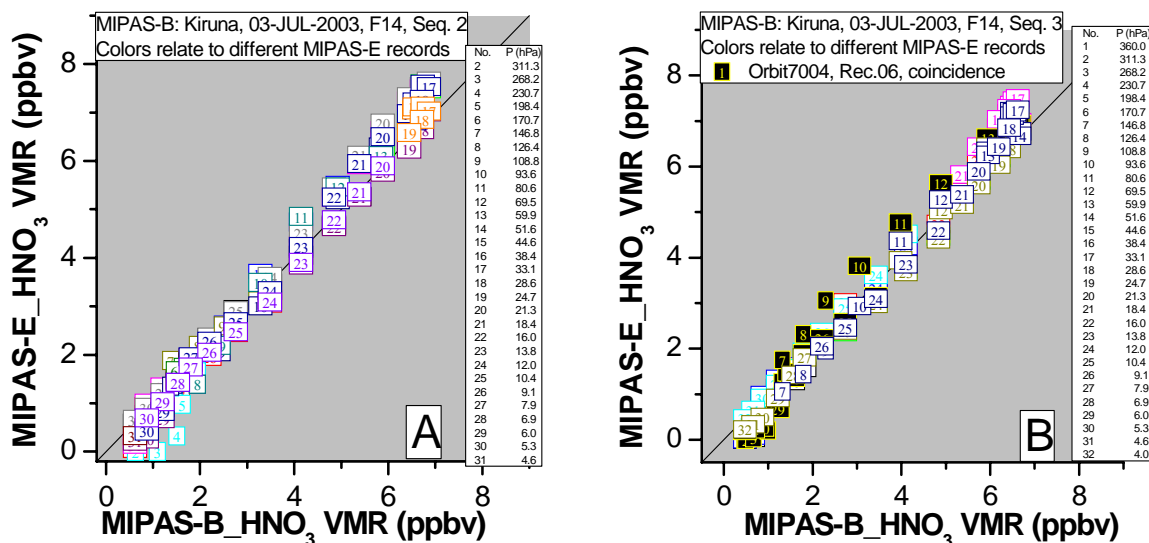


Figure 8.2.4-8: Same as Figure 8.2.4-4 but for Flight No. 14. (A) For Seq. 2. (B) For Seq. 3.

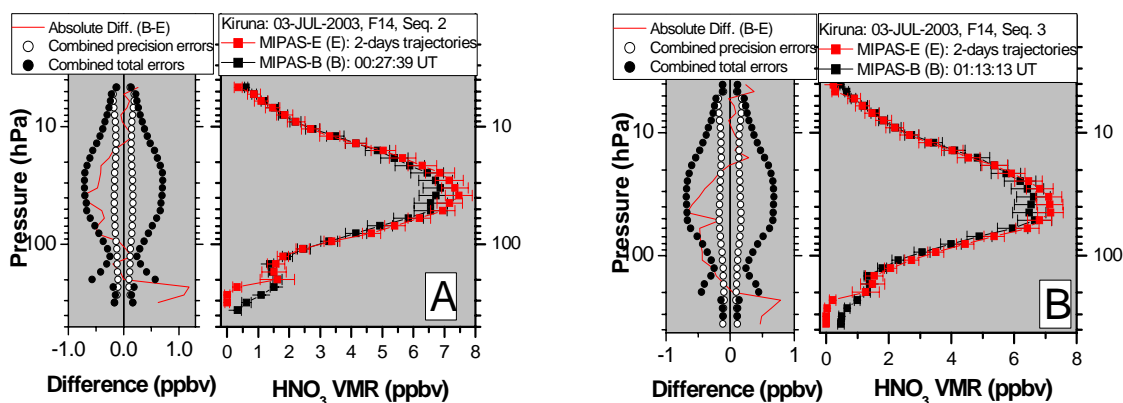


Figure 8.2.4-9: Same as Figure 8.2.4-5 but for Flight No. 14. (A) For Seq. 2. (B) For Seq. 3.

### 3 Summary of HNO<sub>3</sub> comparison

All difference profiles of MIPAS-B minus MIPAS-B for HNO<sub>3</sub> are plotted in Figure 8.2.4-10. In general, the agreements are good. At the lowest altitudes, MIPAS-E measured lower values than MIPAS-B. In the upper part MIPAS-E values also tend to be lower than MIPAS-B data with increasing altitude. The maximum of the discrepancy can reach up to about 2 ppbv due to the oscillation of the MIPAS-E profiles.

The quantitative analysis of the summary comparison was performed in three height regions according to where the MIPAS-E bias is systematically positive or negative (Table 8.5): 356-167 hPa (8-13 km), 167-15 hPa (13-29 km), and 15-3 hPa (29-39 km). MIPAS-E data show a low bias compared to MIPAS-B measurements below the level of 167 hPa. Between 167-15 hPa, MIPAS-E measurements are larger than MIPAS-B data. Above the level of 15 hPa, MIPAS-E values again become lower than MIPAS-B data. All the biases are mostly smaller than the mean combined total errors.

The standard deviation and the corresponding mean combined precision errors of HNO<sub>3</sub> for the coincident case are (0.52 ppbv, 0.19 ppbv). For the trajectory comparison, the values are (0.38 ppbv, 0.18 ppbv). Consequently, MIPAS-E data for HNO<sub>3</sub> show some scatter features.

In summary, MIPAS-E and MIPAS-B measurements of  $\text{HNO}_3$  are consistent in the whole overlapping altitude region in the sense of statistics. Unfavorable oscillation features sometimes appear in the  $\text{HNO}_3$  VMR profiles of MIPAS-E leading to a standard deviation exceeding the precision but not as strong as in the  $\text{H}_2\text{O}$  profiles.

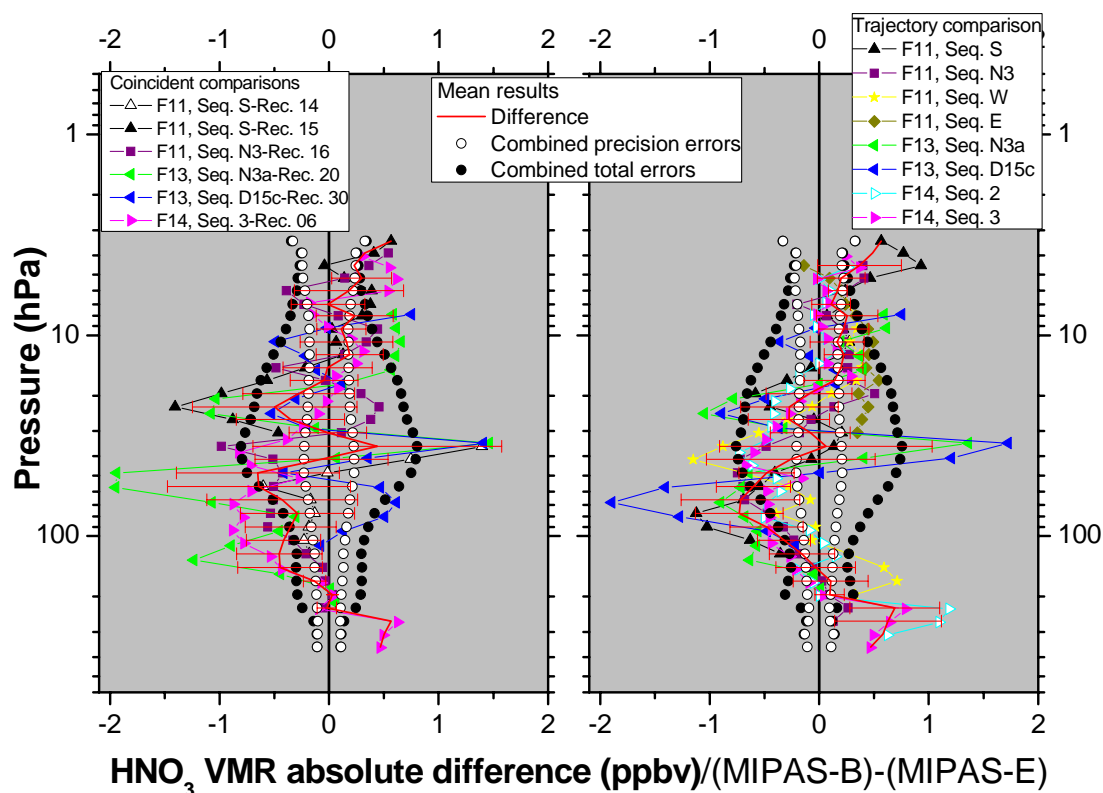


Figure 8.2.4-10: Summary comparison of  $\text{HNO}_3$  VMR between MIPAS-E and MIPAS-B. There are no standard deviation bars for the top and bottom sections of the mean difference profile since only one or two comparisons are available in these altitude regions. Left: coincident comparison. Right: trajectory comparison.

Table 8.5: Mean differences of MIPAS-B minus MIPAS-E  $\text{HNO}_3$  as well as the associated mean combined errors and the mean standard deviations.

Accuracy							
Pressure (hPa)	Height (km)	Absolute difference (ppbv)		Relative difference (%)		Mean combined total errors (ppbv)	
		Coincidence	Trajectory	Coincidence	Trajectory	Coincidence	Trajectory
356-167	8-13	0.17±0.27	0.43±0.29	31.14±50.70	57.01±39.77	0.22±0.08	0.21±0.10
167-15	13-29	-0.27±0.27	-0.24±0.29	-8.70±8.74	-6.28±9.33	0.56±0.19	0.54±0.18
15-3	29-39	0.19±0.11	0.23±0.10	15.03±21.78	15.03±20.61	0.36±0.09	0.36±0.09
Precision							
Pressure (hPa)	Height (km)	Standard deviation (ppbv)		Mean combined precision errors (ppbv)			
		Coincidence	Trajectory	Coincidence	Trajectory		
123-8	15-33	0.52±0.23	0.38±0.20	0.19±0.03	0.18±0.02		

## 8.2.5 CH<sub>4</sub>

### 1 Coincident comparison for CH<sub>4</sub>

#### 1.1 Flight No. 11

For Flight No. 11, the coincident comparisons were performed between Seq. S and Rec. 14, Seq. S and Rec.15 (Panel A of Figure 8.2.5-1) as well as between Seq. N3 and Rec. 16. (Panel B of Figure 8.2.5-1). Considering the match quality described previously, Seq. S should compare with Rec. 14 below the level of about 31 hPa (24 km) and above with Rec. 15. The profiles in Panel A illustrate that the degree of agreement between Rec. 14 and Seq. S below the level of 31 hPa is similar to the consistency between Rec. 15 and Seq. S and even becomes worse near the region of 31 hPa. This may be due to the small horizontal gradient of CH<sub>4</sub> VMR and the obvious oscillation appearing in the Rec. 14 profile. Above the altitude of 31 hPa, the consistency between Seq. S and Rec.14 is also similar to the comparison between Seq. S and Rec. 15 although the latter has better match quality.

The excellent match quality of Rec. 16 to Seq. N3 provided a good opportunity to exhibit how high consistency can be reached between MIPAS-E and MIPAS-B observations for CH<sub>4</sub> VMR. Panel B gives the comparison result. It can be concluded that the agreement is perfect if disregarding the oscillation of MIPAS-E profile around 143 hPa (14 km) and small oscillations at higher altitudes.

#### 1.2 Flight No. 13

The comparison between Rec. 20 of MIPAS-E with Seq. N3a of MIPAS-B is not always straight forward due to the existence of the larger PV offset (see Panel B of Figure 8.1.1-2). Due to the strong oscillation of Rec. 20 profile it is difficult to analyze if the spatial mismatch has been impacting the discrepancy significantly. MIPAS-E values between 80 and 150 hPa are unrealistically high (Panel A of Figure 8.2.5-2). The comparison of Rec. 30 to Seq. D15c presented in Panel B shows that MIPAS-E measurements agree well with MIPAS-B profiles in general (Panel B of Figure 8.2.5-2). The lower dip in MIPAS-B profile at 29 hPa (23 km) which is caused by a strong subsidence of air masses in the vortex is not correctly represented by MIPAS-E profile. Further, in the upper troposphere, MIPAS-E gives unrealistic low data due to the profile oscillation.

#### 1.3 Flight No. 14

The only one coincident comparison, Rec. 06 to Seq. 3, is presented in Figure 8.2.5-3. The difference profiles indicate that MIPAS-E agrees quite well with the MIPAS-B measurements. An exception appears around the 147 hPa (14 km) where the MIPAS-E gives higher values due to the oscillation of the profile. The good agreements suggest that the larger time offset as much as 8.5 hours did not impact the comparison because of the chemical stability of CH<sub>4</sub> species and the stability of polar summer weather.

## 8.2 MIPAS

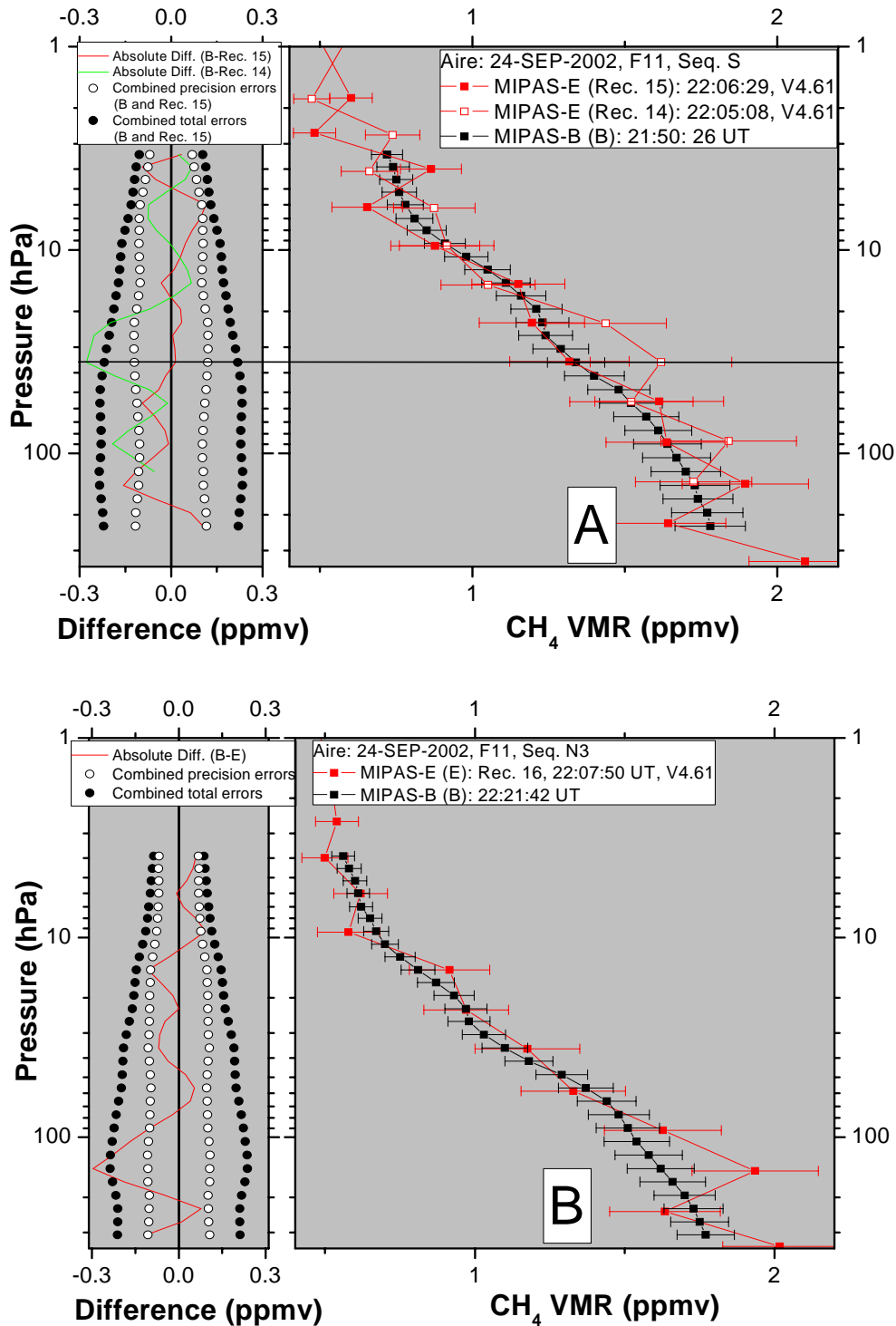


**Figure 8.2.5-1:** CH<sub>4</sub> VMR comparisons for Flight No. 11. MIPAS-B profiles, black curves with black square symbols, the error bars represent the total errors; MIPAS-E profiles, red curves with red square symbols, the error bars represent the total errors; absolute differences of MIPAS-B minus MIPAS-E, solid red line or solid green line; combined precision errors (the combination of MIPAS-E noise errors and MIPAS-B errors including the noise, LOS, and temperature errors), open circles; the combined total errors, solid circles. (A) Comparisons between Seq. S and Rec. 14, Seq. S and Rec. 15. Both kind of combined errors are calculated from the Seq. S and Rec. 15 data. If using Rec. 14 data, the combined errors are almost the same. The straight line denotes that below this level of altitude Seq. S should compare with Rec. 14 and above to Rec. 15. (B) Comparison between Seq. N3 and Rec. 16.

8. Intercomparison of measurements

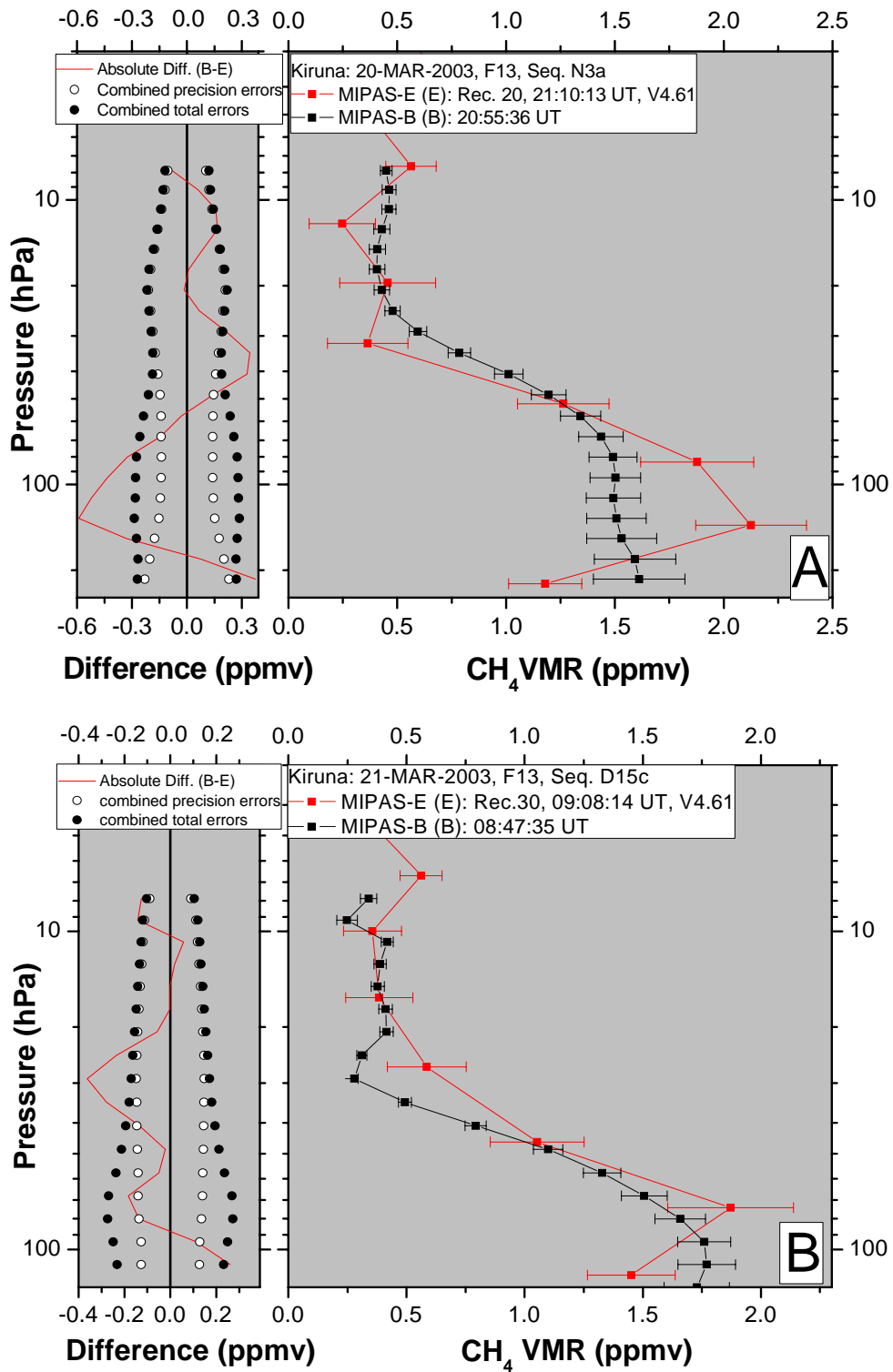


**Figure 8.2.5-2:** CH<sub>4</sub> VMR comparisons for Flight No. 13. (A) Comparisons between Seq. N3a and Rec. 20. (B) Comparison between Seq. D15c and Rec. 30. The notation is the same as in Figure 8.2.5-1.



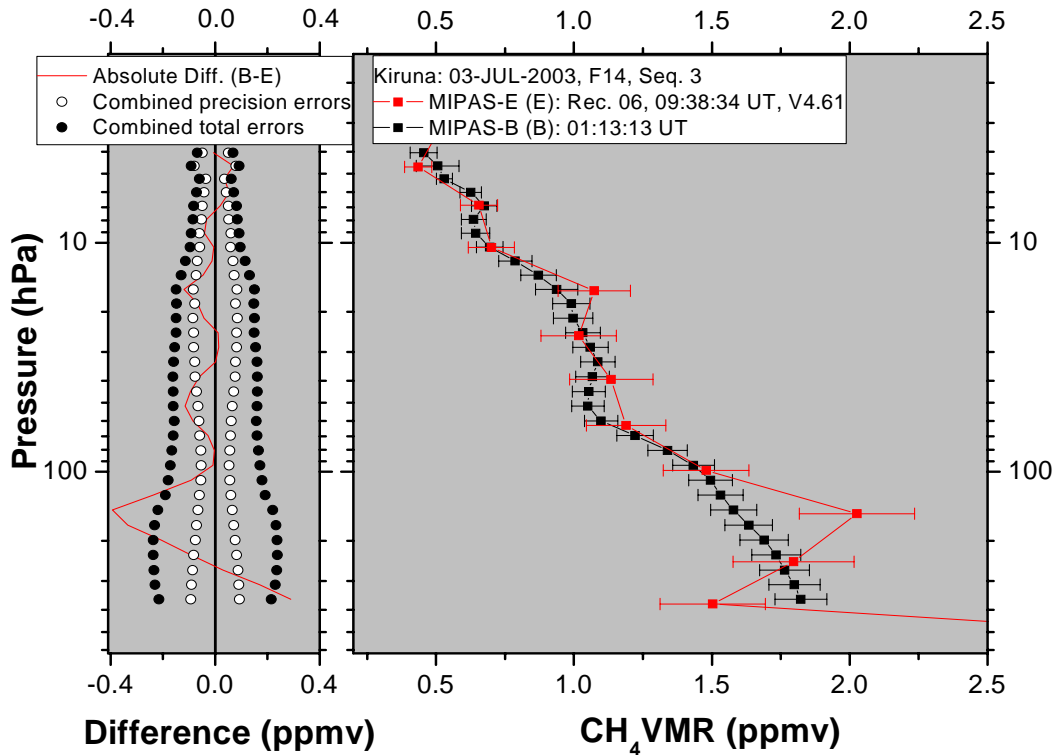


**Figure 8.2.5-3:** CH<sub>4</sub> VMR comparisons for Flight No. 14 between Seq. 3 and Rec. 06. The notation is the same as in Figure 8.2.5-1.

## 2 Trajectory comparison for CH<sub>4</sub>

### 2.1 Flight No. 11

There are four trajectory comparisons during Flight No. 11. Two of them are exhibited as scatter plots and vertical profiles in Figures 8.2.5-4 and 8.2.5-5, separately. Two features can be extracted from the scatter plot. First, some MIPAS-E profiles have oscillations. Secondly, MIPAS-E measurements are higher than MIPAS-B data at lower altitudes. The profile comparisons show that the measurements between MIPAS-E and MIPAS-B for CH<sub>4</sub> are consistent with respect to the combined total error (Figure 8.2.5-5). However, all the comparisons also show that in the lower stratosphere MIPAS-E values are larger than MIPAS-B measured data and also larger as tropospheric values for the years 2002 and 2003. Furthermore, oscillations seem to be a persistent feature at least in the lower atmosphere.

### 2.2 Flight No. 13

The scatter plots in Figure 8.2.5-6 exhibit also a large spread similar to the scatter plots for H<sub>2</sub>O and HNO<sub>3</sub> comparisons (Figure 8.2.2-6 and 8.2.4-6). The explanations are the same as before. The profile comparison in Panel A illustrates that the agreement is better than the result in the correlative coincident comparison especially in the upper part. The reason is that the spatial mismatch or MIPAS-E profile oscillations effects, which added extra discrepancy to the coincident comparison, were reduced by the statistics in trajectory comparison. The trajectory comparison in Panel B gives a similar result as the coincident comparison of Rec. 30 to Seq. 15c. The improvement in consistency lies in the lower altitudes. The benefits are from the depressing of the oscillation effects in a single profile by averaging many profiles.

## 8. Intercomparison of measurements

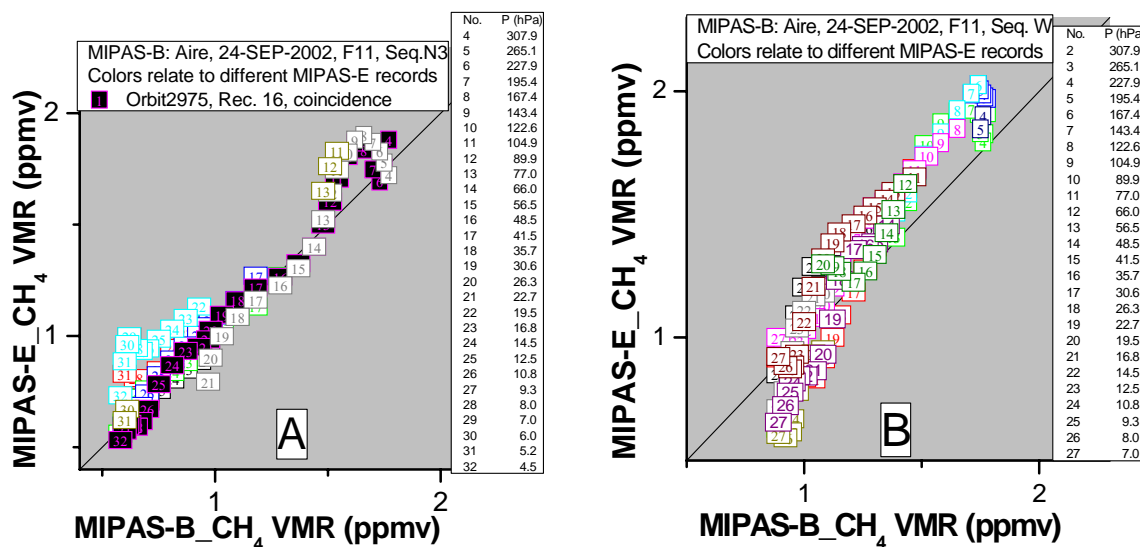


**Figure 8.2.5-4:** Scatter plots of MIPAS-E CH<sub>4</sub> VMR against MIPAS-B CH<sub>4</sub> VMR for match points found in two days forward and backward trajectories for Flight No. 11. (A) For Seq. N3. (B) For Seq. W. The numbers in the square symbols represent the pressure of the match points as listed in the legends. The solid squares denote the match points that have been found during the coincident comparisons. The solid straight lines are diagonals of squares. For clarity, the error bars were not shown here.

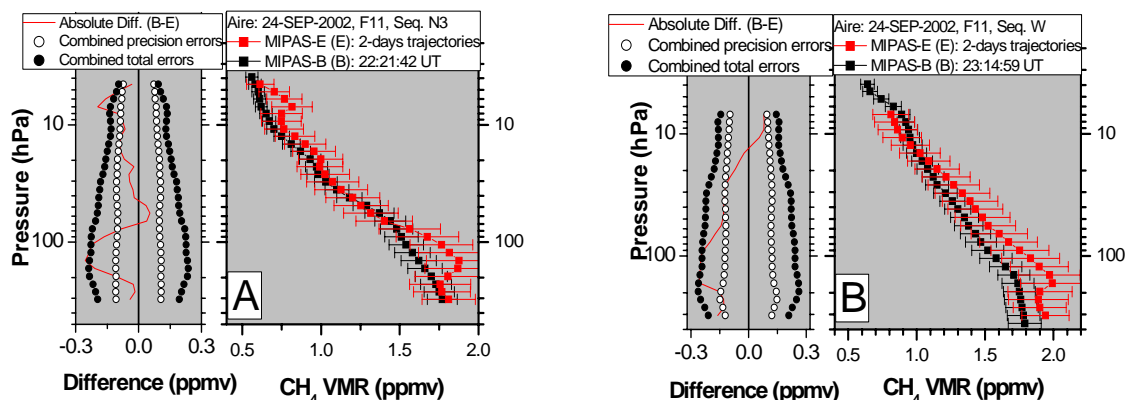


**Figure 8.2.5-5:** MIPAS-B CH<sub>4</sub> VMR profiles comparison with MIPAS-E mean CH<sub>4</sub> VMR profiles which were calculated by averaging all the match points at the same level of altitude considering the weights of the MIPAS-E noise errors. The notation is the same as in Figure 8.2.2-1. (A) For Seq. N3. (B) For Seq. W.

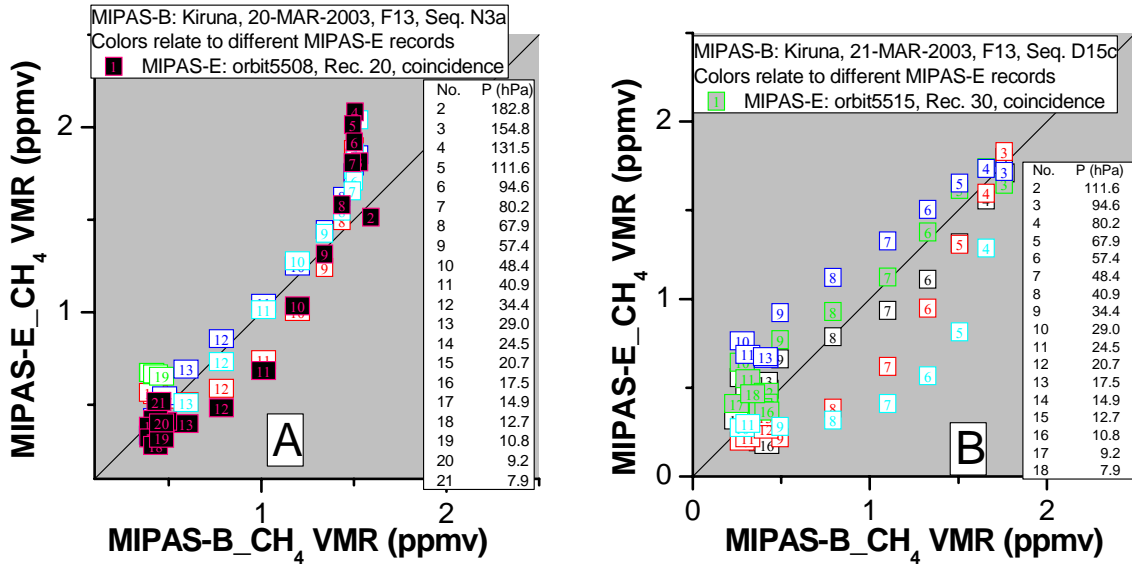


Figure 8.2.5-6: Same as Figure 8.2.5-4 but for Flight No. 13. (A) For Seq. N3a. (B) For Seq. D15c.

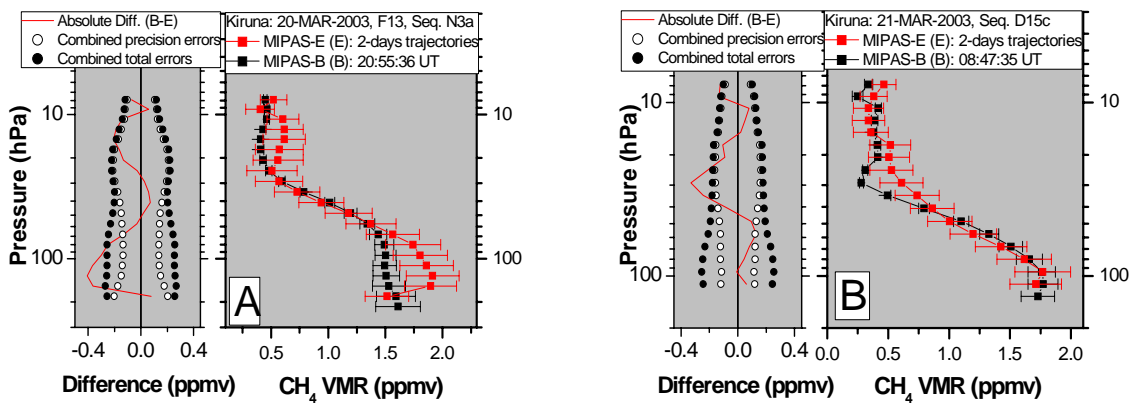


Figure 8.2.5-7: Same as Figure 8.2.5-5 but for Flight No. 13. (A) For Seq. N3a. (B) For Seq. D15c.

### 2.3 Flight No. 14

The features of the scatter plots in Flight No. 14 are obvious. The consistencies of individual points are quite good at high altitudes. In the lower stratosphere, MIPAS-E measured higher values than MIPAS-B. Some profiles also show oscillations at lower altitudes. The comparisons of MIPAS-E mean profiles with the correlative MIPAS-B measurements are plotted in Figure 8.2.5-9. They give the similar conclusions as the scatter plots. The consistencies are quite good in the upper part. In the upper troposphere and lower stratosphere, MIPAS-E values are deteriorated by strong oscillations.

## 8. Intercomparison of measurements

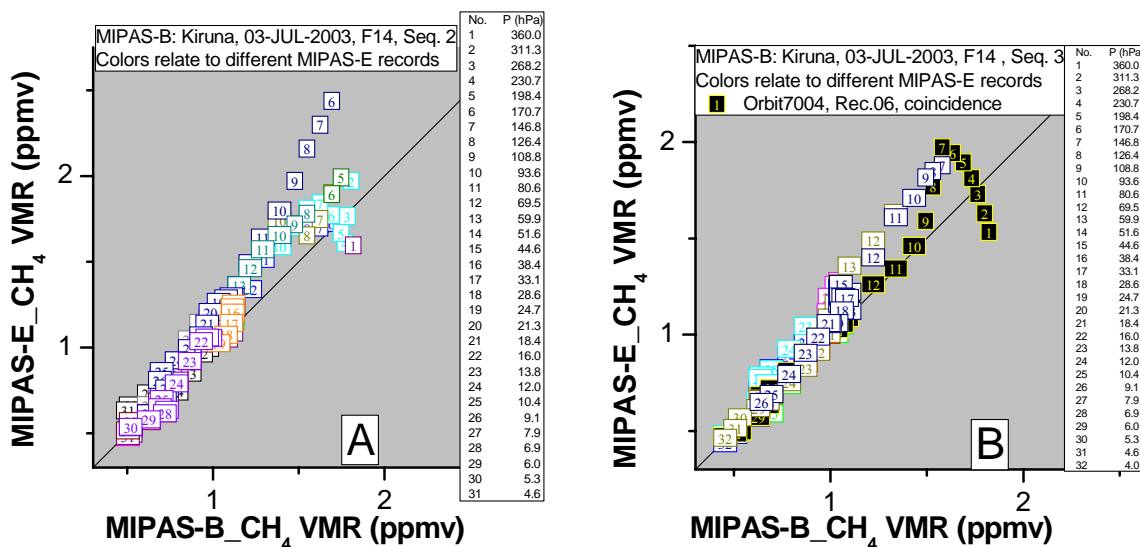


Figure 8.2.5-8: Same as Figure 8.2.5-4 but for Flight No. 14. (A) For Seq. 2. (B) For Seq. 3.

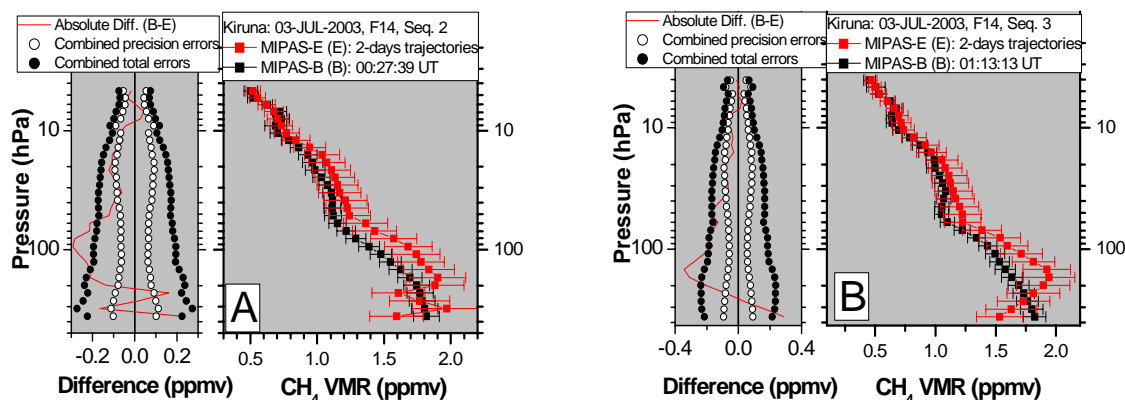


Figure 8.2.5-9: Same as Figure 8.2.5-5 but for Flight No. 14. (A) For Seq. 2. (B) For Seq. 3.

### 3 Summary of CH<sub>4</sub> comparison

For providing an intergratal view, all the absolute difference profiles are plotted together in Figure 8.2.5-10. This figure shows that there are no obvious discrepancies between MIPAS-E and MIPAS-B data in the region of upper altitudes. From the middle stratosphere down to the lower stratosphere, the positive bias of MIPAS-E increases with decreasing altitude. After that, MIPAS-E shows negative biases at the lowest of height. Further, this figure demonstrates that the oscillations of MIPAS-E profiles are strongest in the upper troposphere and lower stratosphere and appear to be consistent.

Based on the above analysis, the whole height region was divided into three parts (Table 8.6): 356-195 hPa (8-12 km), 195-15 hPa (12-29 km) and 15-3 hPa (29-39 km). In 356-195 hPa, MIPAS-E values are lower than MIPAS-B measurements. Between 195-15 hPa, MIPAS-E measurements are higher than MIPAS-B data. Above the level of 15 hPa, MIPAS-E measured values are slightly lower than MIPAS-B. However, for the trajectory case, MIPAS-E shows higher values as above this level. The average of the combined total errors over the whole region of altitude is 0.18 ppmv for both coincident comparison and trajectory comparison. These statistics of comparisons show that the two approaches present similar results. The differences in the whole height region are within the mean combined total errors. Therefore, it can be concluded that the accuracy of MIPAS-E measurements are quite good according to

the MIPAS-B validation data. On the other hand, the strong profile oscillations of MIPAS-E data undermine its general quality.

The standard deviation and the corresponding mean combined precision errors of CH<sub>4</sub> are very close. Therefore the precision of MIPAS-E measurements for CH<sub>4</sub> is satisfactory except for the lowermost altitude.

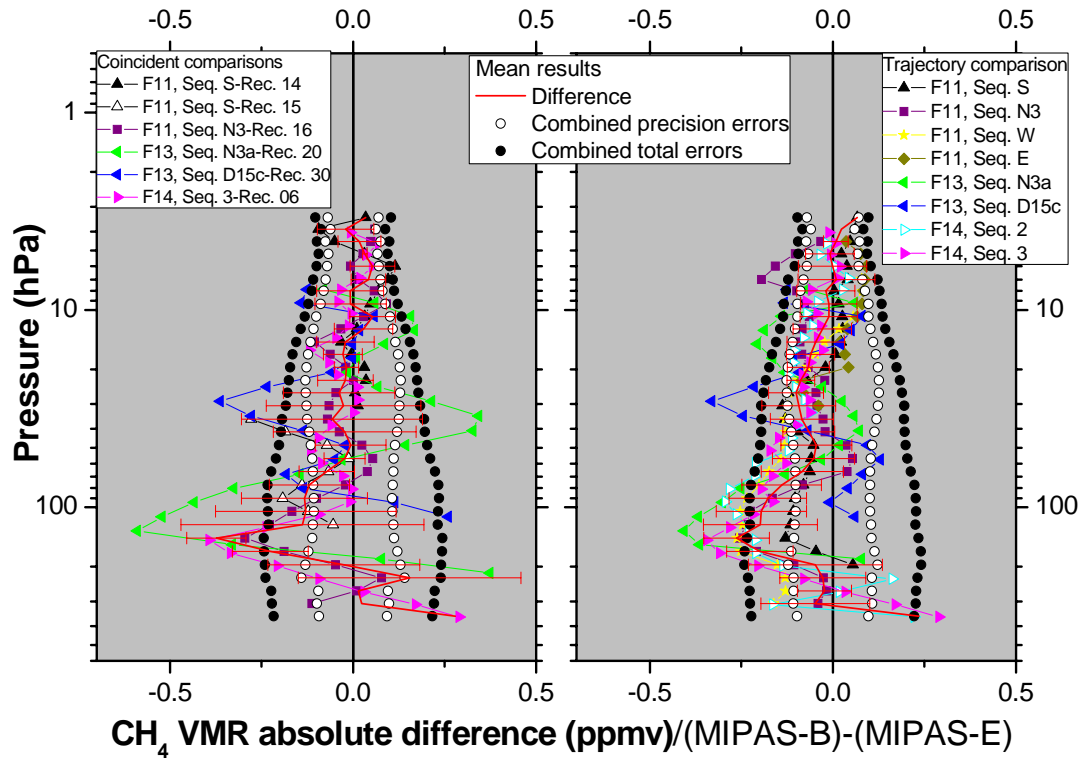


**Figure 8.2.5-10:** Summary comparison of CH<sub>4</sub> VMR between MIPAS-E and MIPAS-B. There are no standard deviation bars for the top and bottom sections of the mean difference profile since only one or two comparisons are available in these altitude regions. Left: coincident comparison. Right: trajectory comparison.

**Table 8.6:** Mean differences of MIPAS-B minus MIPAS-E CH<sub>4</sub> as well as the associated mean combined errors and the mean standard deviations.

Accuracy							
Pressure (hPa)	Height (km)	Absolute difference (ppmv)		Relative difference (%)		Mean combined total errors (ppmv)	
		Coincidence	Trajectory	Coincidence	Trajectory	Coincidence	Trajectory
356-195	8-12	0.10±0.11	0.001±0.108	6.05±6.13	0.24±6.00	0.23±0.03	0.23±0.004
195-15	12-29	-0.08±0.09	-0.11±0.07	-7.47±6.40	-10.39±4.42	0.21±0.03	0.20±0.03
15-3	29-39	0.02±0.03	-0.007±0.018	2.61±7.31	-2.99±3.44	0.11±0.02	0.12±0.02
Precision							
Pressure (hPa)	Height (km)	Standard deviation (ppmv)		Mean combined precision errors (ppmv)			
		Coincidence	Trajectory	Coincidence	Trajectory		
123-8	15-33	0.13±0.08	0.09±0.03	0.11±0.01	0.11±0.01		

## 8.2.6 N<sub>2</sub>O

### 1 Coincident comparison for N<sub>2</sub>O

#### 1.1 Flight No. 11

The coincident comparisons for Flight No. 11 are demonstrated in Figure 8.2.6-1. The strong oscillations of the MIPAS-E profile around 36 hPa (23 km) caused a larger discrepancy between MIPAS-E measurements and MIPAS-B data. Above the level of 36 hPa, the degree of agreements between Seq. S and Rec. 14 is even better than that between Seq. S and Rec. 15. This may be just an occasional event when considering the match quality in space. The comparison of Rec. 16 to Seq. N3 shows that MIPAS-E values agree with MIPAS-B data in general except at the high altitude and in the range of 143-90 hPa (14-17 km). The MIPAS-E profiles plotted here exhibit oscillation features especially in the lower stratosphere. Obviously, the oscillation leads to unreasonable lower VMR values of N<sub>2</sub>O at the lowest level of altitude, because in the troposphere, the N<sub>2</sub>O distributes homogeneously with a normal value of about 319 ppbv.

#### 1.2 Flight No. 13

Two coincident comparisons are available, Rec. 20 to Seq. N3a and Rec. 30 to Seq. N3a. (Panel A and B of Figure 8.2.6-2). The profile of Rec. 20 is consistent with Seq. N3a profile in the upper part. Both profiles present similar small-scale structures. On the contrary, in the region of lower altitudes, their structures are just reverse. However, the extremely low VMR value (236 ppbv at 223 hPa (10 km)) made from Rec. 20 implies that the measurements of MIPAS-E may be not very correct. The comparison of Rec. 30 with Seq. D15c in Panel B demonstrates that a good agreement was obtained this time. The exception happened also in the lower altitude region. There, MIPAS-E again gives some unphysical low measurements for N<sub>2</sub>O VMR.

#### 1.3 Flight No. 14

The only pair of measurements for coincident comparison in Flight No. 14 is presented in Figure 8.2.6-3. It can be concluded that the consistency is nearly perfect, because the small-scale structures of N<sub>2</sub>O vertical distribution in the upper part are consistently characterized. Unfortunately, the strong oscillation of Rec. 06 profile at the level of about 155 hPa (13 km) leads to an exception for the consistency, and MIPAS-E gives unreasonably large data at low altitudes.

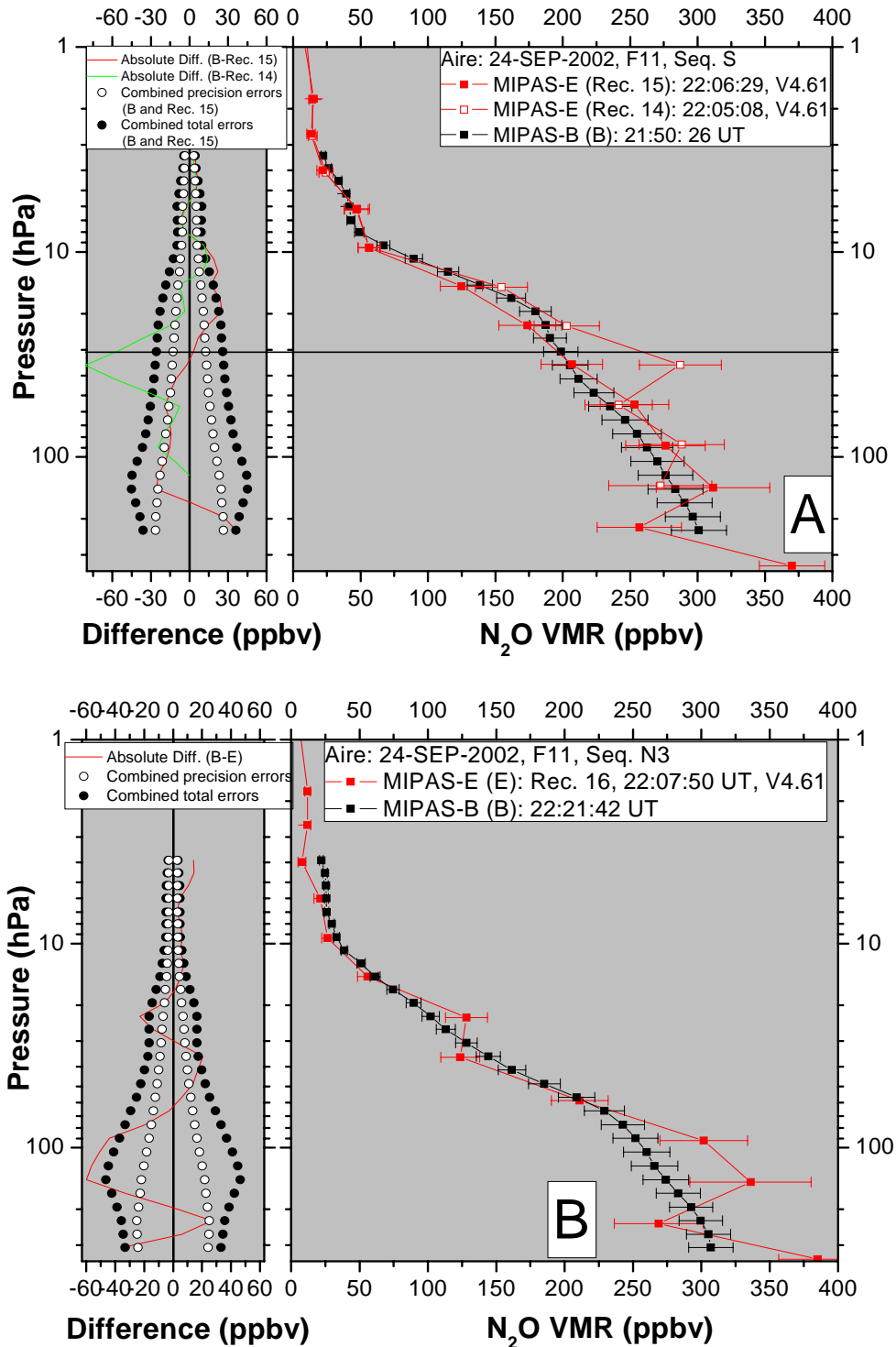


**Figure 8.2.6-1:**  $N_2O$  VMR comparisons for Flight No. 11. MIPAS-B profiles, black curves with black square symbols, the error bars represent the total errors; MIPAS-E profiles, red curves with red square symbols, the error bars represent the total errors; absolute differences of MIPAS-B minus MIPAS-E, solid red line or solid green line; combined precision errors (the combination of MIPAS-E noise errors and MIPAS-B errors including the noise, LOS, and temperature errors), open circles; the combined total errors, solid circles. (A) Comparisons between Seq. S and Rec. 14, Seq. S and Rec. 15. Both kind of combined errors are calculated from the Seq. S and Rec. 15 data. If using Rec. 14 data, the combined errors are almost the same. The straight line denotes that below this level of altitude Seq. S should compare with Rec. 14 and above to Rec. 15. (B) Comparison between Seq. N3 and Rec. 16.

8. Intercomparison of measurements

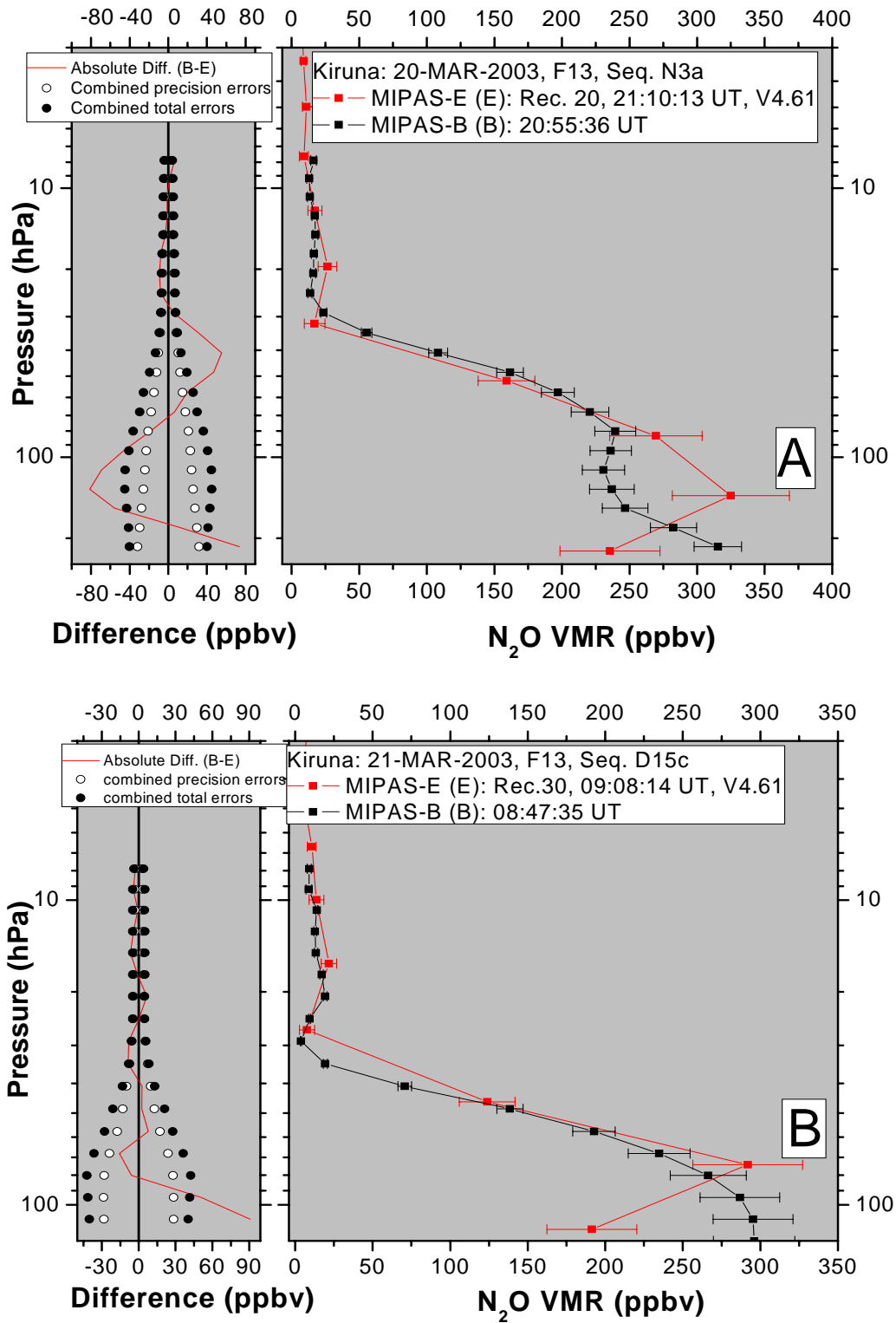
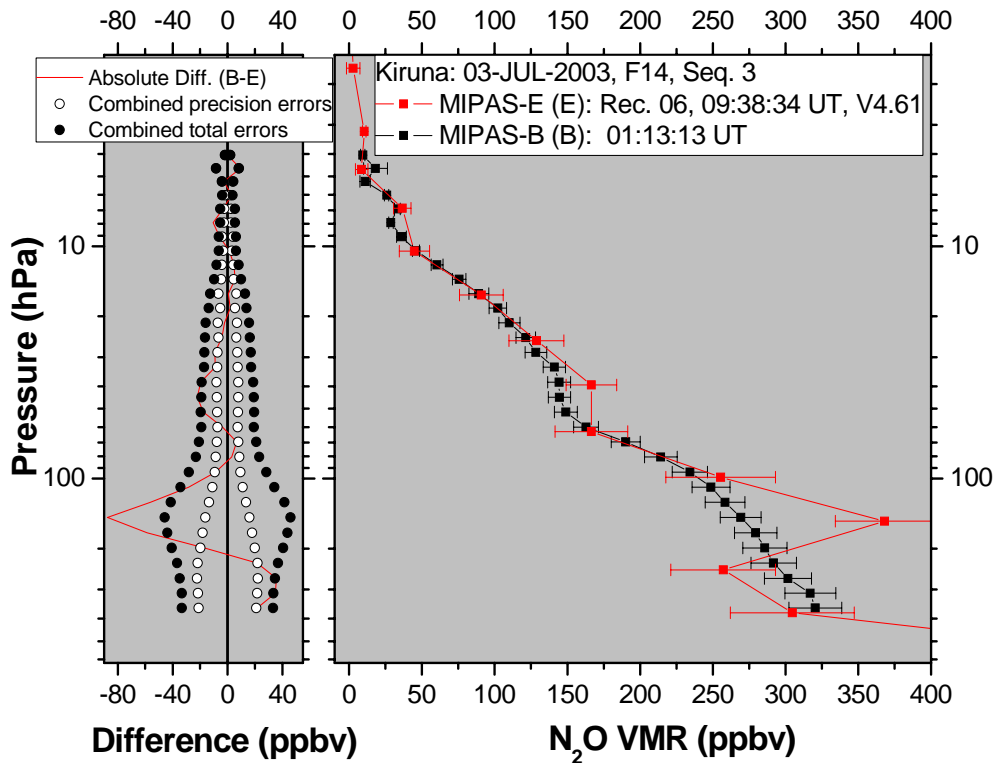


Figure 8.2.6-2: N<sub>2</sub>O VMR comparisons for Flight No. 13. (A) Comparisons between Seq. N3a and Rec. 20. (B) Comparison between Seq. D15c and Rec. 30. The notation is the same as in Figure 8.2.6-1.





**Figure 8.2.6-3:** N<sub>2</sub>O VMR comparisons for Flight No. 14 between Seq. 3 and Rec. 06. The notation is the same as in Figure 8.2.6-1.

## 2 Trajectory comparison for N<sub>2</sub>O

### 2.1 Flight No. 11

The scatter plots of MIPAS-E data against MIPAS-B data for Flight No. 11 are presented in Figure 8.2.6-4. The scatter plots demonstrate a consistent situation for individual match points. In general, most of the match points indicate that MIPAS-E measurements agree with those of MIPAS-B. At the lower altitudes, however, MIPAS-E values are larger than the values of MIPAS-B and the degree of scatter becomes higher due to the oscillation of MIPAS-E profiles. The comparisons of MIPAS-E mean profiles with the correlative MIPAS-B profiles plotted in Figure 8.2.6-5 demonstrate the consistency of the two instruments. One common feature in different panels is that MIPAS-E measured higher values than MIPAS-B in the lower stratosphere. Comparing with the coincident comparisons, the mean profiles of the trajectory matches of MIPAS-E do not show such extremely low values at the lowest altitude due to the averaging effect.

## 8. Intercomparison of measurements

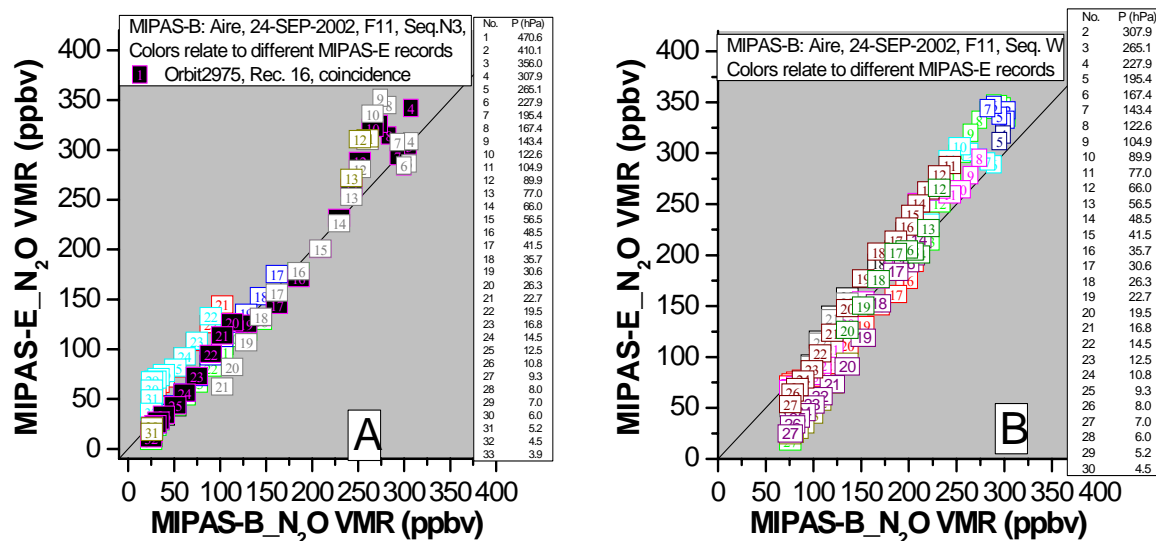


**Figure 8.2.6-4:** Scatter plots of MIPAS-E  $\text{N}_2\text{O}$  VMR against MIPAS-B  $\text{N}_2\text{O}$  VMR for match points found in two days forward and backward trajectories for Flight No. 11. (B) For Seq. N3. (C) For Seq. W. The numbers in the square symbols represent the pressure of the match points as listed in the legends. The solid squares denote the match points that have been found during the coincident comparisons. The solid straight lines are diagonals of squares. For clarity, the error bars were not shown here.

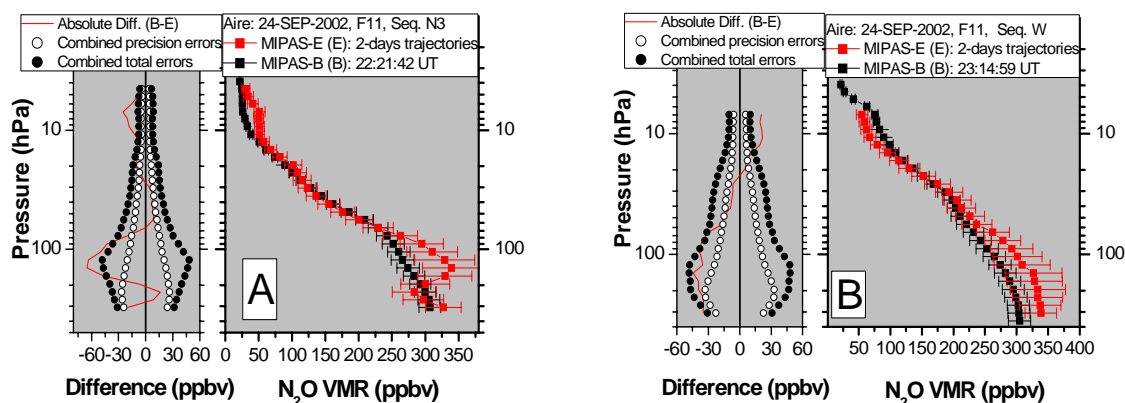


**Figure 8.2.6-5:** MIPAS-B  $\text{N}_2\text{O}$  VMR profiles comparison with MIPAS-E mean  $\text{N}_2\text{O}$  VMR profiles which were calculated by averaging all the match points at the same level of altitude considering the weights of the MIPAS-E noise errors. The notation is the same as in Figure 8.2.2-1. (B) For Seq. N3. (C) For Seq. W.

### 2.2 Flight No. 13

The features of the scatter plots for  $\text{N}_2\text{O}$  shown here are very similar to those of the scatter plots for  $\text{CH}_4$  (Figure 8.2.5-4), i.e., the spread distribution of the points. The explanations are the same as for  $\text{CH}_4$ . The profile comparison in Panel A of Figure 8.2.6-7 gives similar results to the corresponding coincident comparison. An improvement is that the extremely low values of MIPAS-E in coincident cases are averaged out in the mean profile. This is also true to the MIPAS-E mean profile plot in Panel B. The consistency demonstrated in Panel B is not as good as that in the corresponding coincident case (Panel B of Figure 8.2.6-2). One reasonable explanation is that the spatial offset does not influence the coincident comparison of Rec. 30 to Seq. D15c significantly due to the excellent match quality. While in the trajectory comparison, the spatial influences became significant because the relative weakly strict match criteria and the existence of the polar vortex.

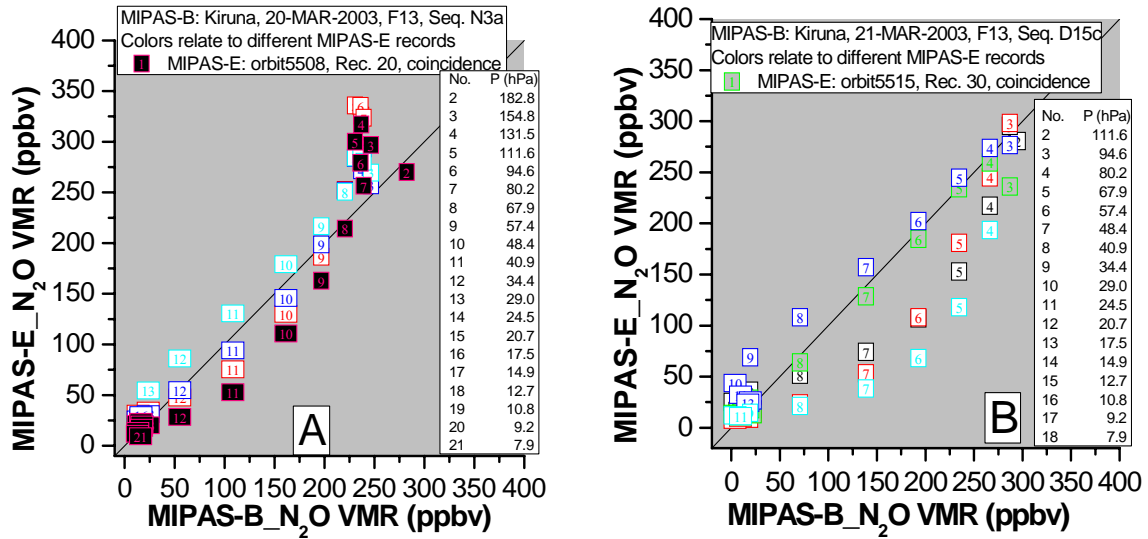


Figure 8.2.6-6: Same as Figure 8.2.6-4 but for Flight No. 13. (A) For Seq. N3a. (B) For Seq. D15c.

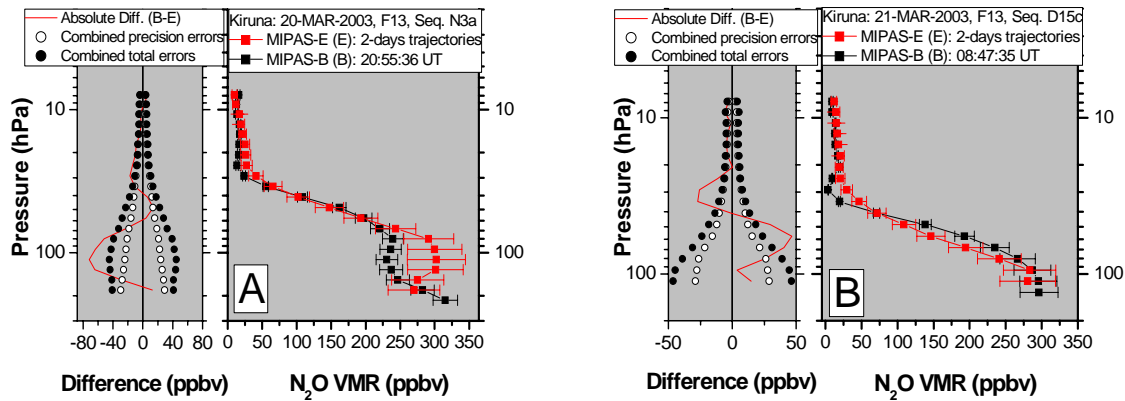


Figure 8.2.6-7: Same as Figure 8.2.6-5 but for Flight No. 13. (A) For Seq. N3a. (B) For Seq. D15c.

### 2.3 Flight No. 14

Two MIPAS-B profiles can be used for MIPAS-E validation during Flight No. 14. Good consistencies between MIPAS-E and MIPAS-B can be seen from the two scatter plots. It can be concluded that in the region of high altitude, both scatter plots show perfect agreements. And they also demonstrate the positive biases of MIPAS-E in the lower stratosphere. The profile comparisons in Figure 8.2.6-9 illustrated that most of the discrepancies between the two instruments measured data are within the combined total errors in spite of the positive biases of MIPAS-E values.

## 8. Intercomparison of measurements

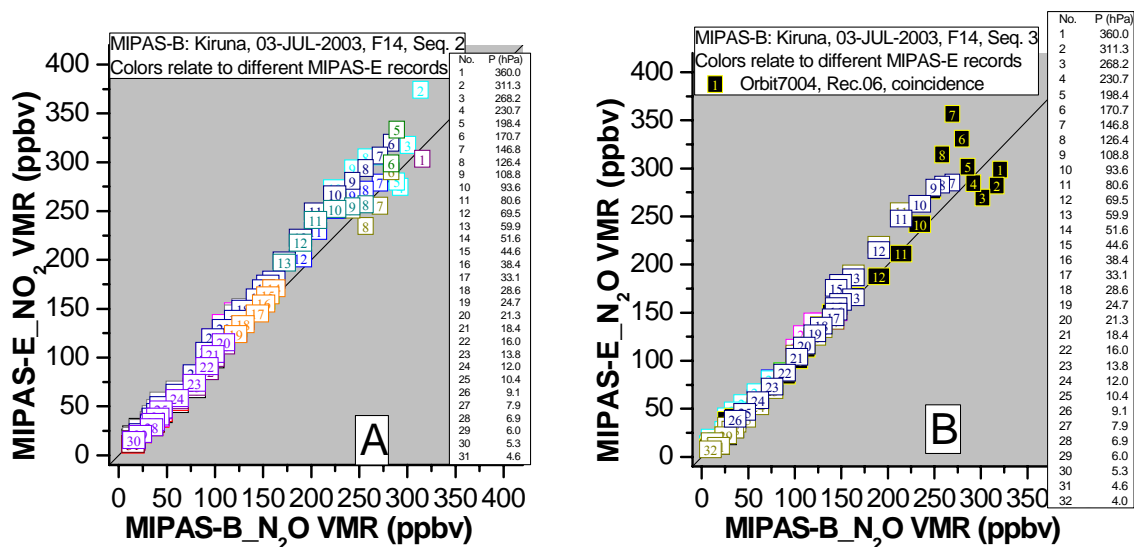


Figure 8.2.6-8: Same as Figure 8.2.6-4 but for Flight No. 14. (A) For Seq. 2. (B) For Seq. 3.

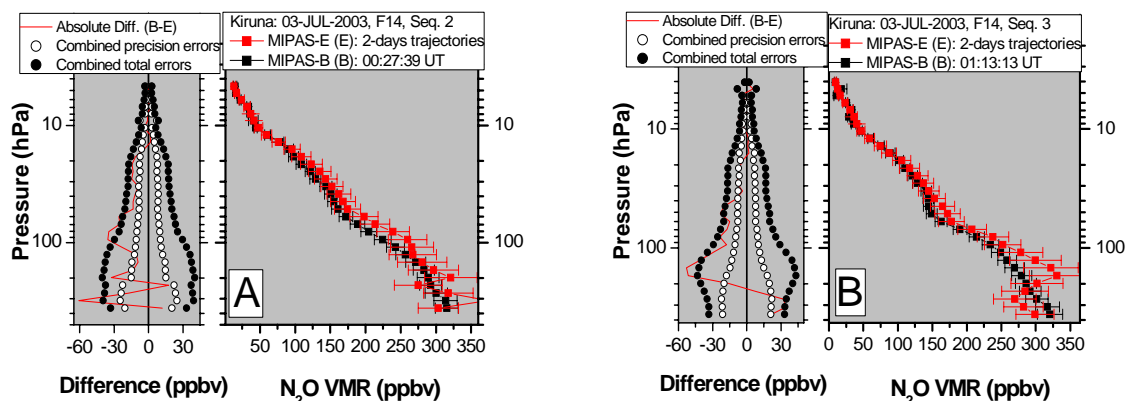


Figure 8.2.6-9: Same as Figure 8.2.6-5 but for Flight No. 14. (A) For Seq. 2. (B) For Seq. 3.

### 3 Summary of N<sub>2</sub>O comparison

For summary, all the absolute difference profiles of N<sub>2</sub>O are plotted together in Figure 8.2.6-10. This figure shows that the agreements of the two instruments data are perfect in the upper part. From the middle stratosphere down to the lower stratosphere, the positive biases of MIPAS-E increase with decreasing altitude. After that, MIPAS-E shows negative biases at the low levels of heights. Further, this figure demonstrates that the strong oscillations of MIPAS-E profiles concentrate in the upper troposphere and lower stratosphere. These features are very similar to the CH<sub>4</sub> comparison. It is worth to note that these molecules are analyzed in the same spectral channel.

Like for CH<sub>4</sub>, the whole height region is divided into three parts: 356-195 hPa (8-12 km), 195-20 hPa (12-27 km) and 20-3 hPa (27-39 km) (Table 8.7). In 356-195 hPa, MIPAS-E values are lower than MIPAS-B measurements in term of absolute difference. However, MIPAS-E shows high bias in terms of relative difference. This contravention is due to the diversity of the data in this altitude region. Between 195-20 hPa, MIPAS-E measurements are higher than MIPAS-B data. Above the altitude of 20 hPa, MIPAS-E measured values are slightly lower than MIPAS-B data. For trajectory comparison, above the level of 20 hPa, MIPAS-E shows slightly lower values in terms of absolute difference but from the point of

mean relative difference MIPAS-E shows higher values. This is due to the sensitivity of the percent difference to the very low N<sub>2</sub>O VMR at the high altitudes. These statistical results indicate that the two approaches of comparison gave similar results except below the level of 195 hPa. They show that the differences between MIPAS-E and MIPAS-B for N<sub>2</sub>O measurements in the whole overlapping height region are within the mean combined total errors. Therefore, it can be concluded that the accuracy of MIPAS-E measurements are quite good according to the MIPAS-B validation data. However, the systematic oscillations undermine the general quality like in the CH<sub>4</sub> case.

The standard deviation and the corresponding mean combined precision errors of N<sub>2</sub>O indicate that the MIPAS-E data for N<sub>2</sub>O are not so compact.

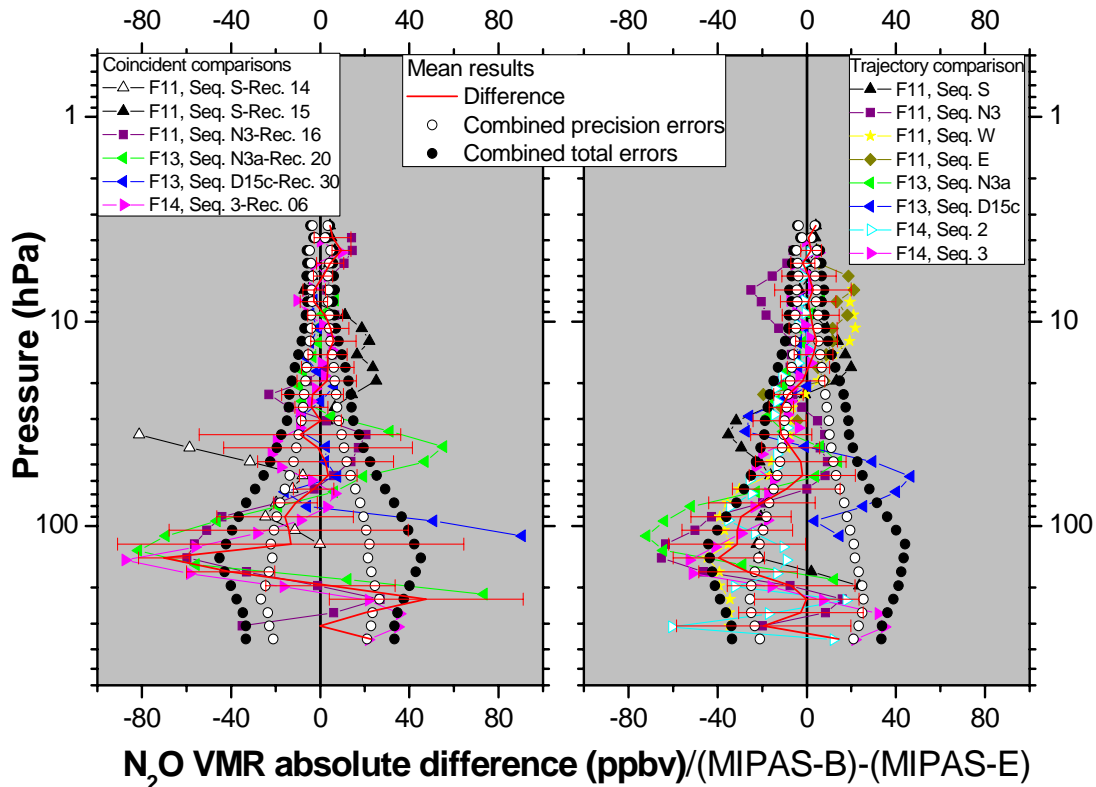


**Figure 8.2.6-10:** Summary comparison of N<sub>2</sub>O VMR between MIPAS-E and MIPAS-B. There are no standard deviation bars for the top and bottom sections of the mean difference profile since only one or two comparisons are available in these altitude regions. Left: coincident comparison. Right: trajectory comparison.

**Table 8.7:** Mean differences of MIPAS-B minus MIPAS-E N<sub>2</sub>O as well as the associated mean combined errors and the mean standard deviations.

Accuracy							
Pressure (hPa)	Height (km)	Absolute difference (ppbv)		Relative difference (%)		Mean combined total errors (ppbv)	
		Coincidence	Trajectory	Coincidence	Trajectory	Coincidence	Trajectory
356-195	8-12	19.97±20.77	-5.05±10.35	6.37±6.77	-1.66±3.34	36.57±3.01	37.49±3.38
195-20	12-27	-12.76±19.88	-17.28±12.12	-9.02±10.75	-18.66±22.16	28.30±11.58	28.98±10.45
20-3	27-39	3.21±3.17	1.54±1.90	1.76±14.15	-5.04±5.85	7.77±2.76	9.03±3.07
Precision							
Pressure (hPa)	Height (km)	Standard deviation (ppbv)		Mean combined precision errors (ppbv)			
		Coincidence	Trajectory	Coincidence	Trajectory		
123-8	15-33	21.50±20	15.47±7.45	10.49±6.06	10.74±5.26		

## 8. Intercomparison of measurements

As had been mentioned in Chapter 2, the stable relationship between  $\text{N}_2\text{O}$  and  $\text{CH}_4$  distribution serves as good check of the internal instrument consistency. Figure 8.2.6-11 presents all MIPAS-B measured  $\text{CH}_4$ - $\text{N}_2\text{O}$  and MIPAS-E measured  $\text{CH}_4$ - $\text{N}_2\text{O}$  correlations during the validation period. As the references, the analysis about  $\text{CH}_4$ - $\text{N}_2\text{O}$  correlations which were performed by Engel et al. (Engel, A., et al., 1996) and by Michelsen et al (Michelsen, H. A., et al., 1998), separately, are also presented after taking into account the adjustments since then to the year of 2003. From the comparison of the fitted lines, it is clear that MIPAS-E  $\text{CH}_4/\text{N}_2\text{O}$  ratios are the largest among the four data sets below the altitude of about 23 hPa (26 km). MIPAS-B  $\text{CH}_4$ - $\text{N}_2\text{O}$  correlation are very consistent with the analysis of Engel, et al. The high  $\text{CH}_4/\text{N}_2\text{O}$  ratios made from MIPAS-E may be due to the overestimation of  $\text{CH}_4$  or the underestimation of  $\text{N}_2\text{O}$  or both case happened simultaneously. Figure 8.2.6-11 also demonstrates that the  $\text{CH}_4$ - $\text{N}_2\text{O}$  correlation of MIPAS-E often reveals unphysical outliers which mainly exhibit on the lower altitudes. These outliers were caused by the oscillations of  $\text{CH}_4$  and  $\text{N}_2\text{O}$  profiles made by MIPAS-E at the lower altitudes. Furthermore, MIPAS-E delivers too high  $\text{CH}_4$  and  $\text{N}_2\text{O}$  values in the troposphere which should not exceed about 1.76 ppmv and 319 ppbv, respectively (WMO, 2003).

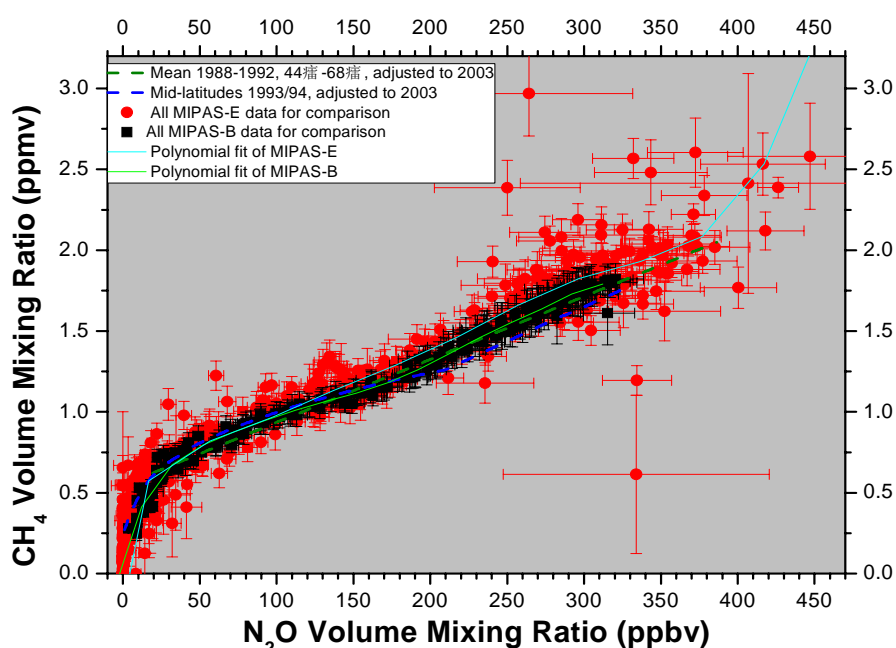


**Figure 8.2.6-11:** The  $\text{N}_2\text{O}$ - $\text{CH}_4$  correlation of MIPAS-E and MIPAS-B measurements along with the Engel, A., et al., 1996 (dashed olive line), and Michelsen, H. A., et al., 1998 (dashed blue line) results.

### 8.2.7 $\text{NO}_2$

#### 1 Photochemical correlation with the chemistry transport-model KASIMA

KASIMA is a model to simulate the middle atmosphere (7-100 km) with a vertical resolution of 1-5 km and a horizontal resolution of  $(2.8-5.6)^\circ \times (2.8-5.6)^\circ$ . It consists of three major modules: The meteorological module integrates the primitive meteorological equations in time. The chemical module consists of 58 chemical species and families which are involved in 101 molecular reactions, 39 photodissociations, and 10 heterogeneous reactions taking place on surfaces of polar stratospheric clouds (PSC) and on liquid sulphuric acid aerosols. The third is a radiation module (details see Kouker, W., et al., 1999). KASIMA simulated reasonable results that had been used in many studies (e.g., Wetzel, G., et al., 2002; Stowasser, M., et al., 2003). The KASIMA results used here were performed by Ruhnke, R., (2005).



## 2 Coincident comparison for NO<sub>2</sub>

### 2.1 Flight No. 11

Figure 8.2.7-1 presents the two coincident comparisons for Flight No. 11: Rec. 15 to Seq. S and Rec. 16 to Seq. N3a.

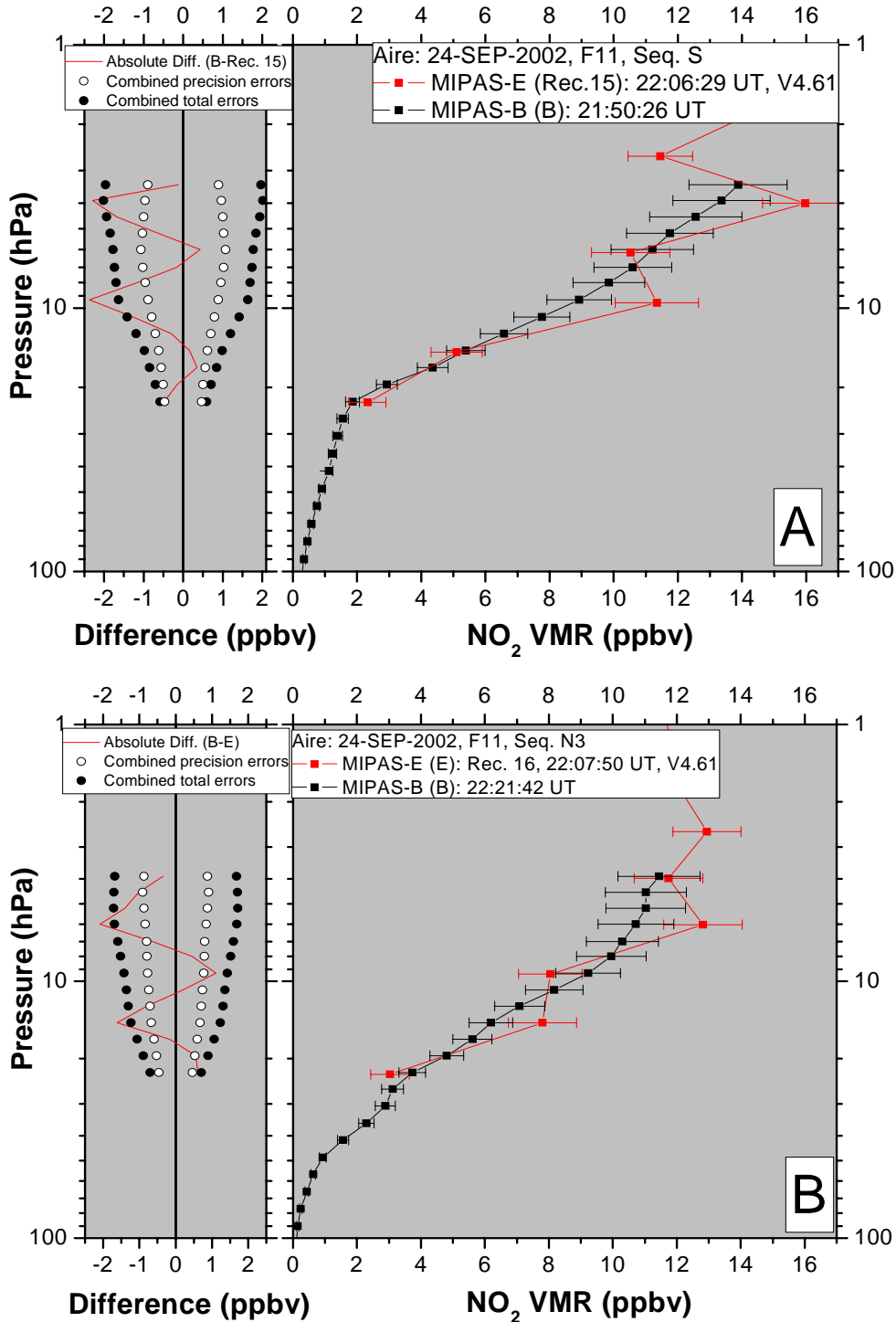


**Figure 8.2.7-1:** NO<sub>2</sub> VMR comparisons for Flight No. 11. MIPAS-B profiles, black curves with black square symbols, the error bars represent the total errors; MIPAS-E profiles, red curves with red square symbols, the error bars represent the total errors; absolute differences of MIPAS-B minus MIPAS-E, solid red line; combined precision errors (the combination of MIPAS-E noise errors and MIPAS-B errors including the noise, LOS, and temperature errors), open circles; the combined total errors, solid circles. (A) Comparisons between Seq. S and Rec. 15. (B) Comparison between Seq. N3 and Rec. 16.

## 8. Intercomparison of measurements

Both sequences of MIPAS-E reveal oscillation features. The comparison of Rec. 15 to Seq. S demonstrates that these data agree well with each other with respect to the combined total errors despite MIPAS-E values have a slightly positive bias. The comparison of Rec. 16 to Seq. N3 in Panel B shows an even better consistency between the two instrument measurements. A feature similar to Panel A is seen in Panel B showing a slightly positive bias of MIPAS-E data especially at higher altitudes.

### 2.2 Flight No. 13

The two coincident comparisons, Rec. 20 to Seq. N3a and Rec. 30 to Seq. D15c, are presented in Figure 8.2.7-2.

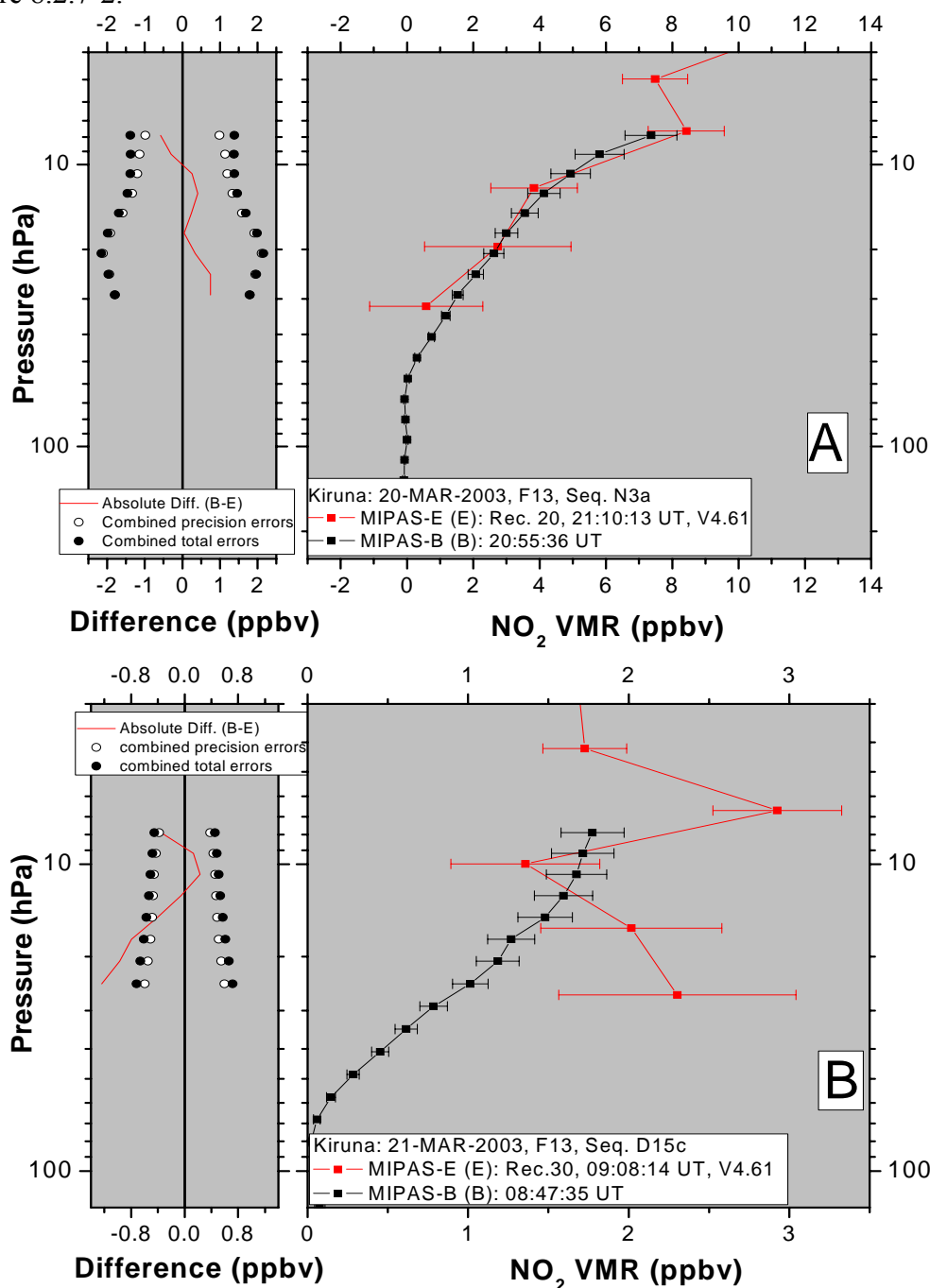


**Figure 8.2.7-2:** NO<sub>2</sub> VMR comparisons for Flight No. 13. (A) Comparisons between Seq. N3a and Rec. 20. (B) Comparison between Seq. D15c and Rec. 30. The notation is the same as in Figure 8.2.7-1.



The agreement of Rec. 20 to Seq. N3a for NO<sub>2</sub> data is excellent (Panel A). Taking into account the larger tangent locations difference in PV, this good consistency seems beyond the expectation especially at higher altitudes. On the contrary, the comparison of Rec. 30 to Seq. D15c in Panel B demonstrates the significant discrepancy of the two instruments measurements in spite of the excellent match quality. The strong oscillation of Rec. 30 profile should be partly responsible for the large discrepancy.

### 2.3 Flight No. 14

The validation results for NO<sub>2</sub> are very sensitive to the match quality in time since it is a photochemically variable species. And its variability usually depends on the sunlight. Figure 8.2.7-3 shows that MIPAS-E measured NO<sub>2</sub> VMRs with a systematically low bias compared to the MIPAS-B data. Due to the fact that there is a time offset, the discrepancy may be caused mainly by the photodissociation of NO<sub>2</sub> during the period of about 8.5 hours, which is the time offset between Rec. 06 and Seq. 3. Moreover, because the validation campaign of Flight No.14 was carried out in the midnight sun, the changes of NO<sub>2</sub> concentration should not be so rapidly. In order to evaluate the chemistry influence to the discrepancy in quantity, KASIMA was used to simulate the NO<sub>2</sub> VMR profiles (Ruhnke, R. 2005). The procedure is: first, calculating the NO<sub>2</sub> VMR profile at the Rec. 06 and Seq. 3 measurements time and tangent geolocations, respectively. They can be denoted as  $X_{ME}$  and  $X_{MB}$ , correspondingly. Second, using the equations of 8.2 and 8.3 the corrected MIPAS-B profile for NO<sub>2</sub> VMR was obtained. (black curve with open squares). Figure 8.2.7-3 demonstrates that the agreement between the MIPAS-E and the corrected MIPAS-B profile is much better than the original comparison.

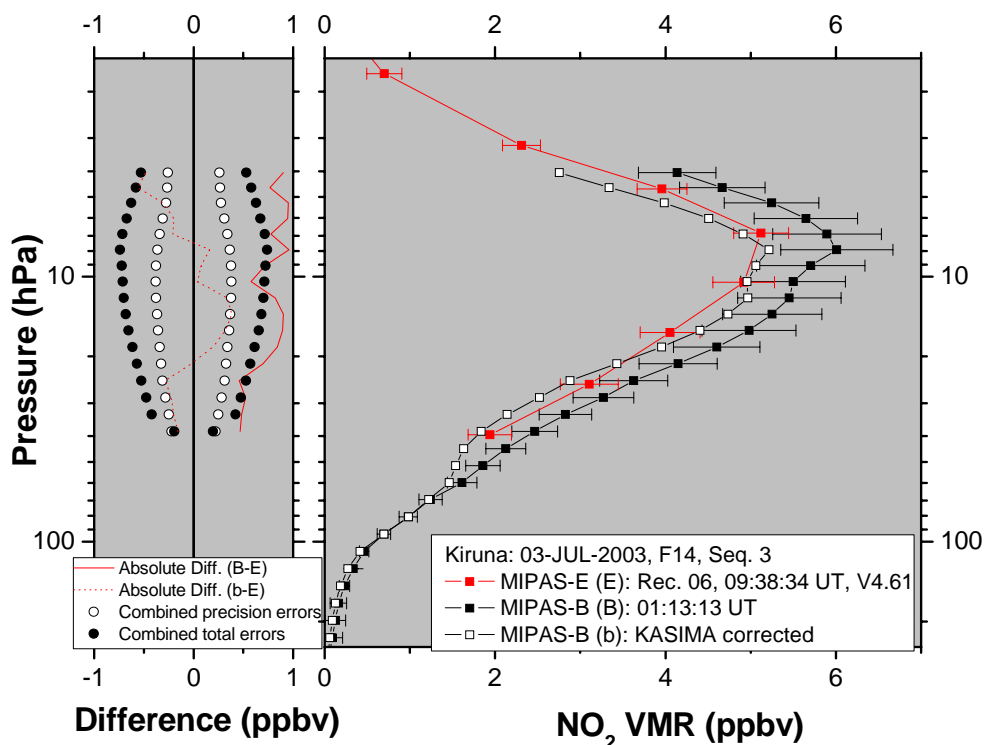


**Figure 8.2.7-3:** NO<sub>2</sub> VMR comparisons between Seq. 3 and Rec. 06 for Flight No. 14. The black curve with open squares represents the corrected MIPAS-B profile by using KASIMA. The red dotted line denotes the difference of the corrected MIPAS-B profile minus that of MIPAS-E. Other notation is the same as in Figure 8.2.7-1.

### 3 Trajectory comparison for NO<sub>2</sub>

#### 3.1 Flight No. 11

The trajectory validation method can not directly be used for the chemical active species like NO<sub>2</sub>. Figure 8.2.7-4 presents the scatter plots of MIPAS-E measured NO<sub>2</sub> VMR in two days trajectories against the NO<sub>2</sub> values from MIPAS-B Seq. N3 as an example. Seq. N3 of MIPAS-B was observed at night. While for MIPAS-E data, a part of the data was measured in the night and the other in the day. The left panel shows the MIPAS-E night data against Seq. N3 data. It indicates that the chemistry influence to the comparison is small if the two instruments perform the observations both in the night. On the other hand, the chemistry influence became significant when one instrument measured NO<sub>2</sub> in the night while another one in the day (right panel of Figure 8.2.7-4). Therefore, model simulations for NO<sub>2</sub> VMR are essential.

For the trajectory cases, the procedures of simulation of NO<sub>2</sub> VMR profiles by using KASIMA and how to calculate the corrected MIPAS-B profiles are the same as described in the last section. Corresponding to individual match points, a corrected MIPAS-B value for NO<sub>2</sub> VMR was calculated. All corrected MIPAS-B values which have the same level of altitude were averaged. Consequently, a corrected MIPAS-B profile was obtained which can be used to compare with the mean profile of MIPAS-E. So, unlike the corrected MIPAS-B profile in the coincident comparison, the corrected MIPAS-B profile for the trajectory comparison is a mean profile of many corrected MIPAS-B values. Figure 8.2.7-5 shows MIPAS-E mean profiles and the MIPAS-B original and corrected profiles as well as the corresponding differences between MIPAS-E and MIPAS-B profiles for Flight No. 11. The differences between the original and the corrected profiles of Seq. S are very small. This is just because the two coincident profiles of MIPAS-E (Rec. 14 and Rec. 15) dominate the correction factors ( $\approx 1$ ), i.e., the  $r(Z)$  in equation (8.3). The other three panels demonstrate that the MIPAS-E measurements agree better with MIPAS-B data after using the simulation results with respect to the combined total errors.

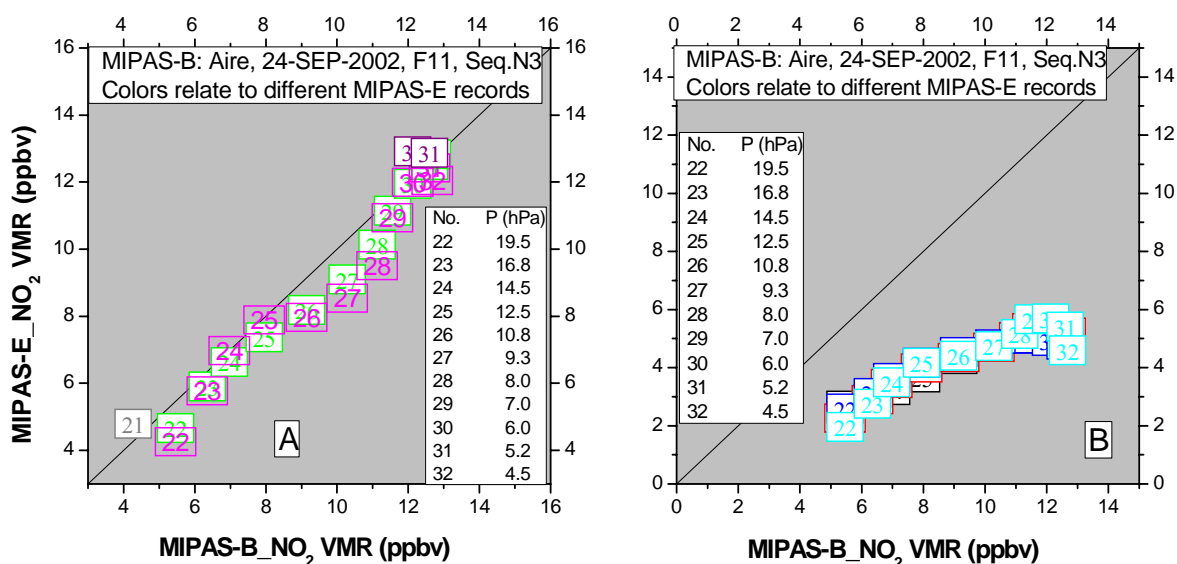


**Figure 8.2.7-4:** An example of scatter plots of MIPAS-E NO<sub>2</sub> VMR against MIPAS-B NO<sub>2</sub> VMR for match points found in two days forward and backward trajectories for Flight No. 11. The numbers in the square symbols represent the pressure of the match points as listed in the legends. The solid squares denote the match points that have been found during the coincident comparisons. The solid straight lines are diagonals of squares. Left: for the match points found in the night. Right: for the match points found in the day. For clarity, the error bars were not shown here.

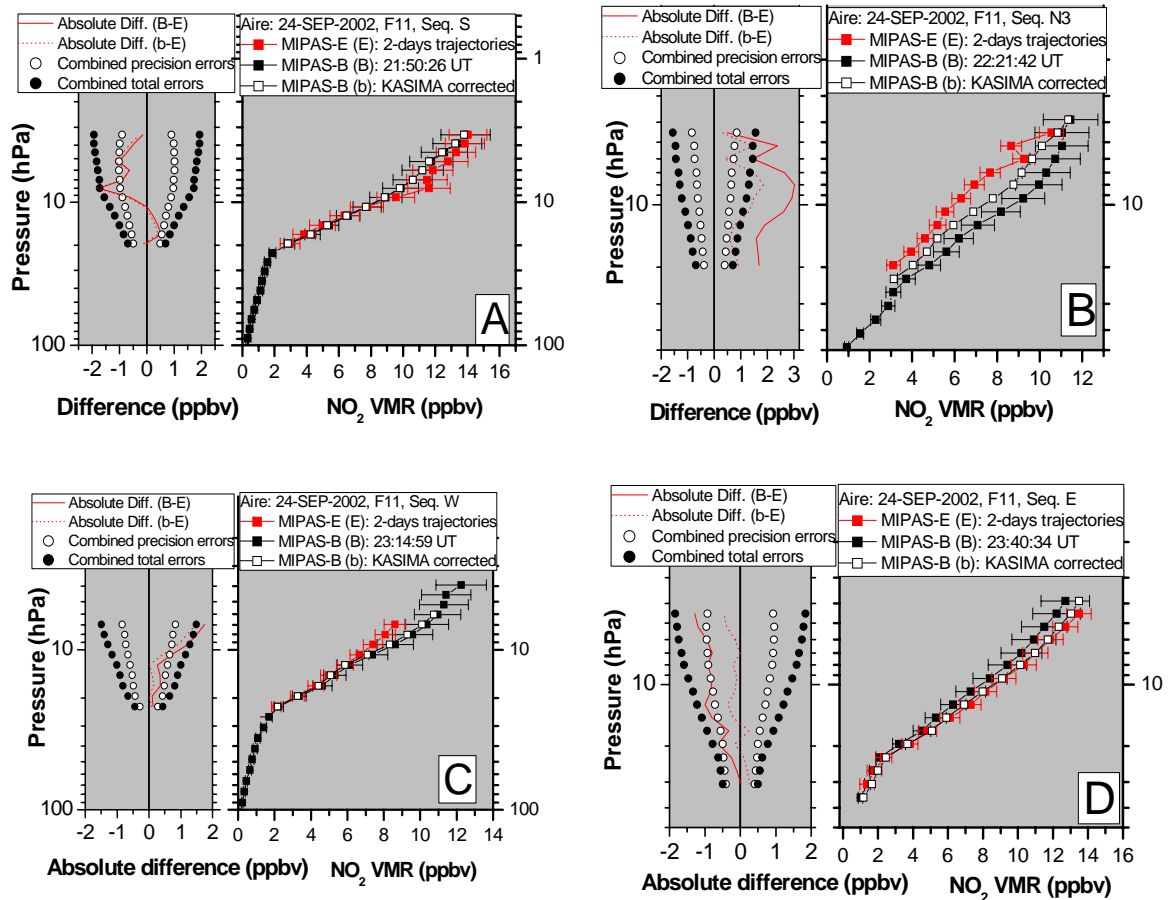


**Figure 8.2.7-5:** MIPAS-B NO<sub>2</sub> VMR profiles comparison with MIPAS-E mean NO<sub>2</sub> VMR profiles which were calculated by averaging all the match points at the same level of altitude considering the weights of the MIPAS-E noise errors. The black curves with open squares represent the MIPAS-B profiles photochemically corrected by using KASIMA. The red dotted line denotes the difference of the corrected MIPAS-B profile minus that of MIPAS-E. Other notations are the same as in Figure 8.2.2-1. (A) For Seq. S. (B) For Seq. N3. (C) For Seq. W. (D) For Seq. E.

### 3.2 Flight No. 13

Two opportunities were available for MIPAS-E NO<sub>2</sub> validation by using the trajectory model with the help of KASIMA simulation results (Panel A and B of Figure 8.2.7-6).

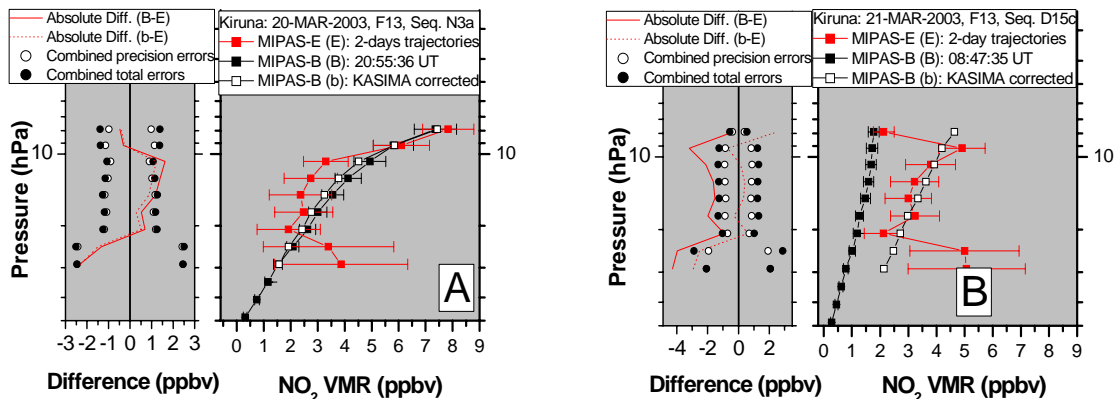


**Figure 8.2.7-6:** Same as Figure 8.2.7-5 but for Flight No. 13. (A) For Seq. N3a. (B) For Seq. D15c.

MIPAS-E mean profiles agree with MIPAS-B corrected profiles in general in both comparisons. In the regions of lower altitudes (Panel A and B) and also higher altitudes (Panel B), the discrepancies are significant. This was caused by the strong oscillation of Rec. 30 profile.

### 3.3 Flight No. 14

The two trajectory comparisons for Flight No. 14 are presented in Figure 8.2.7-7. The consistencies between MIPAS-E and MIPAS-B measurements were improved significantly after the KASIMA simulation results were taken into account.

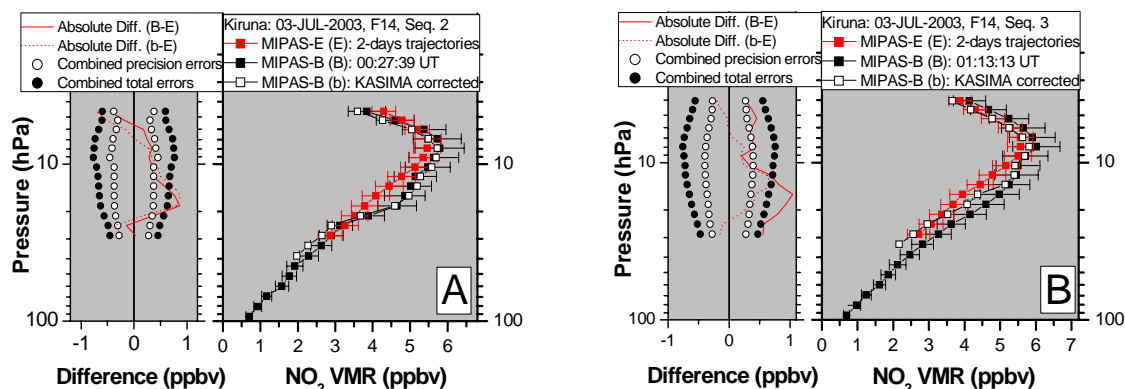


Figure 8.2.7-7: Same as Figure 8.2.7-5 but for Flight No. 14. (A) For Seq. 2. (B) For Seq. 3.

## 4 Summary of NO<sub>2</sub> comparison

The absolute difference profiles of MIPAS-B minus MIPAS-E are summarized in Figure 8.2.7-8 for coincident comparison (Left panel) and for trajectory comparison (Right Panel), separately. Here, the corrected MIPAS-B data were used for the differences calculation when the KASIMA simulation was taken into account. The summary of coincident comparisons indicates that MIPAS-E measured higher values of NO<sub>2</sub> than MIPAS-B in the whole overlapping altitude range. On the contrary, the summary of trajectory comparisons exhibits a slightly low bias at the middle altitudes. This difference may be caused by the KASIMA simulation effects. In the coincident comparison, only one MIPAS-B profile (Seq. 3) was corrected by using the KASIMA model. While in trajectory case, all involved MIPAS-B data were corrected according to the KASIMA simulation outputs.

The quantitative analysis for NO<sub>2</sub> validation is presented in the Table 8.8. For coincident comparison, MIPAS-E data are higher than MIPAS-B measurements by 0.28 ppbv (7.51%) in the whole overlapping height region of 42-3 hPa (22-39 km) but less than the mean combined total error of 1.01 ppbv. For trajectory comparison, the analysis was performed in three height regions. Between 31-23 hPa, MIPAS-E values are larger than MIPAS-B data. In the region of 23-6 hPa, MIPAS-E data are lower than MIPAS-B data. Between 6-3 hPa, MIPAS-E values have again a positive bias. All the mean differences between MIPAS-E and MIPAS-B measurements in the three height regions are within the mean combined total errors. Therefore, it can be concluded that the trajectory comparisons also demonstrated that MIPAS-E measurements are in agreement with MIPAS-B observations. However, the two validation approaches presented the different conclusions about the bias in the region of 23-6 hPa. To be more careful, we tend to take the conclusion from the coincident comparison approach. That is, in 23-6 hPa MIPAS-E measurements are higher than MIPAS-B observations.

## 8.2 MIPAS

The standard deviation and the corresponding mean combined precision errors of NO<sub>2</sub> for coincidence are (0.73 ppbv, 0.74 ppbv), for trajectory comparison the values are (0.57 ppbv, 0.66 ppbv). These data indicate that the precision of MIPAS-E measurements for NO<sub>2</sub> agrees with the expectation value. Unfortunately, the retrieval of NO<sub>2</sub> profiles from MIPAS-E data stop at about 30 hPa. Therefore, the quality of NO<sub>2</sub> data from MIPAS-E in the lower stratosphere could not be assessed.

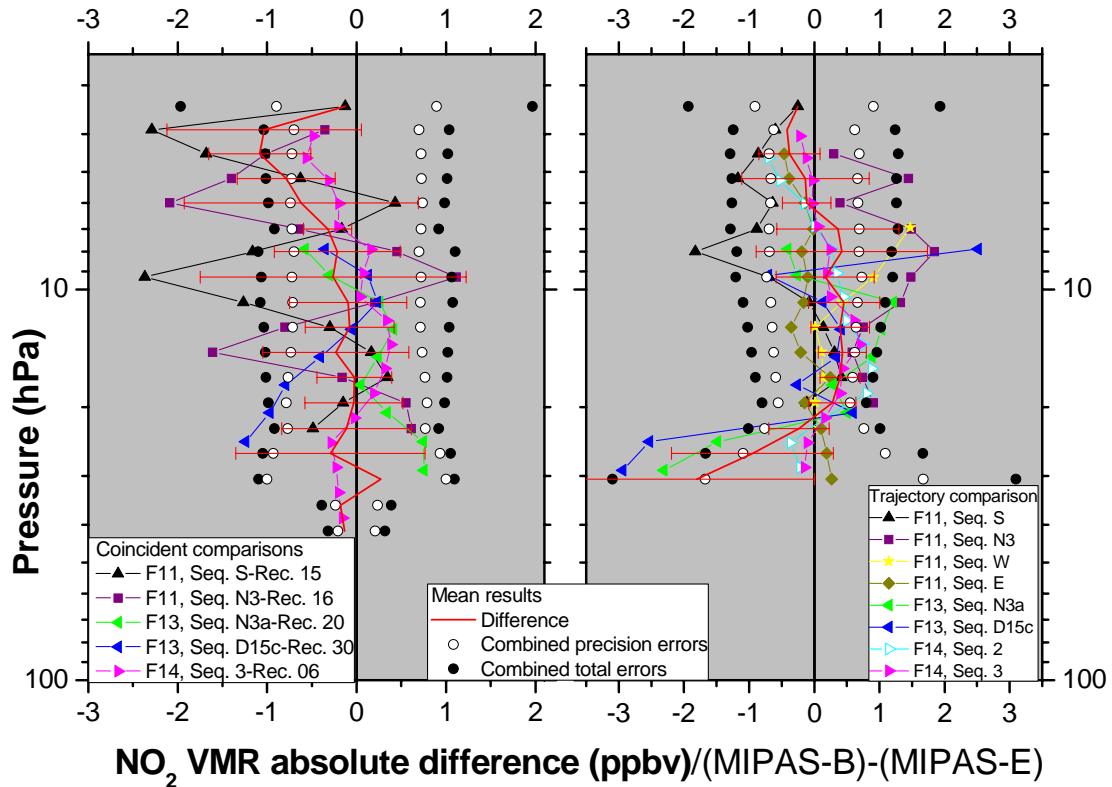


**Figure 8.2.7-8:** Summary comparison of NO<sub>2</sub> VMR between MIPAS-E and MIPAS-B. The differences between MIPAS-E and MIPAS-B were calculated by using the corrected MIPAS-B profiles for which the KASIMA model is necessary. There are no standard deviation bars for the top and bottom sections of the mean difference profile since only one or two comparisons are available in these altitude regions. Left: coincident comparison. Right: trajectory comparison.

**Table 8.8:** Mean differences of MIPAS-B minus MIPAS-E NO<sub>2</sub> as well as the associated mean combined errors and the mean standard deviations.

Accuracy							
Pressure (hPa)	Height (km)	Absolute difference (ppbv)		Relative difference (%)		Mean combined total errors (ppbv)	
		Coincidence	Trajectory	Coincidence	Trajectory	Coincidence	Trajectory
42-31	22-24	-0.28±0.34		-7.51±10.28		1.01±0.18	
31-23	24-26		-0.82±0.74		-36.40±49.88		1.69±0.97
23-6	26-35		0.36±0.10		7.26±2.89		1.06±0.17
6-3	35-39		-0.24±0.14		-3.57±2.39		1.31±0.02
Precision							
Pressure (hPa)	Height (km)	Standard deviation (ppbv)		Mean combined precision errors (ppbv)			
		Coincidence	Trajectory	Coincidence	Trajectory		
23-8	26-33	0.73±0.33	0.57±0.33	0.74±0.03	0.66±0.07		

### 8.3 SCIAMACHY

Among the NRT, off-line and the scientific products of SCIAMACHY, the scientific products have the best data quality so far. Here, we only validate the SCIAMACHY scientific data of O<sub>3</sub> and NO<sub>2</sub> which were retrieved at the Institute of Environmental Physics (IUP/IFE), University of Bremen, Germany. O<sub>3</sub> products were retrieved with the IUP's algorithm version 1.60 based on the Level 0 data. The vertical resolution of the retrieval is about 3 km. NO<sub>2</sub> products were retrieved with the version 1.0 based on the Level 1 data. The obtained vertical resolution is also about 3 km. The preliminary estimated errors for O<sub>3</sub> are 5-10% between 15 and 40 km. For NO<sub>2</sub>, the errors are estimated to 10% at all levels of altitude. Because of the ENVISAT limb pointing errors for SCIAMACHY which can be up to 3 km, a constant offset of 1.5 km was subtracted from the tangent height information provided in the data files prior to the retrieval. The details about the O<sub>3</sub> products retrieved by IUP are given by Brinksma, E. J., et al., (2004). And the detailed descriptions for NO<sub>2</sub> were presented by von Savigny, C., et al., (2004) and Rozanov, A., et al., (2005).

Because the major mission of MIPAS-B was to validate the MIPAS-E measurements, the opportunity to find the coincident comparison between MIPAS-B and SCIAMACHY is very limited. Consequently, the trajectory approach becomes the prior way for SCIAMACHY validation with MIPAS-B observations. The 2-days backward and forward trajectories of the air masses which had been sounded by MIPAS-B were calculated by Grunow, K. (2005). The trajectory model has been described briefly in the section of 8.1.2. The process to find the match points between SCIAMACHY and MIPAS-B observations is similar to that of MIPAS-E trajectory comparison based on the match criteria of (500 km, 1 hour). In the following, MIPAS-B results of Flight No. 11 and 14 are compared to SCIAMACHY observations.

#### 8.3.1 O<sub>3</sub>

Two pair trajectories comparisons are demonstrated for MIPAS-B Flight No. 11 in Figure 8.3.1-1. The combined errors were calculated according to the equation (8.1) but using the SCIAMACHY errors instead of the MIPAS-E errors. Panel A shows that below 27 km, SCIAMACHY measurements (blue curve) agree with MIPAS-B O<sub>3</sub> profile of Seq. S (black curve) with respect to their combined errors except around 18 km. Above the level of 27 km, significant discrepancies appeared. It seemed that the large discrepancies were caused by the unrealistic large observations from SCIAMACHY. Normally, the maximum of the O<sub>3</sub> VMR is 8-10 ppmv around 35 km. However, SCIAMACHY measured values reach 9.5-11.5 ppmv in 28-38 km. The comparison between the O<sub>3</sub> profile of MIPAS-B Seq. N3 and its correlative SCIAMACHY measurements (Panel B) result in the similar conclusions as in Panel A. Further, the SCIAMACHY low bias in 16-21 km becomes more obvious in Panel B.

From MIPAS-B Flight No. 14, two trajectory comparisons for O<sub>3</sub> are available (Figure 8.3.1-2). Panel A shows the comparison of MIPAS-B Seq.2 to the mean profile of SCIAMACHY. In the whole overlapping altitude range of 9-28 km, SCIAMACHY data agree with MIPAS-B data with respect to the combined errors except in 10-13 km. The comparison between MIPAS-B Seq. 3 and the correlative SCIAMACHY data made from the match points in 2-day trajectories (Panel B) indicates that the consistency is quite well in the range of 15-28 km. Above 28 km, SCIAMACHY data give a slight negative bias.

### 8.3 SCIAMACHY

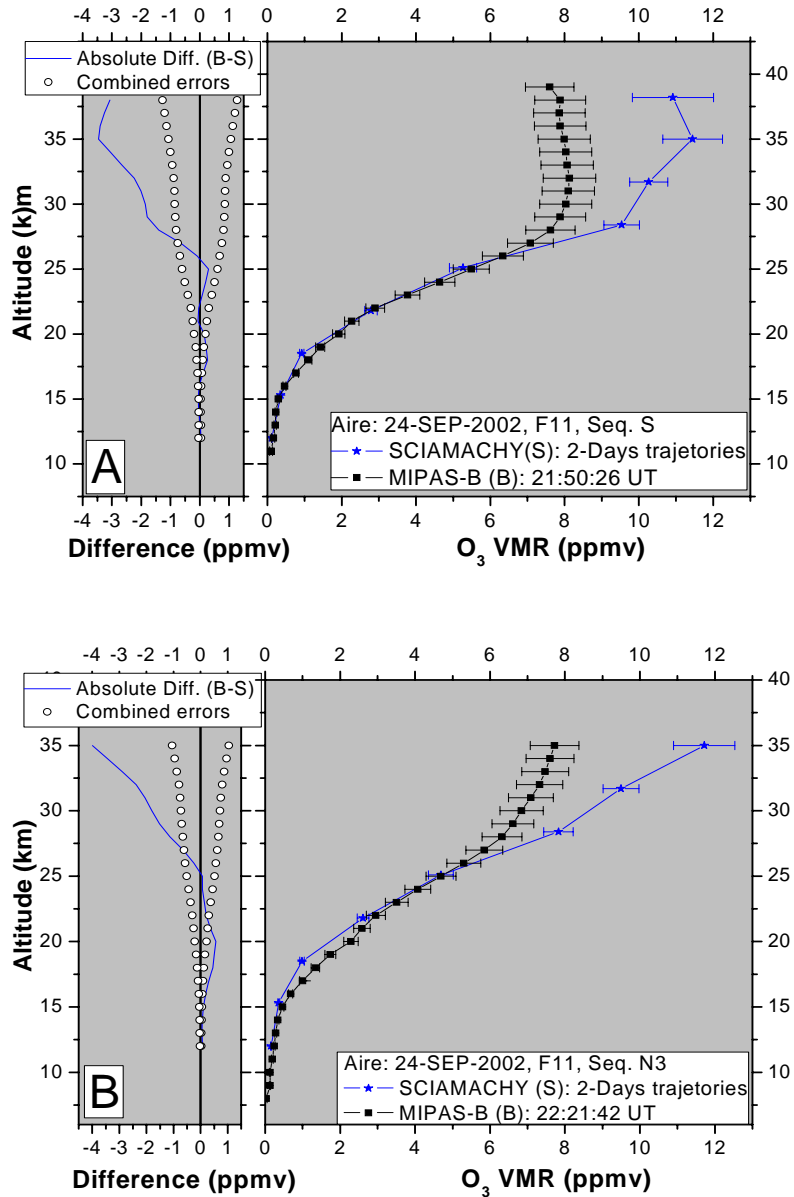


**Figure 8.3.1-1:** O<sub>3</sub> trajectories comparisons between SCIAMACHY and MIPAS-B. The black curves denote MIPAS-B profiles and the blue curves with star symbols stand for the mean profiles of SCIAMACHY. The solid blue lines represent the differences of MIPAS-B data minus SCIAMACHY data. The combined errors (open circles) were calculated based on the total errors of SCIAMACHY and MIPAS-B. (A) For Seq. S. (B) For Seq. N3.



## 8. Intercomparison of measurements

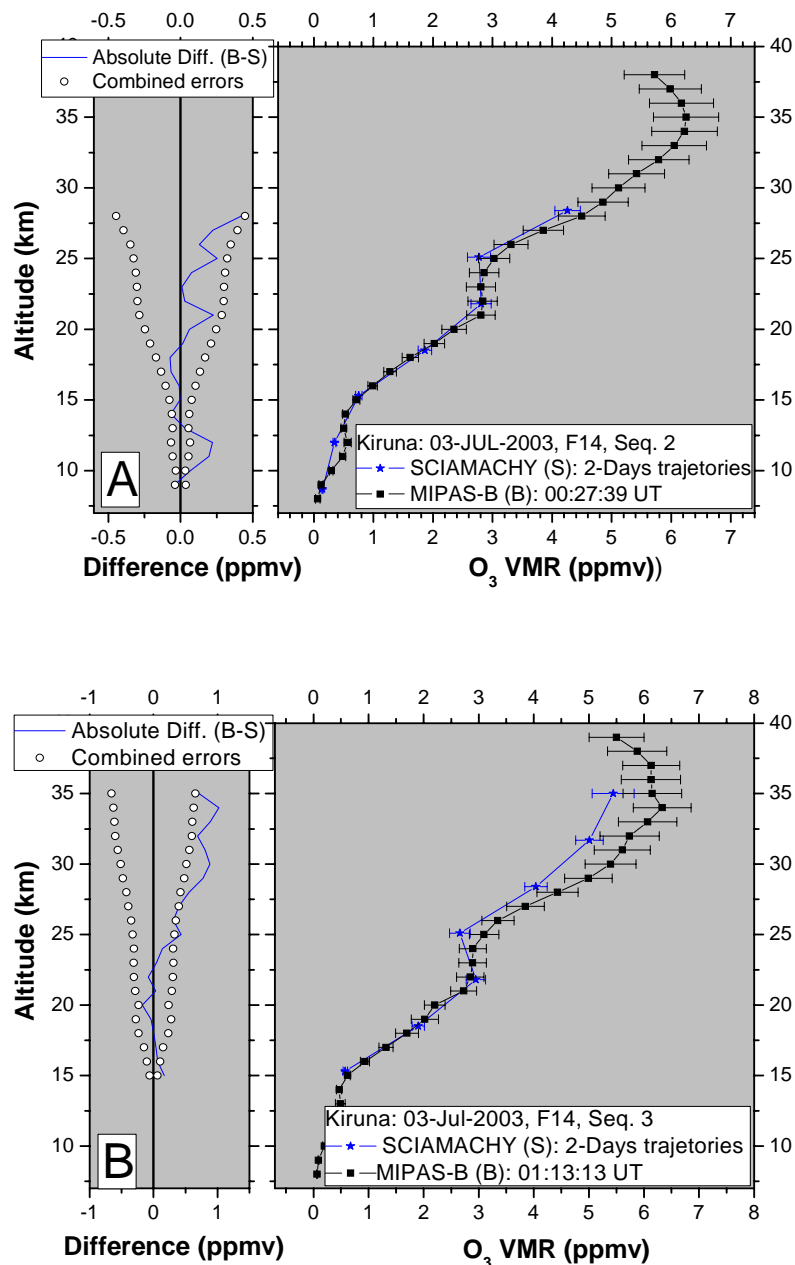


**Figure 8.3.1-2:** O<sub>3</sub> trajectories comparisons between SCIAMACHY and MIPAS-B. (A) For Seq. 2. (B) For Seq. 3. The notations are the same as in Figure 8.3.1-1.

After synthesizing the above comparisons results (Table 8.9), the features of the agreement between SCIAMACHY and MIPAS-B measurements for O<sub>3</sub> are as follows. **a.** In the range of 9-28 km, the agreements are good in general. The mean difference (MIPAS-B minus SCIAMACHY) is -0.28 to 0.10 ppmv (-2.31 to 7.72%) and within the mean combined error. **b.** In the region of 28-38 km, SCIAMACHY measurements show systematically positive biases. The mean difference is -1.63 ppmv (-20.09%) and obviously beyond the mean combined errors of 0.83 ppmv. The mean standard deviation of the differences in the range of 27-35 km implies that the profile-profile variation of SCIAMACHY is large above 27 km. It is necessary to note that the statistical analysis made below 12 km and above 35 km are based on single comparison results. Consequently, the standard deviation estimation is useless in these regions.



### 8.3.2 NO<sub>2</sub>

As already mentioned during the validation for MIPAS-E NO<sub>2</sub>, the significant diurnal variation of stratospheric NO<sub>2</sub> handicaps the direct exploiting of the trajectory model. Here, we also use KASIMA simulation results (*Ruhnke, R., 2005*) to perform the validation of SCIAMACHY measurements for NO<sub>2</sub>. That is, to compare SCIAMACHY NO<sub>2</sub> data with the time corrected MIPAS-B NO<sub>2</sub> measurements. Equations (8.2) and (8.3) can be used for the calculation of the corrected MIPAS-B NO<sub>2</sub> profiles after substituting the subscription ECMWF by KASIMA.

Panel A and B of Figure 8.3.2-1 present the two trajectory comparisons for Seq. S and Seq. N3, respectively. The modification of the MIPAS-B NO<sub>2</sub> profiles (black curves with solid rectangles) with respect to the corrected MIPAS-B profiles (black curves with open rectangle symbols) can be seen clearly. The left subpanels of each Panel demonstrate the absolute difference (blue line) of MIPAS-B corrected data minus SCIAMACHY data and their combined total errors (open circles). The comparison between the Seq. S corrected NO<sub>2</sub> profile and the correlative SCIAMACHY mean profile shows that the differences increase with altitude but are always within their combined errors. (Panel A). The comparison in Panel B demonstrates the similar results as in Panel A.

Two MIPAS-B NO<sub>2</sub> profiles, Seq2 and Seq. 3, from Flight No. 14 can be used for the intercomparisons between SCIAMACHY and MIPAS-B observations (Figure 8.3.2-2). Unlike the situation in Flight No. 11, the changing of the MIPAS-B NO<sub>2</sub> profiles with respect to the corrected NO<sub>2</sub> profiles is small. This is because that both MIPAS-B and SCIAMACHY measurements were performed in the polar summer. In polar summer, all sounded air masses are under the sunlight. Consequently, the NO<sub>2</sub> temporal gradient is not as steep as in the sunrise and sunset period. Panel A shows the comparison for Seq. 2. The absolute difference profile indicates that a good agreement is obtained in the whole comparable levels of altitude. The similar good agreement also appears in Panel B. A common exception in both panels is that around 16 km, SCIAMACHY shows high values and the deviation exceeds the combined errors.

Fortunately, one double coincident measurement situation, Seq. 2 and ID6926, between MIPAS-B and SCIAMACHY, one triple coincident measurement situation, Seq.3, Rec. 06 and ID 6927, among MIPAS-B, MIPAS-E and SCIAMACHY was found. The mean distance between Seq. 2 and ID6926 is about 670 km. The time offset is about 10.5 hours. The mean spatial and temporal offset between Seq. 3 and ID6927, Rec. 06 and ID6927 are (260 km, 10 hours) and (310 km, 1.5 hours), respectively. Therefore, the NO<sub>2</sub> comparison between MIPAS-E Rec. 06 and SCIAMACHY ID6927 can be performed directly. The other two comparisons between SCIAMACHY and MIPAS-B also need the help of KASIMA simulation.

Figure 8.3.2-3 presents the coincident comparisons. Panel A shows that the SCIAMACHY profile agrees quite well with the corrected MIPAS-B measurements except at the high levels of altitudes and the region of 16-20 km. The consistency between ID6927 profile of SCIAMACHY and Seq. 3 profile of MIPAS-B is quite well. The low bias of SCIAMACHY appears also in the region of 16-20 km (Panel B). Panel B also shows that the corrected MIPAS-E profile by virtue of KASIMA simulation results is very close to the original MIPAS-E profile. In order to avoid the additive uncertainty made from the KASIMA model, the difference profile was calculated directly via MIPAS-E original profile minus SCIAMACHY data. This difference profile indicates that the SCIAMACHY data agrees perfectly with the MIPAS-E data.

## 8. Intercomparison of measurements

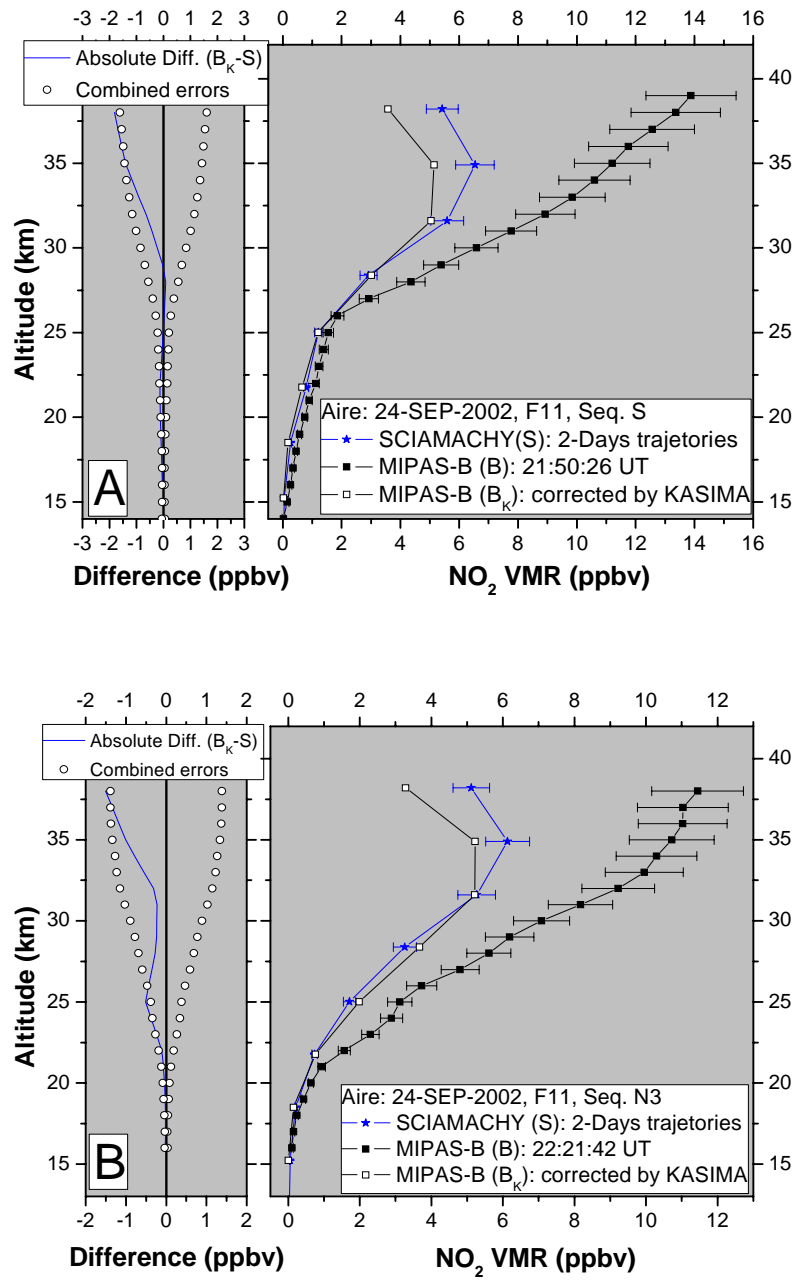


**Figure 8.3.2-1:**  $\text{NO}_2$  trajectories comparisons between SCIAMACHY and MIPAS-B. The black curves denote MIPAS-B profiles and the blue curves with star symbols stand for the mean profiles of SCIAMACHY. The black curves with open rectangle symbols represent the corrected MIPAS-B profile with the help of KASIMA simulations. The solid blue lines represent the differences of the corrected MIPAS-B data minus SCIAMACHY data. The combined errors (open circles) were calculated based on the total errors of SCIAMACHY and MIPAS-B. (A) For Seq. S of Flight No. 11. (B) For Seq. N3 of Flight No. 11.

### 8.3 SCIAMACHY

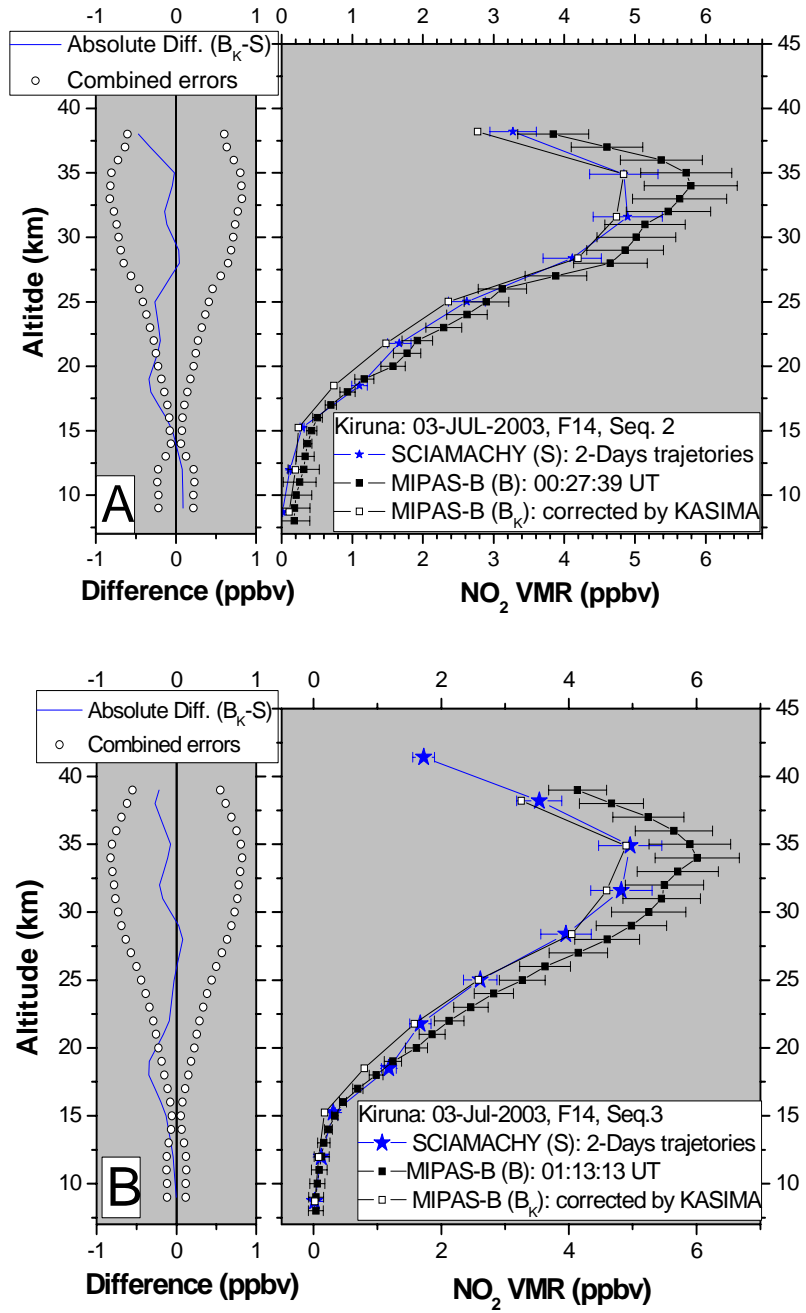
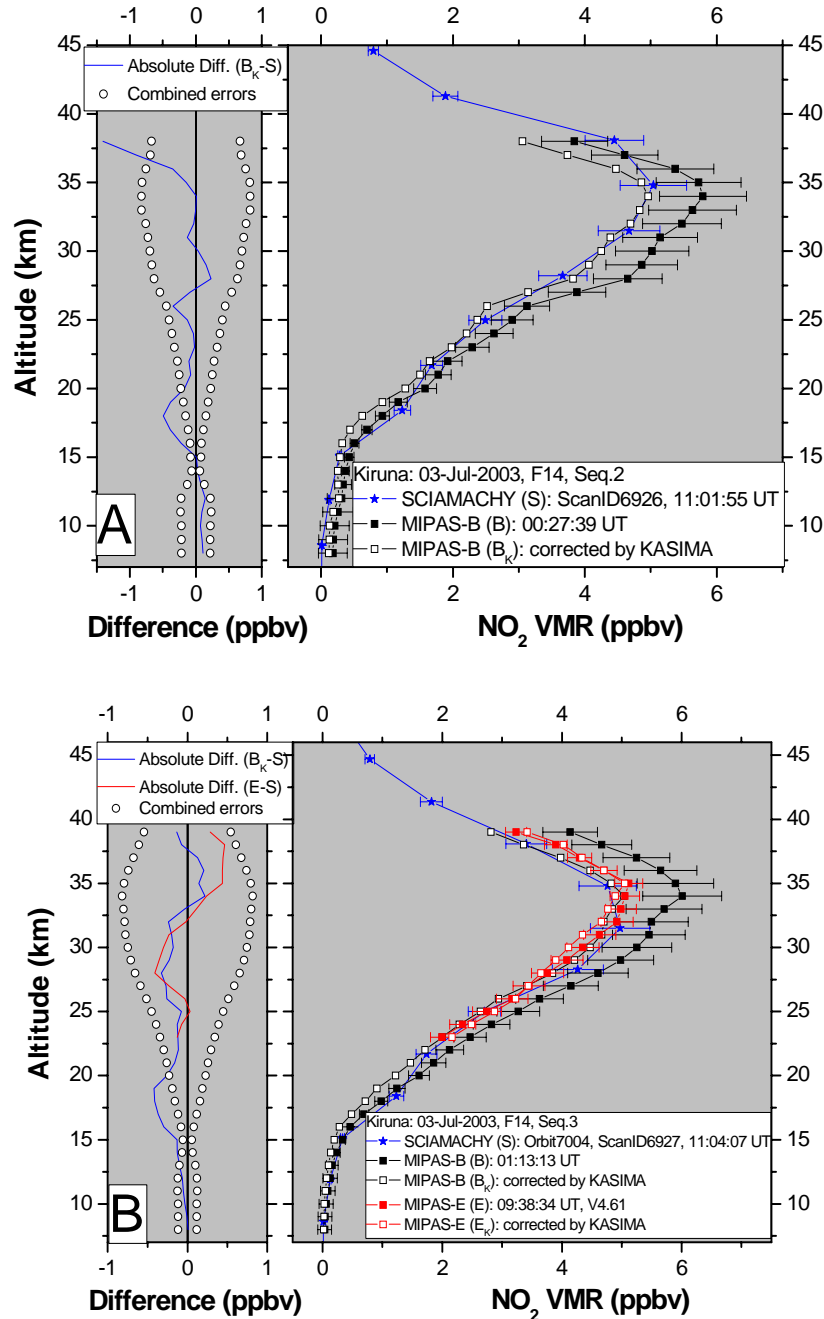


Figure 8.3.2-2: Same as for Figure 8.3.2-1, but (A) For Seq. 2 of Flight No. 14. (B) For Seq. 3 of Flight No. 14.

## 8. Intercomparison of measurements



**Figure 8.3.2-3:** NO<sub>2</sub> coincident intercomparisons among SCIAMACHY, MIPAS-B and/or MIPAS-E. The black curves denote MIPAS-B profiles and the blue curves with star symbols stand for the profiles of SCIAMACHY. The black curves with open rectangle symbols represent the corrected MIPAS-B profile with the help of KASIMA simulations. The red curve with solid rectangle symbols and the red curve with open rectangle symbols represent the MIPAS-E profile and its corrected profile with the help of KASIMA, respectively. The solid blue lines represent the differences of the corrected MIPAS-B minus SCIAMACHY data. While the red line denotes the difference between the MIPAS-E and SCIAMACHY profile. The combined errors (open circles) were calculated based on the total errors of SCIAMACHY and MIPAS-B. (A) For Seq. 2 of Flight No. 14. (B) For Seq. 3 of Flight No. 14.

The summary of the NO<sub>2</sub> validation for SCIAMACHY is as follows (see Table 8.9). The agreement of measurements for NO<sub>2</sub> during Flight No. 14 is better than that during Flight No. 11. This probably could be ascribed to the improvement of the pointing registration errors of ENVISAT (*Brinksmä, E. J., 2004*). The average of all the difference profiles made from the trajectory comparisons indicates that SCIAMACHY measurements are slightly larger than MIPAS-B data in general. In 11-26 km and 29-39 km, SCIAMACHY shows distinct positive

### 8.3 SCIAMACHY

biases. In the narrow regions of 9-11 km and 26-29 km, SCIAMACHY gives the negative biases. However, the mean discrepancies between SCIAMACHY and MIPAS-B measurements are within the corresponding mean combined errors in all these altitude regions. The coincident comparisons demonstrate similar conclusions as the trajectory approach. However, between 33 and 38 km, the coincident comparison between MIPAS-B Seq. 3 and the correlative SCIAMACHY data exhibits that SCIAMACHY shows a negative instead of a positive bias. The standard deviation of 0.28 ppbv in the region of 16-38 km shows that SCIAMACHY has a good measurement precision for NO<sub>2</sub>.

It must be noted that the mean profiles of SCIAMACHY were calculated based on relatively sparse data. i.e., only 1-4 match points (depending on altitude) were found at a specific level of altitude. So, for a mean profile of SCIAMACHY, its point at a level of altitude is the average of only several values (1-4). Therefore, the statistical significance is not very strong.

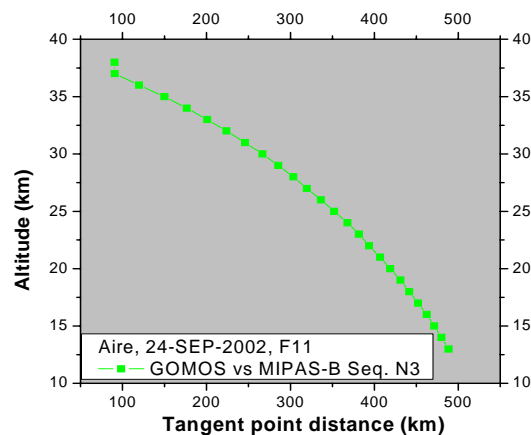
**Table 8.9: Mean differences of MIPAS-B minus SCIAMACHY measurements for O<sub>3</sub> and NO<sub>2</sub> as well as the associated mean combined errors and the mean standard deviations.**

O <sub>3</sub>	Accuracy			
	Altitude (km)	Absolute difference (ppmv)	Relative difference (%)	Combined errors (ppmv)
	9-26	0.10±0.07	7.72±10.63	0.21±0.15
	26-28	-0.28±0.15	-2.31±1.80	0.56±0.03
	28-38	-1.63±0.80	-20.09±10.29	0.83±0.17
Precision				
Altitude (km)	Standard deviation (ppmv)			
12-27	0.14±0.09			
27-35	1.40±0.49			
NO <sub>2</sub>	Accuracy			
	Altitude (km)	Absolute difference (ppbv)	Relative difference (%)	Combined errors (ppbv)
	9-11	0.04±0.01	0.19±0.18	0.17±0.01
	11-26	-0.11±0.07	-6.28±5.39	0.17±0.10
	26-29	0.10±0.04	0.43±0.43	0.57±0.12
	29-39	-0.52±0.35	-5.98±3.83	0.99±0.13
	Precision			
	Altitude (km)	Standard deviation (ppbv)		
16-38	0.28±0.24			

## 8.4 GOMOS

Unfortunately, because of a GOMOS data unavailability during the period of MIPAS-B Flight No. 13 and Flight No. 14, only one O<sub>3</sub> profile and one NO<sub>2</sub> profile of GOMOS is available to compare with MIPAS-B coincident measurements from Seq. N3 in Flight No. 11. The GOMOS data analyzed here have been reprocessed by the prototype processor that corresponds to version 6.0a (Saavedra de Miguel, L., 2005). The GOMOS O<sub>3</sub> and NO<sub>2</sub> data were measured under dark-limb mode. Before performing the comparison, some flagged values of GOMOS for O<sub>3</sub> and NO<sub>2</sub> had been eliminated according to the requirements for GOMOS validation (Saavedra de Miguel, L., 2005). These flagged values were regarded as invalid data because they are unreasonably large or small according to the criteria embedded in the processor. Additionally, the O<sub>3</sub> and NO<sub>2</sub> profiles of GOMOS retrieved by LPCE (Laboratoire de Physique et Chimie de l'Environnement) were also compared with the MIPAS-B data.

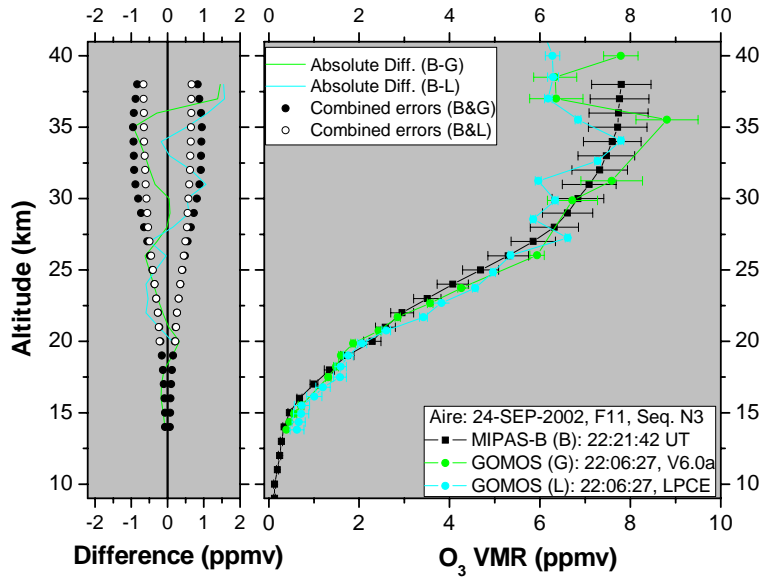
The mean time offset between MIPAS-B Seq. N3 and the corresponding GOMOS scan is about 15 minutes. Their tangent point distances decrease with increasing altitudes and the maximum is less than 500 km (Figure 8.4-1). So, the match quality is quite good. The vertical resolution of O<sub>3</sub> and NO<sub>2</sub> profile made by GOMOS operational processor are 2-3 km and 4 km, respectively. These values are nearly equal to equal the vertical resolution of MIPAS-B profiles approximately. Therefore the vertical resolution influence to the intercomparison was omitted.



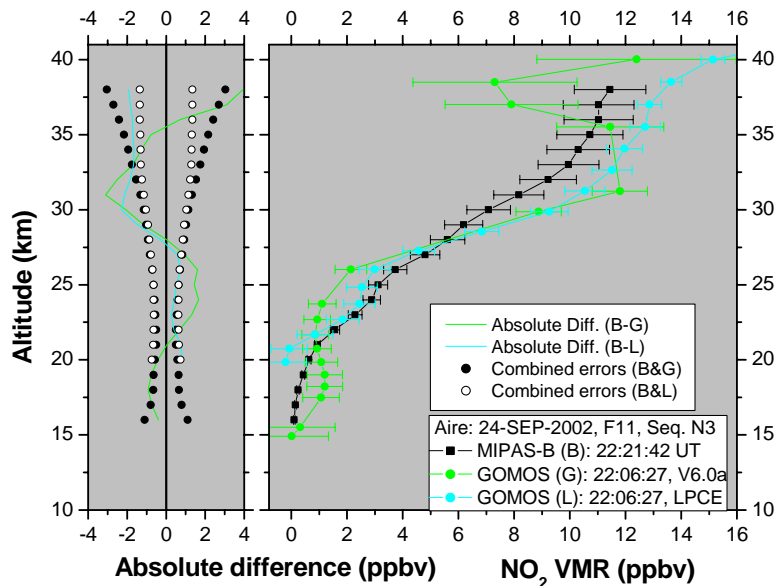
**Figure 8.4-1:** The tangent point distances between MIPAS-B Seq. N3 and the corresponding sequence of GOMOS.

Figure 8.4-2 demonstrates the comparisons for O<sub>3</sub>. Both GOMOS operational profile and the LPCE profile agree with MIPAS-B data in general with respect to their combined errors. Between 21 and 25 km, GOMOS operational profile is more close to the MIPAS-B measurements than LPCE. Around the level of 36 km, the GOMOS profiles exhibit unrealistic oscillations and negative biases. The mean difference between MIPAS-B measurements and the GOMOS operational data over the range of 14-36 km is -7.30% (-0.25 ppmv) (minus sign denotes MIPAS-B data are lower than GOMOS data). Above 36 km, the difference reaches about -18.20% (-1.42 ppmv). These results are similar to the conclusion made by Suortti, T., et al., (2003).

## 8.4 GOMOS



**Figure 8.4-2:** O<sub>3</sub> Comparison between GOMOS (green curve from the off-line data and the cyan curve from LPCE) and MIPAS-B Seq. N3 (black curve) measurements. The combined errors were calculated based on the total errors of MIPAS-B and the standard deviation of GOMOS.



**Figure 8.4-3:** NO<sub>2</sub> Comparison between GOMOS (green curve from the off-line data and the cyan curve from LPCE) and MIPAS-B Seq. N3 (black curve) measurements. The combined errors were calculated based on the total errors of MIPAS-B and the standard deviation of GOMOS.

The NO<sub>2</sub> comparisons are plotted in Figure 8.4-3. Obviously, the agreement between MIPAS-B and GOMOS operational profiles is not satisfactory. The GOMOS operational NO<sub>2</sub> data shows a strong oscillation at higher altitudes. On the contrary, the consistency between MIPAS-B and the GOMOS LPCE data is good below about 28 km and shows a high bias above this altitude. This implies that the version 6.0a of the prototype processor needs to be improved.

A very preliminary finding is that GOMOS profiles show large oscillations exceeding their expected precisions above about 28 km. It is impossible to make a definitely conclusion to the GOMOS O<sub>3</sub> and NO<sub>2</sub> validation here due to the very sparse data. However, these comparison results can be used as a part of the whole GOMOS validation data set.

## Discussion

The validation results depend on many factors. Except the mismatch of measurements in space and time, the vertical grid of the profile, the vertical resolution of the retrieval as well as the vertical coordinate under which the validation was performed are sometimes important.

### 9.1 Vertical grid of profile representation.

The MIPAS-B profiles were retrieved on the vertical grid of 1 km. While for MIPAS-E and GOMOS off-line products as well as the IUP version scientific products of SCIAMACHY, the vertical grids were 3 km, 0.5-1.5 km (10-40 km of height) and 3.3 km (up to about 60 km height), respectively. Before the calculation of the measurement differences between MIPAS-B and the chemistry instruments (MIPAS-E, SCIAMACHY or GOMOS), the data of the chemistry instruments were interpolated onto MIPAS-B pressure levels based on logarithm (for MIPAS-E) or onto MIPAS-B altitude levels by using a linear algorithm (for SCIAMACHY and GOMOS). This is an approximation approach and may introduce an extra uncertainty to the comparison. Although a more accurate approach is possible to interpolate the ENVISAT chemistry instruments profiles onto the MIPAS-B vertical grid (*Carlotti, M., et al., 2001*), we did not exploit this due to its computational burden.

In order to evaluate the error introduced by the vertical grid, a case study was performed (Figure 9.1-1). Firstly, the MIPAS-E profile (red curve with solid rectangle symbols) was interpolated onto the MIPAS-B nominal 1 km grid by using a logarithmic algorithm. Then the difference profile (red line in the left subpanel) was calculated via the MIPAS-B profile, which was retrieved on 1 km grid (black curve with solid rectangle symbols), minus the interpolated MIPAS-E profile. Secondly, a new MIPAS-B temperature profile of Seq. 3 based on exactly the same vertical grid of MIPAS-E was retrieved (black curve with open rectangle symbols). Then, the second difference profile (green curve in the left subpanel) between the new MIPAS-B and the MIPAS-E profiles was obtained. Clearly, the two difference profiles are not overlapping at all levels of altitude. Figure 9.1-1 demonstrates that in the most height regions, the differences of the two cases results are small. The average difference is about 0.03 K. This value is far less than their mean combined total errors. However, at the level of about 200 hPa, the discrepancy of the two difference profiles reaches about 1.6 K. This value nearly equals the combined precision error at the same level. Therefore, since the retrieved values of the target parameters in the regions where small scale structures exist are sensitive to the vertical grid, it can be expected that the errors introduced by using different vertical grids may be not negligible in these regions. However, because the small scale structures arise randomly to some extent, this kind of errors would have weak influence to the validation conclusion which has a significant statistics.



## 9.2 Estimation of the vertical resolution influence

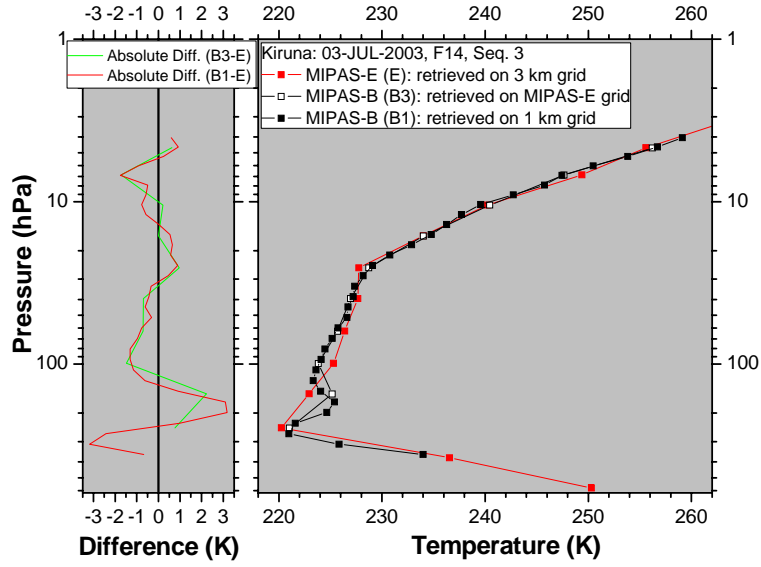


**Figure 9.1-1:** The influence of the vertical grid to the intercomparison. The red curve with rectangle symbols is the MIPAS-E temperature profile retrieved on a 3 km grid. The black curve with solid rectangles and the black curve with open rectangles represent the retrieved MIPAS-B temperature profile on a 1 km grid and on the MIPAS-E grid, respectively. In the left subpanel, the red line and the green line are the difference profiles of MIPAS-E temperature minus the two MIPAS-B temperature profiles, separately.

### 9.2 Estimation of the vertical resolution influence

Some fine vertical structures of the target parameter field could be resolved by the higher resolution, but not by the lower one. Before performing the comparison, the profiles with higher vertical resolution normally need to be smoothed. In general, MIPAS-B profiles have a slightly higher vertical resolution than MIPAS-E and SCIAMACHY profiles. However, because of the small difference it can be expected that the vertical resolution influences to our validation are negligible. In order to confirm this, two case studies are presented.

The method used here is described by Rodgers and Connor (2003), and its application to our cases study is outlined below. When disregarding noise, the retrieved profile  $X_{re}$  is a weighted average of the “true” profile  $X_{true}$  and the a priori profile  $X_a$  in the form of

$$X_{re} = AX_{true} + (I - A)X_a, \quad (9.1)$$

where  $A$  is the averaging kernel and  $I$  denotes identity matrix. The MIPAS-B higher-resolved profiles  $X_B$  are smoothed by applying the averaging kernel of the low-resolved MIPAS-E profiles. Also, the MIPAS-B profiles are transformed to the a priori of MIPAS-E. Both the a priori transformation and smoothing is done by

$$\tilde{X}_B = A_E X_B + (I - A_E)X_{Ea}, \quad (9.2)$$

where  $X_{Ea}$  denotes the a priori profile of MIPAS-E. Because  $X_{Ea}$  is set to zero at all altitudes, the last term of equation (9.2) equals zero. Comparing equation (9.2) with equation (9.1), it is clear that  $\tilde{X}_B$  is the result derived with the MIPAS-E inverse mode, if  $X_B$  is assumed to be the true profile. Thus, in the difference of  $\tilde{X}_B - X_E$  the contributions originating from different vertical resolution are reduced.

## 9. Discussion

Figure 9.2-1 is the averaging kernel of MIPAS-E retrieval for temperature. It was used for smoothing the MIPAS-B temperature profiles.

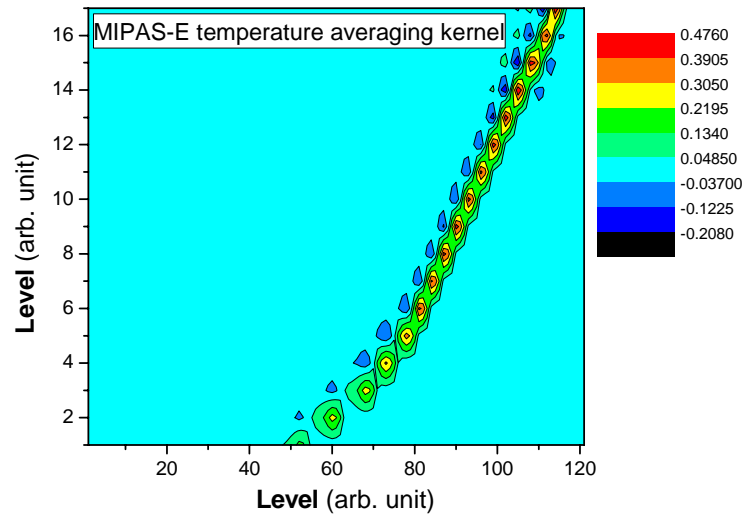


**Figure 9.2-1:** Averaging kernel matrix for the MIPAS-E temperature measurement. Displayed is scaled form.

Two temperature profiles, from Seq. 15c of Flight No. 13 and Seq. 3 of Flight No. 14, were selected for the case study. This is because at most levels of altitude the vertical resolutions of these two profiles are 2-3 km. And also their comparisons with the correlative MIPAS-E profiles represent two typical cases: bad and quite well consistency. The lowermost parts of the MIPAS-B temperature profile where the vertical resolution is larger than 3 km was not smoothed.

Figure 9.2-2 presents the smoothed MIPAS-B temperature profiles and their comparisons with MIPAS-E measurements along with the original MIPAS-B profiles and their intercomparison results. The values of the smoothed MIPAS-B temperature profiles (black curves with open rectangle symbols) are very close to the original values (black curves with solid rectangle symbols). Their difference doesn't go beyond the MIPAS-B errors. The consistency between the smoothed MIPAS-B profiles and MIPAS-E profiles (green line) is slightly better than those between the unadjusted MIPAS-B profiles and the MIPAS-E retrievals (red line), particularly for Seq. D15c. This is caused by the different vertical grids of the profiles for MIPAS-B (based on 1 km grid) and MIPAS-E (based on 3 km grid). Consequently, the vertical resolution influences to the validation are very small and can be omitted.

### 9.3 Comparison in potential temperature frame

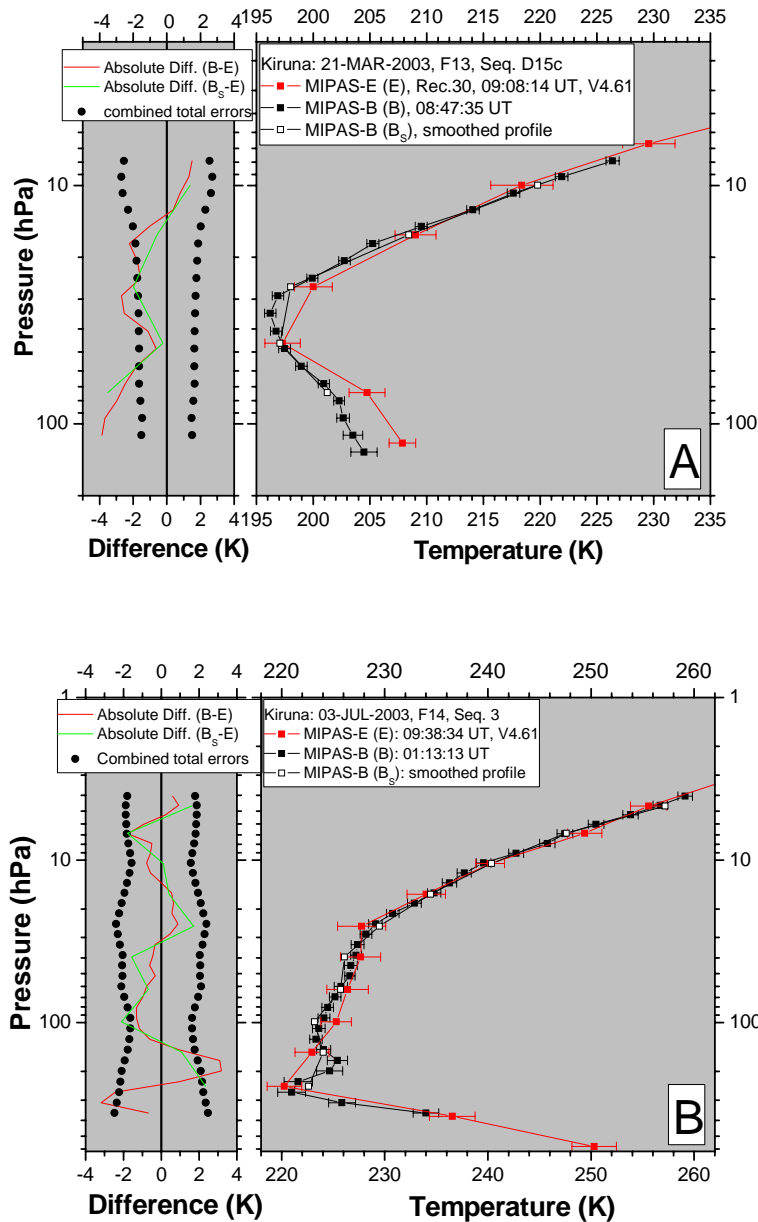


**Figure 9.2-2:** Comparisons of MIPAS-E with MIPAS-B temperature profiles with and without taking into account the vertical resolution influence. The black curves with solid rectangle symbols represent the MIPAS-B original retrieval. The black curves with open rectangle symbols denote the smoothed MIPAS-B profile. The red and green lines represent the differences of MIPAS-B minus MIPAS-E profile corresponding to the two cases, respectively. (A) For Seq. D15c, Flight No. 13. (B) For Seq. 3, Flight No.14.

### 9.3 Comparison in potential temperature frame

The state parameters of air parcels can be exhibited in the potential temperature coordinate. All the coincident comparisons between MIPAS-E and MIPAS-B measurements for temperature, volume mixing ratios of  $H_2O$ ,  $O_3$ ,  $HNO_3$ ,  $N_2O$ ,  $CH_4$ , and  $NO_2$  were also performed in the potential temperature frame. As an example, Figure 9.3-1 demonstrates the  $O_3$  comparisons under the two different frames. Obviously, they exhibit almost the same extent of consistency. For other target parameters, the situation is similar to the  $O_3$  comparison presented here.

## 9. Discussion

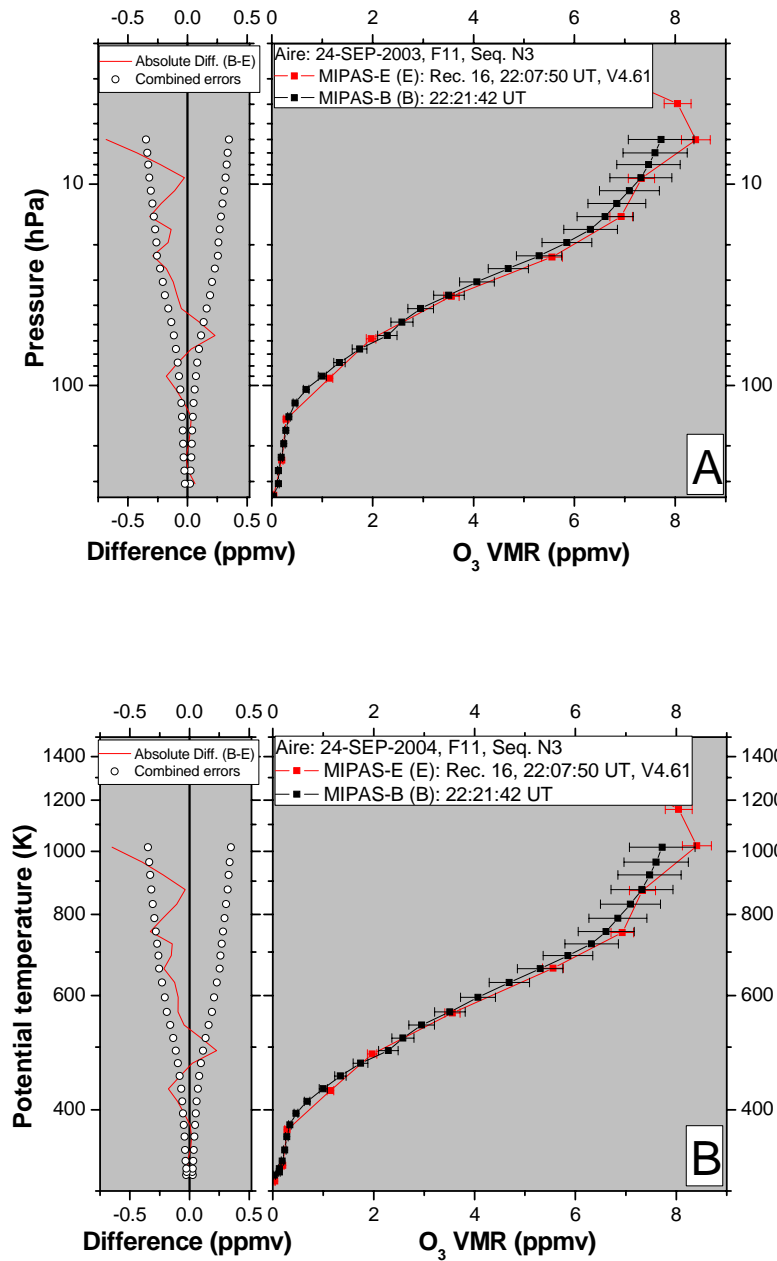


**Figure 9.3-1:** An example of comparisons of MIPAS-E O<sub>3</sub> VMR with MIPAS-B correlative measurements with different altitude coordinates. (A) In pressure coordinate system. (B) In potential temperature coordinate system. The error bars of MIPAS-E denote its noise errors. The combined errors represent the combined precision errors.

## **Summary and outlook**

For validation of the chemistry instruments MIPAS, SCIAMACHY, and GOMOS onboard the satellite ENVISAT, three balloon flights were carried out from 24 September 2002 to 3 July 2003 with MIPAS-B, the balloon version of MIPAS. To validate the instruments' performances in different operational environments, the balloon flights were conducted at middle latitudes in fall (Aire sur l'Adour, France) and at high latitudes (Kiruna, Sweden) in late winter and summer.

Based on the spectra measured by MIPAS-B in the three flights, a total of eight high-quality profiles were obtained through careful retrieval by the MIPAS-B group for each ENVISAT target parameter — temperature, the VMRs of H<sub>2</sub>O, O<sub>3</sub>, HNO<sub>3</sub>, CH<sub>4</sub>, N<sub>2</sub>O, and NO<sub>2</sub>. A detailed data error analysis was made as well.

Carefully selected balloon flight dates and times as well as the chosen observation angle scenarios allowed for a close look at the ENVISAT chemistry instruments' data by a so-called coincident comparison approach. The distance of MIPAS-E and MIPAS-B observed tangent geolocations was inside 300 km and measurement time was within 30 minutes in MIPAS-B Flight No. 11 and Flight No. 13. When a polar vortex existed (Flight No. 13), most of the PV differences between MIPAS-E and MIPAS-B tangent geolocations were less than 15%. Those tangent points with PV differences larger than 15% were not concluded in the final conclusions. Even though the temporal and spatial offsets, 8.5 hours and 500 km in maximum, are larger in Flight No. 14, their influences on the MIPAS-E validation are expected to be small taking into account the advection of the MIPAS-B observed air masses and the stability of the weather conditions of the Arctic summer. A total of five MIPAS-B profiles of each target parameter were used for comparison with MIPAS-E coincident measurements. For SCIAMACHY, only two coincident comparisons are available. These two comparisons refer to O<sub>3</sub> and NO<sub>2</sub> VMR. The mean space and time offsets were (260 km, 10 hours) and (670 km, 10.5 hours), respectively. For GOMOS, a coincident comparison with MIPAS-B is available for O<sub>3</sub> and NO<sub>2</sub>, respectively. The spatial and temporal offset is smaller than (500 km, 0.5 hours).

The restricted number of balloon launches prevents statistically significant conclusions from the coincident comparison approach. To overcome this disadvantage, the trajectory model approach was applied. Corresponding to MIPAS-B measurements, eight mean profiles were created for each MIPAS-E target parameter. Each point of these profiles is the average of several points found along the trajectories of MIPAS-B sounded air masses according to the match criteria of (500 km, 1 hour), with the MIPAS-E noise error weights being on the the same altitude level. Similarly, four SCIAMACHY mean profiles were calculated for each O<sub>3</sub> and NO<sub>2</sub> VMR and compared with MIPAS-B correlative profiles. The trajectory comparison method was not adopted for GOMOS validation due to its sparse data during the balloon flight periods.

NO<sub>2</sub> concentration is sensitive to time variation, especially in the periods around sunrise and sunset. Before performing trajectory comparisons, all MIPAS-B NO<sub>2</sub> profiles were photochemically adjusted to the measurement time and location of the ENVISAT chemistry instruments according to the KASIMA simulation results. For coincident comparisons, only

## 10. Summary and outlook

the MIPAS-B NO<sub>2</sub> profile from Flight No. 14, Seq. 3, was adjusted by using the KASIMA model due to the large time offset (8.5 hours). No sunrise and sunset event happened in the coincident comparison period.

As the coincident comparison and trajectory comparison approaches use the common MIPAS-B data set, comparison results are not independent. The general validation conclusions in quality were made from the synthesis of all comparison results. For NO<sub>2</sub>, however, quantitative conclusion regarding the MIPAS-E accuracy was extracted from the coincident comparison results in order to avoid potential uncertainties by the trajectory model and KASIMA model. For the MIPAS-E, SCIAMACHY, and GOMOS measurements which are systematically higher or lower than MIPAS-B values, accuracy estimations were performed in different altitude regions. Precision estimation of MIPAS-E is based on the trajectory comparison approach only since these data provide better statistics than the data from the coincident approach. The standard deviation of the mean difference was calculated in the altitude region of 123-8 hPa (15-33 km) only for MIPAS-E and in the region of 12-38 km for SCIAMACHY, where extensive comparisons were available. The MIPAS-E data accuracy (or precision) is validated, if the mean values are within the mean total combined errors (or the mean standard deviations are smaller than the mean combined precision errors). Otherwise, the data are not validated.

### Conclusions for MIPAS-E (Off-line products from ESA):

**Table 10.1: Conclusions with respect to MIPAS-E validation**

	<b>Accuracy</b> 356-3 hPa (8-39 km) (based on coincidence and trajectory data)	<b>Precision</b> 123-8 hPa (15-33 km) (based on trajectory data)	<b>Remarks</b>
<b>Temperature (K)</b>	-1.13 to 0.92 (-0.47 to 0.42%), <b>validated</b>	Below ~28 km: 2.48, <b>not validated</b> Above ~28 km: 1.04, <b>validated</b>	
<b>H<sub>2</sub>O (ppmv)</b>	356-195 hPa (8-12 km): 61.79 to 77.58 (35.15 to 39.34%), <b>not validated</b> 195-3 hPa (12-39 km): -0.98 to 1.13 (-38.76 to 5.30%), <b>validated</b>	0.48, <b>validated</b>	Strong oscillations Above ~27 km, positive bias
<b>O<sub>3</sub> (ppmv)</b>	-0.10 to 0.05 (-3.95 to 14.49%), <b>validated</b>	0.19, <b>validated</b>	
<b>HNO<sub>3</sub> (ppbv)</b>	-0.27 to 0.43 (-8.70 to 57.01%), <b>validated</b>	0.38, <b>not validated</b>	Oscillations
<b>CH<sub>4</sub> (ppmv)</b>	-0.11 to 0.10 (-10.39 to 6.05%), <b>validated</b>	0.09, <b>validated</b>	<~18 km, strong oscillations and unphysical values, positive bias
<b>N<sub>2</sub>O (ppbv)</b>	-17.28 to 19.97 (-18.66 to 6.37%), <b>validated</b>	15.47, <b>not validated</b>	<~18 km, strong oscillations and unphysical values, positive bias
<b>NO<sub>2</sub> (ppbv)</b>	42-3 hPa (22-39 km): -0.28 (-7.51%), <b>validated</b>	23-8 hPa (26-33 km) 0.57, <b>validated</b>	Slight oscillation

In general, the mean differences between MIPAS-E and MIPAS-B measurements for the temperature and the six key gas species—H<sub>2</sub>O, O<sub>3</sub>, HNO<sub>3</sub>, CH<sub>4</sub>, N<sub>2</sub>O, and NO<sub>2</sub> are mostly within their combined total errors in the overlapping altitude region of 356-3 hPa (8-39 km)

(for NO<sub>2</sub>, the overlapping region is 42-3 hPa (22-39 km)). The exception is H<sub>2</sub>O in the region of 356-195 hPa (8-12 km). Agreements in the middle stratosphere are better than in the lower stratosphere and upper troposphere. Individual comparison shows that the discrepancies of all target parameters exceed the combined total errors at certain levels of altitude. Generally, the precision of MIPAS-E often exceeds the expected values.

The oscillation features of MIPAS-E profiles may result from the coarse vertical grids for retrieval and the neglect of regularization. As for the scatter of MIPAS-E measurements, the reasons are complicated. From the beginning of the interferogram to the end of the retrieved profiles, a series of processing steps are necessary, and these are possible error sources in data analysis. For example, optimal microwindows selection, homogeneous horizontal assumption, and the continuum effect handling have to be carried out carefully under the different geophysical conditions.

MIPAS on ENVISAT is operating now in a reduced spectral resolution mode (0.42 of the nominal resolution) due to an interferogram driver unit anomaly. Therefore, it may be expected that the newly produced data will differ from the data validated here. Future validation campaigns are needed to assess the quality of the MIPAS-E measurements performed with the new operational mode.

#### **Conclusions for SCIAMACHY (scientific products from IUP/IFE):**

- 1. O<sub>3</sub>.** In the range of 9-28 km, the agreements between MIPAS-E and MIPAS-B measurements are good in general. SCIAMACHY data are slightly lower by 0.10 ppmv (7.72%) in 9-26 km. Between 28 and 38 km, SCIAMACHY measurements show a significant positive bias of 1.63 ppmv (20.09%), which is beyond the mean combined error. The mean standard deviation of the differences within 12-27 km is 0.14 ppmv. Within the range of 27-35 km, this parameter becomes 1.40 ppmv. The standard deviations indicate that the profile-profile variation of SCIAMACHY is significant above 27 km.
- 2. NO<sub>2</sub>.** SCIAMACHY measurements are slightly larger than MIPAS-B data in general. In 9-39 km, the discrepancies are 0.04-0.52 ppbv (0.19-6.28%) and within the corresponding mean combined errors. The standard deviation of the mean difference is 0.28 ppbv in the region of 16-38 km. It indicates that SCIAMACHY has a good performance in terms of precision for NO<sub>2</sub> measurements.

The agreements of O<sub>3</sub> and NO<sub>2</sub> measurements during Flight No. 14 are better than that during Flight No. 11. This may probably due to the improvement of the pointing registration errors (*Brinksma, E. J., 2004*). It must be noted that the above quantitative conclusions based on relatively sparse data. Therefore, the statistical significance is not very high. Furthermore, the KASIMA simulations might affect the NO<sub>2</sub> conclusions slightly.

#### **Conclusions for GOMOS (off-line products from ESA):**

A general conclusion for GOMOS off-line data validation from MIPAS-B data is impossible so far, as only one O<sub>3</sub> profile and one NO<sub>2</sub> profile were compared with MIPAS-B correlative measurements, respectively. The very limited comparison results show that GOMOS measurements for O<sub>3</sub> agree with MIPAS-B data with respect to their combined errors, except in the region of 21-25 km (positive bias of 0.25 ppmv) and above 36 km (negative bias of 1.42 ppmv). The NO<sub>2</sub> profile of GOMOS oscillates around the correlative MIPAS-B NO<sub>2</sub> profile with large amplitude. These comparison results may be integrated in the GOMOS validation activities.

## References:

- Abbas, M. M., M. R. Gunson, M. J. Newchurch, H. A. Michelson, R. J. Salawich, M. Allen, M. C. Abrams, A. Y. Chang, A. Goldman, F. W. Irion, E. J. Moyer, R. Nagaraju, C. P. Rinsland, G. P. Stiller and R. Zander (1996). "The hydrogen budget of the stratosphere inferred from ATMOS measurements of H<sub>2</sub>O and CH<sub>4</sub>." *Geophys. Res. Lett.* 23(17): 2405-2408.
- Andrews, D. G., J. R. Holton, and C. B. Leovy (1987). *Middle atmospheric dynamics*, Academic Press, INC., 1-20.
- Andrews, D. G. (2000). *An introduction to Atmospheric Physics*, Cambridge University Press, 99-113.
- Atkinson, R. J., and R. A. Plumb (1997). "Three-dimensional ozone transport during the ozone hole breakup in Dec. 1987." *J. Geophys. Res.* 102(D1): 1451-1466.
- Blom, C. E., H. Fischer, N. Glatthor, T. Gulde, M. Höpfner (1994). "Airborne measurements during the European Arctic Stratospheric Ozone Experiment column amounts of HNO<sub>3</sub> and O<sub>3</sub> derived from FTIR emission sounding." *Geophys. Res. Lett.* 21(13): 1351-1354.
- Blom, C. E., H. Fischer, N. Glatthor, T. Gulde, M. Höpfner, C. Piesch (1995). "Spatial and Temporal variation of ClONO<sub>2</sub>, HNO<sub>3</sub> and O<sub>3</sub> in the Arctic winter of 1992/1993 as obtained by airborne infrared emission spectroscopy." *J. Geophys. Res.* 100(D5): 9101-9114.
- Blom, C. E., T. Glude, C. Keim, W. Kimmig, C. Piesch, C. Sartorius and H. Fischer (1999). MIPAS-STR: A new instrument for stratospheric aircraft. *Proc. European Symposium on Atmospheric Measurements from Space*, 18-22 Jan. 1999, Noordwijk, European Space Agency, ESTEC, Noordwijk, The Netherland, 693-694.
- Brasseur, G., and S. Solomon (1986). *Aeronomy of the middle atmosphere*, 2nd Edition, D. Reidel, Dordrecht, 256-258.
- Brasseur, G. P., J. J. Orlando and G. S. Tyndall (1999). *Atmospheric chemistry and global change*, Oxford University Press, 237-333.
- Brinksma, E. J., A. J. M. Pijters, I. S. Boyd, A. Parrish, A. Bracher, C. von Savigny, K. Bramstedt, A. -M. Schmoltner, G. Taha, E. Hilsenrath, T. Blumentstock, G. Kopp, S. Mikuteit, A. Fix, Y. J. Meijer, D. P. J. Swart, G. E. Bodeker, I. S. Mcdermid, and T. Leblanc (2004). "SCIAMACHY ozone profile validation." *Proceedings of the Second Workshop on the Atmospheric Chemistry Validation of ENVISAT (ACVE-2) ESA-ESRIN: Frascati, Italy, 3-7 May 2004 (ESA SP-562, August 2004) ESC02EB.*
- Burkert, P., F. Fergg, and H. Fischer (1983). "A compact high resolution Michelson interferometer for passive atmospheric sounding (MIPAS)." *IEEE Trans. Geosci. Remote sensing* GE-21: 345.
- Carlotti, M. (1988). "Global-fit approach to the analysis of limb-scanning atmospheric measurements." *Appl. Opt.* 27(15): 3250-3254.



## References

- Carlotti, M., and B. Carli (1994). "Approach to the design and data analysis of a limb-scanning experiment." *Appl. Opt.* 33(15): 3237-3249.
- Carlotti, M., M. Höpfner, P. Raspollini, M. Ridolfi (2001). High level algorithm definition and physical and mathematical optimisations (MIPAS Level 2 Algorithm Theoretical Baseline Document), Prog. Doc. N.: TN-IROE-RSA9601, Issue: 3.
- Ceccherini, S., M. Ridolfi, B. Carli (2002). Averaging Kernels for MIPAS near real time level 2 retrievals. Delivery of the study "Development of an Optimised algorithm for Routine P, T and VMR Retrieval from MIPAS Limb Emission Spectra," Contract No 11717/95/NL/CN-CCN5.
- Chang, A. Y., R. J. Salawitch, H. A. Michelsen, M. R. Gunson, M. C. Abrams, R. Zander, C. P. Rinsland, M. Loewenstein, J. R. Podolske, M. H. Proffitt, J. J. Margitan, D. W. Fahey, R. – S. Gao, K. K. Kelly, J. W. Elkins, C. R. Webster, R. D. May, K. R. Chan, M. M. Abbas, A. Goldman, F. W. Irion, G. L. Manney, M. J. Newchurch and G. P. Stiller (1996). "A comparison of measurements from ATMOS and instruments aboard the ER-2 aircraft: Tracers of atmospheric transport." *Geophys. Res. Lett.* 23(17): 2389-2392.
- Chen, H. S. (1997). Remote sensing calibration system-an introduction, A Deepak Publishing, 1.
- Cunnold, D. M., J. M. Zawodny, W. P. Chu, J. P. Pommereau, F. Goutail, J. Lenoble, M. P. McCormick, R. E. Veiga, D. Murcray, N. Iwagami, K. Shibasaki, P. C. Simon, W. Peetermans (1991). "Validation of SAGE II NO<sub>2</sub> measurements." *J. Geophys. Res.* 96(D7): 12913-12925.
- Danilin, M. Y., M. L. Santee, J. M. Rodriguez, M. K. W. Ko, J. M. Mergenthaler, J. B. Kumer, A. Tabazadeh, and N. J. Livesey (2000). "Trajectory hunting: A case study of rapid chlorine activation in December 1992 as seen by UARS." *J. Geophys. Res.* 105(D3): 4003-4018.
- Danilin, M. Y., M. K. W. Ko, L. Froidevaux, M. L. Santee, L. V. Lyjak, R. M. Bevilacqua, J. M. Zawodny, Y. Sasano, H. Irie, Y. Kondo, J. M. Russell III, and C. J. Scott (2002). "Trajectory hunting as a powerful technique to validate multi-platform measurements: Analysis of the MLS, HALOE, SAGE-II, ILAS and POAM II data in October-November 1996." *J. Geophys Res.* 107(D20): 4420.
- Dudhia, A., V. L. Jay, and C. D. Rodgers (2002). "Microwindow Selection for High-Spectral-Resolution Sounders." *Appl. Opt.* 41(8): 3665-3673.
- Echle, G., H. Oelhaf, A. Wegner (1992). Measurement of atmospheric parameters with MIPAS. final report. ESA Contract 9597/91/NL/SF: 113-185.
- Echle, G., T. von Clarmann, A. Dudhia, M. Lopez-Puertas, F. J. Martín-Torres, B. Kerridge, and J. –M. Flaud (1999). "Spectral microwindows for MIPAS-ENVISAT data analysis," in Proceedings of the European Symposium on Atmospheric Measurements from Space. ESA Earth Science Division, ed. (European Space Agency ESTEC, Noordwijk, The Netherlands, 1999) Vol. 2, 481-485.
- Echle, G., T. von Clarmann, A. Dudhia, J. -M. Flaud, B. Funke, N. Glatthor, B. Kerridge, M. Lopez-Puertas, F. J. Martín-Torres, G. P. Stiller (2000). "Optimized Spectral Microwindows

## References

- for Data Analysis of the Michelson Interferometer for Passive Atmospheric Sounding on the Environmental Satellite." *Appl. Opt.* 39(30): 5531-5540.
- Engel, A., C. Schiller, U. Schmidt, R. Borchers, H. Ovarlez, and J. Ovarlez (1996). "The total hydrogen budget in the Arctic winter stratosphere during the European Arctic Stratospheric Ozone Experiment." *J. Geophys. Res.* 101(D9): 14495-14504.
- ESA, GOMOS\_concept, <http://envisat.esa.int/instruments/gomos/descr/concept.html>.
- ESA (2000). MIPAS/ENVISAT-An Instrument for Atmospheric Chemistry and Climate Research. ESA report SP-1229.
- ESA (2002). ENVISAT Post-Launch Sample Products-Production Information Note: MIPAS, [http://envisat.esa.int/services/sample\\_products/mipas/mipas\\_sample\\_products.pdf](http://envisat.esa.int/services/sample_products/mipas/mipas_sample_products.pdf).
- ESA, SCIAMACHY, <http://envisat.esa.int/instruments/sciamachy/descr>.
- Farman, J. C., B. G. Gardiner and J. D. Shanklin (1985). "Large losses of total ozone in Antarctica reveal seasonal ClO/NO<sub>x</sub> interaction." *Nature* 315: 207-210.
- Fischer, H. (1992). "Remote sensing of atmospheric trace constituents using Fourier transform spectrometry." *Ber. Bunsenges. Phys. Chem.* 96(3): 306-314.
- Fischer, H. (1993). "Remote Sensing of Atmospheric Trace Gases." *Interdisc. Sci. Rev.* 10(3): 185.
- Fischer, H., and Oelhaf, H. (1996). "Remote sensing of vertical profiles of atmospheric trace constituents with MIPAS limb-emission spectrometers." *Appl. Opt.* 35(16): 2787-2796.
- Flaud, J. -M., C. Camy-Peyret, C. P. Rinsland, M. A. H. Smith and V. M. Devi (1990). *Atlas of Ozone Spectral Parameters from Microwave to Medium Infrared*, Academic press, INC.
- Friedl-Vallon, F., G. Maucher, H. Oelhaf, M. Seefeldner, O. Trieschmann, G. Wetzel and H. Fischer (1999). The balloon-borne Michelson Interferometer for Passive Atmospheric Sounding (MIPAS-B2)-Instrument and Results. *Optical Spectroscopic Techniques and Instrumentation for Atmospheric and Space research III*, Denver, Colorado, July 19-21, SPIE proceedings Vol. 3756, 9-16.
- Friedl-Vallon, F., G. Maucher, M. Seefeldner, O. Trieschmann, A. Kleinert, A. Lengel, C. Keim, H. Oelhaf, and H. Fischer (2004). "Design and characterization of the balloon-borne Michelson Interferometer for Passive Atmospheric Sounding (MIPAS-B2)." *Appl. Opt.* 43(16): 3335-3355.
- Goldman, A., and R. S. Saunders (1979). "Analysis of atmospheric infrared spectra for altitude distribution of atmospheric trace constituents. I-Method of analysis." *J. Quant. Spectrosc. Radiat. Transfer* 21: 155-161.
- Grunow, K. (2005). Private communication.

## References

- Hansen, P. C. (1992). "Analysis of discrete ill-posed problems by means of the L-curve." *SIAM Rev.* 34(4): 561-580.
- Houghton, J. T., (1986). *The physics of atmospheres*, Cambridge University Press, Second edition.
- Höpfner, M., H. Oelhaf, G. Wetzel, F. Friedl-Vallon, A. Kleinert, A. Lengel, G. Maucher, H. Nordmeyer, N. Glatthor, G. Stiller, T. von Clarmann, H. Fischer, C. Kröger, T. Deshler (2002). "Evidence of scattering of tropospheric radiation by PSCs in mid-IR limb emission spectra: MIPAS-B observations and KOPRA simulations." *Geophys. Res. Lett.* 29(8): 1278.
- IUPAC (1978). *Compendium of Analytical Nomenclature*, Pergamon Press, Xford.
- Kleinert, A. (2003). *Quantifizierung und Optimierung der radiometrischen Genauigkeit des Fourierspektrometers MIPAS-B2*, Dissertation. IMK, FZKA 6909, Oktober.
- Kleinert, A. (2006). "Correction of detector nonlinearity for the balloon-borne Michelson Interferometer for Passive Atmospheric Sounding (MIPAS-B2)." *Appl. Opt.*, 45(3), 425-431.
- Kouker, W., I. Langbein, Th. Reddmann, and R. Ruhnke (1999). *The Karlsruhe Simulation Model of the Middle Atmosphere (KASIMA). Version 2*, Wissenschaftliche Berichte, FZKA 7278, Forschungszentrum Karlsruhe, Germany.
- Lait, L. R., M. R. Schoeberl, P. A. Newman, M. H. Proffitt, M. Loewenstein, J. R. Podolske, S. E. Strahan, K. R. Chan, B. Gary, J. J. Margitan, E. Browell, M. P. McCormick, and A. Torres (1990). "Reconstruction of O<sub>3</sub> and N<sub>2</sub>O fields from ER-2, DC-8 and balloon observations." *Geophys. Res. Lett.* 17(4): 521-524.
- Lengel, A. (2004). *Bestimmung der Apparatfunktion des Fourierspektrometers MIPAS-B2 aus stratosphärischen Spektren*. Doctoral Dissertation der Universität Karlsruhe (TH), Forschungszentrum Karlsruhe, Wissenschaftliche Berichte, FZKA 7016.
- Levenberg, K. (1944). "A method for the solution of certain non-linear problems in least squares." *Quart. Appl. Math.* 2: 164-168.
- Li, J., and Hung-Lung Huang (1999). "Retrieval of atmospheric profiles from satellite sounder measurements by use of the discrepancy principle." *Appl. Opt.* 38(6): 916-923.
- Lu, C. -H., G. K. Yue, G. L. Manney, H. Jäger, and V. A. Mohnen (2000). "Lagrangian approach for Stratospheric Aerosol and Gas Experiment (SAGE) II profile intercomparisons." *J. Geophys. Res.* 105(D4): 4563-4572.
- Maucher, G., (1995). "The pointing- and the star-reference system of the MIPAS-B2 gondola Part 2: The star reference system." *Proc. 12th ESA Symp. on Rocket and Balloon Programmes and Related Research*, Lillehammer, Norway, ESA SP-370, 511-514.
- Marquardt, D. W. (1963). "An algorithm for least-squares estimation of nonlinear parameters." *J. Soc. Indust. Appl. Math.* 11 (2): 431-441.
- McIntyre, M. E. (1980). "Towards a Lagrangian-mean description of stratospheric circulations and chemical transports." *Phil. Trans. R. Soc. Lond.* 296: 129-148.

## References

- McKee, T. B., R. I. Whitman, and J. J. Lambiotte (1969). A technique to infer atmospheric water-vapor mixing ratio from measured horizon radiance profiles. NASA Rep. TN D5252, NASA, Washington D. C.
- Michelsen, H. A., G. L. Manney, M. R. Gunson, and R. Zander (1998). "Correlations of stratospheric abundances of  $\text{NO}_y$ ,  $\text{O}_3$ ,  $\text{N}_2\text{O}$ , and  $\text{CH}_4$  derived from ATMOS measurements." *J Geophys. Res.* 103(D21): 28347-28359.
- Morris, G. A., M. R. Schoeberl, L. C. Sparling, P. A. Newman, L. R. Lait, L. Elson, J. Waters, R. A. Suttie, A. Roche, J. Kumer, and J. M. Russell, III (1995). "Trajectory mapping and applications to data from the Upper Atmosphere Research Satellite." *J. Geophys. Res.* 100(D8): 16491-16505.
- Morris, G. A., J. F. Gleason, J. Ziemke, and M. R. Schoeberl (2000). "trajectory mapping: A tool for validation of trace gas observation." *J. Geophys Res.* 105(D14): 17875-17894.
- Norton, R. H., and Beer, R. (1976). "New Apodization functions for Fourier Spectroscopy." *Journ. of the Optical Society of America* 66: 259-264.
- Norton, R. H., and Beer, R. (1977). "Erratum to New Apodization functions for Fourier Spectroscopy." *Journ. of the Optical Society of America* 67: 419.
- Oelhaf, H., T. von Clarmann, H. Fischer, F. Friedl-Vallon, Ch. Fritzsche, A. Linden, Ch. Piesch, M. Seefeldner, and W. Völker (1994). "Stratospheric  $\text{ClONO}_2$ ,  $\text{HNO}_3$  and  $\text{O}_3$  profiles Inside the Arctic Vortex from MIPAS-B Limb emission Spectra obtained during EASOE ." *Geophys. Res. Lett.* 21(13): 1263-1266.
- Oelhaf, H., H. Fischer, G. Wetzel, M. Stowasser, F. Friedl-Vallon, G. Maucher, O. Trieschmann, R. Ruhnke, and Y. Sasano (1998). Intercomparison of ILAS/ADESO with MIPAS-B measurements in late March 1997. *Proc. Optical Remote Sensing of the Atmosphere and Clouds, 15-17 Sept. 1998, Beijing, China, SPIE Vol.3501, 92-100.*
- Oelhaf, H., (2002). Private communication.
- Oelhaf, H., F. Friedl-Valloon, A. Kleinert, A. Lengel, G. Maucher, H. Nordmeyer, G. Wetzel, G. Zhang, and H. Fisher (2003). "MIPAS-B observations for the validation of target parameters of ENVISAT chemistry instruments." *Proceedings of the 16<sup>th</sup> ESA Symposium on European Rocket and Balloon Programmes and Related Research, St. Gallen, Switzerland, 2-5 June 2003 (ESA, SP-530, August 2003), 451-456.*
- Pierce, R. B., W. L. Grose, J. M. Russell, and A. F. Fock (1994). "Evolution of southern hemisphere air masses observed by HALOE." *Geophys. Res. Lett.* 21(3): 213-216.
- Pierce, R. B., J. -U. Grooss, W. L. Grose, J. M. Russell III, P. J. Crutzen, T. D. Fairlie, G. Lingenfelser (1997). "Photochemical calculations along air mass trajectories during ASHOE/MAESA." *J. Geophys. Res.* 102(D11): 13153-13168.
- Randel, W., M. -L. Chanin, and C. Michaut (2002). SPARC intercomparison of Middle Atmosphere Climatologies. WCRP-116, WMO/TD-No-1142, SPARC Rep. 3, Geneva.

## References

- Randel, W. J., and F. Wu (1995). "TOMS total ozone trends in potential vorticity coordinates." *Geophys. Res. Lett.* 22(6): 683-686.
- Reimer, E., and H. Kaupp (1997). Source identification of odour compounds using trajectories. *Proc. ECO-INFORMA 97*, Eco-Informa Press, Bayreuth, 572-577.
- Ridolfi, M., B. Carli, M. Carlotti, T. von Clarmann, B. M. Dinelli, A. Dudhia, J. -M, Flaud, M. Höpfner, P. E. Morris, P. Raspollini, G. Stiller and R. J. Wells (2000). "Optimized forward model and retrieval scheme for MIPAS near-real-time data processing." *Appl. Opt.* 39(8): 1323-1340.
- Rodgers, C. D. (1976). "retrieval of atmospheric temperature and composition from remote measurements of thermal radiation." *Reviews of Geophysic and space physics* Vol. 14(4): 609-624.
- Rodgers, C. D. (1990). "Characterization and error analysis of profiles retrieved from remote sounding measurements." *J. Geophys. Res.* 95 (D5): 5587-5595.
- Rodgers, C. D. (2000). *Inverse Methods For Atmospheric Sounding: theory and practice*, World Scientific, Singapore, (2000).
- Rodgers, C. D., and B. J. Connor (2003). "Intercomparison of remote sounding instruments." *J. Geophys. Res.* 108(D3): 4116-4229.
- Rozanov, A., H. Bovensmann, A. Bracher, S. Hrechanyy, V. Rozanov, M. Sinnhuber, M. Stroh, F. J. P. Burrows (2005). "NO<sub>2</sub> and BrO vertical profile retrieval from SCIMACHY limb measurements: sensitivity studies." *Advances in space research* (in press).
- Ruhnke, R. (2005). Private communication.
- Saavedra de Miguel, L. (2005). GOMOS monthly report, ENVI-SPPA-EOPG-TN-05-0007, Issue: 1.0, P48.
- Salby, M. L. (1996). *Fundamentals of Atmospheric Physics*, Academic Press Inc..
- Schneider, M. (2002). Continuous Observations of Atmospheric trace gases by Ground-based FTIR Spectroscopy at Izaña Observatory, Tenerife island. Doctoral dissertation, Universität Karlsruhe (TH), Forschungszentrum Karlsruhe, Wissenschaftliche Berichte, FZKA 6727
- Schoeberl, M. R., and L. R. Lait (1993). Conservative-coordinate transformations for atmospheric measurements, the use of EOS for studies of atmospheric physics. *Proceedings of the International School of Physics Enrico Fermi, Italian Phys. Soc.:* 419-431.
- Seefeldner, M., and C. Keim, (1995). "The pointing and the star reference system of the MIPAS-B2 gondola. Part 1: The pointing system." *Proc. 12th ESA Symp. on Rocket and Balloon Programmes and Related Research*, Lillehammer, Norway, ESA SP-370, 505-510.
- Seinfeld, J. H., S. N. Pandis (1998). *Atmospheric Chemistry and Physics-From Air Pollution to Climate Change*, John Wiley & Sons, INC. 69-230.

## References

- Simmons, A., M. Hortal, G. Kelly, A. McNally, A. Untch, and S. Uppala (2005). "ECMWF analyses and forecasts of stratospheric winter polar vortex break-up: September 2002 in the southern hemisphere and related events." *J. Atmos. Sci.* 62(3): 668–689.
- Steck, T., T. von Clarmann (2001). "Constrained Profile Retrieval Applied to the Observation Mode of the Michelson Interferometer for Passive Atmospheric Sounding." *Appl. Opt.* 40(21): 3559-3571.
- Steck, T. (2002). "Methods for Determining Regularization for Atmospheric Retrieval Problems." *Appl. Opt.* 41(9): 1788-1797.
- Stiller, G. P., M. R. Gunson, L. L. Lowes, M. C. Abrams, O. F. Raper, C. B. Farmer, R. Zander, and C. P. Rinsland (1995). "Stratospheric and mesospheric pressure-temperature profiles from rotational analysis of CO<sub>2</sub> lines in atmospheric trace molecule spectroscopy /ATLAS 1 infrared solar occultation spectra." *J. Geophys. Res.* 100 (D2): 3107-3117.
- Stiller, G. P. (Editor) (2000). The Karlsruhe optimized and precise radiative transfer algorithm (KOPRA). *Wissenschaftliche Berichte, FZKA 6487*, Forschungszentrum Karlsruhe: 10-20.
- Stowasser, M., H. Oelhaf, G. Wetzel, F. Friedl-Vallon, G. Maucher, M. Seefeldner, O. Trieschmann, T. v. Clarmann, and H. Fischer (1999). "Simultaneous measurements of HDO, H<sub>2</sub>O and CH<sub>4</sub> with MIPAS-B: Hydrogen budget and indication of dehydration inside the polar vortex." *J. Geophys. Res.* 104(D16): 19213-19226.
- Stowasser, M., H. Oelhaf, R. Ruhnke, G. Wetzel, F. Friedl-Vallon, A. Kleinert, W. Kouker, A. Lengel, G. Maucher, H. Nordmeyer, Th. Reddmann, O. Trieschmann, T. v. Clarmann, H. Fischer, and M. P. Chipperfield (2002). "A characterization of the warm 1999 Arctic winter by observations and modeling: NO<sub>y</sub> partitioning and dynamics." *J. Geophys. Res.* 107(D19): 4376.
- Stowasser, M., H. Oelhaf, R. Ruhnke, A. Kleinert, G. Wetzel, F. Friedl-Vallon, W. Kouker, A. Lengel, G. Maucher, H. Nordmeyer, Th. Reddmann, and H. Fischer (2003). "The variation of short-lived NO<sub>y</sub> species around sunrise at mid-latitudes as measured by MIPAS-B and calculated by KASIMA." *Geophys. Res. Lett.* 30(8): 1432.
- Suortti, T., E. Kyrö, T. Turunen, A. Karpetchko (2003). "Results of GOMOS ozone validation against ECC sonde measurements (AO429)." *Geophysical Research Abstracts Vol. 5*: 10386.
- Tikhonov, A. N. and V. Y. Arsenin (1977). *Solution of ill-posed problems*, WH Wiston&Sons, Washington D. C.
- Trieschmann, O., F. Friedl-Vallon, A. Lengel, H. Oelhaf, G. Wetzel, and H. Fischer (1999). An advanced phase correction approach to obtain radiometric calibrated spectra of the optically well balanced balloon borne Fourier Transform Spectrometer MIPAS-B2, Denver, Colorado, SPIE proceedings Vol. 3756, 19-21, July.
- Trieschmann, O. (2000). *Phasenkorrektur und Radiometrie gekühlter Fourierspektrometer: Charakterisierung des Instruments MIPAS-B2*. Dissertation im Fach Physik, IMK, Universität Karlsruhe und Forschungszentrum Karlsruhe, *Wissenschaftliche Berichte FZKA 6411*.

## References

- US. (1976). Standard Atmosphere, U. S. Gov. Print. Off., Washington, D. C..
- von Clarmann, T., and G. Echle (1998a). The Karlsruhe Occupation Matrix Algorithm (KOMA), Technical note to ESA, ESA contract 11717/95/NL/CN, CCN2.
- von Clarmann, T., A. Dudhia, G. Echle, J. –M. Flaud, C. Harrold, B. Kerridge, K. Koutoulaki, A. Linden, M. López-Puertas, M. Á. López-Valverde, F. J. Martín-Torres, J. Reburn, J. Remedios, C. D. Rodgers, R. Siddans, R. J. Wells, and G. Zaragoza (1998b). Study on the simulation of atmospheric infrared spectra. Final Report of ESA Contract Number 12054/96/NL/CN, European Space Agency, ESTEC, Noordwijk, The Netherlands.
- von Clarmann, T. and G. Echle (1998c). "Selection of optimized microwindows for atmospheric spectroscopy." *Appl. Opt.* 37(33): 7661-7669.
- Von Savigny, C., A. Bracher, K., Bramstedt, A. Rozanov, M. Sinnhuber, C. Sioris, A. Butz, M. Dorf, K. Pfeilsticker, K. Grunow, F. Goutail, J. P. Pommereau, and N. Huret (2004). SCIAMACHY limb NO<sub>2</sub> profile validation. Proceedings of the Second Workshop on the Atmospheric Chemistry Validation of ENVISAT (ACVE-2), ESA-ESRIN, Frascati, Italy, 3-7 May 2004 (ESA SP-562, August 2004) ESC02CVS.
- Warneck, P. (1988). Chemistry of the natural atmosphere, Academic Press, Inc..
- Wetzel, G., T. von Clarmann, H. Oelhaf and H. Fischer (1995). "Vertical Profiles of N<sub>2</sub>O<sub>5</sub>, along with CH<sub>4</sub>, N<sub>2</sub>O and H<sub>2</sub>O in the Later Arctic Winter Retrieval from MIPAS-B Limb Emission Measurements." *J. Geophys. Res.* 100(D11): 23173-23181.
- Wetzel, G., H. Oelhaf, T. von Clarmann, H. Fischer, F. Friedl-Vallon, G. Maucher, M. Seefeldner, O. Trieschmann, and F. Lefèvre (1997). "Vertical profiles of N<sub>2</sub>O<sub>5</sub>, HO<sub>2</sub>NO<sub>2</sub>, and NO<sub>2</sub> inside the Arctic vortex retrieved from nocturnal MIPAS-B2 infrared limb emission measurements in February 1995." *J. Geophys. Res.* 102(D15): 19177-19186.
- Wetzel, G., H. Oelhaf, R. Ruhnke, F. Friedl-Vallon, A. Kleiner, W. Kouker, G. Maucher, T. Reddmann, M. Seefeldner, M. stowasser, O. Trieschmann, T. von Clarmann, and H. Fischer (2002). "NO<sub>y</sub> partitioning and budget and its correlation with N<sub>2</sub>O in the arctic vortex and in summer mid-latitudes in 1997." *J. Geophys. Res.* 107(D16): 4280-4291.
- Wetzel, G., T. Blumenstock, H. Oelhaf, G. P. Stiller, D. -Y, Wang, G. Zhang, M. Pirre, F., Goutail, A. Bazureau, J. -P. Pommereau, A. Bracher, M. Sinnhuber, M. Weber, K. Bramstedt, B. Funke, M. López-Puertas, I. Kostadinor, A. Petritoli, A. Alfaro, F. Hendrick, M. Van Roozendael, M. De Mazière (2004). Validation of MIPAS-ENVISAT version 4.61 operational data: NO<sub>2</sub>. ACVE-2 meeting, 3-7 May, Frascati (Italy), ESA-SP-562.
- WMO (1986). Atmospheric Ozone 1985. World Meteorological Organization. WMO Global Ozone Research and Monitoring Project, Report No. 6: Geneva.
- WMO (2003). Scientific Assessment of Ozone Depletion: 2002. World Meteorological Organization. Global Ozone Research and Monitoring Project-Report No. 47: P1.53-1.55.
- Zhdanov, M. S. (2002). Geophysical inverse theory and regularization problems, Elsevier Science B. V.

## Appendix A: Supplementary data for MIPAS-B retrievals

Table 1: Seq. S, Flight No. 11

Seq. S	Temperature	H <sub>2</sub> O	O <sub>3</sub>	HNO <sub>3</sub>	CH <sub>4</sub>	N <sub>2</sub> O	NO <sub>2</sub>
Range of profile (km)	11-39	11-39	11-39	11-39	11-39	11-39	14-39
Number of degrees of freedom	8	7	8	8	7	8	8
Top level of continuum effect (km)	12	12	12	12	12	12	no
Occupation matrix consideration	no	no	yes	no	yes	yes	no
Vertical resolution (km)	(11-38 km): 3-6 (38-39 km): 6-9	(11-14 km): 4-9 (14-39 km): 3-6	(11-38 km): 3-6 (38-39 km): 7-14	(11-38 km): 3-6 (38-39 km): 6-20	(11-17 km): 4-8 (17-39 km): 3-5	(11-18 km): 5-10 (18-39 km): 3-5	3-6

Table 2: Seq. N3, Flight No. 11

Seq. N3	Temperature	H <sub>2</sub> O	O <sub>3</sub>	HNO <sub>3</sub>	CH <sub>4</sub>	N <sub>2</sub> O	NO <sub>2</sub>
Range of profile (km)	6-36	8-36	8-35	7-36	9-38	9-38	16-38
Number of degrees of freedom	13	8	9	11	7	8	9
Top level of continuum effect (km)	12	12	12	12	12	12	no
Occupation matrix consideration	no	yes	no	no	yes	yes	no
Vertical resolution (km)	2-4	(8-13 km): 6-16 (13-36 km): 2-4	(8-16 km): 2-3 (16-35 km): 4-9	3-5	(9-36 km): 2-8 (36-38 km): 3-12	(9-36 km): 2-8 (36-38 km): 2-11	(16-36 km): 2-4 (36-38 km): 3-7

Table 3: Seq. W, Flight No. 11

Seq. W	Temperature	H <sub>2</sub> O	O <sub>3</sub>	HNO <sub>3</sub>	CH <sub>4</sub>	N <sub>2</sub> O	NO <sub>2</sub>
Range of profile (km)	8-37	8-37	8-36	11-38	8-38	8-38	16-37
Number of degrees of freedom	13	8	11	9	7	8	9
Top level of continuum effect (km)	14	14	14	14	14	14	no
Occupation matrix consideration	no	yes	no	no	yes	yes	no
Vertical resolution (km)	(8-9 km): 5-10 (9-36 km): 2-3 (36-37 km): 2-12	(8-18 km): 4-17 (18-36 km): 3-4 (36-37 km): 4-8	3-5	3-4	(8-20 km): 4-11 (20-38 km): 3-6	(8-21 km): 3-11 (21-38 km): 2-5	(16-36 km): 2-4 (36-37 km): 3-7

Table 4: Seq. E, Flight No. 11

Seq. E	Temperature	H <sub>2</sub> O	O <sub>3</sub>	HNO <sub>3</sub>	CH <sub>4</sub>	N <sub>2</sub> O	NO <sub>2</sub>
Range of profile (km)	23-36	23-37	23-36	23-36	23-38	23-38	23-37
Number of degrees of freedom	6	5	4	5	4	5	5
Top level of continuum effect (km)	no	no	no	no	no	no	no
Occupation matrix consideration	no	no	no	no	no	no	no
Vertical resolution (km)	(23-26 km): 4-7 (26-36 km): 2-4	(23-26 km): 5-7 (26-36 km): 3-4 (36-37 km): 3-7	6-8	(23-26 km): 4-7 (26-36 km): 3-4	(23-27 km): 5-8 (27-36 km): 3-5 (36-38 km): 3-16	(23-26 km): 4-7 (26-36 km): 3-4 (36-38 km): 3-11	(23-26 km): 4-7 (26-36 km): 3-4 (36-38 km): 3-17



Table 5: Seq. N3a, Flight No. 13

Seq. N3a	Temperature	H <sub>2</sub> O	O <sub>3</sub>	HNO <sub>3</sub>	CH <sub>4</sub>	N <sub>2</sub> O	NO <sub>2</sub>
Range of profile (km)	11-31	11-31	11-31	11-31	11-31	11-31	20-31
Number of degrees of freedom	12	11	11	12	8	9	10
Top level of continuum effect (km)	11	11	11	no	no	11	11
Occupation matrix consideration	no	no	yes	no	yes	no	yes
Vertical resolution (km)	(11-12 km): 3-4 (12-30 km): 2-3 (30-31 km): 2-4	(11-13 km): 2-6 (13-30 km): 2-3 (30-31 km): 2-4	(11-12 km): 3-6 (12-30 km): 2-3 (30-31 km): 3-5	(11-13 km): 2-5 (13-30 km): 2-3 (30-31 km): 2-4	(11-13 km): 3-4 (13-31 km): 2-3	(11-14 km): 2-7 (14-30 km): 2-3 (30-31 km): 3-5	2-4

Table 6: Seq. D15c, Flight No. 13

Seq. D15c	Temperature	H <sub>2</sub> O	O <sub>3</sub>	HNO <sub>3</sub>	CH <sub>4</sub>	N <sub>2</sub> O	NO <sub>2</sub>
Range of profile (km)	14-31	14-31	14-31	14-31	14-31	14-31	14-31
Number of degrees of freedom	9	8	9	11	8	8	8
Top level of continuum effect (km)	14	14	14	14	14	14	no
Occupation matrix consideration	yes	yes	yes	no	no	no	yes
Vertical resolution (km)	(14-15 km): 3-5 (15-30 km): 2-3 (30-31 km): 3-7	(14-15 km): 3-5 (15-29 km): 2-3 (29-31 km): 3-6	(14-15 km): 3-5 (15-29 km): 2-3 (29-31 km): 4-7	(14-15 km): 3-5 (15-31 km): 1.5-3	(14-18 km): 4-9 (18-30 km): 2-3 (30-31 km): 3-5	(14-19 km): 4-10 (19-30 km): 2-3 (30-31 km): 3-4	(14-15 km): 3-6 (15-30 km): 2-3 (30-31 km): 3-9

Table 7: Seq. 2, Flight No. 14

Seq. 2	Temperature	H <sub>2</sub> O	O <sub>3</sub>	HNO <sub>3</sub>	CH <sub>4</sub>	N <sub>2</sub> O	NO <sub>2</sub>
Range of profile (km)	8-38	9-38	8-38	8-38	8-38	8-38	8-38
Number of degrees of freedom	15	12	13	15	13	15	14
Top level of continuum effect (km)	12	12	12	12	no	no	12
Occupation matrix consideration	no	yes	no	yes	no	no	no
Vertical resolution (km)	2-5	(9-14 km): 2-10 (14-38 km): 2-4	(8-37 km): 2-3 (37-38 km): 2-7	2-4	(8-12 km): 4-9 (12-38 km): 2-4	(8-11 km): 4-8 (11-38 km): 1-4	(8-12 km): 4-12 (12-38 km): 2-4

Table 8: Seq. 3, Flight No. 14

Seq. 3	Temperature	H <sub>2</sub> O	O <sub>3</sub>	HNO <sub>3</sub>	CH <sub>4</sub>	N <sub>2</sub> O	NO <sub>2</sub>
Range of profile (km)	8-39	8-39	8-39	8-39	8-39	8-39	8-39
Number of degrees of freedom	15	14	16	13	15	13	10
Top level of continuum effect (km)	12	12	12	11	12	12	12
Occupation matrix consideration	no	yes	no	yes	yes	yes	no
Vertical resolution (km)	(8-9 km): 3-10 (9-39 km): 2-3	(8-14 km): 3-16 (14-38 km): 2-3 (38-39 km): 3-4	(8-9 km): 3-12 (9-39 km): 2-3	(8-18 km): 3-6 (18-32 km): 2-3 (32-39 km): 2-4	(8-18 km): 3-11 (18-39 km): 2-3	(8-18 km): 3-10 (18-39 km): 2-3	(8-15 km): 4-13 (15-39 km): 2-4

## Appendix B: Number of match points for trajectory comparisons

Table 1: Number of match points at each level of pressure for temperature comparisons

Seq. S		Seq. N3		Seq. W		Seq. E		Seq. N3a		Seq. D15c		Seq. 2		Seq. 3	
P (hPa)	N	P (hPa)	N	P (hPa)	N	P (hPa)	N	P (hPa)	N	P (hPa)	N	P (hPa)	N	P (hPa)	N
195.4	1	307.9	2	307.9	2	30.6	1	182.8	1	111.6	1	360.0	1	360.0	1
167.4	1	265.1	2	265.1	2	26.3	1	154.8	3	94.6	4	311.3	1	311.3	1
143.4	1	227.9	2	227.9	3	22.7	1	131.5	4	80.2	5	268.2	1	268.2	1
122.6	3	195.4	2	195.4	3	19.5	3	111.6	4	67.9	5	230.7	1	230.7	1
104.9	3	167.4	2	167.4	3	16.8	3	94.6	4	57.4	5	198.4	2	198.4	1
89.9	3	143.4	2	143.4	3	14.5	3	80.2	4	48.4	5	170.7	5	170.7	1
77.0	2	122.6	2	122.6	3	12.5	3	67.9	4	40.9	5	146.8	4	146.8	2
66.0	2	104.9	3	104.9	3	10.8	3	57.4	4	34.4	5	126.4	5	126.4	2
56.5	2	89.9	3	89.9	3	9.3	3	48.4	4	29.0	5	108.8	5	108.8	2
48.5	2	77.0	3	77.0	5	8.0	3	40.9	4	24.5	5	93.7	5	93.7	2
41.5	2	66.0	2	66.0	6	7.0	3	34.4	4	20.7	4	80.8	3	80.7	3
35.7	2	56.5	2	56.5	6	6.0	3	29.0	4	17.5	4	69.5	3	69.5	3
30.6	2	48.5	3	48.4	5	5.2	3	24.5	3	14.9	2	59.9	2	59.9	4
26.3	2	41.5	4	41.5	5	4.5	3	20.7	4	12.7	2	51.6	2	51.6	5
22.7	2	35.7	4	35.7	6			17.5	4	10.8	2	44.6	4	44.6	5
19.5	2	30.6	5	30.6	6			14.9	2	9.2	2	38.4	4	38.4	4
16.8	2	26.3	5	26.3	6			12.7	2	7.9	1	33.1	5	33.1	4
14.5	2	22.7	6	22.7	6			10.8	2			28.6	6	28.6	6
12.5	2	19.5	6	19.5	8			9.2	1			24.7	6	24.7	6
10.8	2	16.8	6	16.8	7			7.9	1			21.3	6	21.3	6
9.3	2	14.5	6	14.5	7							18.4	6	18.4	6
8.0	2	12.5	6	12.5	7							15.9	6	15.9	5
7.0	1	10.8	6	10.8	7							13.8	6	13.8	7
6.0	1	9.3	5	9.3	7							12.0	7	12.0	7
5.2	2	8.0	5	8.0	7							10.4	7	10.4	7
4.5	2	7.0	5	6.9	8							9.1	7	9.1	5
3.9	2	6.0	6									7.9	8	7.9	5
3.4	2	5.2	6									6.9	8	6.9	5
		4.5	3									6.0	8	6.0	5
												5.3	7	5.3	5
												4.6	6	4.6	5
														4.1	5

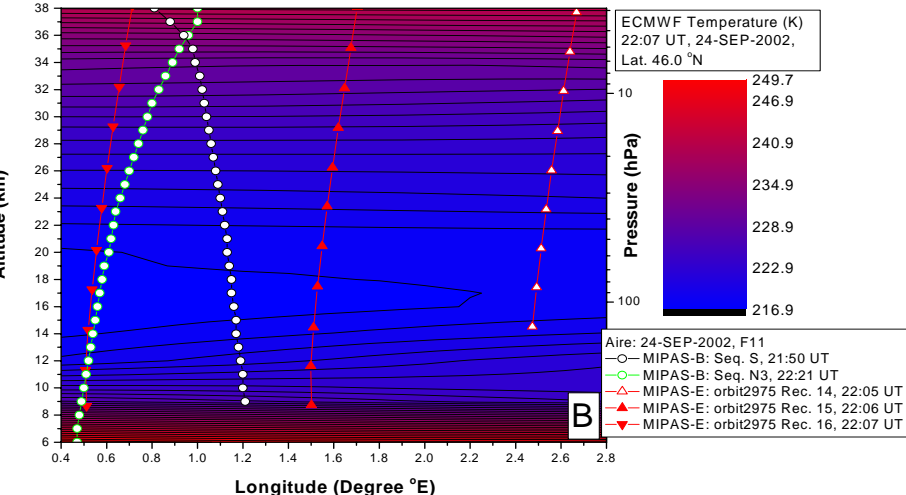
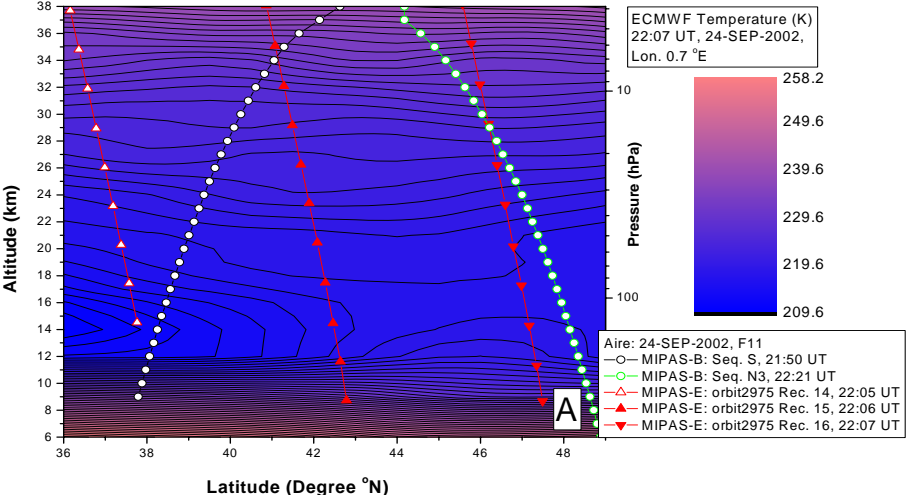
Table 2: Number of match points at each level of pressure for NO<sub>2</sub> VMR comparisons

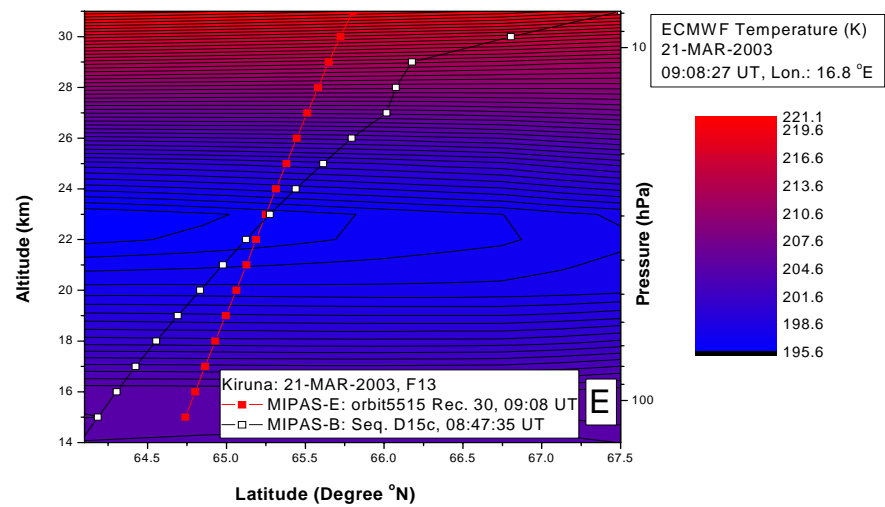
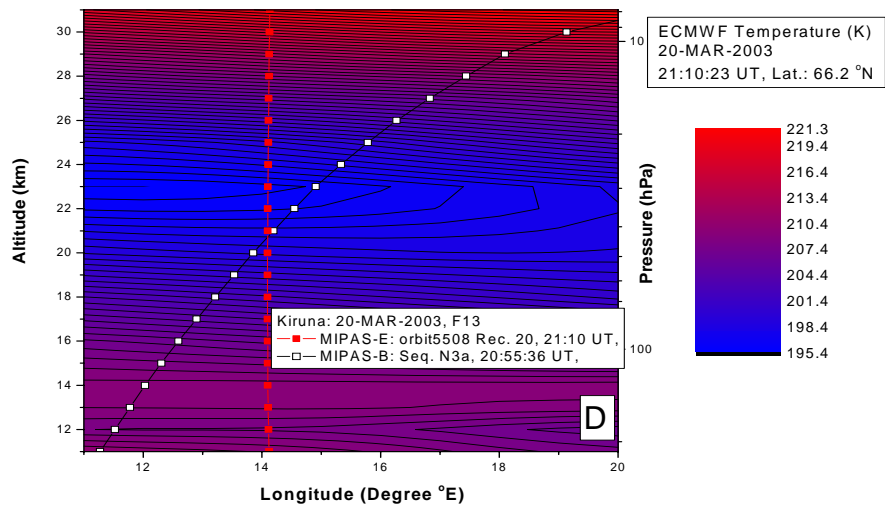
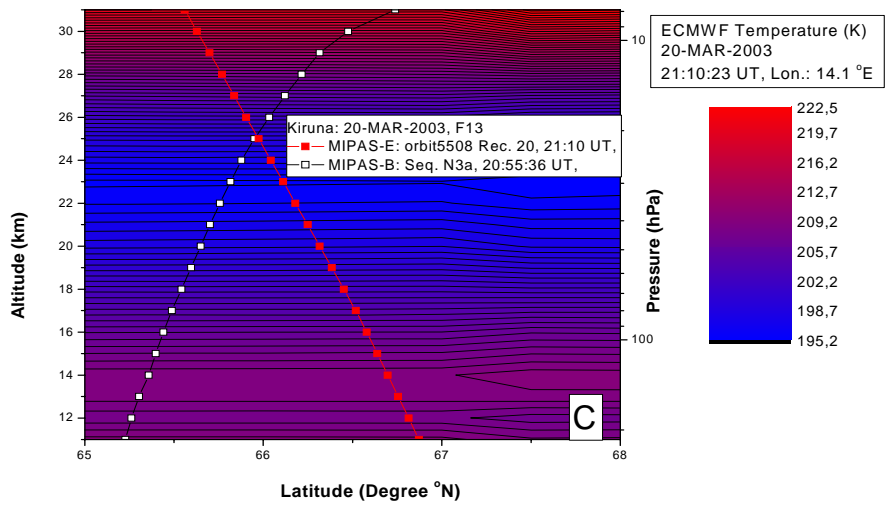
Seq. S		Seq. N3		Seq. W		Seq. E		Seq. N3a		Seq. D15c		Seq. 2		Seq. 3	
P (hPa)	N	P (hPa)	N	P (hPa)	N	P (hPa)	N	P (hPa)	N	P (hPa)	N	P (hPa)	N	P (hPa)	N
19.5	2	19.5	6	22.7	1	30.6	1	29.0	1	29.0	1	28.6	6	28.6	6
16.8	2	16.8	6	19.5	6	26.3	1	24.5	2	24.5	1	24.7	6	24.7	6
14.5	2	14.5	6	16.8	6	22.7	1	20.7	4	20.7	4	21.3	6	21.3	6
12.5	2	12.5	6	14.5	7	19.5	3	17.5	4	17.5	4	18.4	6	18.4	6
10.8	2	10.8	6	12.5	7	16.8	3	14.9	2	14.9	2	15.9	6	15.9	5
9.3	2	9.3	5	10.8	7	14.5	3	12.7	2	12.7	2	13.8	6	13.8	7
8.0	2	8.0	5	9.3	7	12.5	3	10.8	2	10.8	2	12.0	7	12.0	7
7.0	1	7.0	5	8.0	7	10.8	3	9.2	1	9.7	2	10.4	7	10.4	7
6.0	1	6.0	6	6.9	7	9.3	3	7.9	1	7.9	1	9.1	7	9.1	5
5.2	2	5.2	5			8.0	3					7.9	8	7.9	5
4.5	2	4.5	3			7.0	3					6.9	8	6.9	5
3.9	2					6.0	3					6.0	8	6.0	5
3.4	2					5.2	3					5.3	7	5.3	5
						4.5	3					4.6	6	4.6	5
														4.1	5

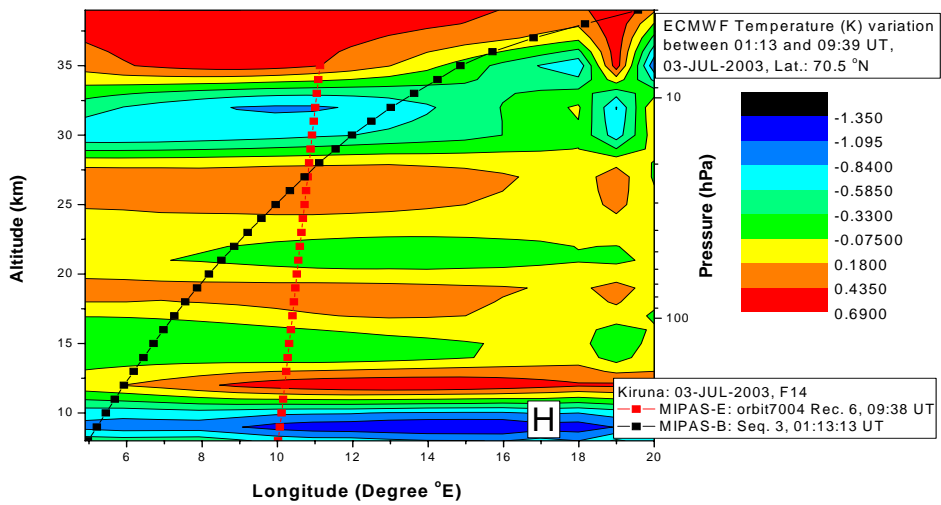
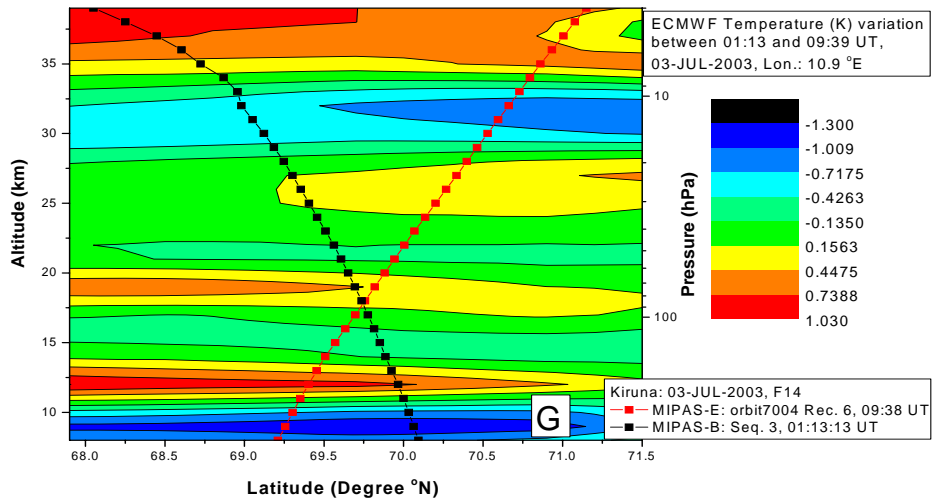
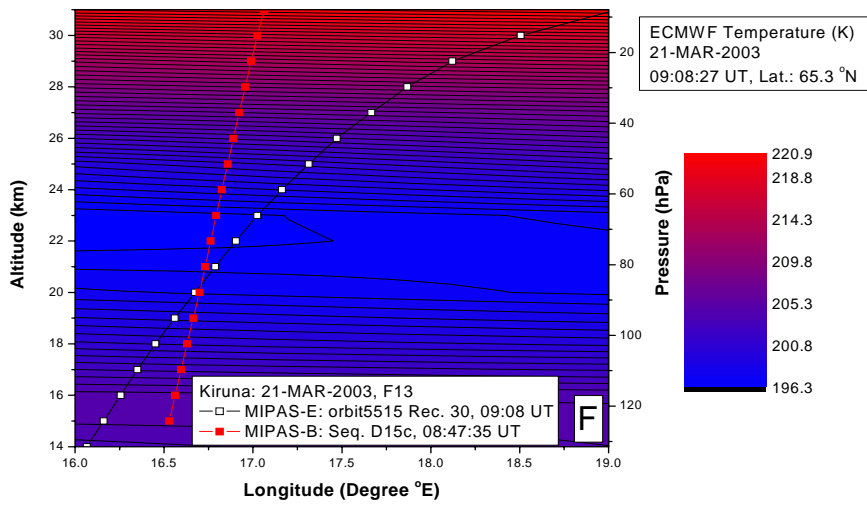
Note: N=number.

# Appendix C: Tangent point geolocations of MIPAS-B and MIPAS-ENVISAT LOS as well as ECMWF temperature fields

Tangent point geolocations of MIPAS-B (black and green) and MIPAS-E (red) LOS for Flight No. 11 (Panel A and B), Flight No. 13 (Panel C, D, E, and F), and Flight No. 14 (Panel G and H). The colour coded fields are the temperature from ECMWF.







## Acronyms

**CM:** Coordinate Mapping  
**CTM:** Chemistry Transport Model  
**DME:** Detector Module Electronics  
**DU:** Dobson Units  
**EASOE:** European Arctic Stratospheric Ozone Experiment  
**ECMWF:** European Center for Medium range Weather Forecast  
**ENVISAT:** ENVIRONMENTAL SATellite  
**ESA:** European Space Agency  
**FOV:** Field of View  
**FWHM:** Full Width at Half Maximum  
**GOMOS:** Global Ozone Monitoring by Occultation of Stars  
**GPS:** Global Positioning System  
**HITRAN:** High-resolution TRANsmiSSion database  
**IFOV:** Instantaneous Field of View  
**ILS:** Instrumental Line Shape  
**IMK:** Institute for Meteorology and Climate Research (Karlsruhe, Germany)  
**IMK-AME:** A research group of Algorithm development and MIPAS-ENVISAT in Institut für Meteorologie und Klimaforschung  
**IUP/IFE:** Institute of Environmental physics, University of Bremen, Germany  
**KASIMA:** Karlsruhe Simulation Model of the Middle Atmosphere  
**KOPRA:** The Karlsruhe Optimized and Precise Radiative transfer Algorithm  
**LOS:** Line Of Sight  
**LPCE:** Laboratoire de Physique et Chimie de l'Environnement  
**LTE:** Local Thermodynamic Equilibrium  
**MIPAS:** Michelson Interferometer for Passive Atmospheric Sounding  
**MIPAS-B:** Balloon version of MIPAS  
**MIPAS-E:** ENVISAT version of MIPAS  
**NESR:** Noise Equivalent Spectral Radiance  
**NRT:** Near Real Time  
**PMD:** Polarisation Measurement Device  
**ppbv:** Parts Per Million by Volume  
**ppmv:** Parts Per Billion by Volume  
**pptv:** Parts Per Trillion by Volume  
**PT:** Potential Temperature  
**PV:** Potential Vorticity  
**SCIAMACHY:** SCanning Imaging Absorption SpectroMeter for Atmospheric CHartographY  
**SPARC:** Stratospheric Processes And their Role in Climate  
**THT:** Trajectory Hunting Technique  
**TIROS:** Television and InfraRed Observing Satellite  
**TM:** Trajectory Mapping  
**UT:** Universal Time  
**UTC:** Universal Time Coordinated  
**VCM:** Variance Covariance Matrix  
**VMR:** Volume Mixing Ratio  
**WMO:** World Meteorological Organization

## List of figures and tables

<b>Figure 2.1:</b> Middle latitude temperature profile below 100 km .....	(4)
<b>Figure 4.1:</b> The scheme of ENVISAT with the three remote sensing instruments, MIPAS, SCIAMACHY, and GOMOS.....	(17)
<b>Figure 4.2:</b> The working principle of MIPAS.....	(18)
<b>Figure 4.3:</b> MIPAS measurement geometry.....	(19)
<b>Figure 4.4:</b> GOMOS measurement principle.....	(22)
<b>Figure 5.1:</b> The principle of the Michelson interferometer.....	(25)
<b>Figure 5.2:</b> Mechanical and optical setup of MIPAS-B.....	(29)
<b>Figure 5.3:</b> NESR of Seq. 2 at a tangent point altitude of 26 km during flight No. 14 in Kiruna, Sweden.....	(30)
<b>Figure 5.4:</b> The scheme of MIPAS-B measurement geometry.....	(31)
<b>Figure 5.5:</b> Typical data processing procedure of MIPAS-B.....	(33)
<b>Figure 7.1:</b> MIPAS-B lines-of-sight (black) for Flight No. 11 and MIPAS-E limb sequences (red) as well as the closest GOMOS star occultation of the same orbit (blue ellipse).....	(41)
<b>Figure 7.2:</b> MIPAS-B lines-of-sight (black) for Flight No. 13 and MIPAS-E limb sequences (white).....	(42)
<b>Figure 7.3:</b> MIPAS-B lines-of-sight (black) for Flight No. 14 and MIPAS-E limb sequences (white).....	(42)
<b>Figure 7.4:</b> Channel 1 spectra at different altitudes recorded in Seq. S of MIPAS-B Flight No. 11.....	(45)
<b>Figure 7.5:</b> Channel 2 spectra at different altitudes recorded in Seq. S of MIPAS-B Flight No. 11.....	(45)
<b>Figure 7.6:</b> Channel 3 spectra at different altitudes recorded in Seq. S of MIPAS-B Flight No. 11.....	(46)
<b>Figure 7.7:</b> The profiles of the absorption coefficients in the microwindows for HNO <sub>3</sub> retrieval of Seq. 3, Flight No. 14.....	(48)
<b>Figure 7.8:</b> An example of the continuum effect on the retrieval.....	(48)
<b>Figure 7.9:</b> Typical retrieval of the temperature.....	(51)
<b>Figure 7.10:</b> Typical retrieval of the H <sub>2</sub> O VMR.....	(53)
<b>Figure 7.11:</b> Typical retrieval of the O <sub>3</sub> VMR.....	(54)
<b>Figure 7.12:</b> Typical retrieval of the HNO <sub>3</sub> VMR.....	(56)
<b>Figure 7.13:</b> Part of the spectral fit of HNO <sub>3</sub> proven microwindow (863.85-868.75) (cm <sup>-1</sup> ) in the height range of 11-20 km.....	(57)
<b>Figure 7.14:</b> Typical retrieval of the CH <sub>4</sub> VMR.....	(58)
<b>Figure 7.15:</b> Typical retrieval of the N <sub>2</sub> O VMR.....	(59)
<b>Figure 7.16:</b> CH <sub>4</sub> VMR profiles based on individual microwindows.....	(60)
<b>Figure 7.17:</b> Typical retrieval of the NO <sub>2</sub> VMR.....	(61)



<b>Figure 8.1.1-1:</b> The tangent points distances and the potential vorticity differences between MIPAS-B Seq. S and MIPAS-E Rec. 14 , Seq. S and Rec. 15 as well as Seq. N3 and Rec. 16 .....	(63)
<b>Figure 8.1.1-2:</b> The tangent points distances and the potential vorticity differences between MIPAS-B Seq. N3a and MIPAS-E Rec. 20, Seq. D15c and Rec. 30.....	(64)
<b>Figure 8.1.1-3:</b> The tangent points distances between MIPAS-B Seq. 3 and MIPAS-E Rec. 06.....	(65)
<b>Figure 8.1.2-1:</b> 2-days backward trajectories of air masses that had been scanned by MIPAS-B Seq. N3 during Flight 11.....	(66)
<b>Figure 8.2.1-1:</b> Temperature coincident comparisons for Flight No. 11.....	(68)
<b>Figure 8.2.1-2:</b> Temperature coincident comparisons for Flight No. 13.....	(71)
<b>Figure 8.2.1-3:</b> Temperature coincident comparisons for Flight No. 14.....	(72)
<b>Figure 8.2.1-4:</b> Scatter plots of MIPAS-E temperature against MIPAS-B temperature for Flight No. 11.....	(73)
<b>Figure 8.2.1-5:</b> Temperature trajectory comparison for Flight No. 11.....	(74)
<b>Figure 8.2.1-6:</b> Scatter plots of MIPAS-E temperature against MIPAS-B temperature for Flight No. 13.....	(75)
<b>Figure 8.2.1-7:</b> Temperature trajectory comparison for Flight No. 13.....	(75)
<b>Figure 8.2.1-8:</b> Scatter plots of MIPAS-E temperature against MIPAS-B temperature for Flight No. 14.....	(76)
<b>Figure 8.2.1-9:</b> Temperature trajectory comparison for Flight No. 14.....	(76)
<b>Figure 8.2.1-10:</b> Summary comparison of temperature between MIPAS-E and MIPAS-B.....	(77)
<b>Figure 8.2.2-1:</b> H <sub>2</sub> O coincident comparisons for Flight No. 11.....	(79)
<b>Figure 8.2.2-2:</b> H <sub>2</sub> O coincident comparisons for Flight No. 13.....	(80)
<b>Figure 8.2.2-3:</b> H <sub>2</sub> O coincident comparisons for Flight No. 14.....	(81)
<b>Figure 8.2.2-4:</b> Scatter plots of MIPAS-E H <sub>2</sub> O against MIPAS-B H <sub>2</sub> O for Flight No. 11.....	(82)
<b>Figure 8.2.2-5:</b> H <sub>2</sub> O trajectory comparison for Flight No. 11.....	(83)
<b>Figure 8.2.2-6:</b> Scatter plots of MIPAS-E H <sub>2</sub> O against MIPAS-B H <sub>2</sub> O for Flight No. 13.....	(83)
<b>Figure 8.2.2-7:</b> H <sub>2</sub> O trajectory comparison for Flight No. 13.....	(84)
<b>Figure 8.2.2-8:</b> Scatter plots of MIPAS-E H <sub>2</sub> O against MIPAS-B H <sub>2</sub> O for Flight No. 14.....	(85)
<b>Figure 8.2.2-9:</b> H <sub>2</sub> O trajectory comparison for Flight No. 14.....	(85)
<b>Figure 8.2.2-10:</b> H <sub>2</sub> O VMR profile of MIPAS-B Seq. 2 and the MIPAS-E H <sub>2</sub> O VMR profiles associated with the H <sub>2</sub> O VMR trajectory comparison for Seq. 2.....	(86)
<b>Figure 8.2.2-11:</b> Comparison of all H <sub>2</sub> O+2*CH <sub>4</sub> VMR profiles of MIPAS-E with MIPAS-B profiles, along with the measurements carried out previously by Engel et al. and Hermann et al.....	(87)
<b>Figure 8.2.2-12:</b> Summary comparison of H <sub>2</sub> O between MIPAS-E and MIPAS-B.....	(88)
<b>Figure 8.2.3-1:</b> O <sub>3</sub> coincident comparisons for Flight No. 11.....	(90)
<b>Figure 8.2.3-2:</b> O <sub>3</sub> coincident comparisons for Flight No. 13.....	(92)
<b>Figure 8.2.3-3:</b> O <sub>3</sub> coincident comparisons for Flight No. 14.....	(93)

<b>Figure 8.2.3-4:</b> Scatter plots of MIPAS-E O <sub>3</sub> against MIPAS-B O <sub>3</sub> for Flight No. 11.....	(94)
<b>Figure 8.2.3-5:</b> O <sub>3</sub> trajectory comparison for Flight No. 11.....	(94)
<b>Figure 8.2.3-6:</b> Scatter plots of MIPAS-E O <sub>3</sub> against MIPAS-B O <sub>3</sub> for Flight No. 13.....	(95)
<b>Figure 8.2.3-7:</b> O <sub>3</sub> trajectory comparison for Flight No. 13.....	(95)
<b>Figure 8.2.3-8:</b> Scatter plots of MIPAS-E O <sub>3</sub> against MIPAS-B O <sub>3</sub> for Flight No. 14.....	(96)
<b>Figure 8.2.3-9:</b> O <sub>3</sub> trajectory comparison for Flight No. 14.....	(96)
<b>Figure 8.2.3-10:</b> Summary comparison of O <sub>3</sub> between MIPAS-E and MIPAS-B.....	(97)
<b>Figure 8.2.4-1:</b> HNO <sub>3</sub> coincident comparisons for Flight No. 11.....	(99)
<b>Figure 8.2.4-2:</b> HNO <sub>3</sub> coincident comparisons for Flight No. 13.....	(100)
<b>Figure 8.2.4-3:</b> HNO <sub>3</sub> coincident comparisons for Flight No. 14.....	(101)
<b>Figure 8.2.4-4:</b> Scatter plots of MIPAS-E HNO <sub>3</sub> against MIPAS-B HNO <sub>3</sub> for Flight No. 11.....	(102)
<b>Figure 8.2.4-5:</b> HNO <sub>3</sub> trajectory comparison for Flight No. 11.....	(102)
<b>Figure 8.2.4-6:</b> Scatter plots of MIPAS-E HNO <sub>3</sub> against MIPAS-B HNO <sub>3</sub> for Flight No. 13.....	(103)
<b>Figure 8.2.4-7:</b> HNO <sub>3</sub> trajectory comparison for Flight No. 13.....	(103)
<b>Figure 8.2.4-8:</b> Scatter plots of MIPAS-E HNO <sub>3</sub> against MIPAS-B HNO <sub>3</sub> for Flight No. 14.....	(104)
<b>Figure 8.2.4-9:</b> HNO <sub>3</sub> trajectory comparison for Flight No. 14.....	(104)
<b>Figure 8.2.4-10:</b> Summary comparison of HNO <sub>3</sub> between MIPAS-E and MIPAS-B.....	(105)
<b>Figure 8.2.5-1:</b> CH <sub>4</sub> coincident comparisons for Flight No. 11.....	(107)
<b>Figure 8.2.5-2:</b> CH <sub>4</sub> coincident comparisons for Flight No. 13.....	(108)
<b>Figure 8.2.5-3:</b> CH <sub>4</sub> coincident comparisons for Flight No. 14.....	(109)
<b>Figure 8.2.5-4:</b> Scatter plots of MIPAS-E CH <sub>4</sub> against MIPAS-B CH <sub>4</sub> for Flight No. 11.....	(110)
<b>Figure 8.2.5-5:</b> CH <sub>4</sub> trajectory comparison for Flight No. 11.....	(110)
<b>Figure 8.2.5-6:</b> Scatter plots of MIPAS-E CH <sub>4</sub> against MIPAS-B CH <sub>4</sub> for Flight No. 13.....	(111)
<b>Figure 8.2.5-7:</b> CH <sub>4</sub> trajectory comparison for Flight No. 13.....	(111)
<b>Figure 8.2.5-8:</b> Scatter plots of MIPAS-E CH <sub>4</sub> against MIPAS-B CH <sub>4</sub> for Flight No. 14.....	(112)
<b>Figure 8.2.5-9:</b> CH <sub>4</sub> trajectory comparison for Flight No. 14.....	(112)
<b>Figure 8.2.5-10:</b> Summary comparison of CH <sub>4</sub> between MIPAS-E and MIPAS-B.....	(113)
<b>Figure 8.2.6-1:</b> N <sub>2</sub> O coincident comparisons for Flight No. 11.....	(115)
<b>Figure 8.2.6-2:</b> N <sub>2</sub> O coincident comparisons for Flight No. 13.....	(116)
<b>Figure 8.2.6-3:</b> N <sub>2</sub> O coincident comparisons for Flight No. 14.....	(117)
<b>Figure 8.2.6-4:</b> Scatter plots of MIPAS-E N <sub>2</sub> O against MIPAS-B N <sub>2</sub> O for Flight No. 11.....	(118)

<b>Figure 8.2.6-5:</b> N <sub>2</sub> O trajectory comparison for Flight No. 11.....	(118)
<b>Figure 8.2.6-6:</b> Scatter plots of MIPAS-E N <sub>2</sub> O against MIPAS-B N <sub>2</sub> O for Flight No. 13.....	(119)
<b>Figure 8.2.6-7:</b> N <sub>2</sub> O trajectory comparison for Flight No. 13.....	(119)
<b>Figure 8.2.6-8:</b> Scatter plots of MIPAS-E N <sub>2</sub> O against MIPAS-B N <sub>2</sub> O for Flight No. 14.....	(120)
<b>Figure 8.2.6-9:</b> N <sub>2</sub> O trajectory comparison for Flight No. 14.....	(120)
<b>Figure 8.2.6-10:</b> Summary comparison of N <sub>2</sub> O between MIPAS-E and MIPAS-B.....	(121)
<b>Figure 8.2.6-11:</b> The N <sub>2</sub> O-CH <sub>4</sub> correlation of MIPAS-E and MIPAS-B measurements .....	(122)
<b>Figure 8.2.7-1:</b> NO <sub>2</sub> coincident comparisons for Flight No. 11.....	(123)
<b>Figure 8.2.7-2:</b> NO <sub>2</sub> coincident comparisons for Flight No. 13.....	(124)
<b>Figure 8.2.7-3:</b> NO <sub>2</sub> coincident comparisons for Flight No. 14.....	(125)
<b>Figure 8.2.7-4:</b> An example of scatter plots of MIPAS-E against MIPAS-B NO <sub>2</sub> VMR for Flight No. 11....	(126)
<b>Figure 8.2.7-5:</b> NO <sub>2</sub> trajectory comparison for Flight No. 11.....	(127)
<b>Figure 8.2.7-6:</b> NO <sub>2</sub> trajectory comparison for Flight No. 13.....	(127)
<b>Figure 8.2.7-7:</b> NO <sub>2</sub> trajectory comparison for Flight No. 14.....	(128)
<b>Figure 8.2.7-8:</b> Summary comparison of NO <sub>2</sub> between MIPAS-E and MIPAS-B.....	(129)
<b>Figure 8.3.1-1:</b> O <sub>3</sub> trajectories comparisons between SCIAMACHY and MIPAS-B for Flight No. 11.....	(131)
<b>Figure 8.3.1-2:</b> O <sub>3</sub> trajectories comparisons between SCIAMACHY and MIPAS-B for Flight No. 13.....	(132)
<b>Figure 8.3.2-1:</b> NO <sub>2</sub> trajectories comparisons between SCIAMACHY and MIPAS-B for Flight No. 11.....	(134)
<b>Figure 8.3.2-2:</b> NO <sub>2</sub> trajectories comparisons between SCIAMACHY and MIPAS-B for Flight No. 13.....	(135)
<b>Figure 8.3.2-3:</b> NO <sub>2</sub> coincident intercomparisons among SCIAMACHY, MIPAS-B and/or MIPAS-E.....	(136)
<b>Figure 8.4-1:</b> The tangent point distances between MIPAS-B Seq. N3 and the corresponding sequence of GOMOS.....	(138)
<b>Figure 8.4-2:</b> O <sub>3</sub> Comparison between GOMOS and MIPAS-B Seq. N3 (black curve) measurements.....	(139)
<b>Figure 8.4-3:</b> NO <sub>2</sub> Comparison between GOMOS and MIPAS-B Seq. N3 (black curve) measurements.....	(139)
<b>Figure 9.1-1:</b> The influence of the vertical grids to the intercomparison.....	(141)
<b>Figure 9.2-1:</b> Averaging kernel matrix for the MIPAS-E temperature measurement.....	(142)
<b>Figure 9.2-2:</b> Comparisons of MIPAS-E with MIPAS-B temperature profiles with and without taking into account the vertical resolution influence.....	(143)
<b>Figure 9.3-1:</b> An example of comparisons of MIPAS-E O <sub>3</sub> VMR with MIPAS-B correlative measurements with different altitude coordinates.....	(144)

<b>Table 7.1:</b> The microwindows used for the retrieval from MIPAS-B spectra.....	(44)
<b>Table 8.1:</b> Mean time and geolocation of the coincident observations.....	(62)
<b>Table 8.2:</b> Mean differences of MIPAS-B minus MIPAS-E temperature as well as the associated mean combined errors and the mean standard deviations.....	(78)
<b>Table 8.3:</b> Mean differences of MIPAS-B minus MIPAS-E H <sub>2</sub> O as well as the associated mean combined errors and the mean standard deviations.....	(89)
<b>Table 8.4:</b> Mean differences of MIPAS-B minus MIPAS-E O <sub>3</sub> as well as the associated mean combined errors and the mean standard deviations.....	(97)
<b>Table 8.5:</b> Mean differences of MIPAS-B minus MIPAS-E HNO <sub>3</sub> as well as the associated mean combined errors and the mean standard deviations.....	(105)
<b>Table 8.6:</b> Mean differences of MIPAS-B minus MIPAS-E CH <sub>4</sub> as well as the associated mean combined errors and the mean standard deviations.....	(113)
<b>Table 8.7:</b> Mean differences of MIPAS-B minus MIPAS-E N <sub>2</sub> O as well as the associated mean combined errors and the mean standard deviations.....	(121)
<b>Table 8.8:</b> Mean differences of MIPAS-B minus MIPAS-E NO <sub>2</sub> as well as the associated mean combined errors and the mean standard deviations.....	(129)
<b>Table 8.9:</b> Mean differences of MIPAS-B minus SCIAMACHY measurements for O <sub>3</sub> and NO <sub>2</sub> as well as the associated mean combined errors and the mean standard deviations ...	(137)
<b>Table 10.1:</b> Conclusions with respect to MIPAS-E validation.....	(146)

# Acknowledgments

This study was carried out in the Institute of Meteorology and Climatology Research of the Karlsruhe Forschungszentrum and the University of Karlsruhe. I greatly appreciate the help from all the people who ever contributed to the study.

Prof. Dr. Herbert Fischer for providing this study opportunity, for advising the Ph.D. dissertation and reviewing the manuscript.

Mr. Hermann Oelhaf for advising the dissertation in details, for revision and comments on the manuscript and the other aspects.

Dr. Gerald Wetzel for comments on the manuscript, for the guidance on the MIPAS-B data retrievals and the productive discussions.

Priv. Doz. Dr. Habil. C. E. Blom for review the manuscript.

I wish to thank Dipl.-Ing. Katja Grunow for the trajectory calculations; Dr. Roland Ruhnke for performing the KASIMA model simulations; Dr. Anne Kleinert for her comments on the manuscript and discussions; Dr. Andreas Wiegele for the discussions and the help on KOPRA operations; Dipl. Annick Olinger for supplying some MIPAS-B data; Dr. Liu Guangyuan for many discussions; Dr. Felix Friedl-Vallon, Dr. Guido Macher, Dr. Anton Lengel and Mr. Hans Nordmeyer and the MIPAS-B field experiment team for supplying the spectral data. Dr. Corneli Keim for discussions.

I also wish to thank Prof. Sun Yiyi for the help on dissertation writing, discussions and suggestions.